Reaction pathways for the formation of hydrogen peroxide in fuel cells:

- a DFT study

Dissertation

submitted in partial fulfilment of the requirements

for the degree of

Master of Science in Engineering

at the

University of Cape Town

2013

BY

Thendo Madala

BSc Chemical Engineering (UCT)

Supervised by:

Professor Eric van Steen

Dr Melissa Petersen

Centre for Catalysis Research
Department of Chemical Engineering
University of Cape Town
Private Bag
Rondebosch, 7701
South Africa

DECLARATION

I certify that this manuscript is my own unaided work, except for information obtained from literature sources and guidance from my project supervisor. All sources of information have been adequately acknowledged and referenced.

Thendo Madala

……

ABSTRACT

The world's dependency on fossil fuel will come to an end in the near future due to depletion of natural resources. Thus, research into alternative energy carriers becomes imperative. Furthermore, the use of fossil fuels is associated with environmental problems, which might be minimised by using alternatives. Hydrogen technology in the form of fuel cells can be a reliable and clean technology to minimise the problems associated with the use of fossil fuels. Fuel cells utilise hydrogen and air, and convert them to electrical energy through electro-catalysis with a co-product being water and heat.

The theoretical efficiency for fuel cells is estimated at~83%, however the recorded efficiency of real operational fuel cells is only between 45-60%.The limited efficiency of these devices remains elusive. To contribute to the understanding of these low efficiencies, the two half reactions occurring in fuel cells, viz. the oxygen reduction reaction and the oxidation of hydrogen need to be understood. It is thought that the slow kinetics of the oxygen reduction reaction is the main contributor to the low efficiency observed.

The oxygen reduction reaction may proceed via a stable peroxide (OOH*) intermediate. It is proposed that the latter species can be hydrogenated yielding hydrogen peroxide, H_2O_2. Formation of hydrogen peroxide is not desired since it is corrosive and may accelerate degradation of the electrodes and/or membrane. In this study, the reaction pathway for the formation of hydrogen peroxide over Pt(111) was investigated using DFT (PAW-PBE). Various reaction pathways for the formation of hydrogen peroxide were investigated, viz. path-1) addition of atomic hydrogen on oxygen, path-2) addition of atomic oxygen on the hydroxyl species(OH*), path-3) interaction of hydroxyl species (OH*+OH*).

A thermodynamic analysis of the potential energy surface diagrams along the reaction pathways (assuming the validity of the Brønsted-Evans-Polanyi relationship), indicates that hydrogen peroxide is most likely formed via the direct addition of (H*) to molecular adsorbed (O_2*) yielding (OOH*) with the further addition of (H*).

The intrinsic activation barriers for the reaction steps were determined using the Nudged Elastic Band (NEB) method. The minimum energy pathway for the formation of hydrogen peroxide in fuel cells is via the oxygen activation step by atomic hydrogen with an overall activation barrier (E_a) of 0.55 eV ($H^*+O_2^*$). The consecutive addition of hydrogen (H^*+OOH^*) has overall activation barrier of only 0.44 eV. In contrast, the dissociation of adsorbed oxygen ($O_2^*+ *\rightarrow O^*+O^*$) is less facile ($E_a$=0.58 eV) than the hydrogen addition on oxygen (E_a= 0.51 eV). Dissociative adsorption of oxygen may occur (depending on the availability of vacant sites) but is energetically not favoured on Pt(111) surface during

oxygen reduction reaction. Hence, the oxygen reduction reaction is thought to proceed via the hydrogen assisted oxygen dissociation step, i.e. the reaction O_2* + H* →OOH* + * → OH* + O*. This last reaction step competes with the formation of hydrogen peroxide, which proceeds via the consecutive addition of hydrogen (H*) to OOH*. The activation barrier for OOH* dissociation (OOH*→OH*+O*) was estimated to be 0.18 eV, whereas the activation barrier for the addition of H* to OOH* was estimated to be 0.44 eV. This indicates a competition between the two steps, with the OOH* dissociation being more facile.

ACKNOWLEDGEMENTS

I would like to thank Professor Eric van Steen, for the opportunity to work on this project. The opportunity has broadened my knowledge of science and engineering. Thank you once again for the learning and inspiration you have given me over my undergraduate Chemical Engineering level. The wisdom I found in your words will never age in me. The 'forever' questions you asked and criticisms, were valuable, and gave me a clear vision of where to take this project.

I would also like to send a special thank you to Dr Melissa Petersen, for the passion you shown in allowing me to learn the basics and applications of computational chemistry. The support you shown will forever be treasured.

To Dr Werner Janse van Rensburg, thank you so much for the support and encouragements during the early stages of my project. I valued the passion and time you took to avail yourself at the UCT campus. I learned a lot and your support laid a foundation for this study.

Jan-Albert van den Berg and Pieter van Helden, thank you for sharing your knowledge on computational chemistry and always showing the will to help, I truly appreciated your time.

To the molecular modelling team, Molefi Matsutsu, Junaid Cariem and Christian de Vries, thank you all for helping with the random problems that always 'popped' up, the time you shared will forever be treasured.

I would also like to extend a special appreciation to Martha Luvhimbi and Rendani Ramaru for reviewing this thesis.

Above all praise to the Almighty God I serve who made it possible to enjoy this experience.

To all my friends and family thank you so much for being there and for cheering me up. It has been an exciting road and I had lots of fun. 'Ndo livhuwa' Ndaa.

TABLE OF CONTENTS

GLOSSARY

Co-adsorption: Simultaneous adsorption of multiple species

Polarisation: Voltage drop in fuel cells with increasing current draw

Vacuum space: The space that separate two surface slabs in a unit cell

Vibrational analysis: Normal mode analysis on the molecules in the current system, to selectively obtain the mass-weighted normal modes of vibration and the corresponding zero-point vibrational frequencies and their intensities, the frequencies are obtained from the matrix Cartesian second derivatives, or better known as Hessian matrix, of a molecular or periodic system

ABBREVIATIONS

AFC : Alkaline Fuel Cells

BEP : Brønsted Evans Polanyi

BZ : Brillouin Zone

CASTEP : Cambridge Sequential Total Energy Package

DC : Direct Current

DFT : Density functional theory

EELS : Electron Energy Loss Spectroscopy

FCC : Face Cantered Cubic

FP-LAPW : Full-Potential Linearised Augmented Plane Wave

GGA : General Gradient Approximation;

HCP : Hexagonal Close Packed

KOH : Potassium Hydroxide

LDA : Local Density Approximation

LEED : Low Energy Electron Diffraction

MEP : Minimum Energy Path

ML : Monolayer

NEB : Nudged Elastic Band

ORR : Oxygen Reduction Reaction

PAW : Projected Augmented Wave

PBE : Perdew, Burke and Ernzerhof

PEMFC : Proton Exchange Membrane Fuel Cells

PES : Potential Energy Surface

PW91 : Perdew–Wang from 1991

RPBE : Revised Perdew, Burke and Ernzerhof

TDS : Thermal Desorption Spectroscopy

TS : Transition State

UPS : Ultraviolet Photoelectron Spectroscopy

Uspp : ultra-soft pseudo-potential

VASP : *Vienna Ab-initio Simulation Package*

XPS : X-ray Photoemission Spectroscopy

ZPE : Zero point energy

LIST OF ILLUSTRATIONS

List of Tables

Chapter 1

Chapter2

Chapter 3

Chapter 4

Chapter 6

List of Figures

Chapter 1

Chapter 2

Chapter 3

Chapter 4

Chapter 5

Chapter 6

Chapter 1

1 INTRODUCTION

The world dependence on fossil fuel energy will sooner or later pose a threat to human kind. According to Barbir (2005), it is as a result of two key problems, fossil fuels depletion and the environmental impact. Problems such as global warming, climate change, acid rain, pollution, ozone layer depletion, forest and agricultural land damage are all attributed to the use of fossil fuels.

It is estimated that production and utilization of fossil fuels, petroleum and natural gas, may peak between the year 2015 and 2020 and from there onwards decline. The resulting impact of the continuous high demand and declining supply will result in a high consumer price for fuel.

Since the early 1970s hydrogen energy utilization technology has been proposed as one of the possible solutions to these two key problems.

Hydrogen is the lightest, most efficient and cleanest fuel, provided a clean source of hydrogen can be found (a possible source is water, since it is formed as a product in fuel cells) (Barbir, 2005). Hydrogen can be 'converted' to electrical energy, through electro-catalysis in fuel cells with a higher theoretical efficiency (>80%) than from conventional fossil fuels. The efficiency of fuel cells can be higher than that of heat engines, since fuel cells are electrochemical devices, unlike heat engines, they are not subjected to the limitations of the Carnot cycle.

1.1 Fuel cells

Fuel cells are electrochemical devices consisting of an electrolyte, an ion exchange mechanism, *'sandwiched'* by two electrodes (anode/cathode). They generally convert chemical energy into electrical energy using a direct, low/high temperature electrochemical reaction. This makes fuel cells simpler and more efficient than the conventional methods to generate electrical energy.

The conventional processes to generate electrical energy typically require:

- Combustion of fossil fuel to convert chemical energy into heat
- Utilization of heat to generate steam
- Converting thermal energy into mechanical energy using steam
- Mechanical energy into electricity using generators

The advantage of a fuel cell is that it bypasses all these steps and generates electrical energy in one step with no moving parts, almost silent in operation. Figure 1.1 depicts a simplified diagram of a fuel cell. The hydrogen fuel is oxidised at the anode and oxygen is reduced at the cathode. The flow of electrons through the external circuit can be used for electrical work. The ions generated at the cathode or anode (depending on the type of fuel cell) flow through an electrolyte to the opposite electrode.

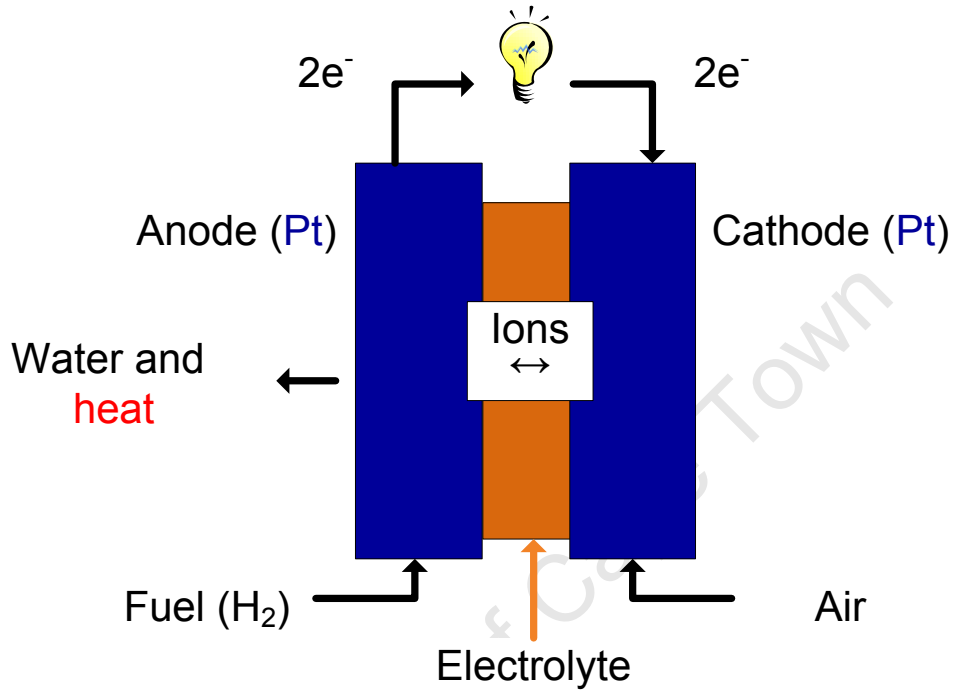

(AFC) $H_2 + 2OH^- \rightarrow 2H_2O + 2e^-$ $\quad$ $½O_2 + 2e^- + H_2O \rightarrow 2OH^-$

(PEM) $H_2 \rightarrow 2H^+ + 2e^-$ $\quad$ $½O_2 + 2H^+ + 2e^- \rightarrow H_2O$

Figure 1.1: Schematic representation of a fuel cell with single step direct DC electricity generation. (PEM: Proton exchange membrane; AFC: Alkaline fuel cell)

1.1.1 Brief history of fuel cells

The invention of fuel cells dates as far back as 1839, when the operating principle was discovered by Sir William Grove, although a Swiss scientist by the name Christian F. Schönbein also independently discovered the very same principle at about the same time (Barbir, 2005). Grove called the device a 'gaseous voltaic battery', this discovery meant less to Grove and most scholars but remained a scientific curiosity for almost a decade (Barbir, 2005). The first application of fuel cells was adopted by the U.S space program. This favoured attraction towards the use of fuel cells for different applications.

1.1.2 Types of hydrogen fuel cells

Fuel cells are categorised according to the type of electrolyte transfer mechanism which is used (see Figure 1.2) (Barbir, 2005). The summary about various hydrogen fuel cells in this section is from Barbir. (2005).

Alkaline fuel cells (AFC) utilize KOH as an electrolyte. The electrolyte is held in a matrix and a wide range of electro-catalysts such as Ni, Ag, metal oxides and noble metals can be used. AFC are intolerant to CO_2, which may be introduced to the cell entrained in the fuel or the oxidant. These types of fuel cells have been used since the 1960s by the US space program (Apollo and Space Shuttle). The operating temperature also varies depending on the concentration of the electrolyte. At KOH concentration of 85 wt% a high operating temperature of 250°C can be attained, however at low concentrations of 35-50 wt% lower operating temperatures of 120°C must be used.

Polymer electrode membrane (proton exchange membrane fuel cell) (PEMFC) uses a thin proton conductive polymer membrane (perfluorosulfonated acid polymer) as an electrolyte. The reactions are mostly catalysed by platinum supported on carbon with a loading of approximately 0.3 mg/cm². CO poisons the electro-catalyst. Alloys of platinum with ruthenium can be used to negate the effect of CO-poisoning. The operating temperatures range between 60°C and 80°C.

Phosphoric acid fuel cell (PAFC) uses concentrated phosphoric acid (~100%) as an electrolyte. The electro-catalyst for both anode and cathode is platinum and the matrix used to retain the acid is SiC. Typical operating temperatures are between 150°C and 220°C. This type of a fuel cell has already found its way into the market in the form of small container packages (200kW) for stationary electricity generation.

Molten carbonate fuel cells (MCFC) uses a combination of alkali (Li,Na,K) carbonate as the electrolyte which is retained in a matrix of $LiAlO_2$. The carbonates form a conductive molten salt at operating temperature conditions of 600°C to 700°C. At these conditions the carbonate ions provide ionic conduction. At these high temperatures, not only noble metals such as platinum can be used as electro-catalysts but also nickel and nickel oxide.

Solid oxide fuel cells (SOFC) uses the solid nonporous metal oxide usually Y_2O_3-stabilized ZrO_2 (YSZ) as the electrolyte. Ionic conduction by oxygen ions takes place at high temperatures of 800°C to 1000°C. SOFC for stationary power generation are in their pre-commercial/ demonstration stage at present.

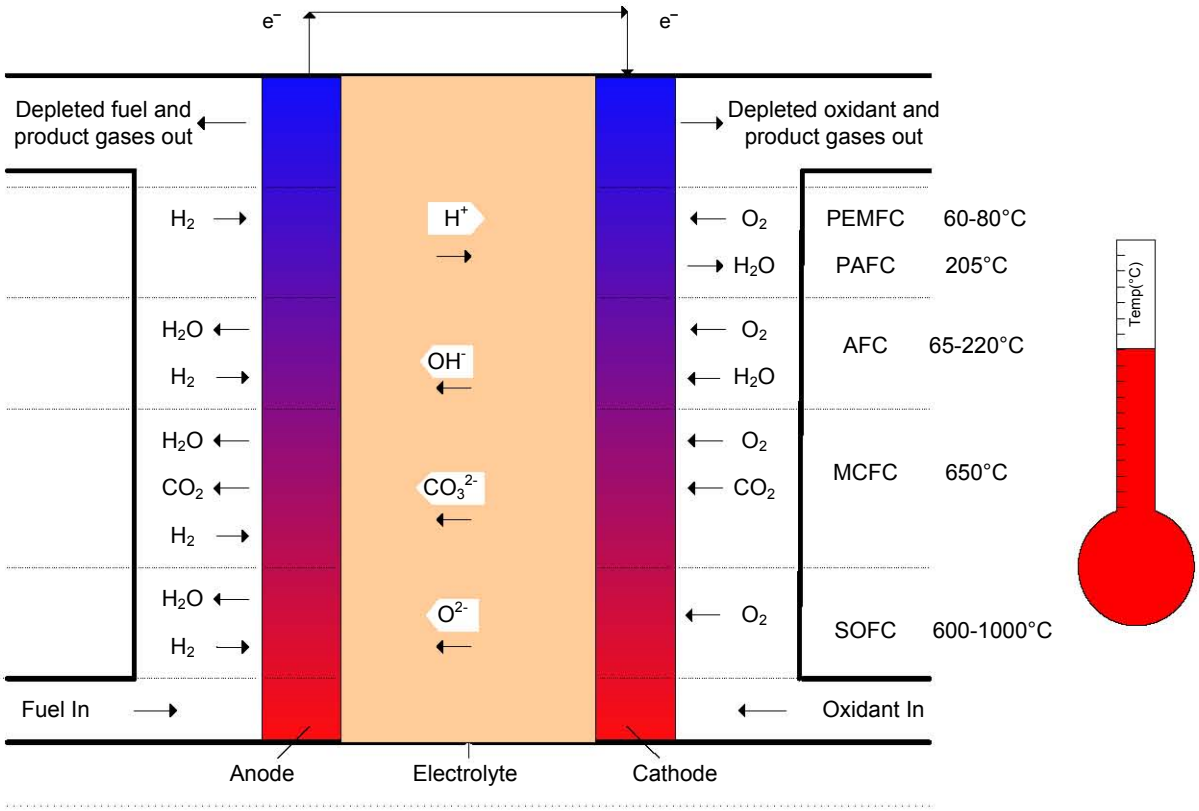

Figure 1.2: Schematic illustration of different types of fuel cells, with the corresponding reactions and operating temperatures indicated (redrawn from Barbir 2005)

The attention has been towards the low operating temperature fuel cells which may provide a wide range of uses, from portable devises to automobile engines.

The PEM-fuel cell is a low operating temperature fuel cell with a unique characteristic of a solid electrolyte, usually a polymer electrode membrane. The disadvantage of this type of fuel cell is the poor kinetics of oxygen reduction reaction in the acid media (Ramani, 2006). Hence the operational efficiency of this type of fuel cell is lower than that of the alkaline fuel cell (AFC). To resolve the poor ORR kinetics high metal loadings (≥ 0.4 mg/cm²) are required, but such loadings result in high cost for PEM fuel cells, making them less attractive for commercial uses.

The type of fuel cell of interest in this study is the alkaline fuel cell (AFC). The low operating temperature for this type of fuel cell makes it the fuel cell of choice. Furthermore the cell operating pressure is low (only a few tens of mbar from ambient), it is insensitive to ambient humidity and has the advantage of a built-in thermal management system, '*the circulating electrolyte',* allowing for heat transfer across the two reactions taking place (Viswanathan et al., 2006). An added advantage of alkaline fuel cells is the use of a non-porous metal catalyst (possibly non-noble metal) due to facile ORR kinetics at high pH (i.e. can attain higher efficiencies) (Ramani, 2006). However the disadvantages of this type of fuel cell are that they suffer from liquid electrolyte lifespan, CO_2 poisoning and electrode degradation.

1.1.3 Alkaline Fuel Cell

The first generation of AFC used the circulating liquid alkaline electrolyte, potassium hydroxide with standard concentration of 30-45% (Viswanathan et al., 2006). At these specifications the cell maintains an effective heat transfer and water management system. The fuel cell (AFC) can produce power at ambient temperatures but full power can be achieved at the design temperature of 70°C. If integrated with electrical heating they can reach the design temperature within 10 minutes of cold start (Viswanathan et al., 2006).

Introduction of the advanced matrix based system has led to the abandonment of circulating electrolyte eliminating moving parts in this type of fuel cells (Viswanathan et al., 2006). The use of matrix based electrolyte (KOH soaked in matrices) became the standard practice adopted mostly by NASA in their space fuel cells. KOH is effectively exchanged within the matrix based electrolyte, suppressing the possible formation of potassium carbonates and making it possible to operate the cell without complete removal of CO_2 (Viswanathan et al., 2006). However, abandoning circulating electrolyte also means leaving out an effective thermal and water management system.

The reactions taking place in the alkaline fuel cell (AFC) is mostly catalysed by platinum with a loading of 0.3 mg/cm² on a semi porous electrode (Viswanathan et al., 2006). The presence of CO_2 in the feed to the fuel cell will result in the formation of carbonates reducing the concentration of the reaction intermediate OH-. The following are the possible CO_2 poisoning reactions.

$$CO_2(g) + 2OH^-(aq) \rightarrow CO_3^{2-} + H_2O\ (\ell) \quad (1.1)$$

$$CO_2(g) + 2KOH(aq) \rightarrow K_2CO_3(aq) + H_2O(\ell) \quad (1.2)$$

$$K_2CO_3(aq) + H_2O(\ell) + CO_2(g) \rightarrow 2KHCO_3(aq) \quad (1.3)$$

The formation of potassium carbonate and in particular potassium bicarbonate may lead to the formation of a precipitate, which blocks both the electrolyte pathway and electrode pores To eliminate potential problems of electrolyte poisoning, an atmospheric scrubber is integrated to remove CO_2 from air prior to introduction into the fuel cell, or alternatively changing the electrolyte at regular service intervals (Viswanathan et al., 2006).

1.1.4 AFC working principle

Hydrogen is supplied to the anode side and oxygen at the cathode side. The voltage attained between the anode and the cathode on a single fuel cell is between 0.5 V and 0.9 V, depending on the loading (theoretical voltage: 1.23V) (Viswanathan et al., 2006). The

summary of the electrochemical reactions taking place at these electrodes are outlined below.

On the cathode (positive electrode), oxygen is catalytically reduced:

$$½O_2(g) + 2e^- + H_2O(\ell) \rightarrow 2OH^-(aq) \quad (1.4)$$

At the anode (negative electrode), hydrogen is catalytically oxidised yielding the product water:

$$H_2(g) + 2OH^-(aq) \rightarrow 2H_2O(\ell) + 2e^- \quad (1.5)$$

Overall reaction:

$$H_2(g) + ½O_2(g) \rightarrow H_2O(\ell) + \text{electrical energy} + \text{heat} \quad (1.6)$$

The theoretical voltage for the above reaction is calculated from the following equation:

$$E^{\circ}_{theor} = -\frac{\Delta^{rxn}\, G(T)}{n \cdot F} \quad (1.7)$$

Where E^0_{theor} is the standard theoretical or ideal potential, $\Delta^{rxn}G(T)$ is the change in Gibbs free energy for the reaction, n is the number of electrons required to complete the reaction (n = 2 equivalent/mole H_2) and F is Faraday's constant (96.485 Coulombs/equivalent)

The change in Gibbs free energy at 25°C for reaction [1.6] is -237.3 kJ/mole assuming liquid water product. Hence E^0_{theor} is 1.23 V.

The recombination of hydrogen and oxygen via this medium (fuel cell) result in the production of water at the anode side, wherein overall electrical energy and heat are generated by the fuel cell.

1.2 Current limitations of fuel cells

Fuel cells are theoretically more efficient than the conventional technology to generate electrical power. However, to date fuel cells are observed to be less efficient than theoretically predicted (80%), with reported alkaline fuel cells (AFC) having efficiencies between 45-60% (Burchardt et al., 2002). The 45-60% efficiency limits the fuel cell voltage at 0.7 V as opposed to the theoretical 1.23 V limit.

Limitation in the efficiency of fuel cells has been attributed to the slow kinetics of the oxygen reduction reaction (highly activated steps), occurring on the cathode side of the cell (Barbir, 2005). High activation barriers for reactions result in high energy to proceed to products, consequently leading to loss of potential in the fuel cells. The overall loss in potential happens in three steps (Barbir, 2005;Ramani, 2006)(see Figure 1.3); **1)** activation

polarization, as a result of the reaction kinetics at the electrode, predominately at low current densities (1-100 mA/cm²); **2)** ohmic polarization, arising due to the resistive losses through the electrolyte and electrode, occurring at intermediate current densities (100-500 mA/cm²). **3)** The third loss is attributed to the concentration polarization which occurs due to the mass transport and concentration problems. According to Bidault et al. (2009) the power output and the life time of fuel cells are directly linked to the behaviour of the cathode where most of the polarization losses occur.

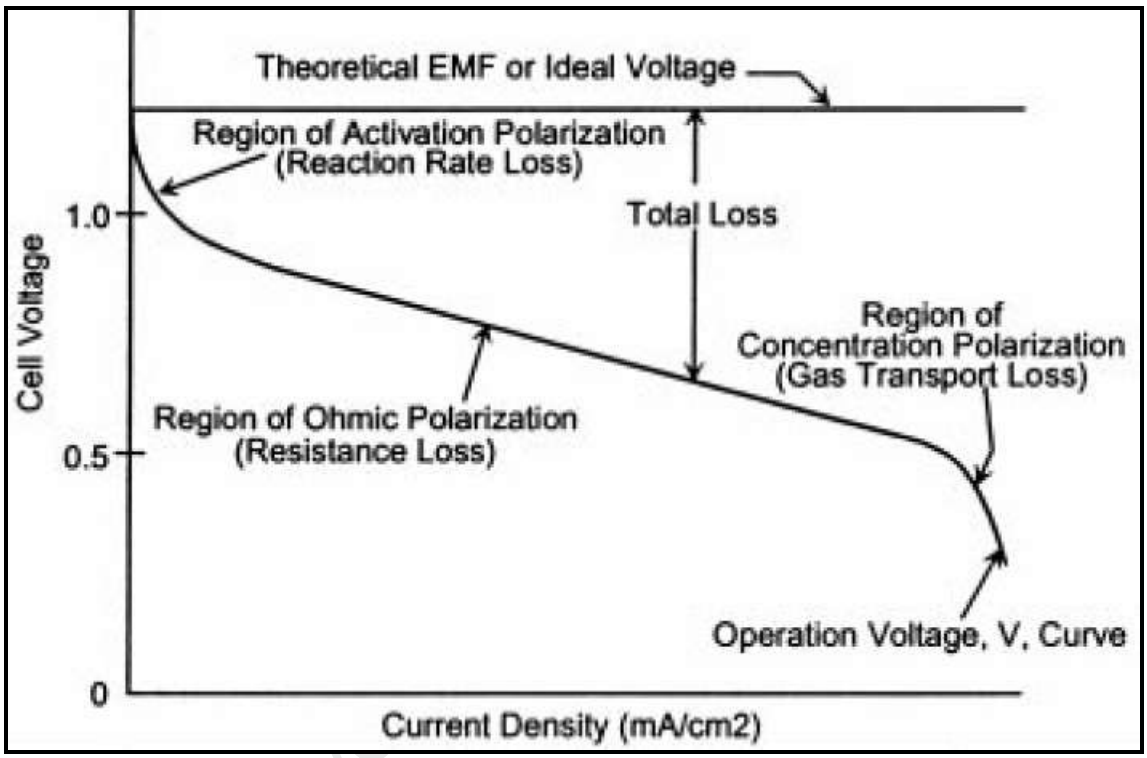

Figure 1.3: Typical polarization curve for hydrogen fuel cells (Rayment et al., 2003)

However polarization is not the only concern identified. There is also a possible loss in catalyst surface area from Pt particle agglomeration, Pt dissolution and/or migration into the membranes as well as electrode contamination and electrode degradation (Zhang, 2008). Platinum dissolution depends on the conditions in fuel cell's solution i.e. temperature, pH, electrolyte composition, potential and particle size.

A further problem of particular interest to this study is that during the oxygen reduction reaction, formation of corrosive hydrogen peroxide (H_2O_2) has been observed (Schmidt et al., 2001; Stamenkovic et al., 2002; Nakanishi et al., 2000). Hydrogen peroxide has strong oxidising properties and their presence in solution may accelerate the degradation of the electrodes and membranes (in the case of PEM-fuel cells). Hydrogen peroxide species may further be reduced to more corrosive radicals OH• and OOH• similarly to the Fenton

reactions (Schmidt et al., 2001). This eventually lowers the catalyst surface area and disrupts the hydroxyl ions (AFC) or proton (PEM) exchange between the two electrodes, consequently leading to low performance or efficiency for fuel cells. Chemical degradation of fuel cell internals affects one of the critical parameters (durability) used to access viability of fuel cell technology. To date stand-alone units operate for 40 000 hours and for mobile units the range is between 5000-10 000 hours (Ramani, 2006). The future plan for this technology is to drive vehicles as well as supply electricity in mass production. The durability of this device has to be resolved to achieve these aims. The desirable durability should compare to vehicles.

1.3 Literature review

The interest to study the oxygen reduction reaction is due to the observed poor fuel cells performance, which is ascribed to the sluggish reaction kinetics, as well as formation of hydrogen peroxide species during the reaction (Ramani, 2006; Schmidt et al., 2001). The slow kinetics of ORR is the major limiting factor with O_2 adsorption speculated to be the rate limiting step (Yeager et al., 1992). There are different speculations and conflicting arguments on why this is so. The most highlighted factor is the hydroxyl (OH) coverage on the Pt surface making it difficult for oxygen to access the catalyst active site, consequently inhibiting the oxygen reduction reaction (Hyman et al., 2006). It is also calculated that adsorption of oxygen onto Pt(111) surface is hindered at low temperatures, due to the surface coverage of adsorbed water, making it difficult at H_2O coverage greater than 0.8 mono layer (ML) (Hyman et al., 2006).

Damjanovic et al. (1967) originally proposed that proton transfer occurs simultaneously with charge transfer after the initial adsorption of molecular oxygen. In their rotating disk electrode experimental work, they demonstrated that simultaneous charge transfer and proton transfer are rate limiting.

Furthermore it has been proposed that the oxygen reduction reaction proceeds through a peroxide intermediate (Markovic et al., 1995), favouring the notion that protonation precedes dissociation as originally proposed by Damjanovic et al. (1967).

In contradiction to the above results Yeager et al. (1992) observed in their kinetic isotope experiment that oxygen does interact with the platinum surface through dissociative adsorption. DFT work done by Eichler et al. (1997) showed that dissociative adsorption of oxygen on platinum is a direct, strongly activated process with barriers varying between 0.3 and 1.5 eV. The range of barriers reported by Eichler et al. (1997), are calculated on various geometries and initial sites.

The overall ORR on Pt is said to be a multi electron complex reaction that includes a number of elementary reactions (Wang et al., 2005). Figure 1.4 shows a schematic representation of proposed possible reaction pathways for oxygen reduction.

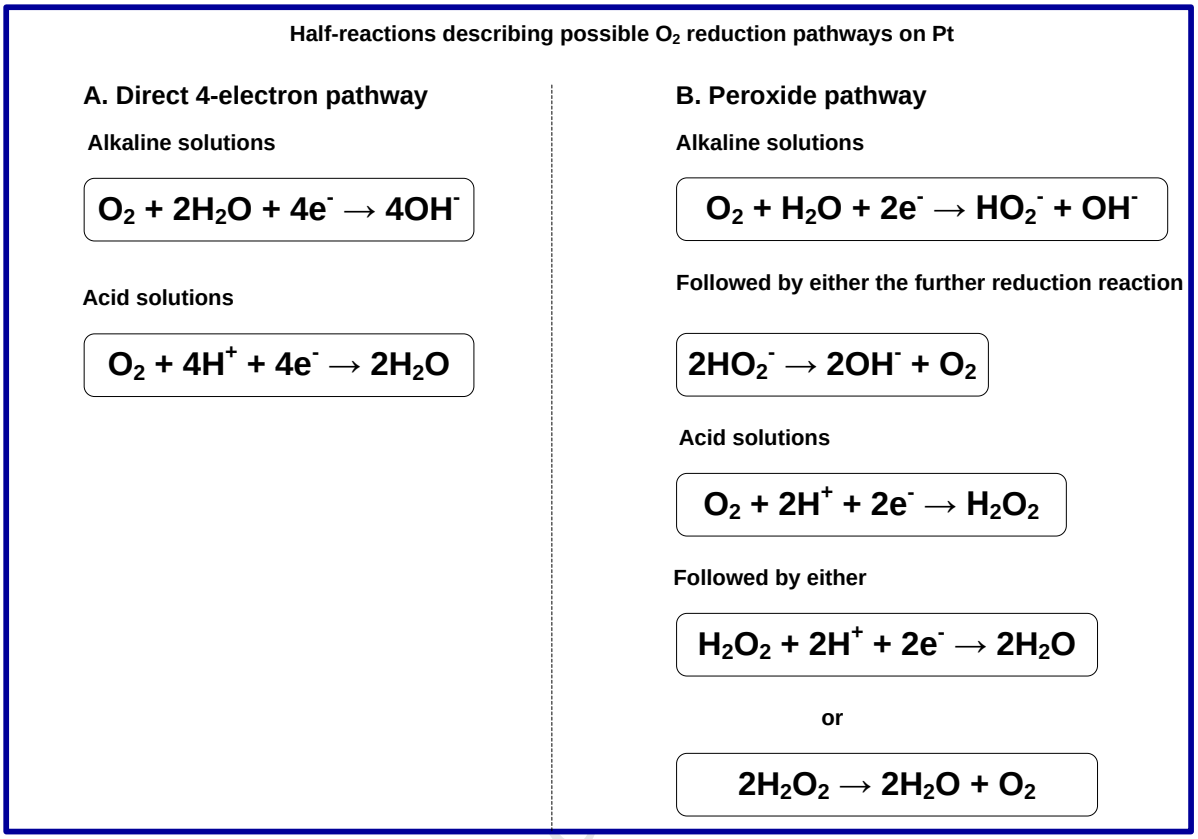

Figure 1.4: Schematic illustration of possible reaction pathways during oxygen reduction reaction (Yeager, 1984)

Shao et al. (2006) reported that there are three possible first steps in the oxygen reduction reaction (ORR) (*note (*) represent a vacant site*).

- Splitting of the O–O bond upon adsorption on two platinum sites in a bridge configuration, $O_2(g) + 2^* \rightarrow O^* + O^*$ (1.8)
- Formation of the superoxide anion, $O_2(g) + ^* + e^- \rightarrow O^-_2{}^*$ (1.9)
- Simultaneous electron and proton transfer, $O_2(g) + 2^* + (H^+ + e^-) \rightarrow HO_2{}^*(aq)$ (1.10)

Nørskov et al. (2004) proposed and studied the two ORR mechanisms, dissociative and associative for PEM fuel cells.

Dissociative mechanism:

$\frac{1}{2}O_2(g) + ^* \rightarrow O^*$ (1.11)

$O^* + (H^+ + e^-) \rightarrow OH^*(aq)$ (1.12)

$OH^*(aq) + (H^+ + e^-) \rightarrow H_2O(\ell) + ^*$ (1.13)

Associative mechanism:

$O_2(g) + * \rightarrow O_2* (g)$ (1.14)

$O_2(g) + (H^+ + e^-) \rightarrow OOH* (aq)$ (1.15)

$OOH* (aq) + (H^+ + e^-) \rightarrow H_2O (aq) + O*$ (1.16)

$O* + (H^+ + e^-) \rightarrow OH* (aq)$ (1.17)

$OH* (aq) + (H^+ + e^-) \rightarrow H_2O (\ell) + *$ (1.18)

Nørskov et al. (2004) concluded that the associative mechanism dominates at high O_2 coverage. Furthermore, they calculated that at low oxygen coverage, the O_2 dissociation has lower activation barrier, indicating that the oxygen dissociation is influenced by the spectator species. They further calculated that O_2 adsorption on Pt(111) tends to be stable at high potentials so that the proton and electron transfer becomes slow. The stability of adsorbed oxygen decreases at lower potentials and hence the reaction may proceed. This may be the origin of the overpotential (loss in cell voltage) on Pt.

More recent DFT study by Ford et al. (2010) proposed the following ORR mechanisms on various metals: 1) dissociative mechanism involving the dissociation of adsorbed O_2 as the initiation step: 2) the peroxyl mechanism involving the formation of OOH upon O_2 adsorption, followed by bond scission of O-O bond on OOH species: 3) the peroxide mechanism involving the hydrogenation of OOH to HOOH which can either desorb or undergo O-O bond scission.

The conclusions from Ford et al. (2010) suggest that the primary factor that determines the prevalence of the dissociative or associative mechanism is the relative ease of O_2 dissociation vs. O_2 hydrogenation. They further concluded that the oxygen reduction reaction will proceed through the associative mechanism on Ag and Au metals. On Cu, Pd, and Pt, the dissociative and associative mechanisms were also studied; on Pt O_2 hydrogenation was calculated to be more facile than O_2 dissociation by 0.28 eV and on Cu the dissociation of O_2 is more facile than hydrogenation by 0.38 eV, on Pd the two reactions were closely competitive.

Burchardt et al. (2002) highlighted that the challenge in further improving fuel cell is to increase the power and efficiency. To achieve this it is important to understand the origin of the voltage losses of the cells (Figure 1.3). To contribute to this knowledge one needs to understand the two half cell reactions, the reduction of oxygen and the oxidation of hydrogen.

There is conflicting information from experimental studies on the proposed mechanisms (direct 4-electron pathway or peroxide pathway: see Figure 1.4) for oxygen reduction half-cell reaction. This has raised questions motivating further research to contribute to the understanding of the key oxygen reduction initiation steps.

The O_2 reduction is said to proceed virtually quantitatively through the peroxide pathway (see Figure 1.4) due to the fast kinetics as compared to the direct 4-electron pathway on a number of electrode surfaces on platinum (Yeager, 1984). It is desired that during ORR the direct 4-electron reduction should take precedent and not the 2-electron reduction due to less activated steps for the direct 4-electron reduction. More studies on ORR suggest and proposed that the peroxide pathway via adsorbed H_2O_2 (ℓ) intermediate may apply to Pt and Pt-based bimetallic catalysts (Markovic et al., 2001). The peroxide pathway has to be avoided since formation and desorption of H_2O_2 may result in corrosion due to the corrosive nature of H_2O_2. Furthermore the direct 4-electron reduction is more favoured since it generates more power due to less activation polarization.

Anderson et al. (2000) proposed that the OOH species is an intermediate for the first electron transfer step and its formation has a lower activation barrier (E_a=0.6 eV) than the direct dissociation of the adsorbed O_2 (E_a=0.7 eV), implying that O_2 may not dissociate on Pt before the first electron transfer.

1.3.1 Thermodynamic for H_2O_2 formation

The thermodynamics for H_2O_2 formation has been calculated at 65°C, a typical operating temperature for fuel cells. Table 1.1 depicts the thermodynamic properties of the gas phase reactions. Hydrogen peroxide formation from H_2O and O_2 is a non-spontaneous reaction ($\Delta G^0_{rxn}>0$; see Table 1.1). This is an endothermic reaction (i.e. more favoured at higher temperatures). The activity-based equilibrium constant at 65°C is low indicating that only a small concentration of $H_2O_2(\ell)$ will be formed at equilibrium from $H_2O(\ell)$ and $O_2(g)$ (the contribution of the Gibbs free energy of evaporation of H_2O and H_2O_2 at 65°C are small to the overall change in the Gibbs free energy upon reaction).

The H_2O_2 formation from H_2 and O_2 is thermodynamically much more favoured (see Table 1.1). The reaction is feasible since there have been claims that with the high diffusive properties of oxygen may allow it (O_2) to diffuse through the electrolyte to react with hydrogen on the anode.

Table 1.1: Thermodynamic calculations for H_2O_2(g)and H_2O(g)formation at 65°C (338.15K), from chemical equilibrium constant calculation program by Sandler (2004). Notations:ΔG^0_{rxn}:Gibbs free energy of reaction; ΔH^0_{rxn}: Heat of reaction; K_a: Equilibrium constant

Reactions	K_a	ΔG^0_{rxn} (kJ/mol)	ΔH^0_{rxn}(kJ/mol)
$2H_2O$ (g)+O_2 (g)→ $2H_2O_2$(g)	2.28E-36	231	111
H_2 (g)+ O_2 (g)→ H_2O_2(g)	1.64E+17	-111	-187
H_2 (g)+ ½O_2 (g)→ H_2O (g) (overall)	1.20E+35	-227	-242

1.3.2 Solvent effect on ORR

The general overview of the oxygen reduction reaction (ORR) studies is that the order of initial electron transfer, proton transfer and O-O bond scission (O_2) is not clear. The effect of water coverage on O_2 adsorption has been shown to have a negative impact on the initial steps in the oxygen reduction with O_2 adsorption almost impossible at H_2O coverage ≥0.8 ML (Hyman et al., 2005). It has been hypothesised experimentally (Ogasawara et al., 2008) and computationally (Janik et al., 2009) that a close competition exist between O_2 and H_2O adsorption that may affect ORR. However Yeh et al. (2009) explains that conflicting conclusions about O_2 reduction chemical surrounding effects arise from the difficulties in both experiment and computation in characterizing the adsorbed O_2 state at the solvated and electrified interface. Hyman et al. (2005) explains that the existence of an electric double layer at the metal solution interface in electrochemical cells may have a profound influence on the oxygen reduction in fuel cells. The existence of the electric double layer at the metal/solution interface is characterised by the excess charge density in the metal and a counter charge of opposite sign in the solution maintaining overall neutrality (Hyman et al., 2005).

However modelling solvent interactions and electrochemical potential effect on oxygen reduction reaction are however challenging in DFT calculations. One of the techniques mostly adopted to model variation on adsorption upon potential effect is to apply homogenous electric field perpendicular to the interface (Nazmutdinov et al., 1996). The latter was adopted by Hyman et al. (2005), and they calculated that the adsorption energies of atomic and molecular oxygen are slightly affected by the presence of external electric field. However, they showed that the activation energy for the dissociation of adsorbed O_2 was lowered by 0.1 eV when a 0.5 V/Å electric filed is applied. However such high electric filed is questionable in fuel cells (Barbir, 2005).

Yeh et al. (2005) agued that the constant electric field method to model the effects of the electric double layer within the Helmholtz model (constant electric field) said that such methods does not incorporate the solvent-solvent, solvent-adsorbed species and solvent-Pt surface interactions at the interface. Furthermore the presumption of a constant electric field during adsorption or reactions is not so accurate.

Work done by Skulason et al. (2008) and Jinnouchi et al. (2008) introduced a model composed of a bilayer of water on Pt(111) slab to try and simulate the electrochemical environment. This model is restricted to a distinct ion distribution in the double layer and only allows calculations of the potential-dependent activation barriers (Yeh et al., 2009), as a result it suffers from a limited potential control to quantised variation.

The much improved method is the introduction of a hexagonal ice-like structure between metal slabs to model the electrode-electrolyte interface. This may provide a more realistic electrochemical environment than a vacuum metal interface (Yeh et al., 2009). To model the electrified metal surface and the electrolyte counter-charge, the double reference method developed by Taylor et al. (2006) can be adopted. The method involves the establishment of two reference potential, one related to the potential of the free electron in vacuo and the second related to the potential of H_2O species far from the electrode (Taylor et al., 2006).

The inclusion of solvation effects and direct control of the electrode potential were studied by Yeh at al. (2009) on oxygen adsorption. They found that oxygen binding becomes more favourable with increasing potential. Furthermore the hydrogen bonding between H_2O and O_2, enhance electron donation from the surface to the O_2, resulting in a O-O bond lengthening, increasing the negative charge on O_2 consequently lowering the stretching vibrational frequency.

The inclusion of solvent-solvent, solvent-adsorbed species and solvent-Pt surface interactions at the interface, as well as the electrode potential is a clear indication of an improvement on the theoretical studies of oxygen reduction.

However, this study is limited to the intrinsic oxygen reduction towards yielding H_2O_2. It is however acknowledged that the inclusion of solvent effect may have an effect on the results, however the inclusion of a solvent requires the debatable art of building the correct representation (density) of a solvent.

1.4 Motivation and aims for the current work

There are two possible oxygen reduction mechanisms (see Figure 1.4) which are the direct 4-electron pathway or peroxide pathway. The earlier kinetic isotope experiments proposed the evidence of peroxide pathway taking president over the direct 4-electron pathway (Demjanovic et al., 1967; Yeger et al., 1992). This is an indication that gaps exist in the understanding of the oxygen reduction reaction mechanism. Recent studies suggest that the two initiation steps are closely competitive with the O_2 hydrogenation being more facile than O_2 dissociation (Ford et al., 2010).

The proposed mechanism for hydrogenation of oxygen, it is a possible indication that oxygen reduction reaction goes through a peroxide intermediate (OOH). If the peroxide intermediate may stay longer on the surface it can then be further hydrogenated to form hydrogen peroxide (H_2O_2). However studies done by Anderson et al. (2000) found that dissociation of OOH ($OOH^* \rightarrow O^* + OH^*$) on Pt has low activation barrier of ~ 0.06 eV, a possible indication that the species may not exist for long on the surface and potentially may dissociate.

The counter-argument that oxygen adsorbs dissociatively on platinum raises questions about the ORR mechanism. However, hydrogen peroxides species have been observed in the fuel cells solutions (Schmidt et al., 2001), so which pathway could possibly be followed yielding this species?

The latter question forms the basis and motivation for this work. The current work will investigate the possible species present on a fuel cell cathode and study their behaviour (adsorbate to substrate interaction) on the platinum surface to determine how they play a role in forming hydrogen peroxide species.

Platinum is the most active metal for oxygen reduction (Nørskov et al., 2004). Platinum crystallizes into a face centred cubic (fcc) structure at ground state (1atm, 25°C). The fcc crystals have the (111) plane as the most exposed one, since it is the lowest in surface energy hence more stable (Wojciechowski, 1999, Jiang et al., 2004).

To elucidate the formation of hydrogen peroxide in fuel cells the following pathways will be investigated based on the summary of ORR paths in Figure 1.4 by Yeager, 1984 (see Figure 1.5 for proposed paths).

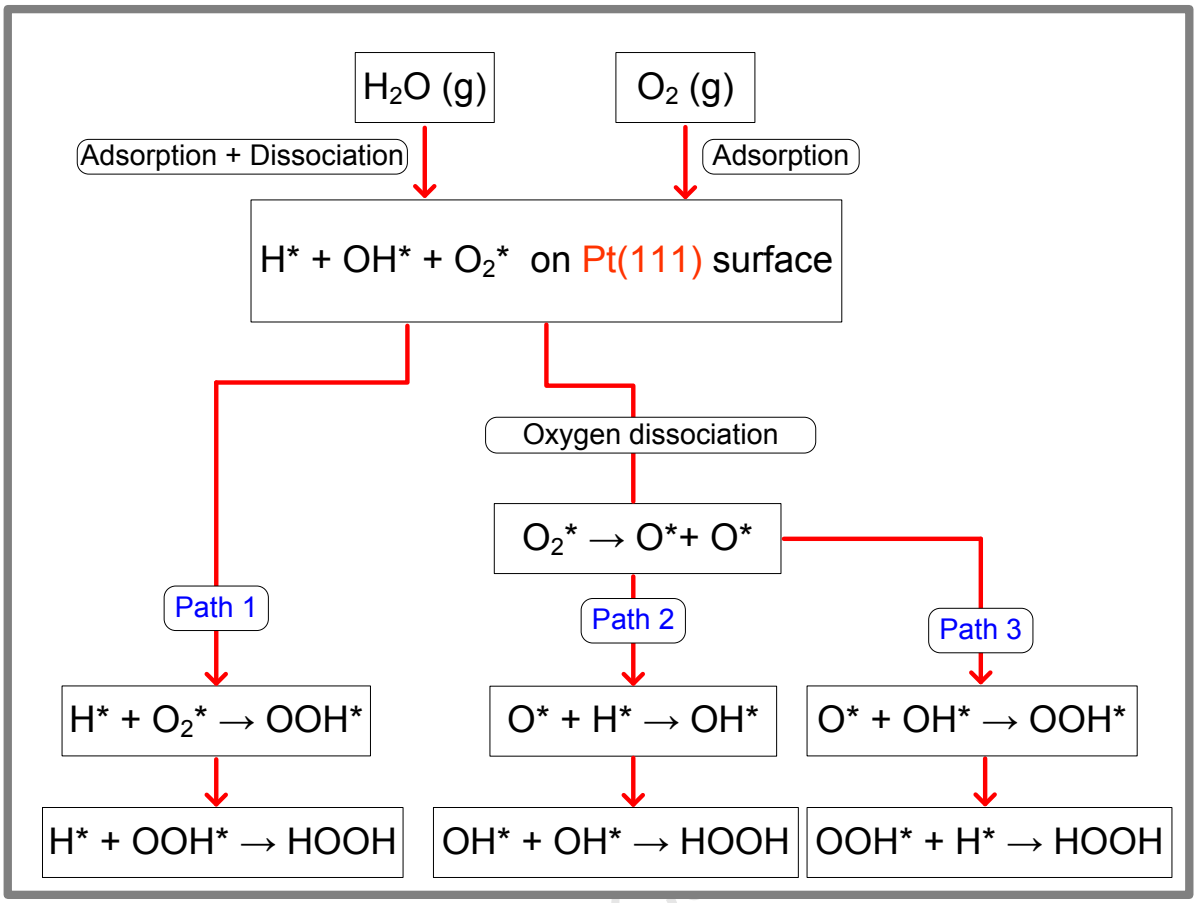

Figure 1.5: Schematic illustration of proposed possible pathways for hydrogen peroxide formation during oxygen reduction reaction (* denotes adsorbates on the catalyst surface)

The interactions of surface species on the electrode surface may be affected by the solvent and the potential gradient. However this study is limited to study the intrinsic oxygen reduction towards yielding H_2O_2. However, the correct representation of a solvent and the potential gradient within a theoretical framework is still debatable and is not included in this study.

1.5 Key questions

The following key questions have been investigated:

- How does oxygen and water interact with the dense Pt (111) surface?

This question is important for the understanding of the first key step in the oxygen reduction reaction. The two species (O_2, H_2O) have to be adsorbed onto the surface for the reaction to commence. It is therefore of importance to study adsorption of the species to gain insight onto the initiation of the reaction (ORR) in alkaline fuel cell (AFC).

- Does dissociation of O_2 and H_2O occur readily?

The calculated activation energy results will shed an insight on the initiation kinetics of ORR

- How do the dissociated intermediates of oxygen and water adsorb on the surface?
- What is the pathway for hydrogen peroxide formation?
  - hydrogenation of O_2 to form (OOH) and further hydrogenation to form HOOH
  - Reaction between the hydroxyl species (OH) and atomic oxygen (O) on the surface yielding (OOH), further hydrogenation yield H_2O_2
  - Reaction of the two hydroxyl species yielding (H_2O_2)

The overall study interrogates the three proposed reaction pathways (see Figure 1.5) on Pt(111), to elucidate which one is kinetically more favourable for the formation of hydrogen peroxide. This has been achieved by studying the activation energies by DFT for the reactions steps under study.

1.6 References

Anderson A.B., Albu T.V., *Journal of the Electrochemistry Society* **147** (2000), 4229–4238

Ashcroft N., Mermin N.D., 'Solid state physics', HRW international editions (1988)

Barbir F., 'PEM Fuels Cells', Elsevier Academic Press (2005)

Bidault F., Brett D.J.L., Middleton P.H., Brandon N.P., *Journal of Power Sources* **187** (2009), 39–48

Burchardt T., Gouerec P., Sanchez-Cortezon E., Karichev Z., Miners J.H., *Fuel* **81** (2002), 2151–2155

Christman K., Lipkowski J., Ross P.N., Electrocatalysis, Wiley, New York (1998), p. 1.

Damjanovic A., BrusicV., *Electrochimica Acta* **12** (1967), 615-628

Damjanovic A., Srinivasan S., Conway B.E., 'Modern Aspects of Electrochemistry', Plenum Press, New York (1992), p. 107

Eichler A., Hafner J., *Physical Review Letters* **79** (1997), 4481–4484

Eichler A., Mittendorfer F., Hafner J., *Physical Review B* **62** (2000), 4744–4755.

Feibelman P.J., *Physical Review B* **64** (2001), 125403–125409

Ferré D.C., Niemantsverdriet J.W., *Electrochimica Acta* **53** (2008), 2897–2906.

Fisher G.B., Gland J.L., *Surface Science* **94** (1980), 446–455

Ford D.C., Nilekar A.U, Xu Y., Mavrikakis M., *Surface Science* **604** (2010), 1565–1575

Gland J.L, Sexton B.A, Fisher G.B, *Surface Science* **95** (1980), 587–602.

Gu Z., Balbuena P.B., *The Journal of Physical Chemistry C* **111** (2007), 17388–17396

Hyman M.P., Medlin J.W., *The Journal of Physical Chemistry B* **109** (2005), 6304–6314

Janik M.J., Wasileski S.A., Taylor C.D., Neurock M., First-Principles Simulation of the Active Sites and Reaction Environment in Electrocatalysis, in Fuel Cell Catalysis: A Surface Science Approach, ed.. Koper M.T.M, John Wiley & Sons, New York, 2009, ch. 4, pp. 93–128.

Jiang Q., Lu H.M., Zhao M., *Journal of Physics* **16** (2004), 521–530

Jinnouchi R., Anderson A.B., Condensed Matter and Materials Physics, Physical Review B **77** (2008), 245417

Juarez L.F. Da Silva, Stampf C., Scheffler M., *Surface Science* **600** (2006), 703–715.

Kittel C., 'Introduction to Solid State Physics', 7th ed., John Wiley & Sons, Inc.(1996).

Kohn W., Sham L.J., *Physical Review* **140** (1965), 1133–1138

Markovic N.M, Gasteiger A.H., Ross P.N., *The Journal of Physical Chemistry* **99** (1995), 3411-3415.

Markovic N.M., Schmidt T.J., Grgur B.N., Gasteiger H.A., Behm R.J., Ross P.N., *The Journal of Physical Chemistry B* **103** (1999),8568–8577

Mattsson A.E., Schultz P.A, Desjarlais M.P., Mattsson T.R., Leung K., *Modelling and Simulation in Materials Science and Engineering* **13** (2005), R1–R31

Michaelides A., Hu P., *Journal of American Chemical. Society* **123** (2001), 4235–4242

Mooney C.E., Anderson L.C., Lunsford J.H., *The Journal of Physical Chemistry* **97** (1993), 2505–2506

Nakanishi S., Mukouyama Y., Karasumi K., Imanishi A.,Furuya N., Nakato Y, *The Journal of Physical Chemistry B* **104** (2000), 4181–4188

Nazmutdinov R.R., Shapnik M.S., *Electrochimica Acta* **41**(1996), 2253–2265.

Nørskov J.K., Rossmeis J., Logadottir A., Lindqvist L., *The Journal of Physical Chemistry B* **108** (2004), 17886–17892

Ogasawara H., Brena B., Nordlund D., Nyberg M., Pelmenschikov A., Pettersson L.G.M., Nilsson A., *Physical Review Letter* **89** (2002), 276102–276103

Phatak A., Delgass W.N., Ribeiro F.H., Schneider W.F., *The Journal of Physical Chemistry C* **113** (2009), 7269–7276

Qi L., Qian X., Li J., *Physical Review Letters* **101** (2008), 146101

Ramani V., *The Electrochemical Society Interface* **15 (1)** (2006), 41-44

Rossmeis J., Skulason E., Bjorketun M.E., Tripkovic V., Nørskov J.K., *Chemical Physics Letters* **466** (2008), 68–71

Sandler S.I., Chemical equilibrium constant calculation program, Department of chemical engineering, University of Delaware, Newark, DE 19716 U.S.A, 2004

Schmidt T.J., Paulus U.A., Gasteiger H.A., Behm R.J.,*Journal of Electroanalytical Chemistry* **508** (2001), 41–47

Shao M.H., Liu P., Adzic R.R., *Journal of American Chemical Society* **128** (2006), 7408–7409

Skulason E., Karlberg G.S., Rossmeis I.J., Bligaard T., Greeley J., Jonsson H., Nørskov J.K., *Physical Chemistry Chemical Physics* **9** (2007), 3241–3250

Stamenkovic V., Schmidt, T.J., Ross, P.N., Markovic, N.M., *The Journal of Physical Chemistry B* **106** (2002), 11970–11979

Taylor C.D., Wasileski S.A., Filhol J.S., Neurock M., *Physical Review B* **73** (2006), 165402–165418

Viswanathan B., Scibioh M.A., 'Fuel cells principles and applications', University Press, India (2006)

Wang Y., Balbuena P.B., *Journal of Chemical Theory and Computation* **1** (2005), 935–943.

Wojciechowski K.F., *Surface Science* **437** (1999), 285–288

Yeager E.B., *Electrochimica Acta* **29** (1984), 1527–1537

Yeager E., Razaq M., Gervasio D., Razak A., Tryk A.D., 'Proceedings of workshop on structural effects in electrocatalysis and oxygen electrochemistry', Electrochemical Society: Pennington, NJ(1992), pp 440–473

Yeh K., Wasileski S.A., Janik M.J., *Physical Chemistry Chemical Physics* **11** (2009), 10108–10117

Zhang J., ‘PEM Fuel Cell Electrocatalysts and Catalyst Layers, Springer-Verlag, London (2008)

Chapter 2

2 MODEL VALIDATION

2.1 Introduction

Catalysis research is usually empirical in nature and has found many answers to most catalysis problems. However empirical methods have their limitations in solving complex mechanisms and reaction pathways in catalytic chemistry. To elucidate some of these complex mechanisms theoretical techniques have gained ground in explaining the nature of catalytic chemistry (Eichler et al., 1997; Nørskov et al. 2004; Yeh et al. 2009). These techniques, in the form of computational chemistry, have found wide uses to clarify and provide clear understanding of experimental observations. Theoretical modelling of catalytic reactions on platinum has been widely studied (see e.g. Eichler et al., 1997; Ford et al., 2010). Understanding the catalytic nature of platinum is of importance since it is also used in fuel cells. It is anticipated that application of theoretical modelling will lead to an improved understanding of electrocatalysis and a further improvement for fuel cell performance.

2.2 Computational chemistry methods

Computational chemistry refers to a theoretical description of chemistry on an atomic scale to obtain reaction chemistry information, which is independent of experimental input if first principles are applied. The results obtained using computational chemistry can be compared with experimental observations.

The computational chemistry methods can be categorised in the following way. The first category use force fields to describe the interatomic interactions. The force field approach is usually parameterised empirically and it is useful in describing geometrical structures, intermolecular interactions and energy trends, mostly applied to systems with many atoms (Mattsson et al., 2005).

The second category is the first principles methods which are used to solve and study the electronic structure of a system. With the application of quantum mechanics the electronic structure of various systems can be approximated.

First principles methods have various implementations, which includes: Hartree Fock (HF), recent post-Hartree Fock *ab initio* methods and Density Functional Theory (DFT). DFT is one of the most used theories to describe chemistry of catalysts and catalytic reactions, since it gives a good description of systems with high concentration of electrons like metals with relatively low computational cost. DFT is said to be an improved method to calculate

the quantum mechanical ground state of condensed matter (Mattsson, 2005), this is compared to the diagrammatic perturbation theory used in physics and configuration interaction methods used in chemistry.

2.2.1 Density Functional Theory

The DFT theory was reviewed from Marder, (2000); Mattsson et al., (2005) and van Helden, (2009)

The energies and properties of catalytic systems are dependent on the system's electronic structure which can be calculated using quantum mechanics. In this work DFT is chosen to be the most suitable method since the theory behind DFT can describe systems with high concentration of electrons like metals. The density functional theory simplifies the many-body Schrödinger equation into a set of coupled single particle equations, which then isolate the many-body interactions into the exchange correlation density functional (used to approximate electron-electron interactions). The growing use of DFT is aided by the development of sufficiently accurate exchange correlation functionals, efficient algorithms and a continuous improvement in computing capabilities. Various functionals can be applied on DFT. Of interest in this work is the application of DFT to study and understand the intrinsic interaction of reactive species with the active catalytic surface (Pt).

2.2.2 Development of the Density Functional Theory

Density functional theory was based on the theorem by Hohenberg et al. (1964), Kohn and Sham. (1965). It is widely used and implemented in many computer programmes to perform quantum chemical calculations (CASTEP; Payne et al. 1992, VASP; Kresse et al. 1996). The starting point for this theory is through an observation by Hohenberg and Kohn that the electron density a system contains in principle all the information contained in a many electron wavefunction (Marder, 2000).

The development on the theorem by Hohenberg and Kohn (1964) on DFT was an extension of the argument by Levy (1979). Levy defined the functional as follows:

$$F[n] \Rightarrow \min_{\psi \to n} \langle \psi | T + V_{ee} | \psi \rangle \qquad (2.1)$$

Where T + V_{ee} are the kinetic and electron-electron interaction operators respectively and ψ is the wavefunction. The minimum is taken over all ψ that gives the density n. F[n] is then defined as universal since it does not refer to a specific system or to the external potential V_{ext}(r). If it can be denoted that E_{gs}, ψ_{gs} and n_{gs} (r) to be the ground state energy, wave function and density, respectively the basic two theorems for DF theory are:

$$E[n] \equiv \int dr V_{ext}(r) n(r) + F[n] \geq E_{gs} \qquad (2.2)$$

For N-representable for n(r) and

$$\int dr V_{ext}(r)n(r) + F\left[n_{gs}\right] = E_{gs} \tag{2.3}$$

The Hohenberg-Kohn theorem in principle allows for the systematic formulation of the corresponding many body problem of interacting electrons in an external potential in terms of the electron density as the basic variable. Like any other first principles methods, the time-independent DFT seeks to solve the Schrödinger equation:

$$\hat{H}\psi(r) = E\psi(r) \tag{2.4}$$

With

$$\hat{H} = -\frac{\hbar^2}{2 \cdot m}\nabla^2 + V(r) \tag{2.5}$$

$\hat{H}$ is the Hamiltonian operator, E represents the energy of the particle or system, ψ is the wave function of the particle or system, the normalised complex conjugate product integral of the wave function gives the probability distribution, $V(r)$ describes the potential energy operator. The Hamiltonian contains kinetic and potential energy operators that are applied to the wave-function to obtain the system energy. In summary, if given any density, specified to be the ground state density for some *N*-electrons system, the Hamiltonian of that particular system can then be uniquely determined. This simply means with the knowledge of only the ground state density of an *N*-electron system, in principle everything about that particular system, including exited states and excitation energies etc. can be determined. The wave-function in the Schrödinger equation can only be solved exactly for a one electron system, as a result of this limitation all the other systems have to be approximated.

The two approximations that are commonly applied to chemical systems are: the Born-Oppenheimer approximation and the mean field approximation.

The Born-Oppenheimer approximation assumes that electronic and nuclear wavefunctions are independent. As a result the nuclear and electronic motion are decoupled, this is assumed since for chemical systems, the nuclei are much larger than the electrons, as a result they move much more slowly (Marder, 2000). Within this approximation, the ground state energy and electronic wave function are determined for a fixed set of nuclear coordinates.

The second approximation relates to the description of the electron-electron interactions. In the mean field approximation, multi-electrons are considered to move within the average

field of the other electrons. The two distinct features for this approach require optimisation of the electronic structure and the nuclear arrangement.

An iterative procedure is required to solve these systems, where the lowest energy for a given nuclear arrangement is found. In practical calculations, one first guess/assumes the initial density, which then gives the input potential *V(r)* which can be solved for a single-particle state, from which a new density is obtained, which again gives a new *V(r)*. The equations are solved in a self consistent procedure called self-consistent field (SCF) (Kohn and Sham 1965). The process is repeated until the self-consistency is obtained, i.e. until the input and the output density in a single iteration is sufficiently close.

2.3 Computational method

The periodic and non-spin polarised (Pt-paramagnetic) DFT calculations were performed using the *Vienna Ab Initio Simulation Package* (*VASP*) (Kresse et al., 1996). The package solves the Kohn-Sham equations (Kohn and Sham 1965) using a self-consistent procedure within the periodic boundary conditions using plane wave basis sets in which the Blöchl's all electron projector augmented-wave (PAW) (Kresse et al., 1999) or the ultra-soft pseudopotential methods are implemented. All the calculations for this section were performed using the generalized gradient approximation with PW91 (Perdew et al., 1992), PBE (Perdew et al., 1996) or RPBE (Hammer et al., 1999) functionals to investigate the effects of correlation energy contribution and electron exchange.

To achieve more efficient convergence of the self-consistent field (SCF), smearing is applied which allows smearing of electrons over several orbitals within a range of the Fermi level using linear integration. Smearing parameters should be chosen with caution since too large or too low smearing parameters may result in the incorrect total energy (high smearing) or high computational demands(low smearing) (Kresse et al., 2007). All the energies reported were obtained after extrapolation to 0 K.

The total energy for the bulk platinum calculation was obtained with single point energy calculations using the tetrahedron method with Blöchl corrections. The geometry energy optimizations the Methfessel-Paxton scheme was adopted, with a smearing width of 0.2 eV (*VASP* default), a reasonable value for metals (Kresse et al., 2007). Variation in smearing width indicated no influence on the energy for the platinum bulk structure.

2.4 Bulk platinum optimization

Performing density functional theory calculations has its own demands. The calculations have to be done using a model that describes the physical properties of the system as accurately as possible. The system refers to the surface and the interaction with the

surface. The structural and electronic properties of the surface depend on the chosen bulk and hence the accuracy of the bulk model is important. This simply means that the bulk model energy should be fully converged with respect to the modelling parameters. The description of the bulk physical parameters by the modelling parameters can easily be validated against the experimental values (e.g. lattice constant). This study focuses on platinum which is paramagnetic and has a face centred cubic (fcc) structure at ground state with a lattice constant of 3.92 Å (Ashcroft and Mermin, 1998).

2.4.1 Model verification procedures

There are several modelling parameters that need to be considered when building a bulk and a surface DFT model. The following parameters were investigated: exchange-correlation energy functional, the pseudo-potentials used to represent the electron-ion interaction, the plane wave cut off energy, the k-points mesh dimensions to sample the Brillouin zone and for surface calculations the slab thickness and the vacuum spacing. To test the accuracy of these modelling parameters the lattice constant and the bulk modulus (a measure of resistance to uniform compression) were calculated by fitting the calculated energies and lattice constant to the Birch-Murnaghan equation of state (Murnaghan, 1994; Birch, 1947). This is compared with experimental values (at 1atm. 25°C):

- Lattice parameter : 3.92Å (Pt-Pt distance, 2.775Å) (Ashcroft and Mermin, 1988)
- Bulk Modulus : 278 GPa (at 300K) (Kittel. 1996)
- Local magnetic moment : Paramagnetic

Platinum crystallizes into face centred cubic structures from which different surfaces can be created (see Fig 2.1). The shape of the nano-crystallites present in fuel cell catalyst can be determined by the relative surface energy of the various surfaces.

The densest surface exposes the (111) plane, which has the lowest surface energy (Wojciechowski, 1999, Jiang et al., 2004). Fisher et al. (1980) showed that upon heating of polycrystalline films, the (111) surface will preferentially form due to its stability (i.e. lowest in surface energy). In this study platinum will be cleaved on a (111) plane to expose the surface of interest. Figure 2.1 is a schematic illustration for the face centred cubic crystal.

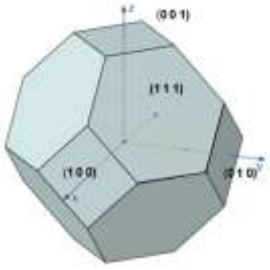

Figure 2.1: Face centred cubic crystal. Illustrating the (111) plane to be the most exposed

The (111) surface has four high symmetry sites i.e. the on-top, hexagonal close packed (hcp) 3-fold hollow, face centred cubic (fcc) 3-fold hollow, and the bridge site (see Figure 2.2). Hence the interaction of the adsorbates with the different sites have to be taken into account to gain insight in the stability of the various adsorbates on the (111) surface.

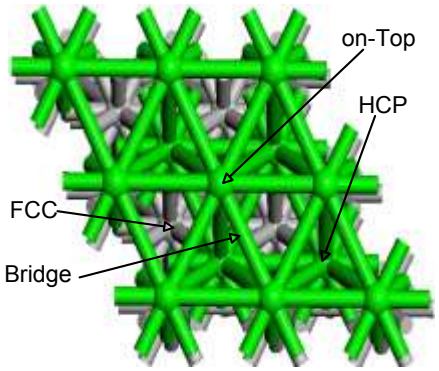

Figure 2.2: High symmetry sites on a (111) surface

To perform surface calculations using the DFT approach a periodic slab is represented by *N*-layers surrounded by a vacuum (see Figure 2.3).

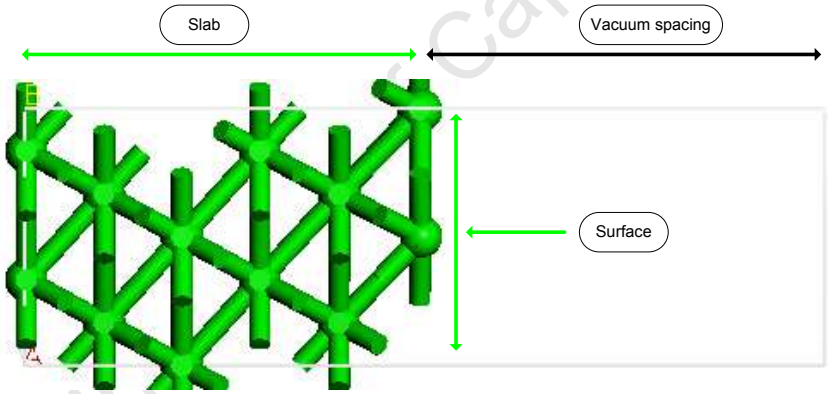

Figure 2.3: Schematic representation of a slab with *N*-layers surrounded by a vacuum (horizontal side view)

Surface energies were calculated to estimate the accuracy of the surface representation. This is vital since metal surfaces have physical properties that play a role in determining the behaviour of the metal surface when used in different application, for example heterogeneous catalysis, electrochemistry and corrosion etc (Juarez et al., 2006). The calculated surface energy can easily be compared to the experimental values. Surface energy is the energy (per surface atom or per unit area) needed to split an infinite crystal into two semi-infinite crystals (Juarez et al., 2006). The surface energy per surface atom is calculated as follows:

$$E_{surf} = \frac{(E_{slab} - N \cdot E_{bulk})}{2} \qquad (2.6)$$

Where E_{slab} is the total energy per unit cell of a slab with N layers and E_{bulk} is the reference total energy per atom of the bulk system. The factor of ½ accounts for the two equivalent surfaces on each side of the slab. E_{bulk} can be calculated from a separate bulk system calculation or it may be determined from the expression:

$E_{bulk} = E_{slab}(N_1+1) - E_{slab}(N_1) = \partial E_{slab}(N) / \partial N$ (Juarez et al., 2006) (2.7)

Provided N_1 is large enough, this applies since two slabs of two different thickness, N_1+1 and N_1, differs by only one layer (Juarez et al., 2006).

Surface energy per unit surface area is represented as follows:

$$\gamma_{surf} = \frac{(E_{slab} - N \cdot E_{bulk})}{N_s \cdot A} \quad (2.8)$$

Where A is the area per surface atom and N_s is the number of surface atoms in the unit cell with surface atoms exposed to the vacuum on both sides of the slab.

2.4.2 Bulk and surface calculation results

Various modelling parameters have been verified and this section presents results for the optimization of the bulk and surface platinum system. The following is the order with which the parameters are discussed k-points, cut-off energy and exchange correlation energy functional.

2.4.2.1 k-points and cut-off energy

Brillouin zone (BZ) sampling

Computational cost increases linearly with the number of k-points, so to reduce the cost 'special points' schemes are employed that use the fewest possible k-points to give the accurate approximation to the full integration over k-space within the Brillouin zone (Mattsson et al., 2005). The schemes date back to Chadi and Cohen, 1973 to the most recent commonly used sampling due to Monkhorst and Pack (Monkhorst et al., 1976) which was adopted for this study. The k-point spacing has a profound effect on the computed properties and it should be noted that the use of finite k-point sampling as opposed to the full integration over the Brillouin zone is an approximation.

For this study the k-points sampling density was varied first using a primitive bulk unit cell with the Pt-Pt distance fixed at the experimental value of 2.775 Å. The cut-off energy set to 600 eV anticipating that the system energy would have been converged, since the recommended cut off energy from the *VASP* guidelines for platinum pseudo-potential used are as follows (PBE: 230 eV; RPBE: 230 eV; PW91: 230 eV; uspp-PW91: 191 eV). The k-point mesh dimensions were varied from 10×10×10 to 16×16×16. The energy convergence

criterion for k-points was within or less than 1 meV per atom, to limit their effect on the bulk energy. From the converged energy relative to the k-point, the cut-off energy was also optimized, varied from 300 to 600 eV.

It was apparent from the calculations that working with 182 irreducible k-points and cut-off energy of 400 eV showed the required energy convergence (see Figure 2.4 and Figure 2.5) for all functionals and their supporting pseudo-potentials and will yield optimised set of bulk parameters to be compared with experimental values.

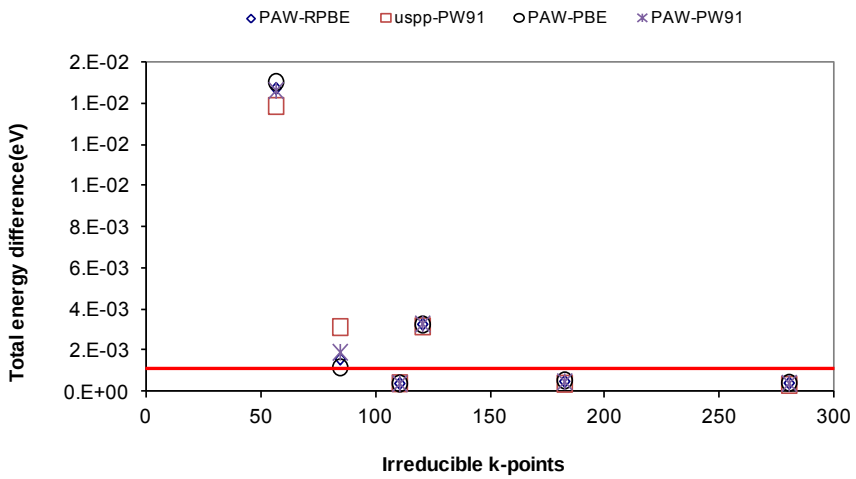

Figure 2.4: Pt bulk energy convergence with respect to irreducible k-points. Cut-off energy at 600 eV;Pt-Pt=2.775Å;σ=0.2 eV. Note: the energy difference is with respect to energy at 16×16×16 k-points (408 irreducible k-points); The redline illustrate the convergence criteria (1 meV)

Figure 2.5 depicts the platinum bulk energy convergence with respect to cut-off energy. The energy for various functionals and their supporting pseudopotentials converged within 1 meV criteria ($E_n - E_{600\text{-}eV}$) from 400 eV, with the exception of PAW-RPBE, for which energy convergence at 500 eV.

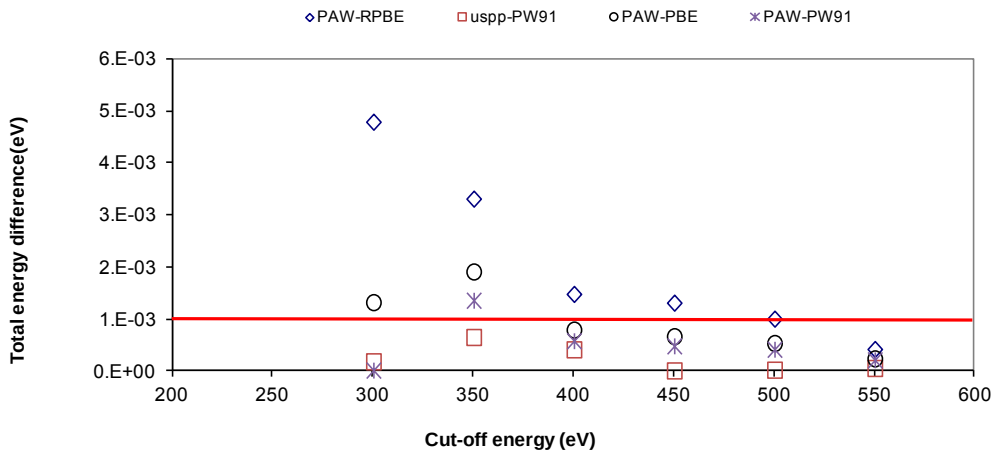

Figure 2.5: Pt bulk energy convergence with respect to cut-off energy. k-points dimensions at 12×12×12;Pt-Pt=2.775Å;σ=0.2 eV. Note: the energy difference is with respect to cut-off energy of 600 eV; the redline illustrate the convergence criteria (1meV)

2.4.2.2 Exchange correlation energy functional

The exchange correlation functional is another important factor to be considered. Various functionals yields different system energies, geometries and electronic properties.

The process of selecting a functional was given full attention. For this work all functionals and their supporting pseudo-potentials available in *VASP* were tested (PAW-PW91, uspp-GGA-PW91, PAW-PBE and PAW-RPBE). The LDA functional was not tested as the GGA functionals generally out-perform LDA in most molecular systems (Mattsson et al., 2005). However it is not neglected that the LDA functional does perform better for certain classes of systems and properties, particularly for calculating surface energy and properties of oxides (Mattsson et al., 2005). The LDA may also performs better than GGA functional in predicting equilibrium properties for certain metals, as demonstrated by Bercegeay et al. (2005) and Swart et al., (2007). However this study is aimed at calculations for surface reactions, for which generally the LDA functional performs poorly (Mattsson et al., 2005). All of these functionals are approximations and their accuracy is dependent on the material and properties under study.

The optimal functional for platinum was selected based on the comparison between the experimental lattice parameter and the optimized, calculated lattice, which was determine with the optimised k-points (12×12×12) and cut off energy (400 eV) using a primitive bulk unit cell and are given in Table 2.1. The lattice constant (unit cell volume) was varied and the energy was calculated using *VASP.* The resulting bulk energy was fitted on the isothermal Birch-Murnaghan equation of state from which the bulk modulus, the pressure derivative of the bulk modulus, the equilibrium volume and the lattice constant were

obtained. The initial guess required for the Birch-Murnaghan equation was obtained by setting up four equations and four unknowns and solve them simultaneously. The model was then regressed by completing the least square against the calculated data from *VASP*. The final predicted energy was then plotted against the lattice constant. Furthermore a polynomial was fitted and the first derivative of the polynomial set to zero yield the corresponding lattice constant at a minimum energy (see Figure 2.6).

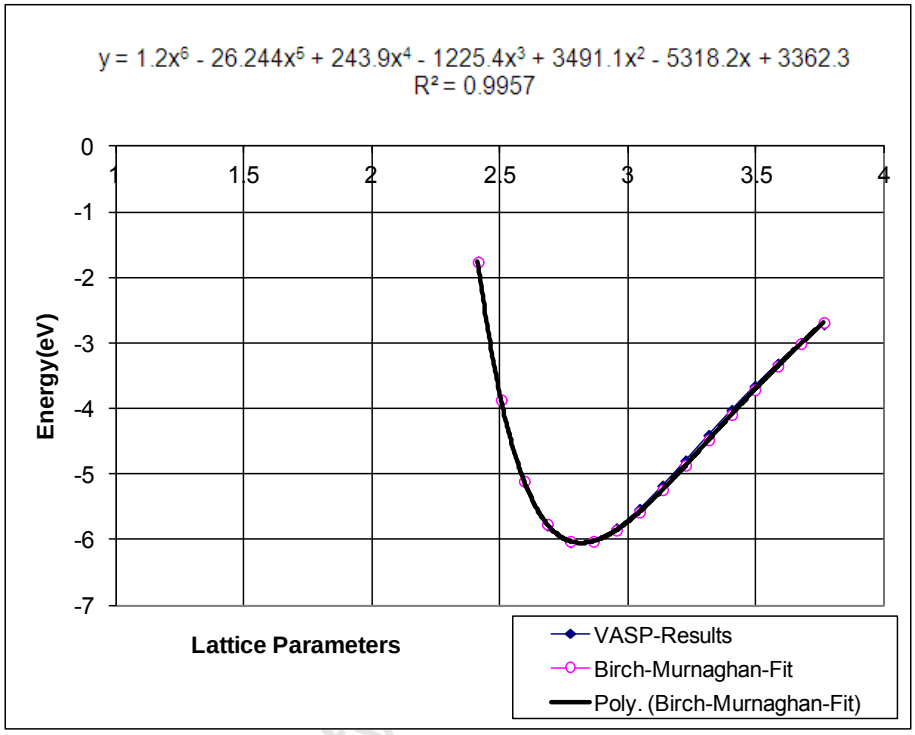

Figure 2.6: Lattice constant v/s energy with Birch-Murnaghan fit on the data, using PAW-PBE (k-point mesh: 12×12×12; $E_{cut\text{-}off}$: 400 eV)

Table 2.1 is a summary of calculated lattice parameter and bulk modulus for platinum, obtained in previous and current studies using various functionals and supporting pseudopotentials. The data from CASTEP are included for comparison, however the aim was to proceed with *VASP* for the bulk of calculations.

Table 2.1: Summary of the calculated Pt bulk properties obtained from literature, and the current values calculated in this study (Notation; uspp: ultrasoft pseudopotential, GGA: General gradient approximation, PAW: Projected augmented wave)

Source	Year	Package	pseudopotential +Functional	a (Å)	B (GPa)
Eichler et al.,	2000	VASP	PAW-PW91	2.821	
Feibelman.	2001	VASP	LDA	2.765	
			Uspp-GGA-PW91	2.821	
Juarez et al.,	2006	FP-LAPW	LDA	2.751	305
			uspp-GGA-PBE	2.807	241
Ferré et al.,	2007	VASP	PAW-RPBE	2.823	
Gu et al.,	2007	VASP	PAW-PBE	2.812	
Liang Qi et al.,	2008	VASP	PAW-PBE	2.812	
[a]This study		CASTEP	uspp-PW91	2.750	250
			uspp-PBE	2.740	255
			uspp-RPBE	2.762	243
		VASP			
			uspp-PW91	2.844	221
			PAW-PBE	2.783	232
			PAW-RPBE	2.838	216
			PAW-PW91	2.776	229
Experimental Values (300K)				**[b]2.775**	**[c]278**

[a]k-point mesh:12×12×12; $E_{cut\text{-}off}$: 400 eV; s: 0.2 eV

[b]Ashcroft and Mermin, 1998

[c]Kittel, 1996

Previous studies and the current study show that the platinum lattice parameter is generally over estimated and the bulk modulus is under estimated (see Table 2.1) with only PAW-PW91 (in *VASP*) yielding a lattice parameter close to the experimentally determined. However this functional yields a bulk modulus which is significantly lower that observed experimentally. The reasons why this is so requires further investigation. It should be further noted that the bulk modulus experimental value was measured at 300K and the calculations are at 0K. An attempt was made to extrapolate the experimental bulk modulus to 0K to enable a direct comparison with the calculated value.

The bulk modulus measures the resistance of a substance to uniform compression. Generally most materials will deform more easily with an increase in temperature and hence

a lower bulk modulus will be obtained with increasing temperature. The following expression for calculating a metal bulk modulus as a function temperature (Kumar, 2000) was used:

$$B(Pa) = B_0 \cdot \left[\left[1 - \frac{1}{A} \ln \left\{ 1 + \frac{A \cdot P}{B_0} - A \cdot \alpha_0 (T - T_0) \right\} \right] \times \left[1 + \frac{A \cdot P}{B_0} - A \cdot \alpha_0 (T - T_0) \right] \right] \quad (2.9)$$

T_0 = 300K

P = 0 Pa *Pressure (the expression derived with equilibrium volume at P = 0 Pa)*

B_0 = 278 *GPa: bulk modulus at 300 K* (Kittel, 1996)

B'_0 = 5.61 *bulk modulus pressure derivative at 300 K* (Holmes et al., 1989)

α_0 = 0.268E-4 K^{-1} *coefficient of volume thermal expansion* (Lide et al., 2005)

$A = B'_0 + 1$

The temperature dependency of the bulk modulus as given by Kumar (2000) results in a decrease in the bulk modulus with increasing temperature. The experimental bulk modulus extrapolated to 0 K (and p = 0 atm) is 291 GPa (see Figure 2.7). The calculated values from the DFT using the GGA-method fitted on the Birch-Murnaghan equation are in a range of 210 to 240 GPa. The only reported value in literature, which comes to the experimentally observed values is the LDA-method used by Juarez et al. (2006). The under-prediction of the bulk modulus is likely to be related to the (slight) overestimation of the lattice parameter (Juarez et al., 2006). The results indicate that the approximation in the applied DFT calculations yields a Pt-Pt interaction potential that is not strong enough resulting in a slightly softer metal than expected from experiments.

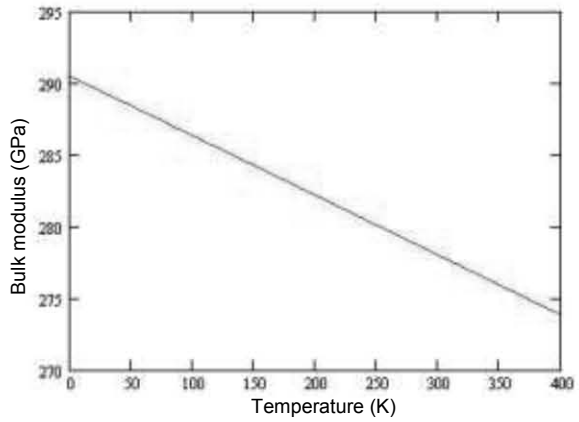

Figure 2.7: Bulk modulus as function of temperature for platinum calculated using the temperature dependency proposed by Kuma (2000)

2.4.3 Surface calculations

In this study the surface of interest is the Pt(111) surface, since it is expected to be the dominant surface present on platinum on platinum nano-crystallites in fuel cells. The surface was cleaved on a (111) plane from the geometry optimized bulk(Pt) unit cell using the calculated lattice constants as summarised in Table 2.1 for each functional and supporting pseudopotential. The various functionals and supporting pseudopotentials were all studied to determine the choice as to which functional describes platinum properties and surface chemistry better. The energy convergence of k-point and cut-off energy with respect to slabs was re-optimised. The new parameters to be optimised are the inter-slab vacuum spacing as well as the number of layers and un-constrained layers needed to perform accurate energy calculations at a reasonable computational cost. For the re-optimised parameters caution was taken to ensure the energy converge at greater than the bulk modelling parameters (k-point and cut off energy), since lower k-points and cut off energy may carry over the in-accuracy level when calculating the surface energy.

2.4.3.1 k-point and cut-off energy

The energy of the system with respect to k-point mesh and cut-off energy for the surface was re-optimised using a p(1×1) unit cell (chosen for faster computational time) with a 5 layer slab and 10 Å vacuum with all the layers being un-constrained. The system (Pt(111)) energy was converged with respect to irreducible k-points and cut-off energy, the convergence criteria of 1 meV per atom was not met (E_n–$E_{14\times14\times1}$ ≤ 5meV) for various functionals (PBE, RPBE, PW91), reasons for the latter is not apparent and it was found that k-points energy converged at 12×12×1 (182 irreducible k-points) and cut-off energy at 400 eV. Figure 2.8 illustrates the energy convergence with respect to both irreducible k-points and cut-off energy.

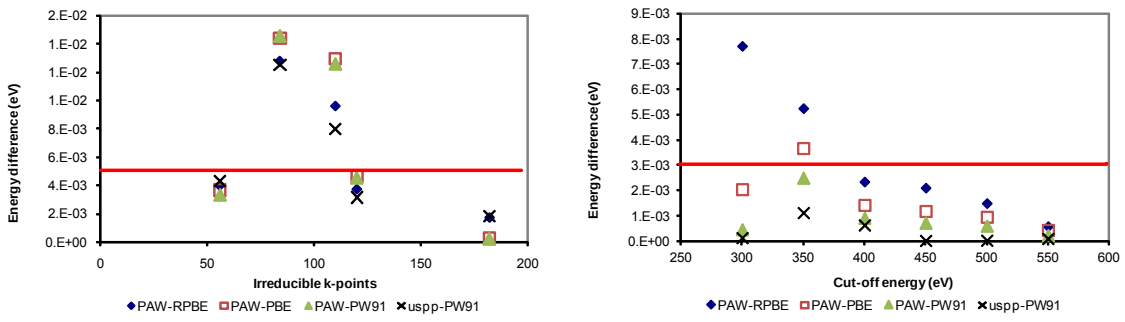

Figure 2.8: Energy convergence for Pt(111) with respect to irreducible k-points. Cut-off energy (σ=0.2 eV; the redline illustrate the convergence criteria)

2.4.3.2 Vacuum spacing

Vacuum spacing is also one of the important model parameter to be optimised. An infinite vacuum is desirable, which will completely eliminate surface-surface interactions and only require repetition of surface unit cell periodically, however the infinite vacuum space comes at a large computational cost. The vacuum space was varied in order to assess the required spacing for which the energy of the system is converged ($E_n - E_{n-1} \leq$ 1meV per atom), since the smallest spacing meeting the convergence criteria will result in reduced computational cost. However the vacuum spacing should be sufficient to fit the molecules to be studied.

Energy convergence with respect to vacuum spacing for this study was investigated on a five layer slab using a p(2×2) unit cell, all the layers free to relax with the 6×6×1 k-point and 400 eV cut off energy. The p(2×2) was chosen at this stage since it is the desired unit cell size that will be used with the rest of the study. Furthermore the energy calculations showed poor energy convergence with respect to vacuum spacing (see Appendix A), reasons for such an observation is not apparent. The vacuum spacing was varied from 5 Å to 20 Å. The energy calculated with the various functionals and supporting pseudopotential converged at a vacuum spacing of 12 Å, to ensure a minimum or no significant surface-surface interaction between the slabs a vacuum spacing of 12 Å was then chosen to proceed with the calculations (see Figure 2.9).

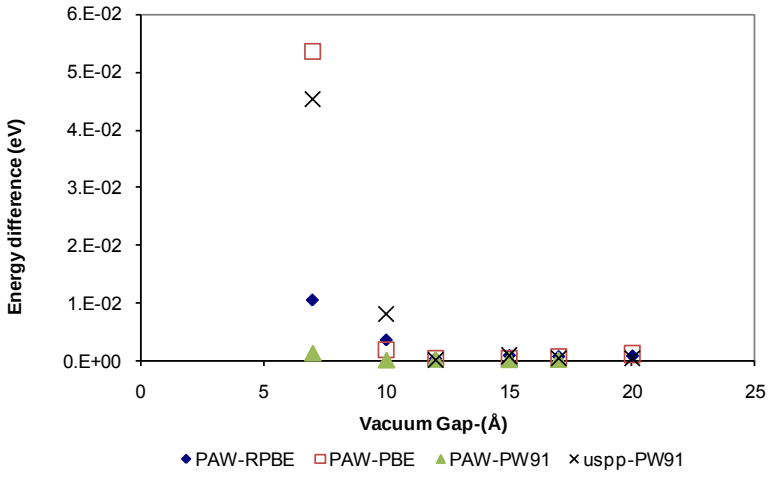

Figure 2.9: Energy differences between calculated energy for p(2×2) Pt(111) slab at a specified vacuum layer spacing and the calculated energy for p(2×2) Pt(111) slab using a vacuum layer spacing of 20 Å (k-points mesh:6×6×1; Ecut-off = 400 eV; σ=0.2 eV)

2.4.3.3 Surface energy comparison

The calculated bulk platinum physical properties by various functional and their supporting pseudo-potential does not give conclusive information as to which best describes the physical properties of platinum, hence the surface was further investigated, and verified for surface chemistry to be studied. Various functionals and supporting pseudopotential were again studied for their estimation of the surface energy of Pt(111) using equation 2.6. This was achieved by fixing the vacuum spacing at the optimised 12 Å on a p(1×1) unit cell at 12×12×1 k-point and 400 eV cut off energy and by varying the surface slab thickness from 2-10 layers, all layers free to relax. The results also gives an indication of the minimum slab thickness (6 layers) required to perform surface calculations. The schematic illustration of the surface energy calculations are shown in Figure 2.10.

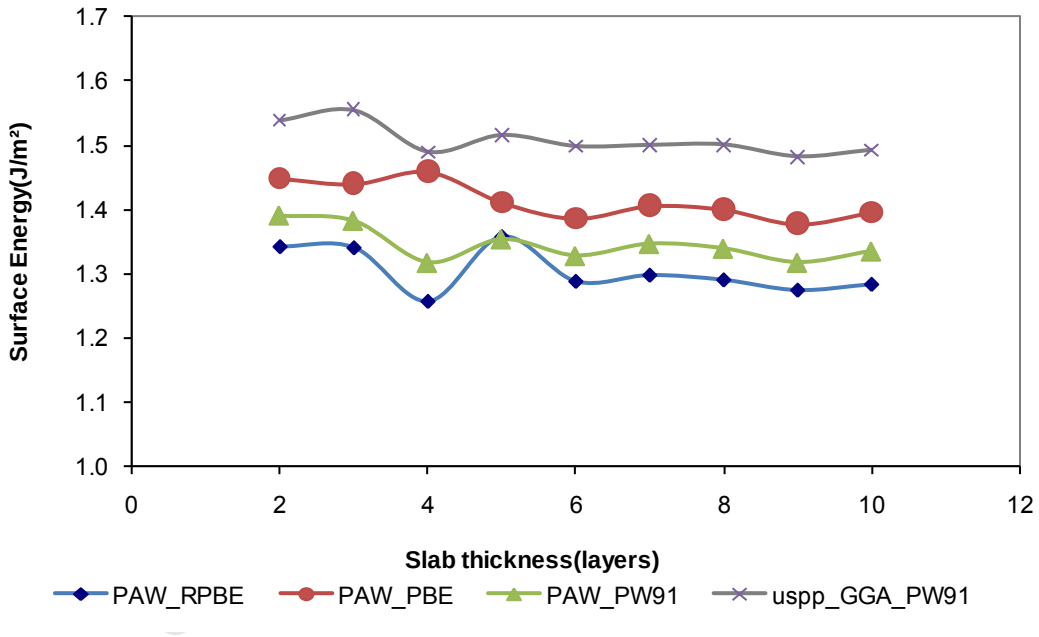

Figure 2.10: Calculated surface energy Pt(111) results as a function of slab thickness. Thecalculations doneusing a 12 Å vacuum spacing; "Note;"*the smoothed fitted lines are given as a* guide

The experimental surface energy values reported by Tyson et al.(1997) and de Boer et al.(1988), are 2.49 J/m² and 2.48 J/m² respectively for the Pt(111) surface. The calculated results are 40% lower than these experimental values. Calculations done by Juarez et al. (2006) on a Pt(111) surface, using an all electron full potential linearized augmented plane wave(FP-LAPW) method also showed similar results for PBE functional with the surface energy of 1.67 J/m² when using the equilibrium calculated lattice parameter for the Pt(111)-cell (3.97 Å; current study 3.94 Å) and 1.47 J/m² when using the experimental lattice (3.92 Å). Generally the GGA functionals give lower surface energies for most systems (Mattsson

et al., 2002). Mattsson et al. (2002) proposed that the predictive nature of first principles calculations for surface energies can be improved by adding a correction for intrinsic surface error in current implementations of density functional theory. The correction is a function of electron density and it can be applied in a wide range of systems (Mattsson et al., 2002).

The bulk platinum electron density of 0.669 $Å^{-3}$ (Mattsson et al., 2002) was used, the following corrections were calculated for PW91 functional: 0.610 J/m² and for PBE functional: 0.462 J/m². Information on how the Mattsson calculator works can be found on Mattson et al. (2006).

Application of this surface energy correction resulted in a slightly improved calculated surface energy for platinum (see Figure 2.11), but the surface energy is still underestimated and not in good agreement with the experimental values. This is a clear indication the DFT applied on this work result in Pt-Pt interaction potential that is not strong enough, resulting in a slightly softer metal, hence overestimated the lattice constant and consequently under-estimated surface energy. The following figure illustrates the surface energy calculations with the Mattsson et al. (2002) corrections.

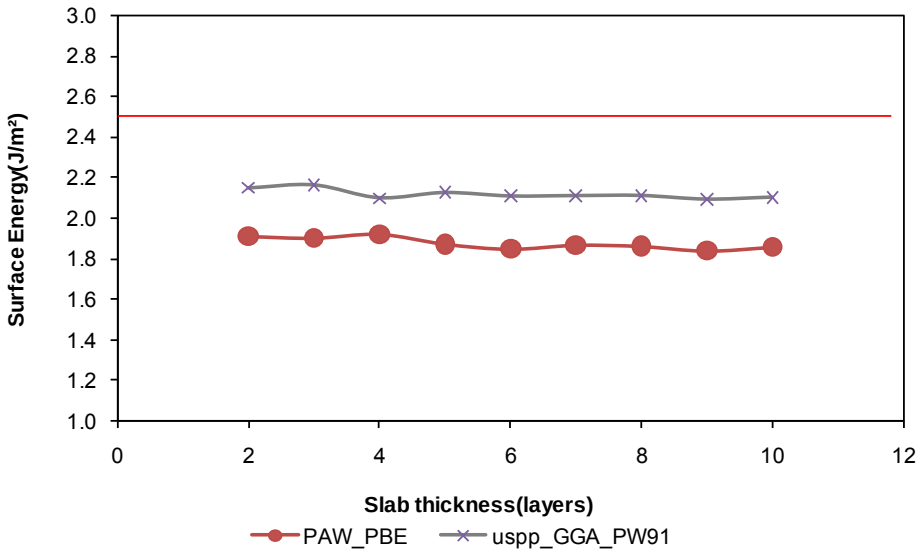

Figure 2.11: Calculated surface energy of Pt(111) including corrections from Mattsson et al. (2002) as a function of slab thickness. The calculations are done using 12 Å vacuum spacing and the red line illustrates the experimental value (2.49 J/m²): Note; *the smoothed fitted lines are given as a guide*

2.5 Functional selection

The energy convergence of the platinum bulk and surface model has been verified with respect to k-point and cut-off energy, the calculated bulk energy is converged at 12×12×12 (primitive unit cell) and 400 eV respectively. However it has been shown that the tested exchange correlation functionals and their supporting pseudopotential do not predict the bulk modulus and the Pt(111) surface energy well. The PAW-PW91 and PAW-PBE however predict the lattice constant fairly well with the difference from the experimental parameter by 0.04% and 0.29% respectively. The Pt to Pt distance is described fairly well, and it is thought to be a dominant factor in the stability and reactivity of the Pt(111) surface (Mavrikakis et al., 1998). The PBE and PW91 functionals are similar by construction and often do not differ remarkably in their results (Mattson et al., 2005). However PBE, by design gives a smoother effective potential than PW91. Furthermore, the functional PW91 suffers from numerical instabilities (Mattson et al., 2005). Hence the functional chosen to proceed within the calculations is the PAW-PBE functional.

2.6 Slab thickness optimisation

To accurately represent the properties of the surface it is desirable to use an infinite slab thickness constrained at the bulk properties (lattice constant). However this comes at a cost of increasing computational time. There is a need to find the smallest slab thickness that minimizes computational time without compromising accuracy. In this study the optimized platinum bulk was cleaved to a desired (111) surface with a 12 Å vacuum gap and calculations were performed using PAW-PBE, using cut-off energy of 400 eV and a k-points 6×6×1 on a p(2×2) unit cell. The surface was probed with atomic oxygen on one side of the slab to study the convergence of adsorption energy (E_{ads}= E_{slab+O}–E_{slab}–$E_{O\text{-}gas}$; E_{ads}: adsorption energy; E_{slab+O}: energy for adsorbed atomic oxygen; $E_{O\text{-}gas}$: gas phase energy) with respect to slab thickness. The energy was corrected for the dipole moment in the direction perpendicular to the surface. The atomic gas phase energy was obtained by placing the atomic species in a 10 Å sided cubic unit cell box with a cut-off energy of 400 eV with gamma k-point setting (1×1×1) with the Gaussian smearing. The latter chosen smearing results in accurate energy calculations, for the set of chosen gamma point k-points (Kresse et al, 2007). The test of how many layers to relax was also performed. Initially the top three layers were allowed to relax and the constraint slab thickness varied from 3 to 8 layers (note on the 3 layer slab all layers were free to relax). Figure 2.12 shows the results for energy convergence with the top three layers free to relax. The convergence criterion was aimed at a difference in the adsorption energy for atomic O of less that 1 meV.

However the convergence for both figures was over the 1 meV criteria, with Figure 2.13, energy converging at 1.2 meV.

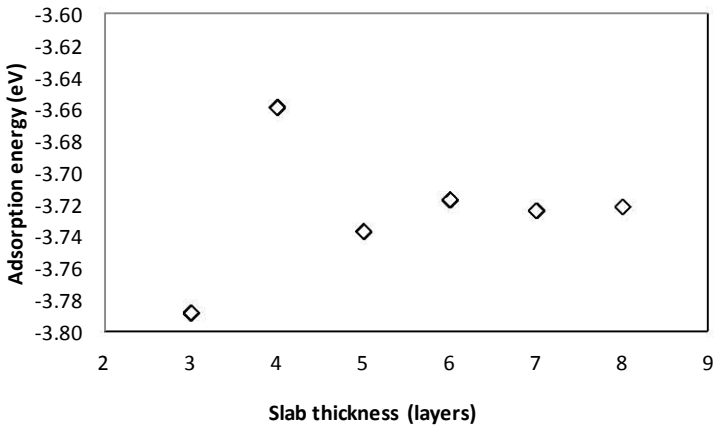

Figure 2.12: Adsorption energy (atomic O) as function of slab thickness. Allowing the top three layers to relax: $E_7 - E_6$ = 7 meV; Cut-off energy at 600 eV; k-point 12×12×1; Pt-Pt = 2.775Å; σ = 0.2 eV

When only allowing the top two layers to relax, the data showed a better energy convergence with an energy difference between layer 6 and 7 to be 1.2 meV (see Figure 2.13).

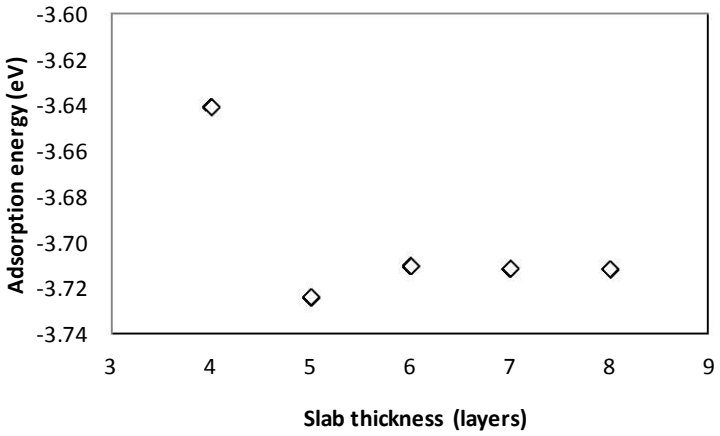

Figure 2.13: Adsorption energy (atomic O) as function of slab thickness. Allowing the top two layers to relax: $E_7 - E_6$ = 1.2 meV

To minimize on computational time it was then decided that the 6-layer slab thickness with the top two layers free to relax and the bottom four constrained to the bulk optimised parameters was adequate to proceed with the surface calculations.

2.7 Gas phase molecules

The reactants and products under study will be assumed to be from the gas phase (the phase transition to the liquid phase can then be computed using standard thermodynamic

procedures). Water and oxygen are the main reaction species at the cathode side of the fuel cell. The energies as well as properties of the gas phase (H_2O, O_2) species were calculated using a spin-polarised with a PAW-PBE, k-point:1×1×1 (gamma centred); cut-off energy: 400 eV, Gaussian smearing and the molecules placed at the centre of a 10 Å sided cubic unit cell.

Oxygen

The equilibrium bond length calculated for oxygen is 1.24 Å, which is a 2% deviation from the experimental oxygen bond length of 1.21 Å (Lide, 2005), vibrational frequency 1565 cm^{-1} (exp: 1581 cm^{-1}; Lide, 2005) and dissociation energy of 5.97 eV (exp: 5.2 eV; Lide, 2005). The dissociation energy is with respect to atomic O on a gas phase, calculated similarly with the calculated magnetic moment for atomic O of $2\mu_B$.

Water

For water the equilibrium O-H bond length is calculated to be 0.97 Å, which is a 1 % deviation from the experimental gaseous water bond length (O-H) of 0.96Å (Lide, 2005). The vibrational analysis yielded the following frequencies (O-H): 3859 cm^{-1}(symmetrical stretch), 3742 cm^{-1}(anti-symmetrical stretch), 1593 cm^{-1}(Bending); (exp: sym. stretch 3657 cm^{-1};anti-sym.stretch 3756 cm^{-1} and bending 1595 cm^{-1}Lide, 2005). The H-O-H angle calculated was 104.38°, which has 0.12 % deviation from the experimental value of 104.51° (Lide, 2005).

H_2O_2

The H_2O_2 species was calculated to have the following properties: O-H bond 0.98 Å, O-O bond 1.47 Å, OOH angle 100° (exp: O-H 0.96 Å, O-O 1.48 Å, OOH angle 95°; Lide, 2005), vibrational frequencies, O-H:3684|3675|1384|1285 cm^{-1},O-O:920 cm^{-1}; bend 372 cm^{-1} (exp: 3608cm^{-1}|3599 cm^{-1}|1402 cm^{-1}|1266 cm^{-1}|877 cm^{-1}|371 cm^{-1} NIST Chemistry WebBook). The calculated properties for H_2O_2 are thus in good agreement with the experimental results.

The PAW-PBE functional was then finally tested to see if it predicts the thermodynamics of the overall gas phase reaction for this study, this is also performed to confirm the accuracy of the DFT study.

$$2H_2O(g) + O_2(g) \leftrightarrow 2H_2O_2(g) \qquad (2.10)$$

The heat of reaction was calculated at 0K and 298K and compared to the data in literature. The calculated values showed to be in agreement with the experimental literature values (see Table 2.2**).**

Table 2.2, the heat of reaction calculations are expressed by the following equation:

$$H^{rxn}_{(0K)} = 2(E_{HOOH(g)}+ZPE)-(2(E_{H2O(g)}+ZPE)+(E_{O2(g)}+ZPE)) \quad (2.11)$$

and

$$H^{rxn}_{(298K)} = (\Delta(E_{tot}+ZPE)) + \Delta H_{(298K)}, \quad (2.12)$$

with $H_{(298K)}$ calculated using thermodynamic equations Hirano, (1993), ZPE: zero point energy, E_i: total gas species energy.

The zero point energy (*ZPE*) corrections were calculated by the following expression.

$$ZPE = \tfrac{1}{2} h \sum \nu_i \quad (2.13)$$

h is the Planck constant and V_i is the individual vibrational frequencies in Hz.

Table 2.2: Heat of reaction from thermodynamics table and the calculated values using DFT. Species standard heat of formation from Sandler (1999)

Species	ΔH^0_f (kJ/mol) Gas at 298°C
O_2	0
H_2O	-242
HOOH	-136
$\Delta H^{rxn}_{(298K)}$	212
Model Calculation	DFT
$\Delta H^{rxn}_{(0K)}$	209
$\Delta H^{rxn}_{(298K)}$	211

2.8 Conclusions

The final functional and supporting pseudopotential selected is the PAW-PBE with the calculated bulk lattice constant of 2.78 Å with a k-point mesh of 12×12×12 k-points and a cut-off energy of 400 eV. The chosen model predicts the lattice constant fairly well (0.29%). However the surface energy and the bulk modulus are under-predicted. Hence the DFT as applied results into a slightly softer metal than expected from experiments.

The surface of Pt(111) and the adsorption of various species on this surface could be determined using a slab containing 6 layers with the top two layers allowed to relax (and the bottom layers fixed at the bulk inter-atomic distance). The vacuum spacing was chosen at 12 Å. The surface modelling parameters were fixed at a k-point mesh of: 6×6×1, for a p(2×2) unit cell and cut-off energy of 400 eV.

2.9 References

Ashcroft N., Mermin N.D., 'Solid state physics', HRW international editions (1988).

Bercegeay C., Bernard S., *Physical Review B* **72** (2005), 214101, 2005

Birch F., *Physical Review* **71** (1947), 809–824

Chadi D.J., Cohen M.L., *Physical Review B* **8** (1973), 5747–5753

De Boer F.R., Boom R., Mattens W.C.M., Miedema, A.R., Niessen, A.K., "Cohesion in Metals", Elsevier Science Publishers, Amsterdam (1988)

Eichler A., Hafner J., *Physical Review Letters* **79** (1997), 4481–4484

Eichler A., Mittendorfer F., Hafner J., *Physical Review B* **62** (2000), 4744–4755.

Feibelman P.J., *Physical Review B* **64** (2001), 125403–12505

Fisher G.B., GlandJ.L., *Surface Science* **94** (1980), 446–455

Ferré D.C., NiemantsverdrietJ.W., *Electrochimica Acta* **53** (2008), 2897–2906

Ford D.C., Nilekar A.U., Xu Y., Mavrikakis M., *Surface Science* **604** (2010), 1565–1575

Gu Z., Balbuena P.B., *The Journal of Physical Chemistry C* **111** (2007), 9877-9883

Hammer B., Hansen L.B, Nørskov J.K.,*Physical Review B* **59** (1999), 7413–742

Hirano T., in "MOPAC Manual", 7th ed., Stewart, J.J.P. (ed.) (1993)

Holmes N.C., Moriarty J.A., Gathers G.R., Nellis W.J., *Journal of Applied Physics* **66** (1989), 2962–2967

Hohenberg, P., Kohn, W., *Physical Review* B **136** (1964), 864-B871

Jiang Q., Lu H.M., Zhao M., *Journal of Physics* **16** (2004), 521–530

Juarez L.F., Da Silva, Stampf C., Scheffler M., *Surface Science* **600** (2006), 703–715

Kittel C., 'Introduction to Solid State Physics', 7th ed.,John Wiley & Sons, Inc.(1996)

Kohn W., Sham L.J.,Physical Review **140** (1965), A1133–A1138

Kresse G., Furthmuller J., *Physical Review B* **54** (1996), 11169–11186

Kresse G., Joubert J., *Physical Review B* **59** (1999), 1758 –1775

Kresse G., Furthmuller J., Universität Wien, viewed 01-03-2007<http://cms.mpi.univie.ac.at/VASP/>

Kumar, M., *Physics and Chemistry of Minerals* **27** (2000), 650-655

Levy M., *Proceedings of the National Academy of Science(USA)* **76** (1979), 6062-6065

Lide D.R. (ed.), CRC Handbook of Chemistry and Physics, Internet Version 2005, <http://www.hbcpnetbase.com>, CRC Press, Boca Raton, FL (2005)

Marder M.P., 'Condensed Matter Physics', A Wiley-Interscience Publication (2000).

Mattsson T.R., Mattsson A.E., *Physical Review B* **66** (2002), 214110–214118

Mattsson A.E, Schultz P.A, Thomas P.D., Mattsson R., Leung K., *Material Science and Engineering* **13** (2005), 1–31

Mattsson A.E., Armiento R., Schultz P.A., Mattsson T.R., *Physical Review B* **73** (2006), 195123–195130

Mavrikakis M. Hammer B., Nørskov J.K., *Physical Review Letters* **81** (1998), 2819-2822

Monkhorst H.J., Pack J.D.,*Physical Review B* **13** (1976),5188–5192

Murnaghan F.D., *Proceedings of the National Academy of Science* **30** (1944), 244–247

NIST Chemistry Webbook, viewed 03-08-2011 <http://webbook.nist.gov/chemistry>

Nørskov J.K., Rossmeis J., Logadottir A., Lindqvist L., *Journal of Physical Chemistry B* **108** (2004), 17886–17892

Payne M., Teter M., Allen D., Arias T., Joannopoulos J., *Reviews of Modern Physics* **64** (1992), 1045-1097

Perdew J.P., Wang Y., *Physical Review* **45** (1992), 13244–13249

Perdew J.P.,Burke K., ErnzerhofM., *Physical Review Letters* **77** (1996), 3865–3868

Qi L., Qian, X., Li, J., *Physical Review Letters* **101** (2008), 146101–146104

Sandler S. I., "Chemical, Biochemical, and Engineering Thermodynamics", 4th ed., John Wiley & Sons (2005)

Swart J.C.W., van Helden P., van Steen E., *The Journal of Physics Chemistry C* **111** (2007), 4998–5005

Taravillo M., Baonza V.G, Rubio J.E.F, Nuriez J., Caceres M., *The Journal of Physics and Chemistry of Solids* **63** (2002), 1705–1715

Tyson W.R., Miller W.A., *Surface Science* **62** (1977), 267–276

van Helden, PhD thesis, University of Cape Town, 2009

Wojciechowski K.F., *Surface Science* **437** (1999), 285–288

Chapter 3

3 ADSORPTION MODELS

In this section the adsorption of molecular oxygen and water from the gas phase on the Pt(111) surface is discussed. This is important since it contributes to the understanding of the initial steps in the oxygen reduction reaction. In addition, the interactions of dissociated species of water and oxygen as well as the proposed intermediate species and products of oxygen reduction have also been investigated.

3.1 Background

3.1.1 General background and molecular oxygen adsorption

The undesirable slow kinetics of the oxygen reduction reaction on a platinum catalyst has motivated research to understand the mechanism by which this reaction takes place. The limited mechanistic understanding of oxygen reduction reaction has also hampered progress in catalytic research on different catalyst designs. Currently platinum is the best catalyst in fuel cells (Nørskov et al., 2004).

Conflicting arguments concerning the oxygen reduction reaction mechanism on platinum surfaces have been presented by earlier research as discussed in chapter one. The early kinetic isotope experiments showed that oxygen adsorbs dissociatively on platinum (Yeager et al., 1992) while much earlier rotating disk electrode experimental research proposed that hydrogenation of oxygen precedes dissociation (Damjanovic et al., 1967). Therefore the current work will interrogate the proposed mechanisms and in this chapter investigate further by studying the intrinsic nature of oxygen to platinum interaction.

3.1.2 General background and water adsorption

In the alkaline fuel cell water is fed to the cathode and reacts with oxygen to yield hydroxide ions. Hence, the oxygen reduction reaction is accompanied by a partial decomposition of water, thus requiring a catalyst that can decompose water.

Faraday (1844) observed that water as formed upon contact of hydrogen and oxygen with platinum at room temperature (Michaelides and Hu, 2001). One of the basic rules of catalysis is that the forward and reverse reactions are catalysed to the same extent (microscopic reversibility). This implies that a good catalyst for a forward reaction must be a good catalyst for the reverse reaction.

Hence knowledge on the interaction of water with the platinum surface is essential to the understanding of oxygen reduction reaction in alkaline fuel cells.

During oxygen reduction reaction the following intermediates and products may be formed on the platinum surface atomic oxygen (O), hydroxyl species (OH), peroxides intermediate (OOH), atomic hydrogen (H) as well as hydrogen peroxide (HOOH). Interaction of these species with the Pt(111) surface was investigated in this section (with water and oxygen in the gas phase and a clean, relaxed P(111) surface as the reference state).

In Table 3.1 previously obtained experimental and calculated adsorption energies of proposed species available during ORR on Pt(111) surface are summarised. The table summarizes the stable adsorption sites as well as the corresponding adsorption energies from various publications.

Table 3.1: Adsorption energy and preferred adsorption sites of surface species present during the oxygen reduction reaction as reported previously

Species	adsorption site	E_{ads} (*eV*)	
		Theory	Experimental
H	3-fold-fcc	-2.9 (ref: H_{gas})[a]	-2.75;-2.55[e]
			-4.1[f]
O	3-fold-fcc	-4.03 (ref: O_{gas})[a]	-3.5[g]
O_2	bridge	-0.72[b]	-0.38[h]
H_2O	on-top site	-0.34[a]	-0.65[i]
OH	Bridge	-1.82 (ref: OH_{gas})[c]	-2.5 to -1.5[j]
OOH	Bridge	-0.96 (ref: OOH_{gas})[c]	
		-0.29[c]	
H_2O_2	Bridge	-0.64[d]	

[a]Michaelidis and Hu (2001); [b]Eichler et al. (1997); [c]Ford et al. (2010; [d]Li et al. (2005);[e]Low energy electron diffraction (Christman et al., 1998);[f]Single crystal adsorption calorimetric (SCAC) at 300 K (Yeo et al., 1999);[g]Single crystal rotating disk electrode(Markovic et al., 1999);[h]Thermal desorption spectroscopy(TDS); T-range: 100-1300K(Gland et al., 1980);[i]Thermal desorption spectroscopy(TDS); T-range: 100-1300K (Fischer et al., 1999); [j] Laser induced fluorescence spectrometer (Mooney et al., 1993)

3.2 Computational method

The calculations to determine the optimal adsorption and the adsorption energy were performed based on the optimised computational set-up discussed in chapter 2 (cut-off energy: 400 eV, k-point mesh: 6×6×1), note that for the p(2×2) unit cell to have the same k-point spacing as in the bulk platinum calculations the corresponding k-point is reduced from 12×12×1 to 6×6×1. The *VASP* computational code (Kresse et al., 1996) was used with the projected augmented wave (PAW) pseudopotential (Kresse et al., 1999) and PBE functional (Perdew et al., 1996). The Methfessel-Paxton smearing scheme was used for the surface calculations with the smearing width of 0.2 eV. For consistency with the bulk computation the surface calculations were non-spin polarised, however it is noted that O_2 in the gas phase is paramagnetic. A test calculation showed an insignificant energy difference between a non-spin polarised and a spin polarised for O_2 adsorbed on an fcc site on Pt(111) surface. The species geometry and the surface geometry for both calculations did not show any variation.

A six layer slab was used with the two top layers allowed to relax and the rest constrained in the bulk-optimised geometry positions. The optimised vacuum gap is 12 Å and a p(2×2) surface unit cell was used. Adsorption was performed on one side of the slab and the energy was corrected for the dipole moment as implemented on the *VASP* computational code. The study was done at 0.25 ML coverage for the considered species. Adsorption energy (E_{ads}) for the species was calculated by the following expression:

$$E_{ads} = (E_{Slab+species} + ZPE) - E_{Slab} - (E_{gas\_phase\_species} + ZPE) \quad (3.1)$$

Where $E_{Slab+species}$ is the energy of the slab and the adsorbed species; E_{Slab} is the total energy of the clean six layer slab (top two free to relax); $E_{gas\_phase\_species}$ is the total gas phase energy of the species in a 10×10×10 (Å) box and *ZPE* is the zero point energy corrections.

Vibrational analysis was performed and the vibrational frequencies were obtained from the matrix of the second derivatives of the energy with respect to the Cartesian coordinates, also known as the Hessian matrix (Wilson et al., 1995). For molecules and periodic system, the Hessian is given by the second derivative of the total energy. Due to the large mass of platinum relative to the species the vibrations of platinum atoms were neglected. The zero point energy (*ZPE*) corrections were calculated by the following expression.

$$ZPE = \tfrac{1}{2} h \sum \upsilon_i \quad (3.2)$$

h is the Planck constant and υ_i is the individual vibrational frequencies in Hz.

3.3 Results and discussion

3.3.1 Molecular oxygen adsorption

The surface chosen for the study is the dense Pt(111) surface. The surface has four high symmetry adsorption sites: on-top, fcc 3-fold hollow, hcp 3-fold hollow and the bridge site as discussed in chapter two. First the sites for O_2 adsorption and their configuration were investigated. It should be noted that eleven different starting configurations on various sites were probed to finally identify the following stable configurations (see appendix B for various studied configurations). Figure 3.1 illustrate the various configurations for O_2 adsorption on Pt(111). Configuration 1 and 2 on the fcc are identical since the surface is symmetrical and it was confirmed by similar adsorption energy, both configurations shown for illustration.

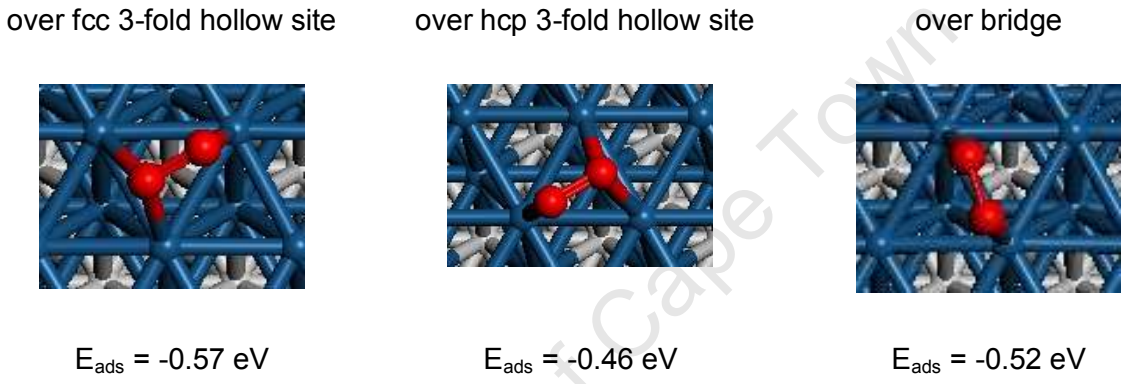

Figure 3.1: Stable geometries for the adsorption of molecular oxygen on various high symmetry sites on Pt(111) at a coverage of 0.25ML (note: the red colour represents oxygen atoms; blue: platinum surface; grey: constrained platinum atoms; adsorption energies relative to gas phase oxygen – not corrected for ZPE)

The zero point energy may significantly change the order for the stability of the various species. The effect of the zero point energy on the adsorption energies for the various high symmetry site on Pt(111) for the adsorption of molecular oxygen is summarised in Table 3.2. The zero point energy reduces the adsorption energy for all the stable adsorption geometries by ca. 0.05 eV.

Table 3.2: Calculated adsorption energy for O_2 on Pt(111) (coverage 0.25ML, the values in brackets include the zero point energy corrections)

Adsorption site	E_{ads} (eV)
fcc 3-fold hollow site	-0.57(-0.52)
hcp 3-fold hollow site	-0.46 (-0.42)
Bridge	-0.52 (-0.48)

Eichler et al. (1997) performed a study of oxygen on platinum from various configurations and identified two minima corresponding to two unique configurations of oxygen on platinum. One of the configuration correspond to oxygen lying parallel to the bridge site so that the oxygen atoms point towards the top sites and the other configuration corresponding to a configuration of oxygen lying parallel to the fcc/hcp 3-fold-hollow site from a bridge site to the top site. The latter geometry is in good agreement with the experimental (STM) observation by Nieminen et al. (1998). The same characteristics of oxygen were also calculated in the current study. Figure 3.2 illustrate detailed characteristics for molecular oxygen adsorbed in the most stable adsorption geometries, *viz*. bridge and the fcc 3-fold hollow site.

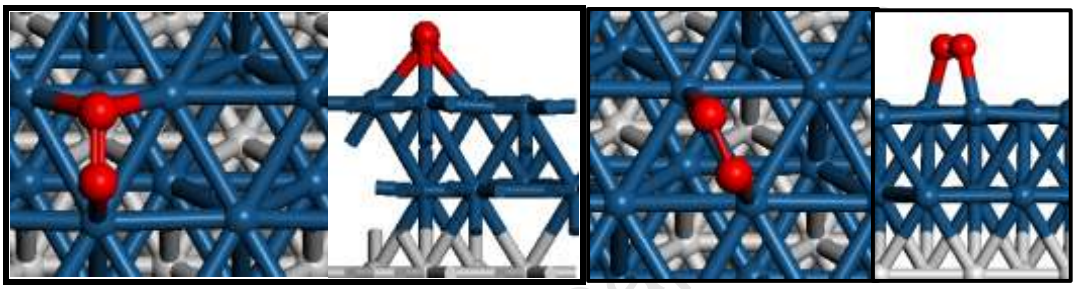

Figure 3.2: Top and side view for oxygen adsorbed on an fcc site parallel to the surface

Left: adsorbed on fcc 3-fold hollow site parallel to the surface (Eads= -0.57 eV; d_{Pt-O} =~2.20 Å; d_{O-O} = 1.40 Å

Right: on a bridge site (Eads = -0.52 eV; d_{Pt-O}=2.04 Å; d_{O-O} = 1.37Å)

The DFT calculations (on VASP-uspp-PW91) by Eichler et al. (1997), showed oxygen adsorption energy of -0.68 eV (fcc 3-fold hollow) and -0.58 eV (hcp 3-fold hollow) and -0.72 eV (bridge). Discrepancies between the current study and Eichler et al. (1997) could possibly arise from the different computational parameters and in particular the use of different functional (PW91 vs. PBE this study). The study by Eichler et al. (1997) was done on a 4-layer slab with a k-points grid of 3×4×1 they further reported that 'most calculations have been performed at fixed substrate geometry, but for the molecular precursors a full relaxation of the adsorbate/substrate complex has been allowed'; this type of computational inconsistencies could have led to the differences. The DFT study by Fu et al. (2011) using the same functional as in the current study (PAW-PBE) reported an adsorption energy for molecular oxygen on Pt(111) on the fcc 3-fold hollow site of -0.78 eV (fcc) using a 4-layer slab with top two free to relax and k-point grid of 3×4×1. It is apparent that the slab thickness and/or the number of layers which may relax have a significant influence on the obtained adsorption energy.

The reported adsorption energy for molecular oxygen on the bridge site is -0.46 eV (Ford et al. (2010) GGA-PW91, DACAPO computational code) is similar to the calculated value in this study (-0.52 eV).

The experimental value reported by Gland et al. (1980) from thermal deposition experiments is -0.38 eV. The experimental value is expected to be lower since it was measured at higher O_2 coverage.

Vibrational analysis was conducted on the stable adsorbed state to investigate if the structure is a minimum on the potential energy surface. The calculated frequencies are given in Table 3.3. The calculated frequencies and bond lengths were compared to the experimental and earlier calculated results.

Table 3.3: Vibrational analysis of molecular oxygen on Pt(111)

		Calculated		Experimental
		This study	Literature	
3-fold hollow site	d_{O-O}, Å	1.40 (fcc) 1.37 (hcp)	1.43/1.42[a]	1.4[b]/1.47[c]
	ν_{O-O}, cm^{-1}	847 (fcc) 827 (hcp)	690/710[a]	700[d]/710[e]
Bridge	d_{O-O}, Å	1.37	1.39[a]	1.39[c]/1.37[f]
	ν_{O-O}, cm^{-1}	883	850[a]	875[d]/842[g]

[a]Eichler et al. (1997); [b]Photon electron spectroscopy (Eberhardt et al., 1988); [c]Photon electron spectroscopy (Puglia et al., 1995); [d]Electron energy loss spectroscopy (Steininger et al., 1982); [e]Electron energy loss spectroscopy (Gland et al., 1980); [f]Near Edge X-Ray Absorption Fine Structure (Wurth et al., 1990); [e]Electron energy loss spectroscopy (Avery, 1983);

The calculated gas phase O-O vibrational frequency for molecular oxygen is 1565 cm^{-1}. When oxygen is adsorbed on Pt(111) on the fcc 3-fold hollow site, the O-O stretching frequency is reduced from 1565 to 827 cm^{-1}. The frequency at which a vibration occurs is determined by the strength of the bonds and mass of the atoms involved. The reduction in O-O frequency for oxygen on the platinum surface is an indication of a weakening of the O-O bond, hence it is anticipated that less energy may be required to break the oxygen bond.

Dissociation of O_2 is desired during oxygen reduction reaction. The calculated gas phase O-O bond length is 1.24 Å and the final bond length on the Pt(111) surface is 1.40 Å (fcc) and

1.37 Å (bridge). The most stable site (fcc) showed a higher bond stretch an indication of the possibility of favourable O-O bond dissociation.

The calculated properties for adsorbed molecular oxygen on the bridge site are in agreement with the previously calculated values (Eichler et al., 1997) and with the experimentally obtained values. The calculated values of the obtained bond lengths for the adsorption on 3-fold hollow sites (fcc or hcp) are lower than the reported values, and the obtained vibrational frequencies are higher than those reported previously (either experimentally or theoretically).

3.3.2 Water adsorption

The traditional water to metal interaction is understood to form a buckled bilayer structure where only every second water molecule binds to the surface (Thiel et al., 1987). Further analysis on the bilayer structure by Doering et al. (1982) suggests that water binds to the metal surface through the oxygen lone pair orbital, indicating that only oxygen directly binds to the surface. However in the X-ray absorption, X-ray emissions and X-ray photoelectron spectroscopy along with the density functional theory study by Ogasawara et al. (2002) concluded that a monolayer of water adsorbs on the Pt(111) surface by forming a flat layer with both metal to oxygen and metal to hydrogen as the bonding species. Michaelides et al. (2003) also found water monomer to lie almost flat on the Pt(111) surface using theoretical study (DFT), with the hydrogen atoms lying at a 7° angle from the surface plane. Michaelides et al. (2003) calculated the following properties of molecule to Pt(111):O to metal distance: 2.36 Å, O-H bond: 0.98 Å. Furthermore they also reported that water adsorbs at a top site with the molecule laterally displaced from a precise top site by 0.3 Å.

Fifteen different starting configurations on various sites were probed for the adsorption of water molecule on Pt(111) (see Appendix B) to find a stable configuration and site.

A water molecule initially was placed directly on top of a hexagonal close packed site on a tilted position (~45°). The final configuration is a flat water molecule with the entire molecule facing the hexagonal close packed site, however with the oxygen atom shifted towards the on top site but slightly displaced by 0.1 Å (see Figure 3.3).

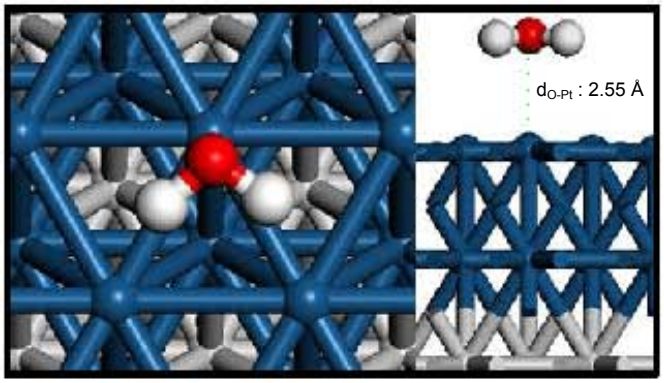

Figure 3.3: Water adsorbed on the on top site: d_{O-Pt}=2.55Å; d_{O-H}=0.98 Å, note the red colour represents oxygen atoms; white: hydrogen atoms; blue: platinum atoms, grey: constrained platinum atoms

Similar characteristics as compared to Michaelides et al. (2003) for water interaction with Pt(111) surface has also been calculated in this study (see Figure 3.3) with water almost lying flat on the surface, as reported by Ogasawara et al. (2002), with the following properties O to metal distance (surface plane): 2.55 Å, O-H bond length: 0.98 Å.

Figure 3.4 shows the final geometry for water adsorbed at various orientations on the Pt(111) surface as obtained from different starting geometries. The similarity in the adsorption energy is a consequence of the rotational symmetry of this adsorbed species on Pt(111).

E_{ads} = -0.18 eV 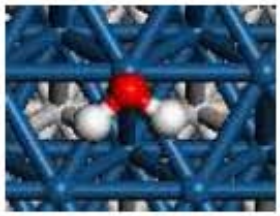 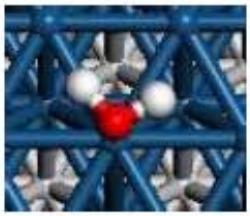 E_{ads} = -0.18 eV

E_{ads} = -0.18 eV 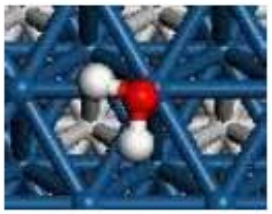 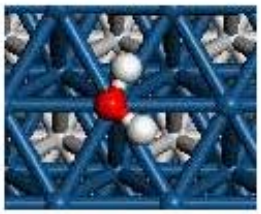 E_{ads} = -0.14 eV

Figure 3.4: Various orientations of adsorbed water on Pt(111) surface (Note E_{ads} exclude zero point corrections, note the red colour represents oxygen atoms; white: hydrogen atoms; blue: platinum atoms, grey: constrained platinum atoms)

The zero point energy correction for the adsorbed water species amounts to 0.06 eV. Hence the adsorption energy for the on-top water molecule with the zero point energy corrections

is -0.12 eV. The energy is consistent with the calculated value of -0.18 eV by Ford et al. (2010).

Vibrational analysis was also conducted on the stable adsorbed water species this is done to investigate if the site and configuration of water on the surface is at a minimum on the potential energy surface. A gas molecule with N number of atoms has 3N degrees of freedom of which 6 are translations and rotation of the molecule. This lead to 3N – 6 vibrational degrees of freedom, however for linear molecules is 3N – 5 vibrational freedom. Water has 3 atoms, the resulting vibrational freedom is 3(3) – 6 = 3, however on the surface additional translational and rotational modes can be calculated, due to the molecule interaction with the surface. The following properties and vibrational frequencies of H_2O on the Pt(111) surface were calculated for bending of the H-O-H, the symmetrical and asymmetrical stretch of the O-H bond and compared to those for gas phase water (see Table 3.4).

Table 3.4: Comparison between the geometry and vibrational frequencies between gas phase water and water adsorbed on Pt(111) surface

	H_2O(g)	H_2O(adsorbed)
d_{O-H}, Å	0.97	0.98
∟H-O-H,°	104	104
$\nu_{bending}$, cm^{-1}	1593	1576
$\nu_{sym.\ stretch}$, cm^{-1}	3742	3581
$\nu_{asym.\ stretch}$, cm^{-1}	3860	3685

The vibrational frequency of water adsorbed on Pt(111) showed a slight change from the gas phase to the surface, with the O-H stretching mode changing by only 175 cm^{-1}. This is an indication that water is weakly adsorbed (E_{ads}=-0.12 eV) on the Pt(111) surface and the O-H bond is hardly activated. As a result of the slight change in O-H bond frequency a high activation energy for water dissociation can be anticipated.

3.3.3 Atomic hydrogen

All high symmetry sites were studied and found to be stable for H adsorption with the most stable adsorption site for hydrogen on the 3-fold hollow fcc site as shown in Table 3.5 and the configuration shown in Figure 3.5.

fcc 3-fold hollow hcp 3-fold hollow bridge on-top

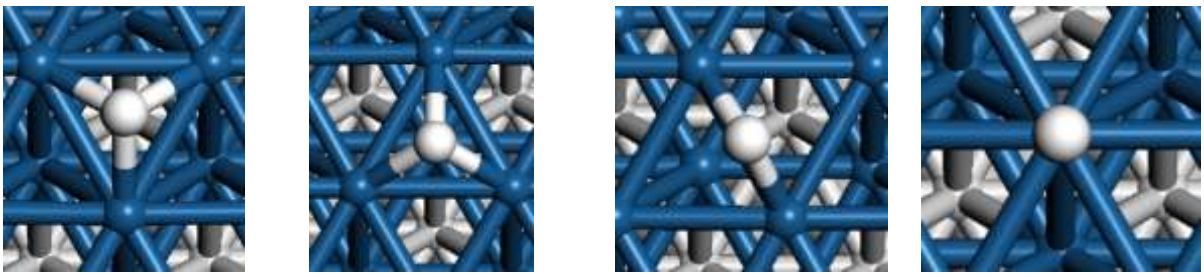

Figure 3.5: Atomic hydrogen adsorption on four sites: (HCP: d_{Pt-H} 1.9 Å; FCC: d_{Pt-H} 1.9 Å; Bridge: d_{Pt-H} 1.8 Å; on Top: d_{Pt-H} 1.6 Å

The results were confirmed by vibrational analysis and all configurations were found to be at a minimum. This is consistent with the study by Michaelides et al. (2001), who reported similar adsorption energies on the four high symmetry sites on Pt(111), with a slight preference by 0.1 eV for the fcc 3-fold hollow site. Similar results were also calculated by Papoian et al. (2000). The values in brackets are with respect to O_2 gas and H_2O gas and calculated by the following expression:

$$E_{ads} = \left(E_{slab+H} + ZPE\right) + \frac{1}{4}\cdot\left(E_{O_2(g)} + ZPE\right) - E_{slab} - \frac{1}{2}\cdot\left(E_{H_2O(g)} + ZPE\right) \qquad (3.3)$$

with E_{ads}: adsorption energy; E_{slab+H}: total energy of the adsorbed H; E_{i_gas} is the energy for the species in a gas phase; E_{slab}: total energy for the clean slab.

Table 3.5: Adsorption energy for atomic hydrogen (0.25 ML coverage), with respect to atomic hydrogen in a gas phase; energies with zero point energy corrections, (values in brackets are with respect to gas phase atomic hydrogen)

Adsorption sites	HCP	FCC	Bridge	onTop
E_{ads}(eV)	-2.59(0.77)	**-2.62(0.8)**	-2.58(0.81)	-2.56(0.83)

The current results (in Table 3.5) are in agreement with the calculated (DFT;uspp-GGA-PW91) value of -2.9 eV for all sites (0.25ML) by Michaelides et al. (2001) and good agreement with the experimental value reported by Christman et al. (1998) is in the range from -2.75 to -2.55 eV.

3.3.4 Atomic oxygen

All high symmetry sites were probed for atomic O adsorption and the results are summarised in Table 3.6. The bridge site was also studied for O adsorption but atomic O

moved away and fell to the nearest hollow sites. The on-top site showed two imaginary frequencies, indicating that the on-top site is not a stable adsorption site. The imaginary vibrational modes point towards the bridge and the hollow sites. This is a possible indication that this adsorption geometry is a precursor toward the hollow sites.

Table 3.6: Summary table for atomic oxygen adsorption energy on different sites (0.25ML coverage), with respect to ½O_2 gas phase (values in brackets are with respect to gas phase atomic oxygen) Energies with zero point energy corrections

Adsorption sites	HCP	FCC
E_{ads}(eV)	-0.70 (-3.64)	**-1.10(-4.07)**

Atomic oxygen is more stable in the fcc3-fold hollow site. This is consistent with the study done by Feibelman et al. (1996) where they calculated that the fcc 3-fold hollow site is more preferred than the hcp 3-fold hollow site by ~ 0.4 eV. The calculated adsorption energy values for atomic oxygen adsorbed on the fcc 3-fold hollow site with respect to atomic O in the gas phase are in agreement with the reported value by Michaelides et al.(2001)(-4.03 eV (uspp-GGA-PW91), but larger than the values reported by Ford et al. (2010)(-3.59 eV; GGA-PW91; DACAPO computational code). All calculated values are with the range of the experimentally determined adsorption energies for atomic oxygen, which are within the range of -4.1 to -3.5 eV (Yeo et al., 1997; Markovic et al., 1999).

3.3.5 Hydroxyl species (OH)

All the high symmetry sites were studied for OH adsorption (see Appendix B). The calculations indicated that OH is not stable on either of the 3 fold hollow sites, and will move away from the 3-fold hollow site to the bridge site and on-top sites (see Figure 3.6).

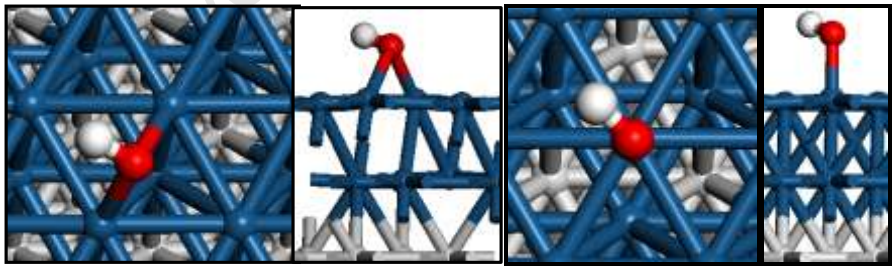

Figure 3.6: OH adsorption on the bridge and top site (note the red colour represents oxygen atoms; white: hydrogen atoms; blue: platinum atoms, grey: constrained platinum atoms)

Left: OH adsorption on the bridge(d_{Pt-O} = 2.16 Å; d_{O-H} = 0.95 Å)
Right: OH on the on-top site (d_{Pt-O} = 1.99 Å; d_{O-H} = 0.98 Å)

The vibrational analysis confirmed that adsorption on the bridge and on-top sites both represent a minimum on the potential energy surface. In Table 3.7, the absorption energy

with respect to OH in the gas phase has also been calculated. The energy for OH gas was calculated in a 10 Å sided box, similarly to the other gas phase species, from which the O-H bond of 0.99 Å and bond dissociation (D_e) energy of 4.72 eV and O-H vibrational frequency of 3619 cm^{-1} were obtained, which is in reasonable agreement with the experimental data reported at 298K (D_e=5.15 eV; $v_{O\text{-}H}$=3738 cm^{-1}; data from Lide, 2005).

The adsorption energy was also calculated with respect to H_2O and O_2 gas, since these are the main reactants during ORR in alkaline fuel cells:

$$E_{ads} = \left(E_{slab+OH} + ZPE\right) + \frac{1}{4}\cdot\left(E_{O_2(g)} + ZPE\right) - E_{slab} - \frac{1}{2}\cdot\left(E_{H_2O(g)} + ZPE\right) \quad (3.4)$$

Table 3.7: Adsorption energy for hydroxyl (OH*) (0.25 ML), In brackets is the energy with respect to OH in a gas phase; values outside the brackets is with respect to O_2 and H_2O gas phase. Energies with zero point energy corrections

Adsorption site	E_{ads}(eV)
bridge	**-0.32(-2.09)**
top	-0.30(-2.07)

Michaelides et al. (2001), also determine that OH on Pt(111) is stable on either the bridge and the top site, however with the top site binding more strongly by 0.04 eV. Furthermore they reported that the recombination of O+H will yield OH on bridge site which then can diffuse to the top site with a diffusion barrier of 0.1 eV. Ford et al. (2010) reported the OH to be stable on a bridge site with a tilted configuration (E_{ads}= -1.82eV with respect to OH radical). Adsorption energy reported by Phatak et al. (2009) on their DFT study (VASP-uspp-PW91, p(3×3) unit cell), is -2.33 eV with respect to OH gas for both the tilted bridge and the top site. The values are not consistent with the current study, with large difference compared to Phatak et al. (2009). The reasons for the differences are not apparent, however it is noted that the H-coverage in the study by Phatak et al. (2009) is at much lower coverage (0.11ML).

3.3.6 Peroxide intermediate (OOH)

All the high symmetry sites were also studied for OOH adsorption (see Appendix B). The results showed that the species will not adsorb on the hollow sites and will subsequently move away towards the bridge site with the hydrogen parallel to the surface plane, with an O-O bond length of 1.43 Å (see Figure 3.7).

The DFT calculations by Ford et al. (2010) reported OOH to be stable on a 'bent' top site with the O-O bond-length of 1.45 Å (E_{ads} = -0.96 eV). The configuration proposed by Ford et al. (2010) is in agreement with the current calculations as illustrated in Figure 3.7.

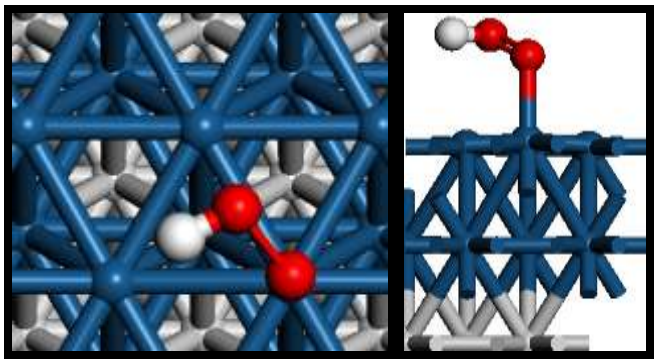

Figure 3.7: Adsorption geometry of OOH on a bridge site with; d_{O-Pt}:2.02 Å, d_{O-O}: 1.43 Å, d_{O-H}:0.99 Å, note the red colour represents oxygen atoms; white: hydrogen atoms; blue: platinum atoms, grey: constrained platinum atoms

The adsorption energy for OOH on Pt(111) was calculated to be -1.04 eV with respect to H_2O(g) and O_2(g). The adsorption energy was also calculated with respect to OOH in the gas phase. The energy for OOH gas was calculated on a 10 Å sided box, similarly to the other gas phase species. The OOH-species in the gas phase has a O-O bond length of 1.35Å and a O-H 0.99 Å. The following vibrational frequencies were determined: symmetrical stretch of 3449 cm^{-1}; bending mode of 1369 cm^{-1} and anti-symmetrical stretch of 1126 cm^{-1} (Experiment:3436 cm^{-1}(symmetrical stretch);1392cm^{-1}(bend);1098cm^{-1}(anti symmetrical stretch): Lide. 2005). The current OOH gas phase properties calculations are in good agreement to the experimental values.

Studying adsorption energy calculations of OOH with respect to H_2O and O_2 gas showed repulsive adsorption energy but attraction energy with respect to OOH gas. Overall observation on this study for the intermediates adsorption energy with respect to H_2O and O_2 gas did not show a good description of the adsorption energy in comparison to experimental values.

Furthermore, the adsorption energy for peroxide intermediate (OOH) (0.25ML coverage) is 0.22 eV (including zero point energy corrections) the gas phase energy is with respect to H_2O and O_2 gas, and -1.04 with respect to OOH in the gas phase. Hence the formation of OOH is not favoured with respect to H_2O and O_2 in the gas phase, but favoured with respect to OOH in the gas phase.

Activating oxygen by atomic hydrogen stretched the O-O bond length further to 1.43 Å, larger than when the molecular oxygen is adsorbed (d_{O-O}=1.40Å). This is a possible indication that activating oxygen with atomic hydrogen will favour O-O bond breaking. However the stretching frequency for O-O bond in OOH adsorbed on Pt(111) is 843 cm^{-1} which is slightly higher than that of O_2 adsorbed (827 cm^{-1}). This is an indication that hydrogen has stabilised the O-O bond strength on the surface, however this effect is not very significant.

The surface OOH-species is labile, since the initial configuration of OOH on the fcc 3-fold-hollow site, resulted in a final configuration in which OOH was dissociated into hydroxyl ion (OH) and atomic oxygen (O), thus representing co-adsorbed OH and atomic O (see Figure 3.8).

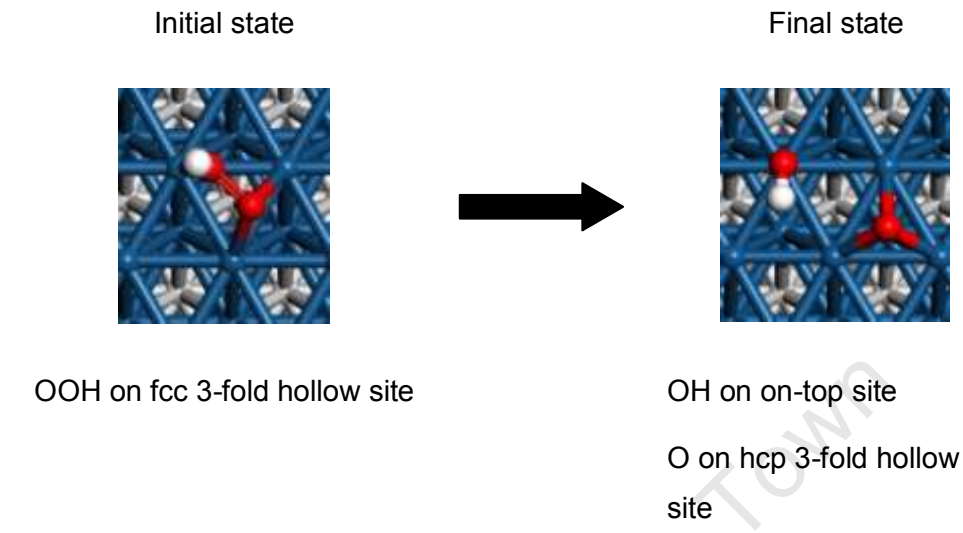

Figure 3.8: Initially adsorption of OOH on fcc 3-fold hollow site on Pt(111), final optimized geometry (dissociated) with OH (top site) and H (hcp), note the red colour represents oxygen atoms; white: hydrogen atoms; blue: platinum atoms, grey: constrained platinum atoms

3.3.7 H_2O_2 adsorption

All the high symmetry sites were probed as adsorption sites for H_2O_2. However, some starting configurations yielded the dissociated product of two hydroxyl species co-adsorbed on the p(2×2) Pt(111) surface (see Appendix B).

The stable adsorbed hydrogen peroxide molecule on Pt(111) was found to lie on a bridge site, with one oxygen atom anchored at the top site (see Figure 3.9):

Properties for the hydrogen peroxide species adsorbed on Pt(111) surface has been calculated in this study with the O-O bond length of 1.47 Å (gas:1.47 Å); O-H bond length of 0.99 Å (gas:0.98 Å); Oxygen to metal bond distance 2.43 Å.

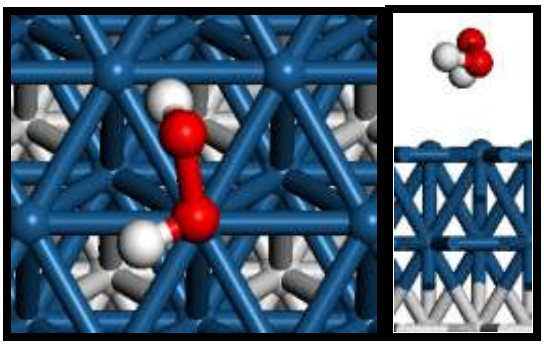

Figure 3.9: Stable H_2O_2 on a bridge site with; $d_{O\text{-}Pt}$: 2.43 Å, $d_{O\text{-}O}$ 1.47 Å, $d_{O\text{-}H}$: 0.99 Å, (note the red colour represents oxygen atoms; white: hydrogen atoms; blue: platinum atoms, grey: constrained platinum atoms)

The adsorption energy for the configuration given in Figure 3.9 is -0.21 eV and was calculated with respect to H_2O_2 in a gas phase. The reported energy is with zero point energy corrections.

Considering the properties of H_2O_2 on Pt(111) relative to the gas phase, it is apparent that H_2O_2 is weakly bonded to the surface, since the bond lengths and frequency are slightly changed from the gas phase frequencies, a possible evidence that this species would not easily decompose at the bridge site. Furthermore it is noted the O-O bond stretch frequency for adsorbed H_2O_2 is lower than that of molecular O_2.

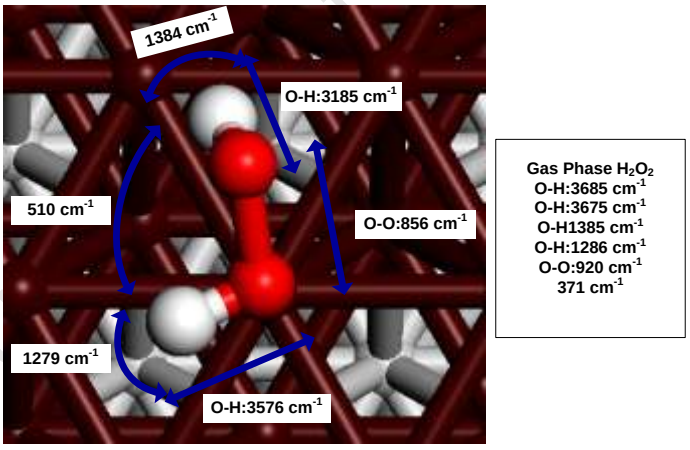

Figure 3.10: Calculated vibrational frequency for H_2O_2 on Pt(111)

The DFT study by Li et al. (2005) on Pt(111) surface, using CASTEP (GGA-PW91), reported that each oxygen atom of H_2O_2 molecule is found close to on-top site with the entire molecule aligned along a bridge site. They further indicated that the O-O bond forms a 25° angle with the surface plane. The other geometric parameters for adsorbed H_2O_2 were reported to be: O-O bond length = 1.46 Å, O-H bond length = 0.99 Å and oxygen to metal bond distance = 2.5 Å. Furthermore they reported adsorption energy of -0.64 eV, with respect to gas phase H_2O_2. The discrepancies between the current adsorption energy and that of Li et al. (2005) could be as a result of different computational parameters (in

particular the slab used in their study). They performed their calculation using CASTEP with the GGA-PW91 functional and on a 3 layer slab only allowing the top layer free to relax. Furthermore the gas phase species was calculated at the same super cell arrangement as the surface (p(2×2) unit cell).

Ford et al. (2010) using GGA-PW91;DACAPO computational code on a 4-layer slab with top two free to relax by reported an adsorption energy of -0.29 eV for H_2O_2 on Pt(111) surface, the value is in good agreement to the current results. They also calculated an H_2O_2 configuration on the Pt(111) surface with one of the oxygen binding to the top site and one hydrogen pointing to the surface (d_{O-O} bond: 1.47 Å; d_{O-H}:1.01 Å; ν_{O-O}:849 cm^{-1}; $\nu_{O-H\alpha}$:3287 cm^{-1}: $\nu_{O-H\beta}$:3673 cm^{-1})

Adsorption of H_2O_2 on the 3-fold hollow fcc and the bridge site transformed upon geometry optimization into a unique product (see Figure 3.11). The final geometry is a species of oxygen bridged by a hydrogen atom. The species also could be a representation of a precursor towards forming a water molecule co-adsorbed with atomic O.

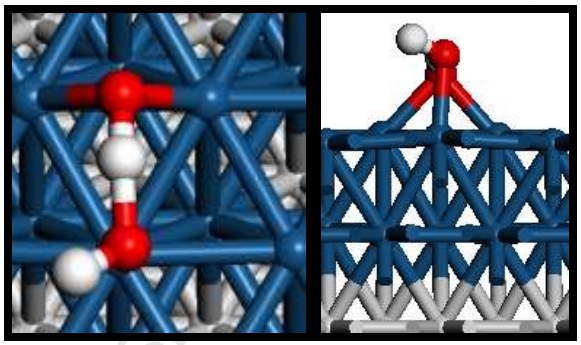

Figure 3.11: Final geometry obtained from an initial position of H_2O_2 adsorbed on the fcc 3-fold hollow site, resulting in an optimized geometry with oxygen linked by a hydrogen bridge over the fcc 3-fold site (note red: oxygen atoms; white: hydrogen atoms; blue: platinum atoms, grey: constrained platinum atoms)

3.4 Vibrational analysis on the di-oxygen species

An interesting phenomenon was observed for the di-oxygen species. The adsorbed O^*_2, OOH*, HOOH* showed a distinctive trend in O-O vibrational frequencies. The frequencies decreased in the following order: HOOH*(ν_{O-O} 856 cm^{-1})>OOH* (ν_{O-O} 846 cm^{-1})>O^*_2 (ν_{O-O} 827 cm^{-1}). In principle this could be an indication that di-oxygen species on metal surfaces can be identified using some form of vibrational spectroscopy (Ford et al., 2010).

The wavenumber increases when the oxygen containing surface species contains more hydrogen. The change in the mass of the vibrating species (going from O-O to HO-O to HO-OH) would result in a decrease in the wavenumber, but an increase is observed. Hence, the addition of hydrogen to the adsorbed oxygen species causes a change in the strength of the O-O bond.

3.5 Potential energy profiles for the formation of surface H_2O_2

A thermodynamic potential energy surface can be formulated based on calculated adsorption energies of the intermediates of interest for the oxygen reduction reaction (ORR) on Pt(111). This excludes activation barriers. Figure 3.12 shows the reaction networks of elementary steps on Pt(111) for the three possible proposed paths form hydrogen peroxide. Each of these reaction networks has a reaction unique step to form the surface hydrogen peroxide species or the intermediate OOH species. For path-1 the unique site is the hydrogen addition to adsorbed O_2 ($H^*+O_2^* \rightarrow OOH^*$). The unique reaction step according to path-2 is the dimerization of surface hydroxyl species ($OH^*+OH^* \rightarrow HOOH^*$), path-3 is the addition of a surface oxygen to the surface hydroxyl species ($O^*+OH^* \rightarrow OOH^*$). Path-2 and path-3 proceed via a dissociation step of adsorbed molecular oxygen, whereas path-1 proceeds via hydrogen activated oxygen dissociation. The reaction steps are given in Table 3.8.

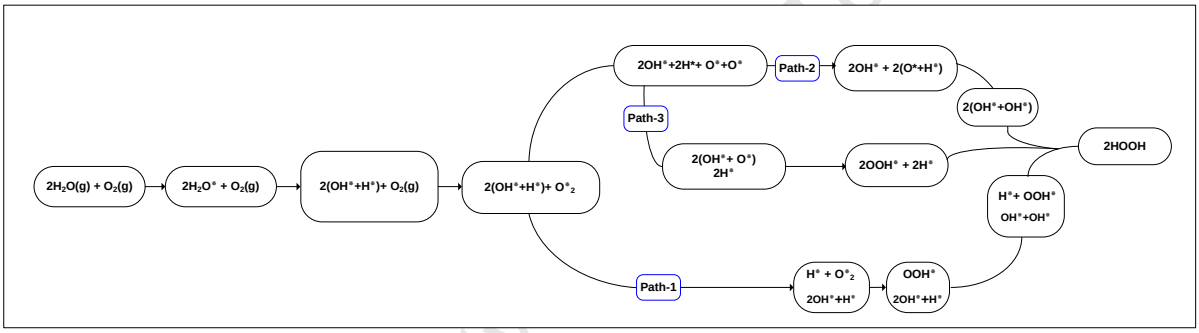

Figure 3.12: Reaction network, of possible reaction steps to form hydrogen peroxide

The reaction steps are numbered on the graphs (Figure 3.13 and Figure 3.14) as described inTable 3.8

Table 3.8: Summary of reaction steps as shown on the potential energy surfaces of Figure 3.13 and Figure 3.14 (Notation: *denotes an adsorbate on the surface).

Path-1	Path-2	Path-3	
$2H_2O(g)+O_2(g)$	$2H_2O(g)+O_2(g)$	$2H_2O(g)+O_2(g)$	0
$2H_2O^*+O_2(g)$	$2H_2O^*+O_2(g)$	$2H_2O^*+O_2(g)$	1
$2(OH^*+H^*)+O_2(g)$	$2(OH^*+H^*)+O_2(g)$	$2(OH^*+H^*)+O_2(g)$	2
$2(OH^*+H^*)+O_2^*$	$2(OH^*+H^*)+(O_2^*)$	$2(OH^*+H^*)+(O_2^*)$	3
$2(OH^*)+H^*+\mathbf{((H^*+O_2^*)} \rightarrow OOH^*)$	$2(OH^*)+2(H^*)+\mathbf{((O_2^*)} \rightarrow O^*+O^*)$	$2(OH^*)+2(H^*)+\mathbf{((O_2^*)} \rightarrow O^*+O^*)$	4
$2(OH^*)+\mathbf{((H^*+OOH^*)} \rightarrow HOOH^*)$	$2(OH^*)+\mathbf{2((H^*+O^*)} \rightarrow 2OH^*)$	$2(H^*)+\mathbf{2(OH^*+O^*)} \rightarrow 2OOH$	5
$((HOOH^*)+\mathbf{(OH^*+OH^*))} \rightarrow 2HOOH^*$	$\mathbf{2(OH^*+OH^*)} \rightarrow 2HOOH^*$	$\mathbf{2(OOH^*+H^*)} \rightarrow HOOH^*$	6
$2HOOH(g)$	$2HOOH(g)$	$2HOOH(g)$	7

The potential energy diagram for the proposed reaction network has been formulated (see Figure 3.13 and Figure 3.14). The energy is normalized with respect to the calculated energy of O_2 and 2 H_2O in the gas phase using DFT. The definition of the various reaction steps is given in Table 3.8.

Figure 3.13 represents species energies as pseudo-classical particles. In practise atoms of an ideal crystal lattice will not sit exactly on their equilibrium positions (Peierls, 2001). In DFT if they are to be represented as quantum particles, the zero point vibrations have to be taken into account.

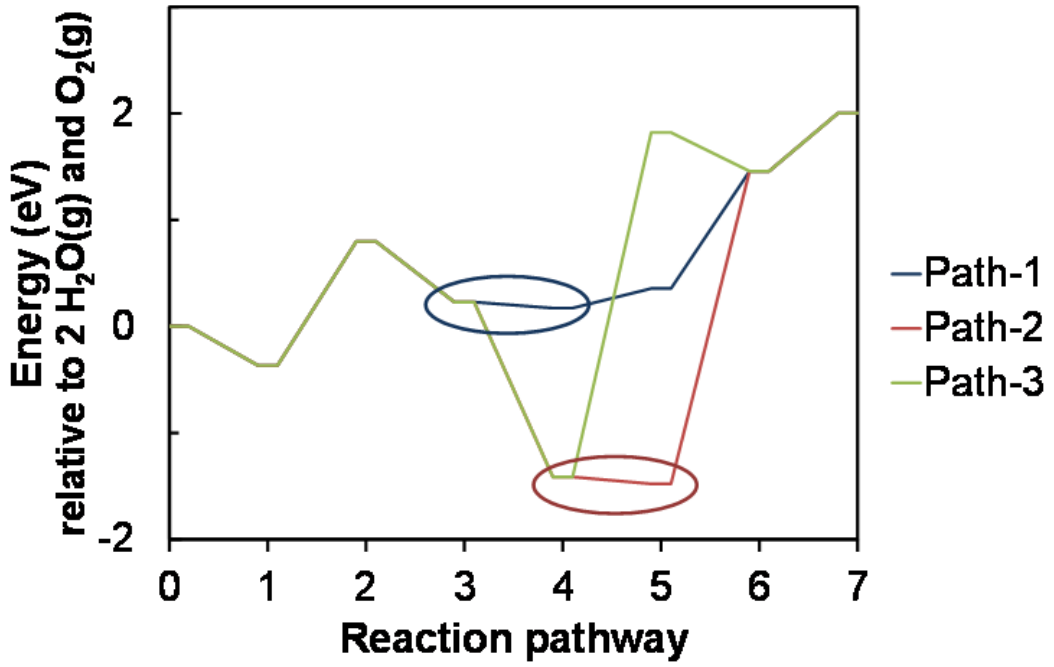

Figure 3.13: Potential energy profiles, illustrating reaction steps to form hydrogen peroxide on Pt(111). The energy values exclude the zero point corrections

The profile with zero point energy corrections (Figure 3.14) shows an interesting phenomenon. Attention should be drawn towards reaction steps representing a reaction where O-H bond is formed. In Figure 3.13 it is apparent that in path-1 reaction step from 3 to 4 is slightly exothermic and in path-2 reaction step 4 to 5 is also exothermic. It was then noted that after the zero point energy corrections were included, reaction steps on path one (3-4) and on path two (4-5) changed to endothermic reactions. This observation is as a result of a transition from a low vibration of individual species (H, O and O_2) to a higher vibrational stretching covalent O-H bond on the surface. The higher vibrational frequency such as associated with an O-H bond, will result in a large zero point energy corrections.

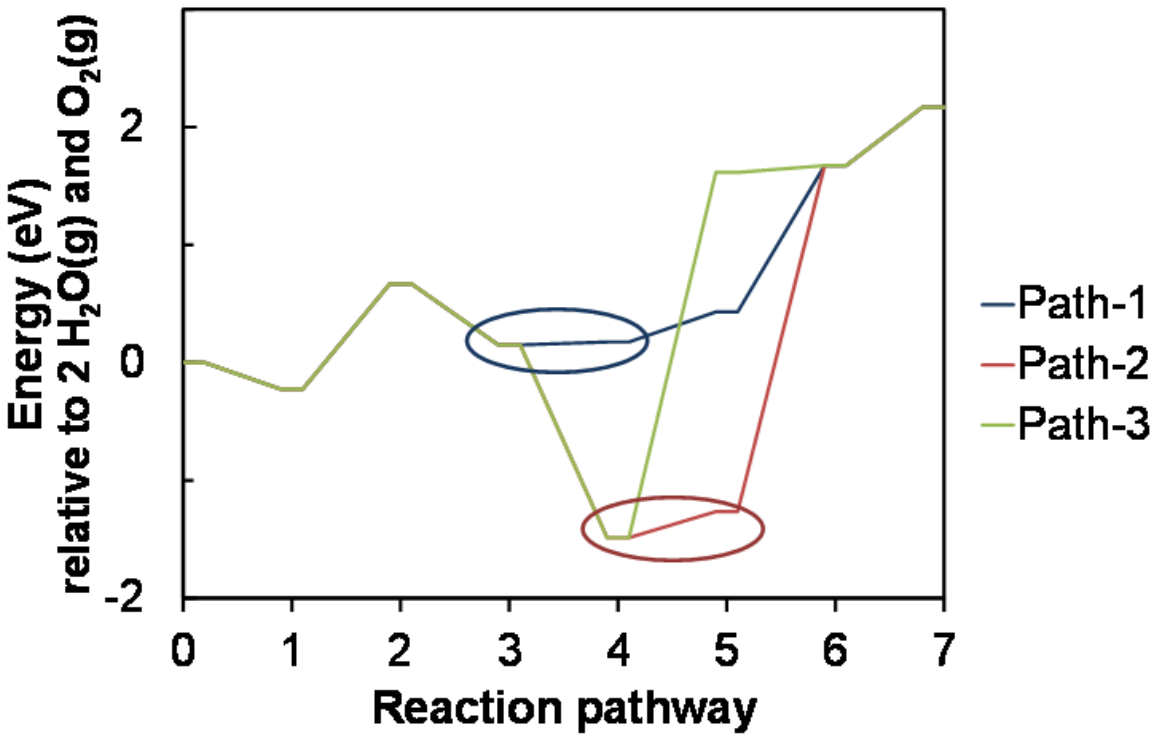

Figure 3.14: Potential energy profile representing reaction steps to form hydrogen peroxide, energies include zero point energy corrections

3.5.1 Activation energy estimates using BEP

In recent studies it has been shown that for dissociative chemisorption of a number of diatomic molecules the activation energy is linearly dependent on the reaction energy (Barteau, 1991). This observation is simply the Brønsted Evans Polanyi relation and has often been assumed to implicitly hold for surface reactions (Barteau, 1991). The BEP relation was used to calculate the activation energy for proposed reaction steps on the potential energy diagram. All the energy differences are in eV and they include zero point energy corrections.

$$\Delta E_a = \alpha\,(E_{products} - E_{reagents}) + \beta \text{ where } 0 < \alpha < 1 \qquad (3.5)$$

The constants investigated by Nørskov et al. (2002) on a flat closed packed surface for dissociation of various diatomic species are: α = 0.9 and β = 2.07. The constants were tested in this study to elucidate their validity for oxygen dissociative barrier.

Michaelides et al. (2003) investigated a number of classes of reactions and found the following BEP relations for different reaction types for dehydrogenation reactions (e.g. the reaction $H_2O^* \rightarrow H^* + OH^*$) the constants were α = 0.92 ± 0.05 and β = (0.87 ± 0.05) eV. For diatomic activation and hydrocarbon cracking (The reactions categorised in this class involve C-C bond cleavage in e.g. C_2H_4), Michaelidis et al. (2003) obtained α = 0.97 ± 0.05 and β = (1.69 ± 0.15) eV. The activation of triatomic species yielded α = 0.74± 0.05 and β =

(1.03± 0.08) eV (it should be noted that this class comprised typically of small triatomic species with a double bond such as CO_2).

For this study most of the reactions involve either dissociation or addition reactions. The activation energy for the addition reaction was determined using the assumption of microscopic reversibility which links the activation barrier for the addition reaction to the activation barrier of the reverse, dissociation step.

$$E_a^{addition} = E_a^{dissociation} + \Delta H \qquad (3.6)$$

where E_a is the activation barrier for the addition and the dissociation reaction respectively and ΔH is the enthalpy changes between the reactant and a product. The activation energies are summarised in Table 3.9.

The BEP relation can be used to calculate the activation energy for proposed reaction steps on the potential energy diagram. All the energy differences are in eV and they include zero point energy corrections. The highly endothermic reactions, viz. the formation of a surface OOH species via the addition of surface oxygen to a surface hydroxyl species, and the combination of two surface hydroxyl species yielding a surface HOOH species, have according to the BEP-relationship a high activation barrier.

Table 3.9: Calculated transition state energies (E_a) in eV using the BEP relation

Reaction step		α^a	β^a (eV)	ΔH (0K) (eV)	E_a (eV)
$H_2O^* + * \rightarrow OH^* + H^*$	(2)	0.92	0.87	0.45	1.29±0.05
$O_2^* + H^* \rightarrow OOH^*$	(4) – path-1	0.74[b] 0.92[c]	1.03[b] 0.87[c]	0.02	1.07 0.91
$O_2^* + * \rightarrow 2\ O^*$	(4) – path-2/3	0.9[d] 0.97	2.07[d] 1.69	-1.63	0.60 0.11
$H^* + OOH^* \rightarrow HOOH^* + *$	(5) –path 1 (6) – path 3	0.92	0.87	0.02	0.92±0.05
$O^* + H^* \rightarrow OH^* + *$	(5) –path 2	0.92	0.87	0.11	1.08±0.05
$O^* + OH^* \rightarrow OOH^* + *$	(5) –path 3	0.74	1.03	1.55	3.73±0.08
$OH^* + OH^* \rightarrow HOOH^* + *$	(6) – path 1/2	0.97	1.69	1.47	4.58±0.15

[a]Values given by Michaelidis et al. (2003), unless otherwise stated; [b]considering the reverse of the dissociation of a triatomic species; [c]considering the dehydrogenation of OOH; [d]data given by Nørskov et al. (2002)

Figure 3.15 shows the energy profile to generate hydrogen peroxide from $H_2O(g)$ and $O_2(g)$ during the oxygen reduction reaction in an alkaline fuel cell. This profile, which includes the estimated activation barriers according the BEP-relationship, shows that the formation of H_2O_2 is strongly endothermic, but also kinetically inhibited. Especially reaction path-1 and reaction path-2 are kinetically not favoured, since the recombination of two surface hydroxyl species yielding hydrogen peroxide has a high activation barrier of 4.6 eV according to the

BEP relationship (see Table 3.9), however path-1, already yield a hydrogen peroxide molecule (step-5) before the recombination of hydroxyl species. Therefore the most favourable reaction pathway for the formation of $H_2O_2(g)$ is reaction path-1. Assuming similar pre-exponential factors and ignoring differences in the concentration of the various species and only considering the activations energies, the H_2O_2 formation via path-1 is more faster than the formation via reaction path-2 or reaction path-3 according to BEP-relationship.

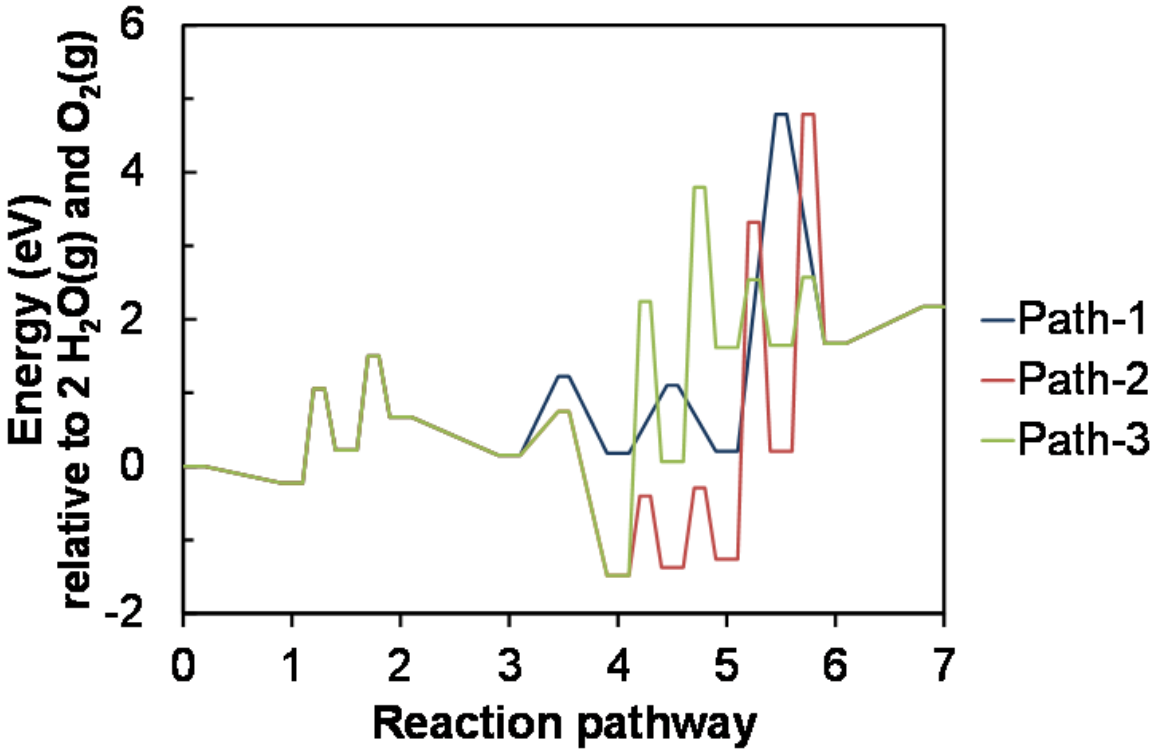

Figure 3.15: Combined potential energy profile illustrating reaction steps to form hydrogen peroxide on Pt(111)

The overall potential energy diagram (PES; Figure 3.15) further indicates that the formation of surface hydroxyl species is both thermodynamically and kinetically favoured, if the activation energy can be estimated using the BEP-relationship. It is further indicated that the surface hydroxyl species according to this analysis represent a rather deep-well in the formation of H_2O_2. It can thus be expected that the surface concentration of surface hydroxyl species will be large, unless the desorption of these species from the surface (as hydroxyl ions) is being accelerated.

3.6 Conclusions

The adsorption of separate species with the Pt(111) surface has been investigated using PAW-PBE functional on *VASP*. All the adsorption calculations were performed at 0.25ML coverage. The adsorption energies were compared to the experimental observations as well as earlier calculated values. The current adsorption energy comparison to the experimental values as well as the calculated values from earlier research is summarised in Table 3.10.

Table 3.10: Adsorption energies of various intermediates on Pt(111) in comparison to the experimental values and published calculated values, including zero point energy corrections: Note, the numbers in brackets are with respect to free gas radicals for the intermediates species(O,H,OH,OOH).

Species	Stable Adsorption Site	Source	Calculated Adsorption Energy(eV)	Experimental Adsorption Energy(eV)	Source	**Current Study E_{ads}(eV)**	**Stable Adsorption Site**
Atomic Hydrogen	3-fold-fcc	Michaelides et al. (2001)	-2.9	-2.75;-2.55	Christman et al. (1998)	**-1.79:½H_2(-2.62)**	**3-fold-fcc**
Atomic Oxygen	3-fold-fcc	Michaelides et al. (2001) Phatak et al. (2009)	-4.03; -1.3	-4.1;-3.5	Yeo et al. (1997) Markovic et al. (1999)	**-1.11: ½O_2(-4.07)**	**3-fold-fcc**
Oxygen	3-fold-fcc	Eichler et al. (1997)	-0.68	-0.38	Gland et al. (1980)	**-0.52**	**3-fold-fcc**
Water	on-Top site	Michaelides et al. (2001); Ford et al. (2010)	-0.34;-0.18	-0.65	Fisher et al. (1980)	**-0.12**	**on-Top 3-fold-hcp**
OH	Bridge	Ford et al. (2010)	-1.82	-2.5;-1.5	Mooney et al. (1993)	**-0.32(-2.09)**	**Bridge**
OOH	A Top site	Ford et al. (2010)	-0.96			**0.22(-1.04)**	**Bridge**
Hydrogen Peroxide	Bridge	Xiao Li et al. (2005) Ford et al. (2010)	-0.64;-0.29			**-0.21**	**Bridge**

The current DFT calculation (E_{ads}) results are in good agreement with the experimental values as well as the earlier calculated values, with an exception for adsorbed O_2 and H_2O. It was anticipated that the adsorption energies for the intermediates (O, H, OH, OOH) with respect to H_2O and O_2 gas will yield good estimate for the adsorption energies since the properties of the reference species ($H_2O(g)$,$O_2(g)$) are well described. However for this

study it was found that adsorption energies for intermediate species (O, H, OH, OOH) with respect to gas phase radicals gave a better description of adsorption energies comparing them to the experimental values. It is acknowledged that different reference species yield different adsorption energies, therefore explaining the discrepancies in the calculated results from both references.

The potential energy profiles showed that path-1 could potentially be the hydrogen peroxide forming path in oxygen reduction reaction. This is however based on the validity of the Brønsted-Evans-Polanyi relationship, i.e. a linear relationship between the activation barrier and the reaction energies. The limitation of using the Brønsted Evans Polanyi relation (BEP) to predict reaction activation energies is that it requires the knowledge of the type of transition state a reaction undergoes. Transition states are categorised as either being early, normal or late. This type of information for a specific reaction on specific metals is rarely available (in particular for association reactions) and hence some uncertainty exists on the actual activation energy when using BEP.

In the following chapters a full search for the transition states of the elementary surface reactions by applying the Nudged Elastic Band (NEB) method will be conducted.

3.7 References

Avery N.R., *Chemical Physics Letters* **96** (1983), 371–373

Barteau M.A., *Catalysis Letters* **8** (1991), 175–184

Christman K., Lipkowski J., Ross P.N., 'Electrocatalysis', Wiley, New York, 1998, p. 1

Damjanovic A., Brusic V., *Electrochimica Acta* **12** (1967), 615–628

Doering D.L., Madey T. E., *Surface Science* **123** (1982), 123, 305–337

Eberhardt W., Upton T., Cramm S., Incoccia L.,*Chemical Physics Letters* **146** (1988), 561–565

Eichler A., Hafner J., *Physical Review Letters* **79** (1997), 4481–4484

Feibelman P.J., Esch S., Michely T., *Physical Review Letters* **77** (1996), 2257–2260

Fisher G.B., Gland J.L., *Surface Science* **94** (1980), 446–445

Ford D.C, Nilekar A.U, Xu Y., Mavrikakis M., *Surface Science* **604**, 1565–1575

Fu Q., Yang J., Luo Y., *The Journal of Physical Chemistry C* **115** (2011), 6864–6869

Gland J.L., Sexton B. A., Fisher G.B., *Surface Science* **95** (1980), 587–602

Hannes Jónsson's group, 2010, UT Austin, viewed 16-07-2010<http://theory.cm.utexas.edu/vtsttools/neb/>

Kresse G., Furthmuller J., *Physical Review B* **54** (1996), 11169–11186

Kresse G., Joubert J., *Physical Review B* **59** (1999), 1758–1775

Li X., Heryadi D., Gewirth A.A., *Langmuir* **21** (2005), 9251–9259

Markovic N.M., Schmidt T.J., Grgur B.N., Gasteiger H.A., Behm R.J., Ross P.N., *The Journal of Physical Chemistry B* **103**(1999), 8568–8577

Michaelides A., Hu P., *Journal of the American Chemical Society* **123** (2001), 4235–4242.

Michaelides A., Ranea V.A., de Andres P.L., King D.A., *Physical Review Letters* **90**(2003), 216102–216106

Michaelides A., Liu Z.P., Zhang C.J., Alavi A., King D.A., Hu P., *Journal of the American. Chemical Society* **125** (2003), 3704–3705

Mooney C.E., Anderson L.C., LunsfordJ.H., *The Journal of Physical Chemistry* **97**(1993), 2505–2506

Nieminen J.A., Paavilainen S., *Surface Science* **405** (1998), 573–579

Nørskov J.K., Bligaard T., Logadottir A., Bahn S., Hansen L.B., Bollinger M., Bengaard H.,Hammer B., Sljivancanin Z., Mavrikakis M., Xu Y., Dahl S., Jacobsen C.J.H., *Journal of Catalysis* **209** (2002), 275–278

Nørskov J.K., Rossmeis J., Logadottir A., Lindqvist L., *The Journal of Physical Chemistry B* **108** (2004), 17886–17892

Ogasawara H., Brena B., Nordlund D., Nyberg M., Pelmenschikov A., Pettersson L.G.M., Nilsson A., *Physical Review Letter* **89** (2002), 276102–276103

Papoian G., Nørskov J.K., Hoffmann R., *Journal of the American of Chemical Society* **122** (2000), 4129–4144

Perdew J.P., Burke K., Ernzerhof M., *Physical Review Letters* **77** (1996), 3865–3868

Puglia C., Nilsson A., Hernnäs B., Karis O., Bennich P., Martensson N., *Surface Science* **342** (1995), 119–133.

Peierls R.E, Quantum Theory of Solids, Clarendon Press Oxford (2001)

Sandler S.I., 'Chemical Engineering Thermodynamics', John Wiley & Sons (1999)

Steininger H., Lehwald S., Ihbach H., *Surface Science* **17** (1982), 342

Stipe B.C., *Current Opinion in Solid State and Materials Science* **4** (1999), 421–428

Thiel P. A., Madey T.E., *Surface Science Reports* **7** (1987), 211–385

Wilson E.B., Decius J.C., Cross P.C., 'Molecular Vibrations', Dover: New York (1955).

Wurth W., Stöhr J., Feulner P., Pan X., Bauchspiess K.R., Baba Y., Hudel E., Rocker G., Menzel D., *Physical Review Letters* **65** (1990), 2426–2429

Yeager E., Razaq M., Gervasio D., Razak A., Tryk A.D., 'Proceedings of workshop on structural effects in electrocatalysis and oxygen electrochemistry'Electrochemical Society: Pennington, NJ, 1992, pp 440–473

Yeo Y.Y., Vattuone L., King D.A., *The Journal of Chemical Physics* **106** (1997), 392–401

Chapter 4

4 CO-ADSORPTION MODELS

Prior to calculating reaction pathways, co-adsorbed states for reactants in the case of addition reactions and products in the case of dissociation reactions, have to be studied. This is important in contributing to the knowledge of species interactions when brought together to a higher coverage (0.5ML) within the chosen reaction boundaries (unit cell size:p(2×2)). The results for the co-adsorbed state aid towards finding an energy pathway from reactant to product further more enhance in finding the transition state for the elementary steps. This section only considered the co-adsorbed states that represent a pre-curser towards forming a stable product identified from the previous section.

4.1 Computational method

The non-spin polarised quantum chemical calculation in this section were performed using the *VASP* code (Kresse et al., 1996), with the PBE functional (Perdew et al., 1996) following the PAW method (Kresse et al., 1999). The Methfessel-Paxton smearing scheme was adopted with a width of 0.2 eV.

A six layer slab was used to represent the Pt(111) surface with an optimised 12 Å vacuum space. The unit cell size was represented by a p(2×2) periodic supercell with the top two layers free to relax and the rest fixed to represent the bulk interatomic distances. The k-points sampling mesh of 6×6×1and cut-off energy of 400 eV were used. Co-adsorption was performed at 0.5ML coverage on one side of the slab. Corrections for the dipole moment on the energy perpendicular to the surface were incorporated (by setting the IDIPOL tag to 3 in the *VASP* computational code).

The interaction energy was calculated from the following expression:

$$E_{int} = E_{slab+co\text{-}ads\text{-}ij} + E_{slab} - E_i - E_j \quad (4.1)$$

Where $E_{slab+co\text{-}ads\text{-}ij}$is the energy of the co-adsorbed species (at a coverage of 0.5ML) on the Pt(111) surface, E_{slab}, is the energy of the clean slab, E_i and E_j is the energy of the individual species i and j adsorbed on Pt(111) at a coverage of 0.25ML.

The charge analysis was performed using the Bader analysis (Henkelman et al., 2006; Sanville et al., 2007). The charge analysis is used to gain some understanding on the lateral interaction between the co-adsorbed species. The Bader method assigns a charge based on electron density within a volume partition according to the minimum points in the electron

density distribution. The Bader analysis is useful in assigning the charge to atoms and most importantly allowing the determination of the charge distribution in systems. The original charge for each species in the gas phase was first calculated and the difference in the charge when the species is adsorbed on the surface indicated a charge gain or charge loss relative to the original gas phase charge.

The electrostatic forces acting between the co-adsorbed species was calculated by the following expression:

$$F_{electro-static} = \frac{1}{4\pi \cdot \varepsilon_0} \cdot \frac{q_1 \cdot q_2}{(r_1 - r_2)^2} \quad (4.2)$$

$$W = F_{electro-static} \cdot d \quad (4.3)$$

where ε_0 permittivity constant ($8.854 \cdot 10^{-12}$ $C^2/N \cdot m^2$), q_i is the charge of species in Coulomb, r_1–r_2 is the distance between the charged species, W, is the work done to move the charged species, and d is the shortest distance travelled by the atom to form the bond.

4.2 Co-adsorption of OH* and H* on Pt(111)

The study of co-adsorbed OH* and H* on Pt(111) is important since it forms part of the proposed first initiation step in oxygen reduction reaction in alkaline fuels cells. Co-adsorbed OH* and H* is proposed to form upon dissociation of water. The rationale in studying the stable co-adsorbed state is to start by co-adsorbed OH* and H* in their individual favourable sites, OH*(bridge) and H*(fcc 3-fold hollow). However this did not yield a local minimum as shown by the imaginary frequencies from the vibrational analysis. A stable co-adsorbed state was found at OH* and H* at the nearest-neighbour on-top sites (see Figure 4.1). This was confirmed by the vibrational analysis. This configuration is consistent with the DFT study using *VASP* by Phatak et al. (2009) where they also calculated the most stable co-adsorbed state (H*+OH*) to be within the nearest-neighbour on-top site for both OH* and H*.

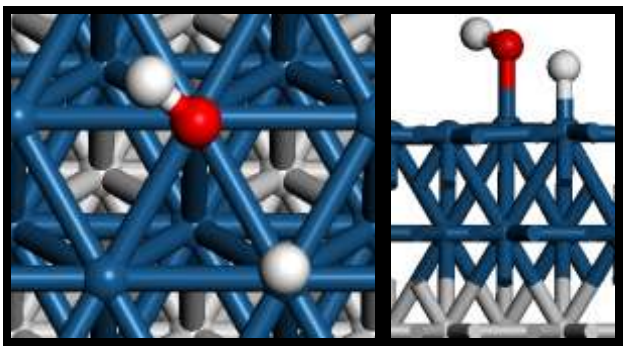

Figure 4.1: Top and side view for co-adsorbed OH* and H* on a p(2×2) unit cell on Pt(111) surface; $d_{H^*-OH^*}$ = 2.64 Å; d_{H^*-Pt} = 1.56 Å; d_{HO^*-Pt} = 2 Å

The interaction energy between the species is 0.16 eV, indicating some repulsion interaction between the adsorbed species. The Bader analysis also showed a low charge transfer to the co-adsorbed species with the charge gain on H at the top site of 0.21 electrons and on atomic O in adsorbed OH a charge gain of 0.22 electrons with respect to their charge as a gas phase radical. The charge gained on the species is from the top layer of platinum atoms, the subsurface (2^{nd}-layer) gained some charge from the bottom platinum atoms as well as some charge from the top layer since the overall charge lost by the top platinum layer is 0.61 electrons and the adsorbate species only gained a total of 0.43 electrons. There is no charge assigned to H bonded to O. This is not a surprise since the H atom is pointing away from the surface plane, indicating little or no interaction with the surface and hence no charges transfer. The repulsive electrostatic force acting along a straight line between the two adsorbed charged species is 3.78×10^{-10} N (~0.39 eV, assuming a force applied on the distance travelled between the reactive species), an indication of a low energy cost to bring the species together to a 0.5ML coverage. The repulsive energy due to electro-static interaction is larger than calculated repulsion for the co-adsorbed state of 0.15 eV, which is likely to be due to the attractive electro-static interaction between the surface and the adsorbed species.

4.3 Co-adsorption state for O*+H* on Pt(111)

During the oxygen reduction reaction on alkaline fuel cells water and oxygen react to form hydroxyls on the catalyst surface (Barbir, 2005). The formation of surface hydroxyl species (OH) requires interaction between atomic hydrogen and oxygen on the surface. These species ultimately desorbs to form hydroxide ions in the alkaline fuel cell. To study this interaction a co-adsorbed state of atomic hydrogen and oxygen at a higher coverage is essential. Figure 4.2 illustrates the co-adsorbed state with hydrogen (H) on the on-top site and oxygen (O) on the hcp 3-fold hollow site. The configuration was confirmed to be a minimum on the potential energy surface by the vibrational analysis. Michaelides et al. (2001) also reported on their DFT study that atomic H will prefer the on-top site when co-adsorbed with atomic O.

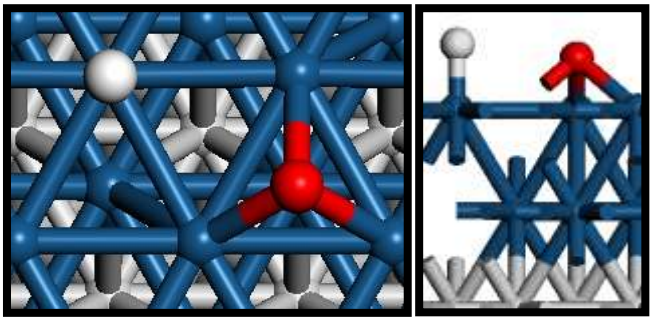

Figure 4.2: Top and side view for O*+H* co-adsorbed on a p(2×2) unit cell on Pt(111) surface; $d_{O^*-H^*}$ = 3.20 Å;d_{H^*-Pt} = 1.56 Å; d_{O-Pt}=~2.00 Å; electrostatic force : 6.69×10^{-10} N

The repulsive interaction energy between the species is 0.61 eV. The repulsion between co-adsorbed H and O is relatively high. The large value can be explained by the high overall charge transfer from the metal to the adsorbate with a charge gain on H of 0.29 electrons and 0.49 electrons on O. The repulsive electrostatic force acting on a straight line between the species is $6.69\cdot10^{-10}$ N (~0.93 eV assuming a force applied on the distance travelled between the reactive species). This is a possible indication that the OH bond formation may require high activation barrier from this configuration.

4.4 Co-adsorption of molecular O^*_2 and H* on Pt(111)

One of the proposed reaction pathways to form a surface OOH-species is via hydrogenation of O_2 (path-1). Hence, the co-adsorbed state of molecular oxygen and hydrogen on Pt(111) has to be investigated at the 0.5ML coverage with respect to adsorbed molecular O_2 plus H. The geometry for the co-adsorbed state is similar to the geometries obtained for the individual species at a coverage of 0.25ML with H being stable in all the high symmetry sites and O_2 being stable at the fcc 3-fold hollow site. Figure 4.3 illustrates the stable co-adsorbed state, which was confirmed by the vibrational analysis.

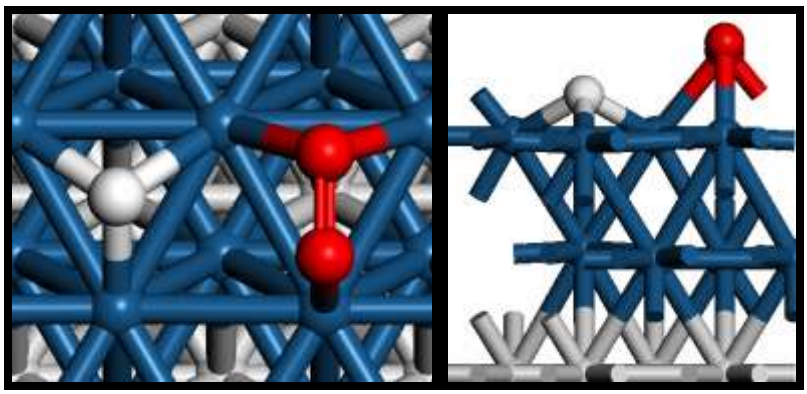

Figure 4.3: Top and side view for co-adsorbed O_2* and H* on a p(2×2) unit cell on Pt(111) surface; $d_{O^*-H^*}$ = 3.20 Å;d_{Pt-H^*}:1.9 Å; d_{Pt-O^*} = 2.00 Å

Upon co-adsorption with H the O-O bond length is slightly reduced to 1.38Å, compared to the O-O bond length of 1.40 Å for O^*_2 adsorbed on Pt(111) at a coverage of 0.25ML. This is as possible indication that hydrogen co-adsorption will stabilizes the O-O bond in adsorbed O_2, this is also confirmed by the higher vibrational frequency of 849 cm^{-1} for the O-O bond (827 cm^{-1} for O-O at 0.25ML). The repulsive interaction energy between the species is 0.30 eV. The interaction energy is relatively low. This could be explained by the low net-charge distribution between the metal and the adsorbates. The charge gained on H* is 0.12 electrons and an average net charge gain of 0.27 electrons on both oxygen atoms. The charge gained by the adsorbates originates from is from the top surface platinum atoms, with the overall charge loss of 0.54 electrons by the three adjacent platinum atoms to the oxygen and a total loss by the top surface of 0.87 electrons, meaning that some of the charge from the top platinum layer is transferred to the second subsurface layer. The repulsive electrostatic force acting between the charged species is 4.26×10^{-10} N (~0.53 eV, assuming a force applied on the distance travelled between the reactive species). This is an indication of a low energy cost to bring these two species together at a higher coverage (local) of 0.5ML.

4.5 Co-adsorption state for O* at a coverage of 0.5ML on Pt(111)

In this study it has been proposed that oxygen may adsorb and dissociate on a platinum surface. For the dissociative pathway to occur within the current reaction boundary conditions (unit cell size) a co-adsorbed state for 0.5ML atomic oxygen is essential since it represents the products of the dissociated oxygen. There are various configurations for co-adsorbed oxygen atoms possible (see Figure 4.4). These co-adsorbed states must have originated from the dissociation of an adsorbed molecular oxygen species.

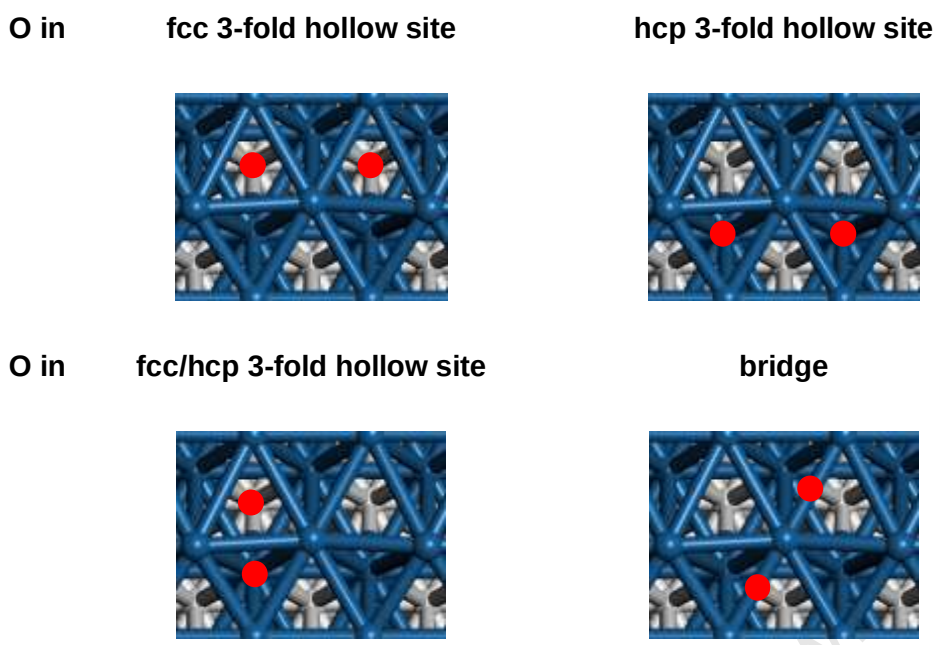

Figure 4.4: Top view for possible symmetrical adsorption of atomic O* at a coverage of 0.5ML on various high symmetry sites on a p(2×2) unit cell on Pt(111) surface

The co-adsorbed state that is represented by atomic O* in two fcc 3-fold hollow sites, would require adsorbed molecular oxygen to be on a bridge to bridge configuration over the hcp 3-fold hollow site. Adsorbed molecular oxygen is unstable in this geometry. Similarly for the atomic O* at 0.5ML in the two hcp 3-fold hollow sites. The originating molecular oxygen species must be configured on the bridge to bridge site over the fcc 3-fold hollow site. This is not stable, with the final oxygen molecule configured on the fcc site (see Appendix B). The O atoms on the two bridge sites are not stable as well with the final configuration of the two atomic oxygen on the neighbouring fcc 3-fold hollow sites (see Figure 4.5).

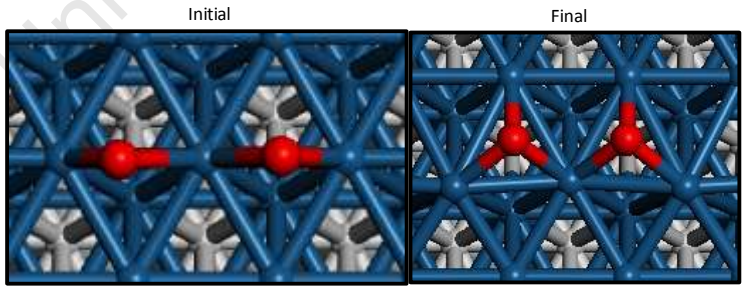

Figure 4.5: Top view for the adsorption of atomic O at 0.50 ML on a p(2×2) unit cell on Pt(111) surface starting with O on the bridge site (left) and a final configuration with atomic O on the fcc 3-fold hollow site (right)

In Figure 4.6 the co-adsorbed state for atomic oxygen is shown, where one of the atomic oxygen is located on the hcp 3-fold hollow site and the other oxygen on the fcc 3-fold site. This unique configuration is chosen to try and elucidate the dissociative behaviour of O_2 on

the most stable fcc 3-fold hollow site laying parallel to surface plane. This configuration was found to be at a minimum on the potential energy surface confirmed by the vibrational analysis.

The experimental work done by (Gland et al., 1980; Steininger et al., 1982; Materer et al., 1995), observed that above 120K oxygen dissociates to form an ordered (2×2) structures with a 0.25ML coverage where the oxygen atom (O) occupy the fcc 3-fold hollow sites. In this study the high coverage (0.5ML) of O* was investigated and calculated to have the repulsive interaction between the species of 1.21 eV, an indication of a high degree of interaction at this coverage. This is accompanied by a high charge transfer from the surface to the atomic O* with an average charge gained by the O* species of 0.75 electrons. The top surface donated 1.7 electrons to the adsorbates and the bottom subsurface. The repulsive electrostatic force acting on the two species is relatively high at 8.58×10^{-10}N (~6.59 eV), an indication of a high activation barrier required to bring the two species to form a bond.

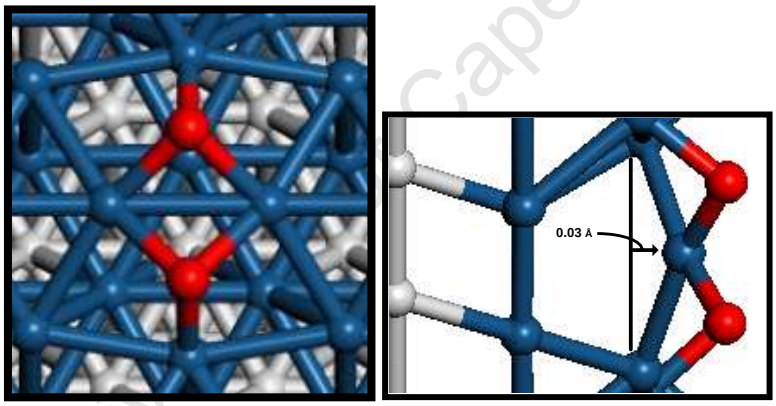

Figure 4.6: Top and rotated side view for the adsorption of atomic O* on a p(2×2) unit cell on Pt(111) surface; $d_{O^*-O^*}$ = 2.63 Å

The substrate structure has evolved during the atomic oxygen insertion on the hollow sites at 0.5ML coverage, as apparent in Figure 4.6, with a shift of some platinum atoms by ~ 0.01 Å, this phenomenon has also been observed in the DFT study by Legare (2005) on a Pt(111) surface, where they observed a geometrical evolution which they called surface plane roughening. Furthermore the origin of this strong roughening effect was explained by the formation of O chains in the $[0\,\bar{1}\,1]$ direction. The net result of this 'surface roughening' is the increased space in the tetrahedral subsurface site which is available to accommodate another O atom (Legare, 2005).

4.6 Co-adsorption state for OOH*+H* on Pt(111)

One route for the formation of a surface HOOH*-species is via the hydrogenation of the surface OOH*-species (path-1 and path-3). Hence, the peroxide intermediate (OOH*) and hydrogen(H) have to be co-adsorbed prior to the addition reaction. Their interaction was studied within the p(2×2) unit cell size to form a 0.5ML coverage, with respect to OOH* plus H. Figure 4.7 illustrates the mixed state with the hydrogen on the on-top site and the peroxide (OOH*) tilted over the fcc 3-fold hollow site with one of the oxygen pointing towards a neighbouring on-top site.

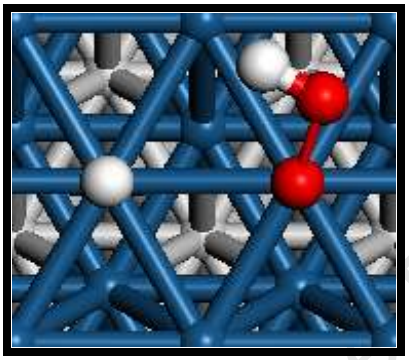

Figure 4.7: Top view for H*+OOH* co-adsorbed on a p(2×2) unit cell on Pt(111) surface; $d_{H^*-OOH^*}$ = 2.83 Å, $d_{O^*-O^*}$ = 1.42Å; $d_{O^*-H^*}$ = 0.99 Å; d_{H^*-Pt} = 1.56 Å; d_{O^*-Pt} = 2.02 Å

The OOH species when studied individually (0.25ML) was found to be stable at the bridge site with respect to the O—O atoms. Similar configuration was also found when co-adsorbed with atomic H with the repulsive interaction energy between the species of 0.2 eV. The O-O bond is reduced slightly by 0.01 Å compared to the 1.43 Å for OOH* studied at a coverage of a 0.25ML. The reduced bond length resulted in a higher O-O bond vibrational frequency of 864 cm^{-1} (ν_{O-O}: at 0.25ML-OOH*:843cm^{-1}). The charge analysis on the co-adsorbed species showed a charge gain of 0.09 electrons on the on-top H and 0.18 electrons on the atomic O* in OOH* bonded to the surface at the top site. The charge is donated from the top surface with an overall charge loss of 0.55 electrons, however the platinum atom at the centre of the unit cell closest to the H* on OOH* showing a minimal change in the number of electrons (gain of 0.0034 electrons was observed). The OOH* molecule is bent away from the surface plane and as expected a smaller charge gain of 0.1 electrons on the second O and a zero charge assigned to the hydrogen facing away from the surface plane. The repulsive electrostatic force acting on the charged species is 1.6×10^{-10} N (~0.18 eV, assuming a force applied on the distance travelled between the reactive species) this is be an indication of low energy cost to bring these two charged species.

4.7 Co-adsorption state for OH*+O* on Pt(111)

Another reaction pathway to form the peroxide intermediate (OOH*) is via the addition of atomic oxygen (O*) to a hydroxyl (OH*) on the catalyst surface (path-3). If this reaction step is feasible under the current unit cell boundaries, the study of co-adsorbed state existence of (OH*+O*) on 0.5ML coverage, with respect to OH* plus atomic O*, is essential. Figure 4.8 illustrates the co-adsorbed state and note that the unique chosen state represents reactants to form OOH* on the bridge site. The results were confirmed by the vibrational analysis and it was found that the configuration is at a minimum potential energy surface.

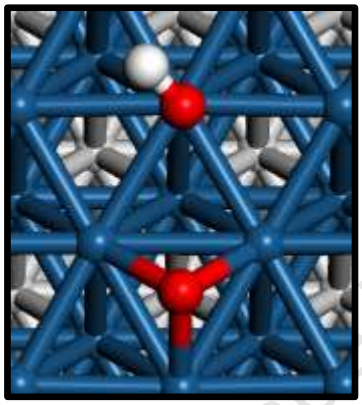

Figure 4.8: Top view for co-adsorbed O* and OH* on a p(2×2) unit cell on Pt(111) surface; $d_{O^*-OH^*}$ = 3.54 Å; d_{O-Pt} = ~2.00 Å; d_{HO^*-Pt} = 1.99 Å; electrostatic force: 8.85×10^{-10} N

The adsorption study for atomic oxygen showed that the fcc 3-fold hollow site is the more energetically favoured site. When co-adsorbed with OH* a similar site was calculated (see Figure 4.8) with the interaction energy between the species of 0.06 eV. The charge distribution on both oxygen atoms (O) is relatively high with a 0.4 electrons charge gain on O* with H*, 0.62 charge gain on atomic O and a zero charge assigned to the hydrogen. The overall charge loss by the top surface is 1.17 electrons, some of the charge is transferred to the adsorbate and the other to the subsurface layer. The repulsive electrostatic force acting between the charged species is 8.85×10^{-10}N (~1.41 eV, assuming a force applied on the distance travelled between the reactive species). It is clear that the electro-static repulsion between the two adsorbed species is compensated (partially due to the electro-static interaction with the surface) resulting in a relatively low co-adsorption energy.

4.8 Co-adsorption state for OH* and OH* on Pt(111)

One of the proposed mechanisms for hydrogen peroxides formation in fuel cells is via the coupling of two surface hydroxyl species (OH*+OH*→HOOH*, path-1 and path-2). This pathways requires the existence of a co-adsorbed state on a high coverage of 0.5ML. Two co-adsorbed states were found. Both configurations were to be at a minimal on the potential energy surface by the vibrational analysis.

The surface hydroxyls in the co-adsorbed state represented by Figure 4.9 are stabilised with an interaction energy of -0.18 eV. The attractive potential is an indication of the effect of hydrogen bonding between these two species. It should be noted that this configuration is a potential pre-curser towards the formation of water. The hydrogen atom facing the O atom stabilizes the interaction between the two species hence an attractive force between the two species. The charge distribution is also relatively high at an average value of 0.39 electrons for the O atoms and a zero charge assigned to the H. The electrostatic force acting on the charged species is slightly high ($1.16 \cdot 10^{-9}$ N~ 1.24 eV). The electrostatic force is due to the 0.39 electrons for both charged species.

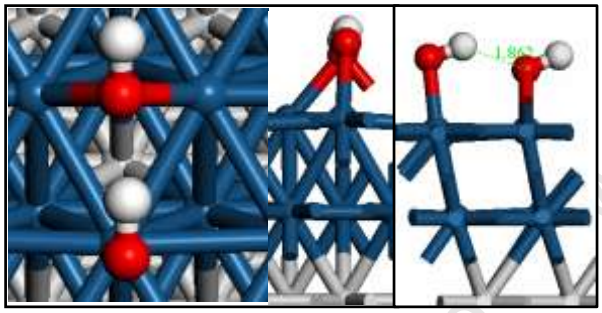

Figure 4.9: Top and side view for co-adsorption of OH on a p(2×2) unit cell on Pt(111)surface (d_{O-O} = 2.70 Å;$d_{Pt(top)-OH}$= 2 Å; $d_{Pt(bridge)-OH}$ = 2.18 Å; hydrogen bonding between two OH species:1.86 Å)

The second, stable state for surface hydroxyl groups at a coverage of 0.50ML is shown in Figure 4.10. This state does not have hydrogen-bonding between adsorbed hydroxyl groups and is therefore slightly repulsive with interaction energy of 0.10 eV (repulsive). The charge gain on the bridge O atom in OH is 0.4 electrons and the charge gain for the on-top O in OH is 0.3 electrons with respect to a gas phase hydroxyl radical. The atomic hydrogen does not gain any charge. The repulsive electrostatic force acting between the species is $1.04 \cdot 10^{-9}$N (~1.11eV).

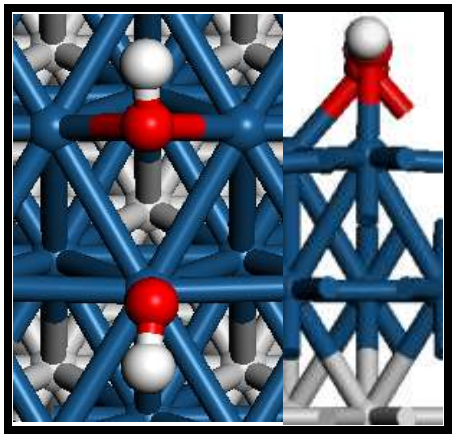

Figure 4.10: Top and side view for OH*+OH* co-adsorbed state on a p(2×2) unit cell on Pt(111) surface with hydrogen atom facing away from the oxygen atoms (d_{O-O}: 2.70 Å)

4.9 Co-adsorption state for H_2O^* and O* on Pt(111)

The co-adsorbed state of H_2O^* and O*, may potentially occur in alkaline fuel cells, and may provide an alternative route for the dissociation of adsorbed water. This will assist to form hydroxyls (OH). This step will however only be favoured, if atomic oxygen is available on the surface.

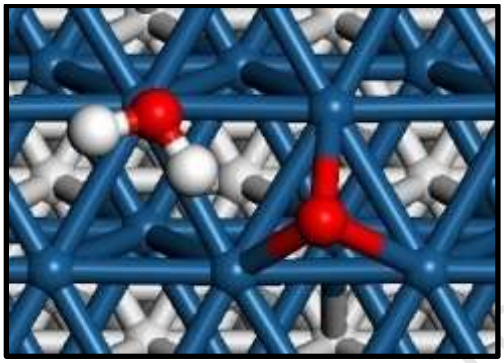

Figure 4.11: Co-adsorbed state H_2O^* +O* on a p(2×2) unit cell on Pt(111) surface; $d_{O^*-H^*}$ = 1.54 Å

The co-adsorbed state for H_2O^* plus O* was investigated and found to be repulsive and have an interaction energy of 0.38 eV. The co-adsorbed atomic oxygen gained a charge of 0.64 electrons and on the oxygen in the water molecule gained a charge of 0.075 electrons. The resultant repulsive electrostatic force is relatively high due to the high charge transfer, the force is 3.56×10^{-9} N (~1.25 eV, assuming a force applied on the distance travelled between the reactive species). The latter is indications that that this reaction step will not occur at ease, hence a high activation barrier is anticipated.

4.10 Conclusions

The co-adsorbed states at 0.5ML coverage was investigated to elucidate the nature of species interaction to assist in the NEB calculations. The study only considered the co-adsorbed state possibilities towards forming the desired most stable configuration identified in Chapter-3. The reasons for the unique co-adsorbed states studied on this section will be apparent in the next chapter. Table 4.1 is a summary of the calculation results in Chapter 4.

Strong repulsion is obtained for the interaction between adsorbed atomic oxygen species, and co-adsorbed atomic oxygen and atomic hydrogen. This implies that upon oxygen dissociation there is a thermodynamic driving force to separate the atomic oxygen species. Furthermore, the high interaction energy between atomic oxygen and atomic hydrogen implies that the formation of surface hydroxyl species may become kinetically hindered.

Table 4.1: Summary table for co-adsorbed species

Co-adsorbed State	Interaction Energy(eV)	Electrostatic Force (N)	Reactant or Product	BEP-Ea (eV)
H*+OH*	0.16	3.78E-10	←H_2O*	1.29
H*+O_2*	0.26	4.26E-10	→OOH*	1.07
H*+OOH*	0.23	1.60E-10	→HOOH*	0.92
O*+OH*	0.06	8.85E-10	→OOH*	3.73
O*+H*	0.61	6.69E-10	→OH*	1.08
OH*+OH*-1	-0.18	1.16E-09	→HOOH*	1.60
OH*+OH*-2	0.10	1.04E-09	→HOOH*	1.58
O*+O*	1.21	8.58E-09	←O_2*	0.60
H_2O*+O*	0.38	3.56E-09	→2OH	1.61

Arrows in the table indicate the direction of the desired reaction

The BEP estimations are in agreement with the predictions on this section for most of the reactions, as underlined on Table 4.1. The high electrostatic forces calculated for most reactions, showed relative high activation barriers. The dissociation of water has a low electrostatic force, however the BEP predicted a high activation barrier, an indication that the BEP model may not apply for this reaction, however it will be validated in the next section. The gaps that exist in the BEP's model predictions will be cleared in the next chapter, with an accurate method of calculating activation energies (Nudged Elastic Band method).

Figure 4.12 shows the potential energy surface for the formation of hydrogen peroxide in the gas phase from water and oxygen in the gas phase for the reaction pathways postulated in Chapter 3 including the interaction energies and excluding the activation energies.

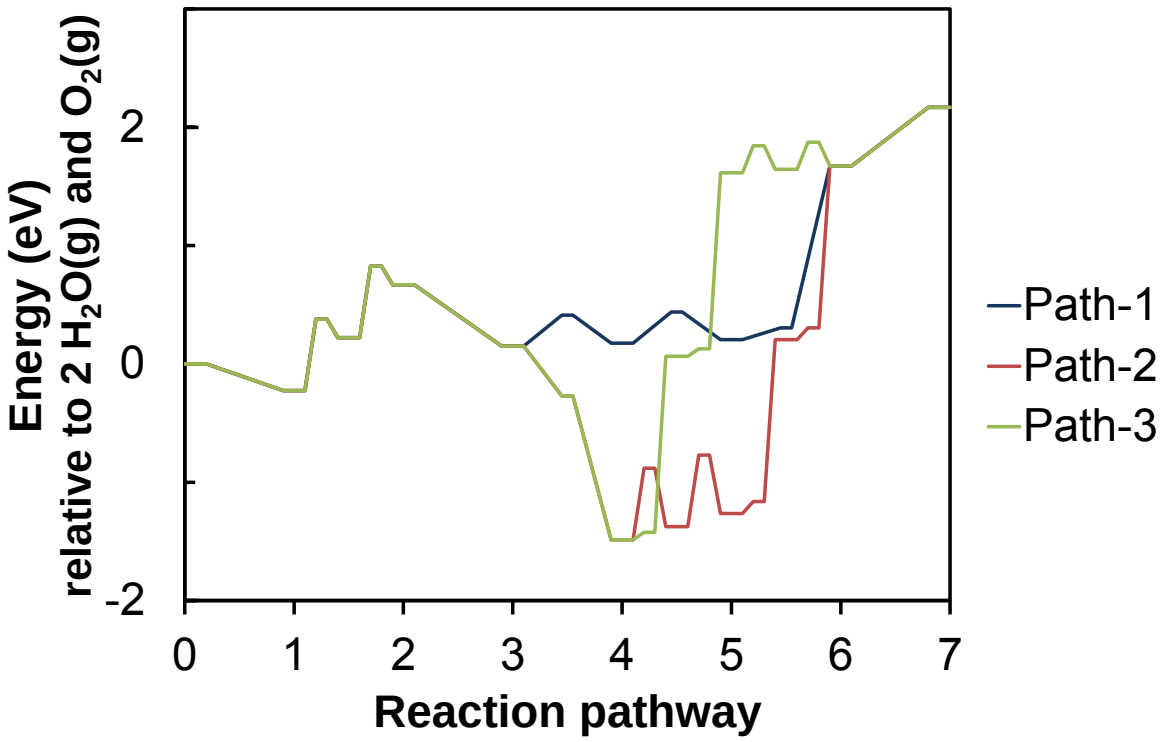

Figure 4.12: **Potential energy surface for the formation of H_2O_2(g) from H_2O(g) and O_2(g) on Pt(111) including the zero point energy contribution and the interaction energies**

4.11 References

Barbir F., 'PEM Fuels Cells', Elsevier Academic Press (2005)

Damjanovic A., Brusic V., *Electrochimica Acta* **12** (1967), 615–628

Ford D.C., Nilekar A.U., Xu Y., Mavrikakis M., *Surface Science* **604** (2010), 1565–1575

Gland J.L., Sexton B.A., Fisher G.B., *Surface Science* **95** (1980), 587–602

Henkelman G., Arnaldsson A., Jonsson H., *Computational Materials Science* **36** (2006), 254–360

Kresse G., Furthmuller J., *Physical Review B* **54** (1996), 11169–11186

Kresse G., Joubert J., *Physical Review B* **59** (1999), 1758–1775

Legare P., *Surface Science* **580** (2005), 137–144

Materer N., Starke U., Barbieri A., Doll R., Heinz K., Van Hove M.A., Somorjai G.A., *Surface Science* **325** (1995), 207–222

Michaelides A., Hu P., *Journal of the American Chemical Society* **123** (2001), 4235–4242

Perdew J.P.,Burke K., Ernzerhof M., *Physical Review Letters* **77** (1996), 3865–3868

Phatak A.A., Delgass W.N., Ribeiro F.H., Schneider W.F., *The Journal of Physical Chemistry C* **113** (2009), 7269–7276

Sanville E., Kenny S.D., Smith R., Henkelman H., *Journal of Computational Chemistry* **28** (2007), 899–908

Steininger H., Lehwald S., Ibach H., *Surface Science* **123** (1982), 1–17

Yeager E., Razaq M., Gervasio D., Razak A., Tryk A.D., 'Proceedings of workshop on structural effects in electrocatalysis and oxygen electrochemistry' Electrochemical Society: Pennington, NJ, pp 440–473 (1992)

Chapter 5

5 TRANSITION STATES

The nudged elastic band method (NEB) method was used to accurately calculate the activation energies for the proposed reaction steps for the possible paths to form H_2O_2 in fuel cells.

A summary of the three proposed pathways to form hydrogen peroxides in fuel cells is shown in Figure 5.1.

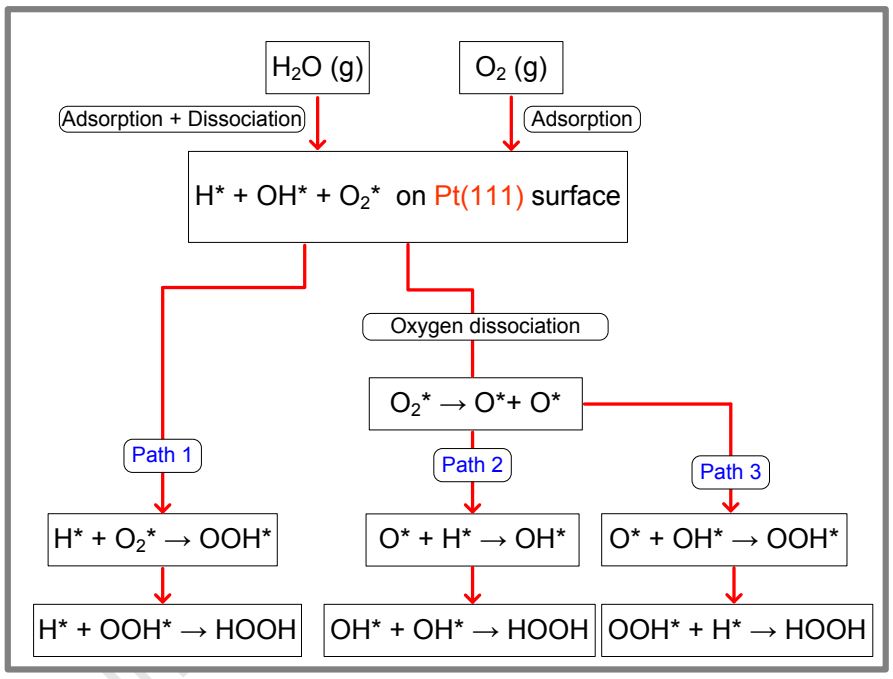

Figure 5.1: Proposed reaction pathways for forming hydrogen peroxides in fuel cells (*notation represents adsorbates on the surface)

5.1 Computational method

The nudged elastic band method (NEB) is an efficient way for finding the minimum energy path between a given initial and final state of a transition (Jonsson et al., 1998; Mills et al., 1994 and1995). The NEB method finds minimum energy paths between known reactants and products. The minimum energy path holds the highest statistical weight on identifying the saddle points, therefore one needs to get a good enough estimate of the shape of the minimum energy path (Henkelman et al., 2000). The NEB method requires the initial and final state and optimises a number of intermediate images along a reaction path. The selected and optimized images find the lowest energy possible through the algorithm, while

maintaining equal spacing to neighbouring images. To maintain the lowest energy for each image the technique works by minimizing the force projected on each image perpendicular to the path, hence finding the minimum energy path (MEP). This only allows a stationary energy for a perpendicular degree of freedom (Henkelman et al., 2000), hence ensuring a minimum interference to the distribution of images along the minimum energy path.

The non-spin polarised NEB calculations were performed using the optimised computational set up. The *VASP* computational code (Kresse et al., 1996) was used with projected augmented wave (PAW) (Kresse et al., 1999) pseudo-potential and the PBE functional (Perdew et al., 1996). The Methfessel-Paxton smearing scheme was used for the surface calculations with a smearing width of 0.2 eV.

A six layer slab was used with the two top layers allowed to relax and the rest fixed at the bulk optimised interatomic distances. The optimised vacuum gap was calculated at 12 Å and a p(2×2) unit cell size was used. Adsorption was performed on one side of the slab however energy corrections for the dipole moment perpendicular to the surface were incorporated as implemented in the *VASP* computational code(by setting the IDIPOL tag to 3). The k-point mesh was set at 6×6×1 and the cut-off at 400 eV. The first approximation of the few highest identified points on the potential energy path were further refined with a convergence criteria for forces (acting on the saddle point) of less than 0.03 eV/Å. To verify for the identified transition state (saddle point), the quasi-Newton BFGS algorithm (to relax the ions) and vibrational analysis were calculated on the image representing the saddle point (Bonnans et al., 1997). At a saddle point the direction of the reaction coordinate is given by the normal mode eigenvector corresponding to the negative curvature (Henkelman et al., 2000), hence a single imaginary frequency in the direction of the reaction co-ordinate is expected in the vibrational analysis for the saddle point.

5.2 Water dissociation

During oxygen reduction at the cathode of the alkaline fuel cell adsorbed water (H_2O*) and molecular oxygen (O_2*) react to form surface hydroxyl species (OH*). The reaction is catalysed by platinum. It is proposed in this study and earlier literature that water dissociates on the platinum surface to form hydrogen (H*) and hydroxyls (OH*). This step is proposed to form part of the key initiation steps for the oxygen reduction reaction in alkaline fuel cells.

The dissociation of adsorbed water is visualized as the stretching of one of the O-H bonds. A transition state is passed and atomic hydrogen and a surface hydroxyl group will be formed in a co-adsorbed state. The last step of the process is the separation of the co-

adsorbed species to separate species. This study only considered the reaction steps illustrated by most stable configuration given in Figure 5.2.

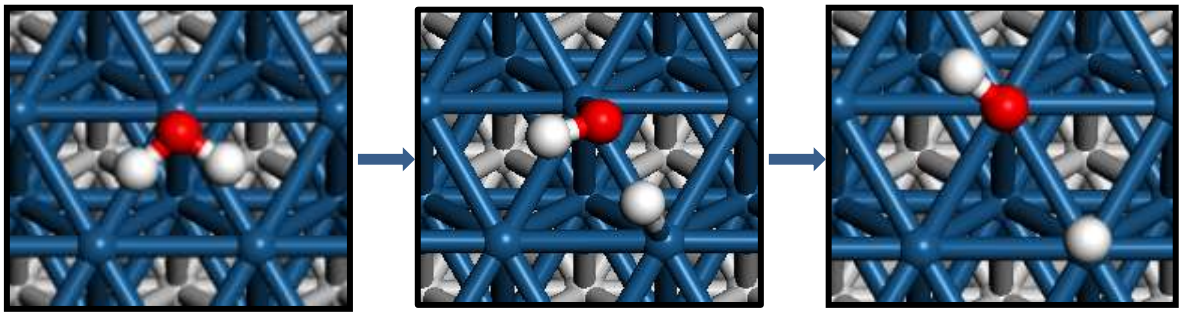

Figure 5.2: Water dissociation pathway on Pt(111): TS; $d_{O^*-H^*}$:1.71 Å

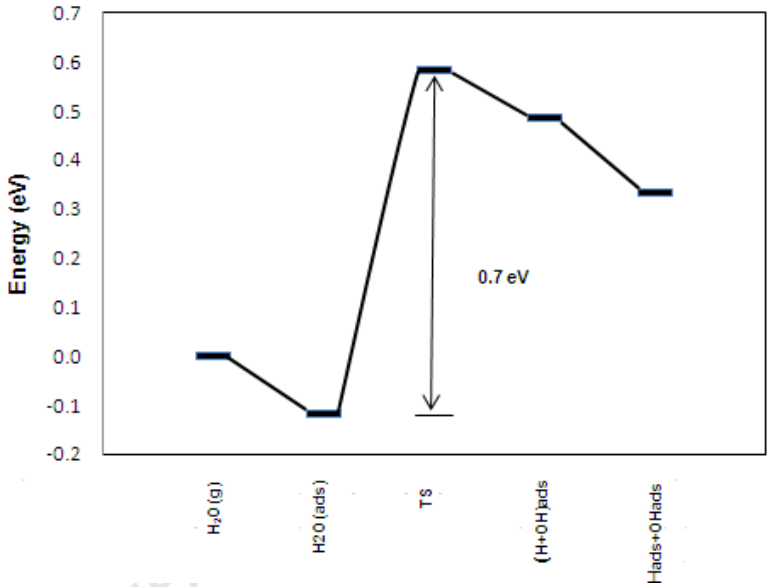

Figure 5.3: Potential energy profile for water dissociation, with an indication of the activation barrier (0.70 eV) and the co-adsorbed energy for OH* and H*

In this study the adsorption energy (-0.1 eV) of the most stable adsorption site and configuration for water and its co-adsorbed dissociated products (OH* and H*) have been investigated. In previous experimental studies (Thiel et al., 1987 and Stair et al., 1982) it has been argued that the preferred adsorption site for water is the on-top site since water acts as an electron donor and the substrate as the electron accepter. In this study water was found to lie flat on the on-top site, also acting as an electron donor with -0.1 electrons donated by oxygen to the substrate as deduced from the Bader analysis. The dissociation of water was found to be an endothermic step (0.45 eV from the adsorbed water state relative to the OH* and H* on their separate state) on Pt(111) with an activation barrier of 0.70 eV. The activation barrier reported by Phatak et al. (2009) in their DFT (VASP: uspp-GGA-PW91) study is 0.8 eV. The activation barrier for this reaction using BEP was calculated to a

value of 1.29 eV. This indicates that BEP approximation parameters used, describe the activation energy calculation for this reaction poorly.

The rate of the elementary reaction step of the dissociation of adsorbed water to separately adsorbed atomic hydrogen and surface hydroxyl species can be estimated knowing the energy profile of the reaction and the vibrational frequencies of the reactant and the transition state. The rate of reaction is given according to the transition state theory (van Santen and Niemantsverdriet, 1995) by:

$$r_{H_2O\ dissociation} = k_{H_2O\ dissociation} \cdot \left(\theta_{H_2O} \cdot \theta_* - \frac{\theta_H \cdot \theta_{OH}}{K_{eq,\, H_2O \rightarrow H + OH}} \right) \tag{5.1}$$

with

$$k_{H_2O\ dissociation} = \frac{k_B \cdot T}{h} \cdot \frac{(p.f.')_{TS}}{(p.f.')_{H_2O\ adsorbed}} \cdot e^{\frac{-(E_{TS} - E_{H_2O\ adsorbed})}{k_B \cdot T}} \tag{5.2}$$

with k_B the Boltzmann constant ($1.38 \cdot 10^{-23}$ J/K), h Planck constant ($6.626068 \cdot 10^{-34}$ J·s) and (p.f.') the partition function excluding the internal energy contribution, and (E_{TS}-$E_{H_2O\ adsorbed}$) the difference in the electronic energy plus the zero point vibrational energy between the transition state and adsorbed water. The partition function can be defined via the vibrational frequencies of adsorbed H_2O and the real frequencies for the transition state, i.e.

$$(p.f.') = \prod_i \frac{1}{1 - e^{\frac{-h \cdot \nu_i}{k_B \cdot T}}} \tag{5.3}$$

The equilibrium constant given in eq. 5.1 is for the overall reaction and can be determined in terms of the partition function for the reactants and products and the difference in the electronic energy plus the zero point vibrational energy between the reactants and the products. For the dissociation of adsorbed water, the equilibrium constant can be defined as

$$K_{eq,\, H_2O \rightarrow H + OH} = \frac{(p.f.')_{H@0.25\,ML} \cdot (p.f.')_{OH@0.25\,ML}}{(p.f.')_{H_2O@0.25\,ML} \cdot (p.f.')_{free\,slab}} \cdot e^{\frac{-(E_{H@0.25\,ML} + E_{OH@0.25\,ML} - E_{H_2O@0.25\,ML} - E_{free\,slab})}{k_B \cdot T}} \tag{5.4}$$

The alkaline fuel cell typically operates in the range between 65-220°C (Barbir, 2005; see Figure 1.2). At a temperature of 65°C (338.15 K), the rate for the elementary dissociation of adsorbed water at a coverage of 0.25 ML yielding separated surface hydrogen and surface hydroxyl, each at 0.25 ML, is given by:

$$r_{H_2O\ dissociation} = 5.90 \cdot 10^{11} \cdot e^{\frac{-0.70eV}{k_B \cdot T}} \cdot \left(\theta_{H_2O} \cdot \theta_* - \frac{\theta_H \cdot \theta_{OH}}{8.21 \cdot 10^{-2} \cdot e^{\frac{-0.45eV}{k_B \cdot T}}} \right)$$

or

$$r_{H_2O\ dissociation} = 2.04 \cdot 10^{1} \cdot \left(\theta_{H_2O} \cdot \theta_* - 5.49 \cdot 10^{7} \cdot \theta_H \cdot \theta_{OH} \right) \quad (5.5)$$

This study also investigated a possibility of oxygen assisted water dissociation. This is the more favourable reaction in alkaline medium (fuel cells) and it will favour a complete O_2 reduction to OH. The co-adsorbed state for co-adsorbed H_2O*+O* on Pt(111) at a coverage of 0.5ML was investigated and found to have an interaction energy of 0.38 eV.

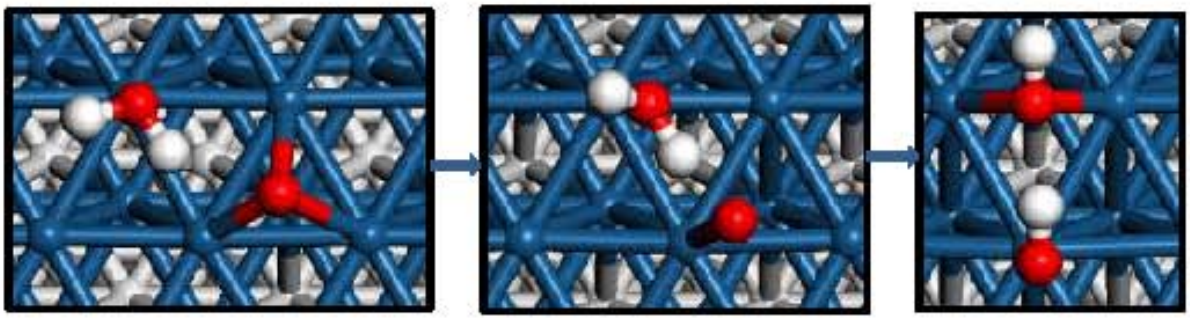

Figure 5.4: Water dissociation pathway on Pt(111): TS; $d_{O^*-H^*}$ = 1.54Å

The activation barrier of 0.56 eV for the oxygen assisted water dissociation was calculated relative to the co-adsorbed state. This intrinsic barrier is much lower compared to the activation energy 0.70 eV for the direct water dissociation. However, the overall reaction is endothermic with an energy difference of 0.56 eV (relative to separate state). This includes the energy cost (0.38eV) to bring adsorbed H_2O, and the energy cost of 0.18 eV of separating co-adsorbed OH (the co-adsorption of OH is exothermic possibly due to hydrogen bonding between co-adsorbed species). The rate of the elementary oxygen assisted water dissociation taking into consideration that adsorbed water and atomic oxygen have to approach each other can be expressed as:

$$r_{O\text{-}assisted H_2O\ dissociation} = k_{O-assisted H_2O\ dissociation} \cdot K_{approach O\ and\ H_2O} \cdot \left(\theta_{H_2O} \cdot \theta_O - \frac{\theta_{OH}^2}{K_{eq, H_2O + O \rightarrow 2\,OH}} \right) \quad (5.6)$$

At a temperature of 65°C (338.15 K), the rate for the elementary oxygen assisted dissociation of adsorbed water, each at a coverage of 0.25 ML, yielding surface hydroxyl species at a coverage of 0.25 ML, is given by:

$$r_{\text{O-assisted}H_2O\text{ dissociation}} = 9.38 \cdot 10^{12} \cdot e^{\frac{-0.56\,eV}{k_B \cdot T}} \cdot 0.32 \cdot e^{\frac{-0.38\,eV}{k_B \cdot T}} \cdot \left(\theta_{H_2O} \cdot \theta_O - \frac{\theta_{OH}^2}{0.16 \cdot e^{\frac{-0.56\,eV}{k_B \cdot T}}} \right)$$

or

$$r_{\text{O-assisted}H_2O\text{ dissociation}} = 2.98 \cdot 10^{-2} \cdot \left(\theta_{H_2O} \cdot \theta_O - 1.32 \cdot 10^{9} \cdot \theta_{OH}^2 \right) \qquad (5.7)$$

This means that at a temperature of 65°C, the oxygen assisted water dissociation on a clean Pt(111) surface (i.e. neglecting the reverse reaction) is $1.46 \cdot 10^{-3} \cdot \theta_O/\theta_*$ slower than the direct water dissociation. The main contributing factor here is the energy cost for the approach of adsorbed water and atomic oxygen to yield a co-adsorbed state. Hence, atomic O on the surface will not favour oxygen assisted water dissociation during oxygen reduction reaction.

5.3 Oxygen dissociation

This study presents a density functional theory study for oxygen adsorption on Pt(111) in order to probe the intrinsic mechanism for reduction. Yeager et al. (1992) proposed the dissociative adsorption of oxygen on a platinum surface using kinetic isotope experiment. To investigate the pathway followed for oxygen dissociation on Pt(111) the pathway shown on Figure 5.5 has been studied.

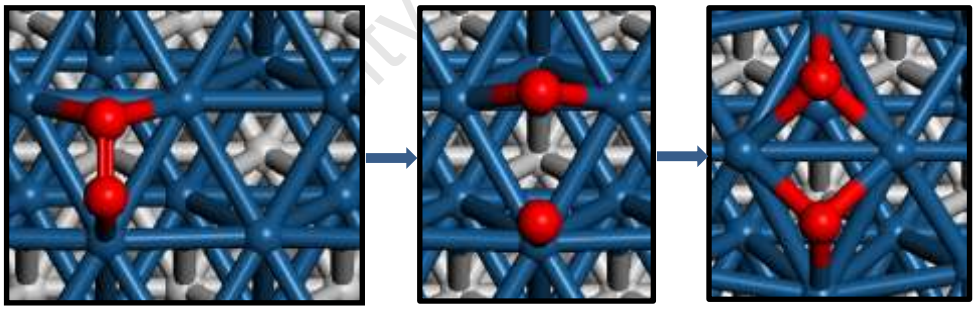

$(O_2)_{ads}$ TS $(O+O)_{co\text{-}ads}$

Figure 5.5: Oxygen dissociation pathway on Pt(111); TS: $d_{O^*-O^*}$ = 2.31 Å

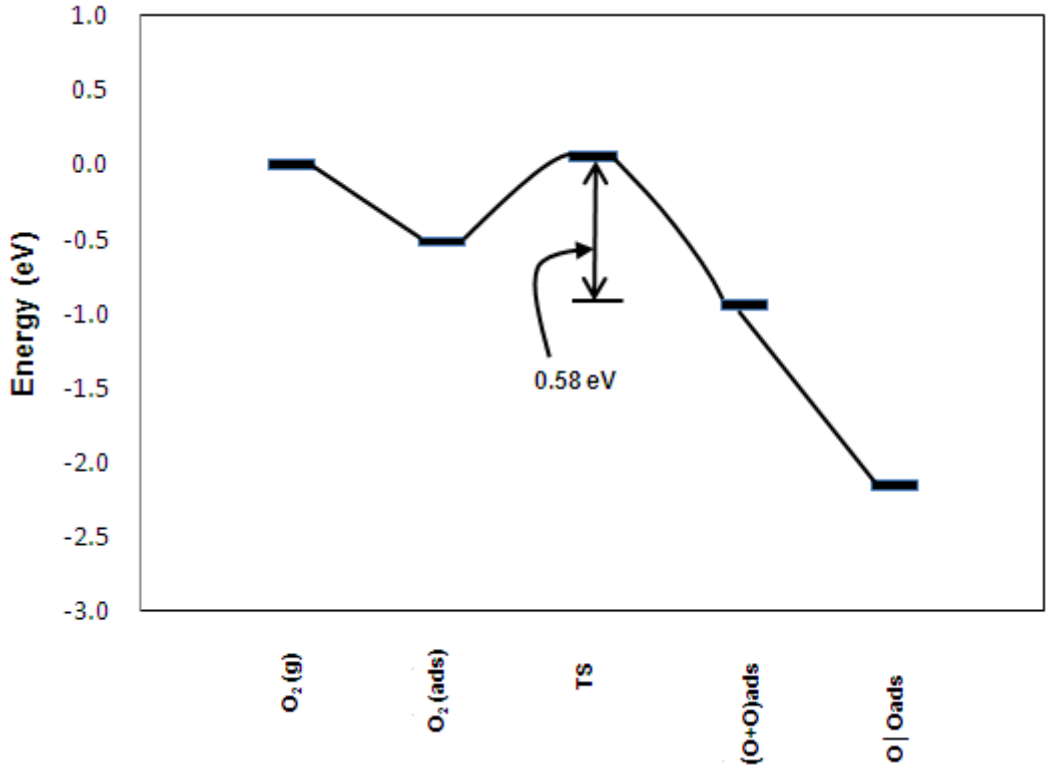

Figure 5.6: Potential energy diagram for direct dissociation of oxygen on Pt(111) with an activation barrier of (0.58 eV) relative to the stable state of adsorbed molecular oxygen

The activation barrier for oxygen dissociation on Pt(111) was calculated to a value of 0.58 eV with respect to molecular O_2. Oxygen dissociation was found to be exothermic by -1.64 eV. Ford et al. (2010) reported an activation barrier of 0.71 eV using the DACAPO computational code with a GGA-PW91 functional.

Theoretical calculations on finite cluster on a Pt(111) surface by Hyman et al. (2005) yielded an activation energy for direct O_2 dissociation barrier of 0.5 eV (using Amsterdam Density Functional (ADF)). Earlier studies on periodic slabs done by Sljivancanin et al. (2002) and Eichler et al. (1997) reported activation energies for the direct oxygen dissociation at the 'top-fcc-bridge' to be 0.6 eV (GGA-RPBE) and 0.9 eV (VASP-GGA-PW91) respectively. The NEB (VASP-uspp-PW91) calculation by Eichler et al., (2000) reported the O_2 dissociation barrier of 0.18 eV relative to the free molecule (the dissociation energy for the direct oxygen dissociation relative to gas phase oxygen in this study is 0.06 eV). The difference in reported activation energies for oxygen dissociation from various techniques is an indication of challenges in identifying reasons for the sluggish kinetics of oxygen reduction reaction. The differences in reported activation energies are unclear. It should however be noted that the reported activation energies in literature refer to maximum values for the activation energy, since there may be pathways for the oxygen dissociation, which were not explored. Hence, the various techniques and initial configurations used to calculate such energies

could be a contributing factor in the accuracy of predicting the actual activation energy for the direct oxygen dissociation on Pt(111).

The BEP-estimation for the activation energy for the direct oxygen dissociation is E_a= 0.60 eV using the parameters given by Nørskov et al. (2002). The value given by the BEP-relationship is in agreement with the calculated value from the current NEB results, this in an indication of a good BEP linear relationship prediction for diatomic molecules.

The rate of the direct oxygen dissociation on Pt(111) can be expressed as:

$$r_{direct\,O_2\ dissociation} = k_{direct\,O_2\ dissociation} \cdot \left(\theta_{O_2} \cdot \theta_* - \frac{\theta_O^2}{K_{eq,\,O_2 + * \rightarrow 2O}} \right) \tag{5.8}$$

At a temperature of 65°C (338.15 K), the rate for the elementary direct dissociation of adsorbed molecular oxygen at a coverage of 0.25 ML yielding separated surface oxygen species at a coverage of 0.25 ML, is given by:

$$r_{direct\,O_2\ dissociation} = 8.55 \cdot 10^{12} \cdot e^{\frac{-0.58\,eV}{k_B \cdot T}} \cdot \left(\theta_{O_2} \cdot \theta_* - \frac{\theta_O^2}{0.25 \cdot e^{\frac{-1.64\,eV}{k_B \cdot T}}} \right)$$

or

$$r_{direct\,O_2\ dissociation} = 2.34 \cdot 10^4 \cdot \left(\theta_{O_2} \cdot \theta_* - 1.70 \cdot 10^{-24} \cdot \theta_O^2 \right) \tag{5.9}$$

The direct oxygen dissociation is in essence an irreversible reaction. Furthermore, the direct oxygen dissociation is much faster than the direct water dissociation ($1.15 \cdot 10^3 \cdot \theta_{O_2}/\theta_{H_2O}$ faster), which in turn is faster than the oxygen assisted water dissociation. Hence, the oxygen reduction reaction in alkaline fuel cells seems to be limited by water dissociation rather than oxygen dissociation. The latter is typically assumed to be the slowest step in PEM-type of fuel cells (Yeager et al., 1992). Furthermore is noted that oxygen coverage is low, since OH will dominate the surface and the sticking probability of O_2 will be low, hence O_2 coverage can also be rate limiting.

5.4 Hydrogenation of molecular oxygen

It has been proposed by earlier experiments that hydrogenation of oxygen precedes O_2 dissociation during the oxygen reductio reaction (ORR), suggesting that the dissociation of oxygen is hydrogen assisted. For this study the proposed reaction was studied by calculating the activation barrier for the reaction. The first step in the hydrogen assisted oxygen dissociation is the addition of atomic hydrogen to adsorbed molecular oxygen. This

reaction is almost thermo-neutral (0.03 eV relative to the separate state of adsorbed H and molecular oxygen) to form the peroxide intermediate as shown in Figure 5.7.

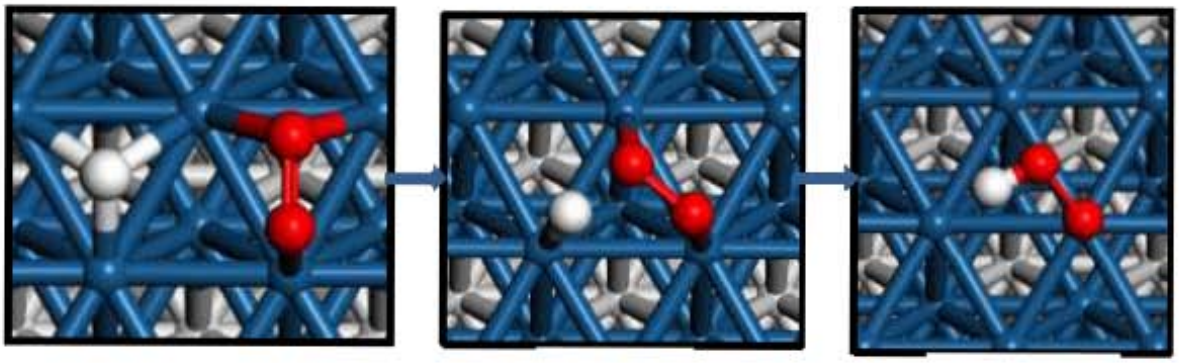

Figure 5.7: Hydrogenation of oxygen on Pt(111); TS: $d_{H^*-O^*}$ = 1.49 Å

The calculated activation barrier for this reaction is 0.25 eV with respect to the co-adsorbed state and 0.51 eV with respect to the separate adsorption of atomic H and molecular O_2, each at a coverage of 0.25ML. The calculated activation energy is consistent with the activation barrier of 0.29 eV (relative to the co-adsorbed state) calculated by Ford et al. (2010) using GGA-PW91 (DACAPO computational code). The BEP-relationship predicts a much higher activation barrier (1.07 eV assuming parameters for the dehydrogenation of OOH and 0.92 eV assuming the parameters for the dissociation of a tri-atomic species) even when considering the energy required for the approach of atomic hydrogen and molecular oxygen on Pt(111).

The rate of the elementary reaction of the hydrogen addition to adsorbed molecular oxygen taking into consideration the approach of atomic hydrogen and molecular oxygen can be expressed as:

$$r_{\text{H-addition to O}_2} = k_{\text{H-addition to O}_2} \cdot K_{\text{approachH and O}_2} \cdot \left(\theta_{O_2} \cdot \theta_H - \frac{\theta_{OOH} \cdot \theta_*}{K_{\text{eq, O}_2 + H \rightarrow OOH}} \right) \qquad (5.10)$$

At a temperature of 65°C (338.15 K), the rate for the elementary addition of hydrogen to adsorbed molecular oxygen, each at a coverage of 0.25 ML, yielding surface OOH at 0.25 ML, is given by:

$$r_{\text{H-addition to O}_2} = 6.02 \cdot 10^{12} \cdot e^{\frac{-0.25\text{eV}}{k_B \cdot T}} \cdot 1.12 \cdot e^{\frac{-0.26\text{eV}}{k_B \cdot T}} \cdot \left(\theta_{O_2} \cdot \theta_H - \frac{\theta_{OOH} \cdot \theta_*}{1.55 \cdot e^{\frac{-0.03\text{eV}}{k_B \cdot T}}} \right)$$

or

$$r_{\text{H-addition to O}_2} = 1.56 \cdot 10^5 \cdot \left(\theta_{O_2} \cdot \theta_H - 1.53 \cdot \theta_{OOH} \cdot \theta_* \right) \qquad (5.11)$$

These results also shows that during the oxygen reduction reaction the addition of hydrogen to adsorbed molecular oxygen is favoured over the direct dissociation of adsorbed molecular oxygen (by a factor of $6.65 \cdot \theta_H/\theta_*$). The extent to which the hydrogen addition to molecular adsorbed oxygen is favoured over the direct dissociation of adsorbed molecular oxygen is thus a function of the coverage of the surface with atomic hydrogen on Pt(111). Hence, the extent of hydrogen assisted oxygen dissociation versus direct oxygen dissociation can be different in alkaline fuel cells versus PEM-fuel cells.

5.4.1 Dissociation of the peroxide intermediate (OOH⟶O*+OH*)*

The dissociation of OOH* was also investigated (see Figure 5.8). The decision to study this reaction is to understand if the dissociation of OOH* on Pt(111), is favoured. This unique configuration was chosen, because the most stable adsorbed OOH* species was calculated at the bridge site. This reaction competes during oxygen reduction reaction (ORR) with a further hydrogen addition yielding HOOH* on the surface (hydrogen peroxide formation is not desired). The reaction is exothermic by -1.55 eV relative to the separate state.

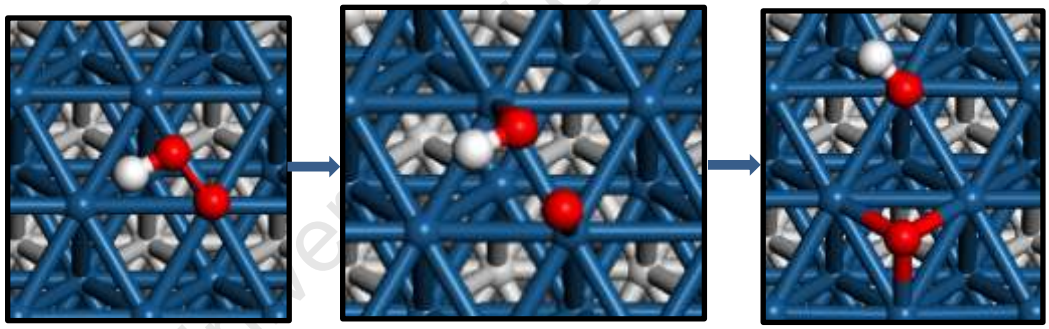

Figure 5.8: Dissociation of OOH* on Pt(111), with an activation barrier of 0.18 eV; TS:$d_{O^*-O^*}$=1.49Å

The dissociation barrier for the OOH* species is 0.18 eV. Calculations for the same reaction by Ford et al. (2010) on their DFT study yielded an activation energy of 0.16 eV, which is consistent with the current calculations.

The rate of the elementary dissociation of OOH* on Pt(111) yielding separate atomic oxygen and surface hydroxyl species, each at a coverage of 0.25ML, can be expressed as:

$$r_{OOH\text{-}dissociation} = k_{OOH\text{-}dissociation} \cdot \left(\theta_{OOH} \cdot \theta_* - \frac{\theta_O \cdot \theta_{OH}}{K_{eq,\,OOH+*\rightarrow O+OH}} \right) \qquad (5.12)$$

At a temperature of 65°C (338.15 K), the rate for the elementary dissociation of OOH is given by:

$$r_{OOH\text{-}dissociation} = 6.32 \cdot 10^{12} \cdot e^{\frac{-0.18eV}{k_B \cdot T}} \cdot \left(\theta_{OOH} \cdot \theta_* - \frac{\theta_O \cdot \theta_{OH}}{0.55 \cdot e^{\frac{1.55eV}{k_B \cdot T}}} \right)$$

or

$$r_{OOH\text{-}dissociation} = 1.41 \cdot 10^{10} \cdot \left(\theta_{OOH} \cdot \theta_* - 1.49 \cdot 10^{-23} \cdot \theta_O \cdot \theta_{OH} \right) \quad (5.13)$$

The dissociation of surface OOH species on Pt(111) into atomic oxygen and a surface hydroxyl species is fast. This implies that under these reaction conditions the dissociation of OOH can be considered to be at equilibrium.

5.5 Further hydrogenation of the peroxide intermediate (H*+OOH*)

The initial thermodynamic analysis of the possible reactions taking place during oxygen reduction reaction suggests that further hydrogenation of the peroxide intermediate (OOH*) could be the dominating step to form hydrogen peroxides in fuel cells. To substantiate the latter activation barriers for the reaction were calculated as shown in Figure 5.9. The reaction is thermo-neutral (energy difference of 0.03 eV relative to the atomic hydrogen and OOH* in the separate state at a coverage of 0.25ML).

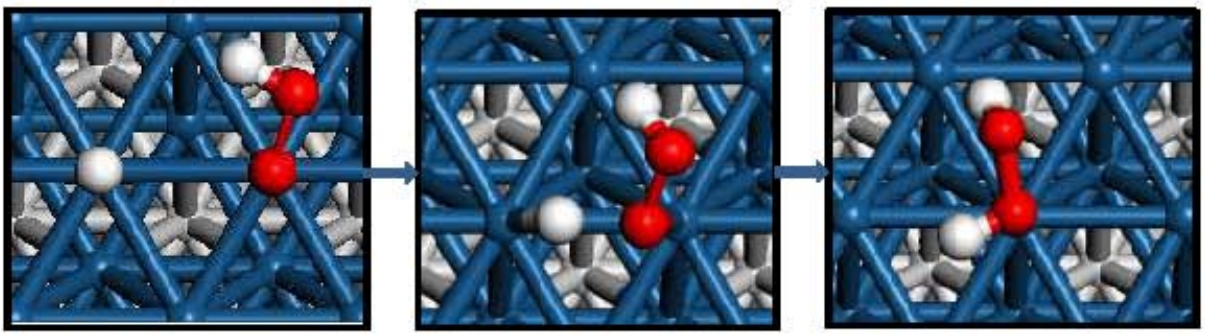

Figure 5.9: Hydrogenation of peroxide intermediate to form H_2O_2 on Pt(111);TS:$d_{H^*\text{-}O^*}$ = 1.5 Å

The calculated activation barrier for this reaction path is 0.21 eV (*Ea*: 0.44 eV relative to the separate state) which is consistent with the calculated value of 0.21 eV (relative to the co-adsorbed state) by Ford et al. (2010) using GGA-PW91 (DACAPO computational code). The estimate from the Brønsted-Evans-Polyani relationship is much higher (0.93 eV).

The rate of the elementary reaction of the hydrogen addition to the surface OOH species taking into consideration the approach of atomic hydrogen and OOH can be expressed as:

$$r_{\text{H-addition to OOH}} = k_{\text{H-addition to OOH}} \cdot K_{\text{approach H and OOH}} \cdot \left(\theta_{OOH} \cdot \theta_H - \frac{\theta_{HOOH} \cdot \theta_*}{K_{\text{eq, OOH} + H \rightarrow HOOH}} \right) \qquad (5.14)$$

At a temperature of 65°C (338.15 K), the rate for the elementary addition of hydrogen to OOH, each at a coverage of 0.25 ML, yielding surface HOOH* at 0.25 ML, is given by:

$$r_{\text{H-addition to OOH}} = 2.67 \cdot 10^{12} \cdot e^{\frac{-0.21\text{eV}}{k_B \cdot T}} \cdot 5.73 \cdot e^{\frac{-0.23\text{eV}}{k_B \cdot T}} \cdot \left(\theta_{OOH} \cdot \theta_H - \frac{\theta_{HOOH} \cdot \theta_*}{27.47 \cdot e^{\frac{-0.03\text{eV}}{k_B \cdot T}}} \right)$$

or

$$r_{\text{H-addition to OOH}} = 4.32 \cdot 10^{6} \cdot \left(\theta_{OOH} \cdot \theta_H - 9.74 \cdot 10^{-2} \cdot \theta_{HOOH} \cdot \theta_* \right) \qquad (5.15)$$

This is an indication that dissociation of the peroxide (OOH*) intermediate is more facile than further addition of hydrogen to the peroxide intermediate step. The hydrogen addition to a surface OOH* species is $3.06 \cdot 10^{-4} \cdot \theta_H / \theta_*$ slower than the dissociation of OOH.

5.6 Hydrogen addition to atomic oxygen (H*+O*⟶OH*)

AFC usually use the circulating liquid alkaline electrolyte, potassium hydroxide (KOH) with standard concentration of 30-45% KOH (Barbir, 2005). Potassium is the carrier of the migrating hydroxyl ions from the cathode to the anode side of the cell. Maximising the formation of hydroxyls (OH*) on the surface of the cathode, which upon desorption yield the hydroxide ions, is therefore vital to complete the circuit in alkaline fuel cells. However in this work formation of hydroxyls is studied with a rather different interest. One of the proposed pathways leading to the formation of hydrogen peroxide (H_2O_2*) is via the interaction of the hydroxyls (OH*+OH*) on Pt (111). Figure 5.10 illustrates the transition state for OH* formation via O*+H*, the reaction is endothermic by 0.11 eV relative to the atomic hydrogen and atomic oxygen separately, each at a coverage of 0.25ML. The hydroxyl species can be formed with H* on the top side and atomic oxygen on the less stable hcp 3-fold hollow site.

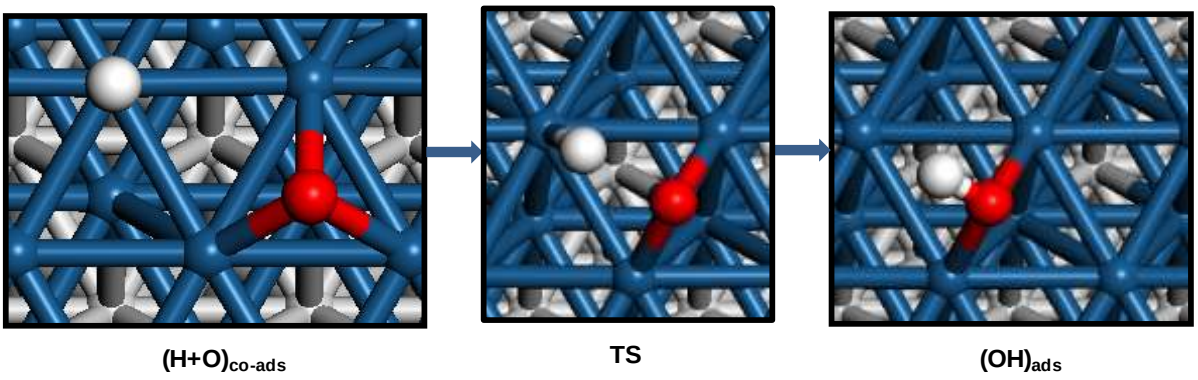

Figure 5.10: Association reaction of hydrogen and oxygen on Pt(111);TS: $d_{H^*-O^*}$ = 1.72 Å

The calculated activation barrier for oxygen hydrogenation is 0.35 eV relative to the co-adsorbed state and 0.96 eV relative to the state in which atomic hydrogen and atomic oxygen are adsorbed separately, each at a coverage of 0.25 ML. The activation barrier calculated by Ford et al. (2010) using GGA-PW91 (DACAPO computational code) is 0.72 eV (relative to the co-adsorbed state). The reason for the higher energy could be as a result of the path chosen by Ford et al. (2010). It is not clear where their starting reactants (at a combined coverage of 0.5ML) are positioned. However, they reported a stable adsorption site for the separate (0.25ML) atomic hydrogen and oxygen at the fcc 3-fold hollow site. The DFT study by Michaelides et al. (2001) also shows a high activation barrier for hydrogen addition to atomic oxygen of 0.96 eV. They reported a co-adsorbed state for O*+H*, with H* on the top site and O on the fcc 3-fold hollow site, which was observed in this study to be the most stable position for atomic oxygen at 0.25 ML. The current study obtained a different, stable co-adsorbed state for atomic hydrogen and atomic oxygen with H on the top site and O on the hcp 3-fold hollow site (see Figure 5.10). The current co-adsorbed (0.5ML) state has atomic O* on the hcp site, therefore it may have to diffuse from the stable fcc 3-fold hollow site to the hcp 3-fold hollow site, which subsequently may include additional energy cost for this reaction. The energy cost to bring these species (O* and H*) together from their most stable sites is 0.61 eV, thus the total activation energy is 0.96 eV in reasonable agreement with the estimation from the BEP-relationship (1.08 eV).

The rate of the elementary reaction of the hydrogen addition to adsorbed atomic oxygen taking into consideration the approach of atomic hydrogen and atomic oxygen from their respective most stable state at a coverage of 0.25 ML can be expressed as:

$$r_{\text{H-addition to O}} = k_{\text{H-addition to O}} \cdot K_{\text{approach H and O}} \cdot \left(\theta_O \cdot \theta_H - \frac{\theta_{OH} \cdot \theta_*}{K_{\text{eq, O+H} \rightarrow \text{OH}}} \right) \qquad (5.16)$$

At a temperature of 65°C (338.15 K), the rate for the elementary addition of hydrogen to adsorbed atomic oxygen, each at their most stable state a coverage of 0.25 ML, yielding surface OH* at 0.25 ML, is given by:

$$r_{\text{H-addition to O}} = 6.65 \cdot 10^{12} \cdot e^{\frac{-0.35eV}{k_B \cdot T}} \cdot 1.45 \cdot e^{\frac{-0.61eV}{k_B \cdot T}} \cdot \left(\theta_O \cdot \theta_H - \frac{\theta_{OH} \cdot \theta_*}{1.89 \cdot e^{\frac{-0.11eV}{k_B \cdot T}}} \right)$$

or

$$r_{\text{H-addition to O}} = 4.33 \cdot 10^{-2} \cdot \left(\theta_O \cdot \theta_H - 2.40 \cdot 10^{1} \cdot \theta_{OH} \cdot \theta_* \right) \quad (5.17)$$

The addition of atomic hydrogen to surface oxygen is relatively slow due to the large energy cost associated with bringing the species together prior to the addition reaction. The rate constant for the hydrogen addition to atomic oxygen is about 0.5 times the rate constant for the water addition to atomic oxygen.

5.6.1 Association of surface hydroxyl species yielding HOOH on Pt(111)

The association of two surface hydroxyl species may lead to the formation of an adsorbed hydrogen peroxide species. The reaction for the formation of HOOH at a coverage of 0.25 ML from hydroxyl species at 0.25 ML on Pt(111) is strongly endothermic with an energy difference of 1.47 eV (including zero point energy correction). The association of two surface hydroxyl species require the co-adsorption of two hydroxyl species on a p(2x2) unit cell resulting in a coverage of 0.50 ML (see section 4.8). Each of these co-adsorbed states may react further.

The initial configuration for co-adsorption of OH* in Figure 5.11 was found to be the most stable state (by 0.18 eV in comparison to the less stable state given in Figure 5.13). This reaction path for the configuration given in Figure 5.11 has a calculated activation barrier of 1.90 eV (1.80 eV relative to hydroxyl species at a coverage of 0.25 ML). The BEP-relationship yielded a very high activation energy of 4.58 eV indicating that the association reaction is not correctly predicted by this model.

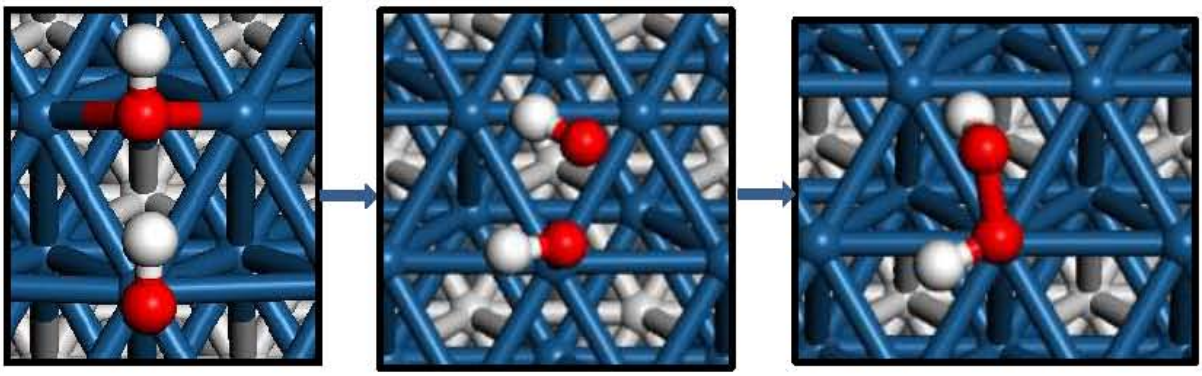

$(OH+OH)_{co\text{-}ads}$ TS $(HOOH)_{ads}$

Figure 5.11: Direct formation of H_2O_2 by OH* recombination on Pt(111);p(2×2) unit cell

The rate of the elementary association reaction of surface hydroxyl species yielding a surface HOOH species taking into consideration the approach of the hydroxyl species can be expressed as:

$$r_{\text{OH-aassociationI}} = k_{\text{OH-aassociationI}} \cdot K_{\text{approachOHI}} \cdot \left(\theta_{OH}^2 - \frac{\theta_{HOOH} \cdot \theta_*}{K_{eq,\,2\,OH \rightarrow HOOH}} \right) \qquad (5.18)$$

At a temperature of 65°C (338.15 K), the rate for the elementary association of surface hydroxyl species each at a coverage of 0.25 ML going via the specified initial state given in Figure 5.11 yielding surface HOOH at a coverage of 0.25 ML, is given by:

$$r_{\text{OH-aassociationI}} = 1.46 \cdot 10^{13} \cdot e^{\frac{-1.90\,eV}{k_B \cdot T}} \cdot 2.01 \cdot e^{\frac{0.09\,eV}{k_B \cdot T}} \cdot \left(\theta_{OH}^2 - \frac{\theta_{HOOH} \cdot \theta_*}{26.36 \cdot e^{\frac{-1.47\,eV}{k_B \cdot T}}} \right)$$

or

$$r_{\text{OH-aassociationI}} = 4.14 \cdot 10^{-14} \cdot \left(\theta_{OH}^2 - 2.73 \cdot 10^{20} \cdot \theta_{HOOH} \cdot \theta_* \right) \qquad (5.19)$$

The initial configuration shown in Figure 5.11 may also lead to the formation of water (see Figure 5.12; the reverse of this reaction was discussed in section 5.2). The rate of the reverse reaction can thus be derived from equation 5.7 as:

$$r_{\text{OH-association yielding } H_2O \text{ and } O} = 3.93 \cdot 10^{7} \cdot \left(\theta_{OH}^2 - 7.58 \cdot 10^{-10} \cdot \theta_{H_2O} \cdot \theta_O \right) \qquad (5.20)$$

Hence, the association reaction will yield water much faster than hydrogen peroxide. However it should be noted that the reaction dynamics of oxygen reduction at the cathode for alkaline fuel cells may not favour this reaction since water is co-fed with oxygen (Le

Chatelier's principle) therefore it is more likely to go the H_2O_2 route. It is also noted that these conclusions can only be validated by a full kinetic analysis.

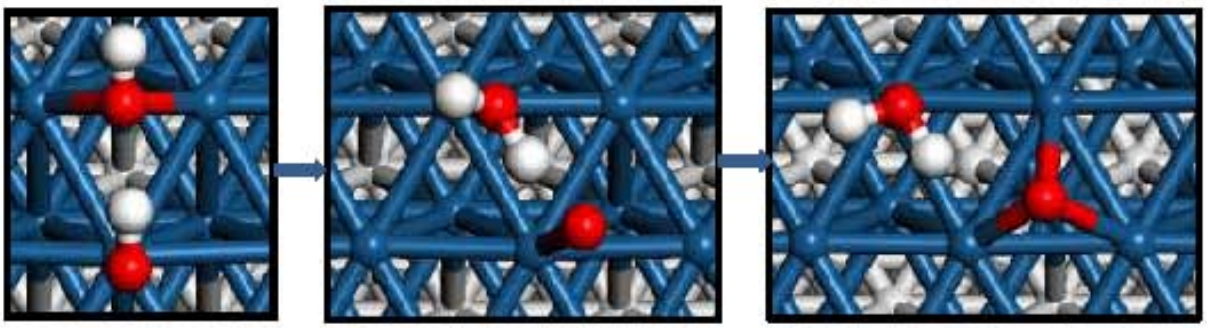

Figure 5.12: OH recombination pathway yielding $H_2O^*+O^*$ on Pt(111);p(2×2) unit cell: TS;O*–H*:1.54 Å

The reaction (Figure 5.12) was found to have an activation barrier of 0.47 eV, which is significantly lower (1.43 eV less) as compared to the formation of H_2O_2 (E_a =1.9 eV).

5.6.2 Interaction of hydroxyls on Pt(111) (OH+OH*→HOOH*) rxn-2*

The second configuration illustrated by Figure 5.13 indicates a precursor towards forming H_2O_2. The obtained transition states for the two starting configurations are very similar with only minor variations in the obtained geometry, energy and vibrational frequencies.

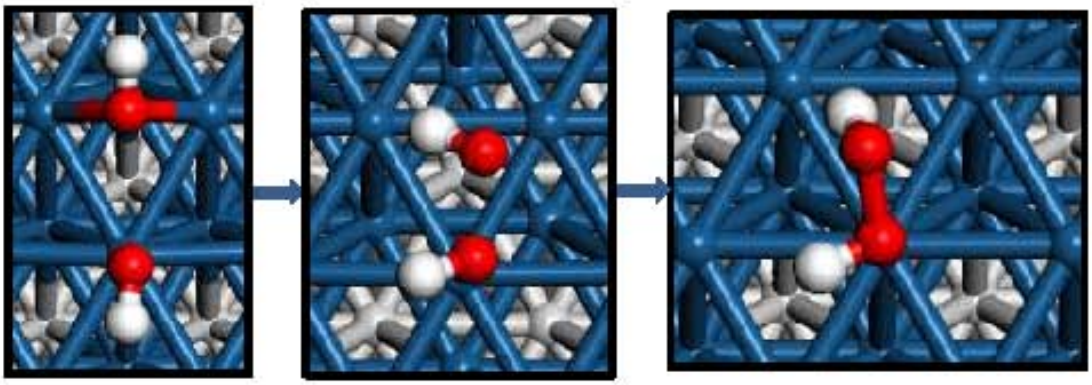

Figure 5.13: Pathway for H_2O_2 formation from OH association on Pt(111); p(2×2) unit cell

When considering the hydroxyls interaction step on Pt(111), starting with the less stable hydroxyls co-adsorbed state in Figure 5.13 as compared to Figure 5.11 the reaction path showed a minimum pathway with a lower activation barrier of 1.7 eV (relative to the co-adsorbed state).

The rate of the elementary association reaction of surface hydroxyl species yielding a surface HOOH* species taking into consideration the approach of the hydroxyl species and proceeding via the less stable co-adsorbed state for the surface hydroxyl species can be expressed as:

$$r_{\text{OH-aassociationI}} = k_{\text{OH-aassociationII}} \cdot K_{\text{approachOHII}} \cdot \left(\theta_{OH}^2 - \frac{\theta_{HOOH} \cdot \theta_*}{K_{eq,\,2\,OH \rightarrow HOOH}} \right) \tag{5.21}$$

At a temperature of 65°C (338.15 K), the rate for the elementary association of surface hydroxyl species each at a coverage of 0.25 ML going via the specified initial state given in Figure 5.13 yielding surface HOOH at a coverage of 0.25 ML, is given by:

$$r_{\text{OH-aassociationI}} = 1.35 \cdot 10^{13} \cdot e^{\frac{-1.70\,eV}{k_B \cdot T}} \cdot 2.01 \cdot e^{\frac{-0.09\,eV}{k_B \cdot T}} \cdot \left(\theta_{OH}^2 - \frac{\theta_{HOOH} \cdot \theta_*}{26.36 \cdot e^{\frac{-1.47\,eV}{k_B \cdot T}}} \right)$$

or

$$r_{\text{OH-aassociationI}} = 5.11 \cdot 10^{-14} \cdot \left(\theta_{OH}^2 - 2.73 \cdot 10^{20} \cdot \theta_{HOOH} \cdot \theta_* \right) \tag{5.22}$$

Hence, the rate of reaction is not dependent on the configuration of an intermediate state (i.e. the co-adsorbed state for OH*). This result is expected, since the co-adsorbed intermediate state does not affect the overall rate of the separate surface hydroxyl groups to a surface HOOH-species, but rather the pre-equilibrium distribution of OH species on the surface.

5.7 Potential energy diagram

Knowing the stability of the various intermediates and their transition states, a potential energy diagram for the reaction of interest can be constructed. It should however be recognized that the potential energy surface is located in a multi-dimensional space, and that typically only a 1-dimensional projection is given. Hence, the interpretation of these diagrams should take into consideration that this is only a projection.

5.7.1 Potential energy diagram for the surface reactions in the oxygen reduction reaction (ORR) in an alkaline fuel cell

In an alkaline fuel cell water is converted with oxygen yielding hydroxide ions. In this study most of the possible surface reactions were investigated (one notable exception is the reaction of adsorbed molecular oxygen with water yielding OOH and a surface hydroxide species). Hence, a preliminary potential energy diagram can be constructed involving solely surface reactions. The potential energy diagrams shown in Figure 5.14 and Figure 5.15 has been formulated such that the energy level of the hydroxide ions and the electrons (4 OH^- + 4e) equals the energy of gas phase oxygen and 2 molecules of gas phase water. This means in reality that this is the potential energy diagram at a potential of 0.90 V (the electro-potential of the reduction of oxygen with water yielding the hydroxide ion extrapolated to 0K).

The manner, in which the potential energy diagram is constructed, is of importance. Two different sequences are shown in Figure 5.15 and Figure 5.16, respectively. The reaction sequence, in which the dissociation of adsorbed molecular oxygen precedes the dissociation of water, is shown in Figure 5.15 (also shown here is the oxygen assisted dissociation of water). The reaction sequence, in which the dissociation of adsorbed water precedes the dissociation of adsorbed molecular oxygen precedes the dissociation of water, is shown in Figure 5.16 (also shown here is the hydrogen assisted dissociation of molecular oxygen).

The 1-dimensional projection of the potential energy surface with the reaction sequence, in which the dissociation of adsorbed molecular oxygen precedes the dissociation of water gives the impression that the desorption of the hydroxide species is the reaction step with the highest barrier, whereas the 1-dimensional projection of the potential energy surface with the reaction sequence, in which the dissociation of adsorbed molecular oxygen precedes the water dissociation, gives the impression that the oxygen dissociation is the reaction step with the highest barrier. A true insight in the limiting steps of the oxygen reduction reaction can only be obtained by employing a full micro-kinetic model.

The oxygen assisted water dissociation results in a more facile formation of surface hydroxyl species (see Figure 5.14). In the overall profile, oxygen-assisted water dissociation seems to result in a more facile reaction sequence, although the oxygen-assisted water dissociation has a higher activation barrier (due to the approach of surface oxygen to adsorbed water). The formation of surface hydroxyl groups by the addition of surface hydrogen to atomic oxygen on the surface has a relative high barrier due to the energy cost of bringing surface hydrogen and surface oxygen in close proximity (0.61 eV). Hence, the oxygen-assisted water dissociation may play an important role in the conversion of water and oxygen to hydroxide ions in an alkaline fuel cell.

The hydrogen-assisted oxygen dissociation has a slightly lower activation barrier than the direct oxygen dissociation (see Figure 5.16). Hence, the presence of surface hydrogen will accelerate the dissociation of adsorbed molecular oxygen.

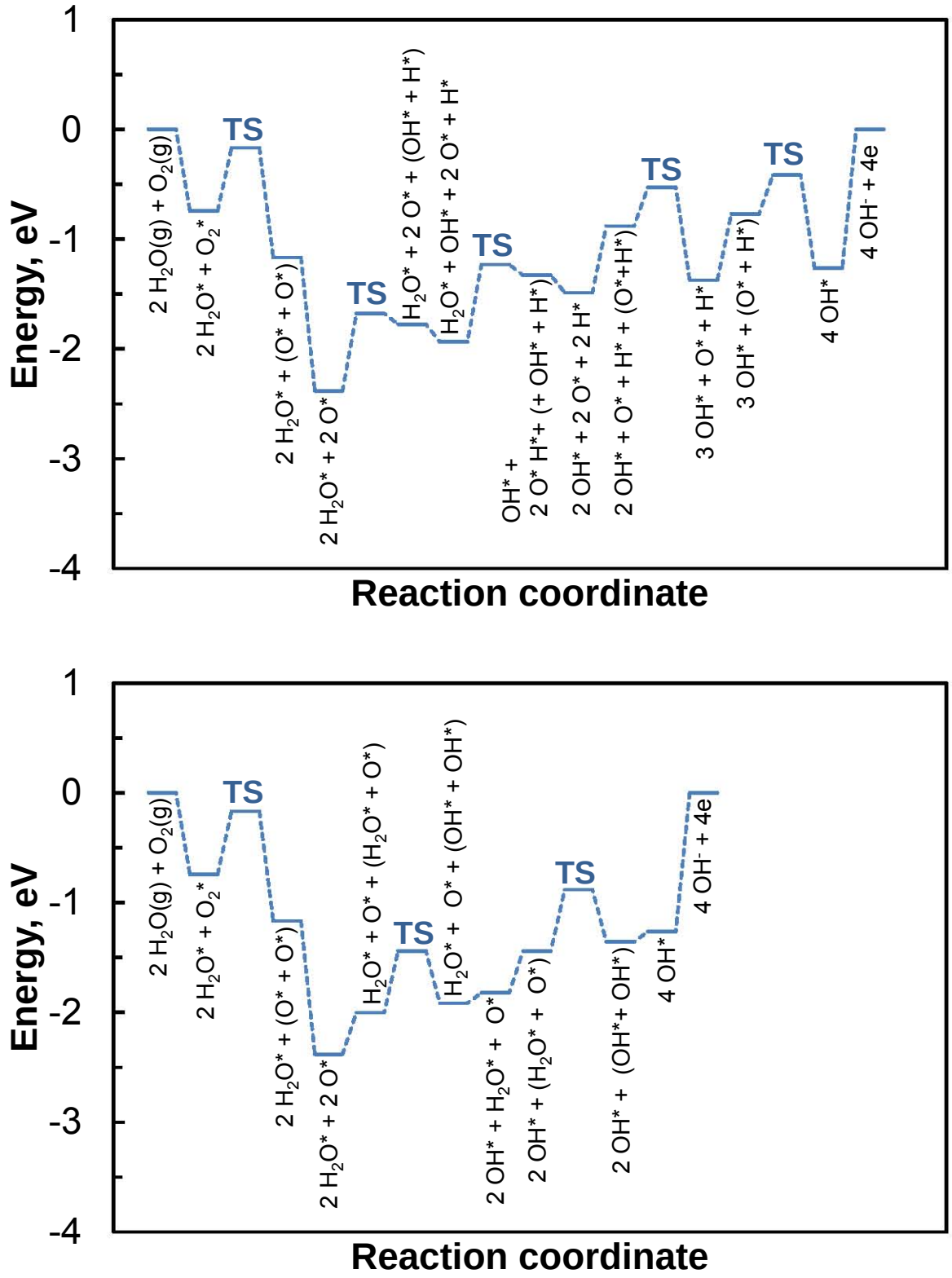

Figure 5.14: **1D potential energy surface (PES) for the oxygen reduction reaction in alkaline fuel cells involving only surface reactions on Pt(111) (TS: transition states; species in brackets are in close proximity), in which the dissociation of adsorbed molecular oxygen precedes the dissociation of adsorbed water**

Top: unassisted water dissociation

Bottom: O-assisted water dissociation

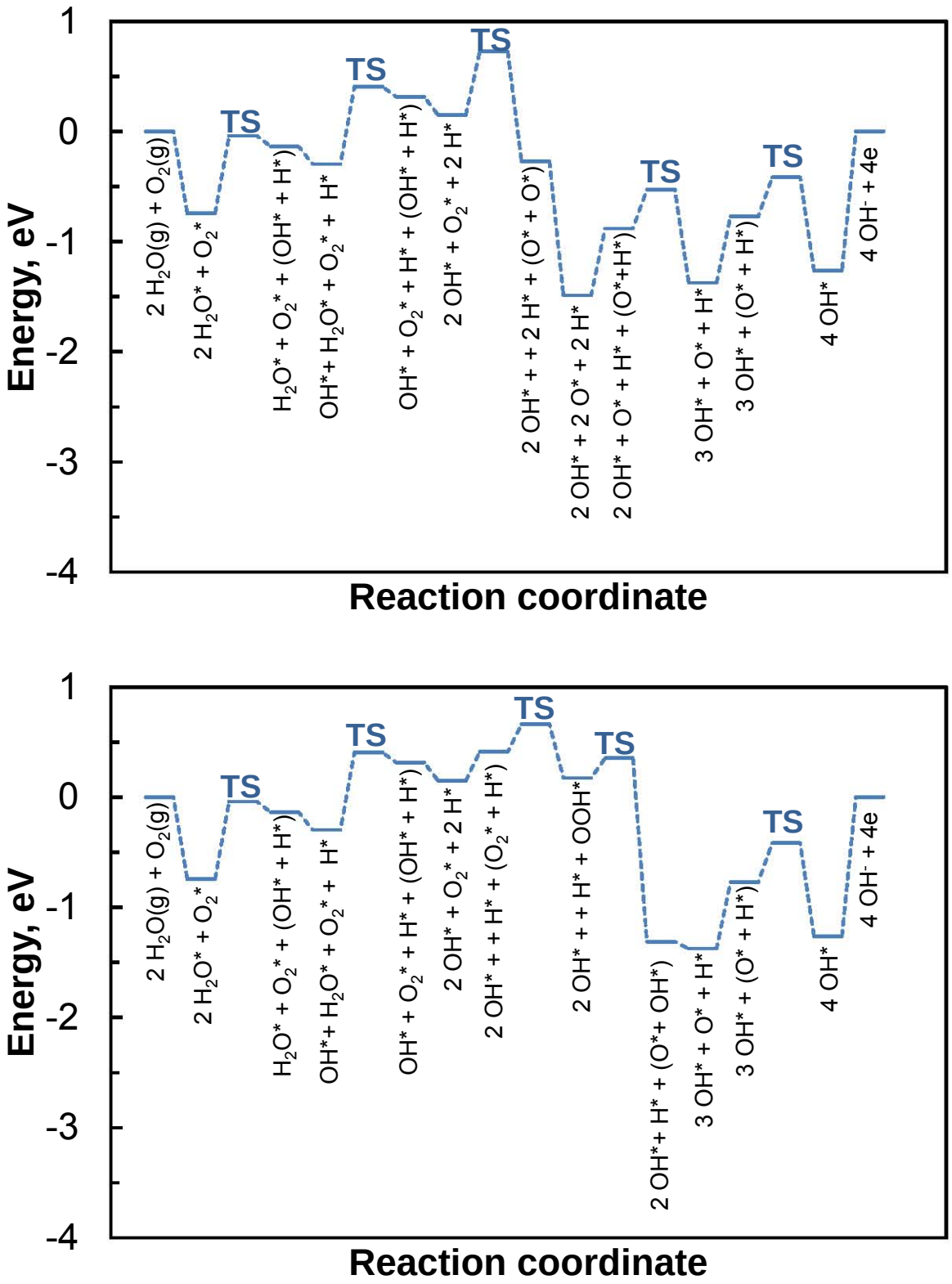

Figure 5.15: **1D potential energy surface (PES) for the oxygen reduction reaction in alkaline fuel cells involving only surface reactions on Pt(111) (TS: transition states; species in brackets are in close proximity), in which the dissociation of adsorbed molecular oxygen precedes the dissociation of adsorbed water**

Top: unassisted oxygen dissociation

Bottom: H-assisted oxygen dissociation

5.7.2 Potential energy diagram for the surface reactions in the oxygen reduction reaction (ORR) in an alkaline fuel cell for the formation of H_2O_2

The one dimensional potential energy surface for hydrogen peroxide formation during oxygen reduction reaction has been studied. Three different pathways for the formation of hydrogen peroxide in the alkaline fuel cell have been proposed (see section 3.5). The reaction pathways starting from water and oxygen in the gas phase up to the point where water is dissociated in atomic H and OH and molecular oxygen is adsorbed are for all three pathways identical (see Figure 3.12). Hence, the potential energy diagrams for the formation of H_2O_2(g) as given in Figure 5.16 starts with the surface species H, OH, OOH and O_2 and the energies are normalized with respect to the adsorbed surface species H, OH, OOH and O_2.

It is apparent from Figure 5.16 that path-1 via the activation of oxygen with hydrogen (H*) and a further hydrogenation of the peroxide (OOH*) intermediate is energetically favoured due to the lower activation barriers for most of the elementary step. This is not only apparent in the lower barrier for the dissociation of adsorbed molecular oxygen, but also in the more facile formation of the surface OOH-species (in comparison to path-3, in which this species is proposed to form via the addition of atomic oxygen to a surface hydroxide species), and thus more facile formation of a surface HOOH-species (in comparison to path-2, in which HOOH is formed upon the combination of two surface hydroxide species). The reaction path indicates that the facile steps, will reduce the concentrations of the intermediates hence driving the reaction forward.

The thermodynamics (endothermic or exothermic) gives information on the energy requirement to drive the reaction, the lower the thermodynamic energy change the less energy required to drive the reaction. The presence of strongly endothermic reactions will result in a high barrier, which is difficult to cross, whereas the presence of strongly exothermic reactions will result in very stable surface species, which will not easily react further. A good mix of moderate endothermic and moderate exothermic elementary steps, as shown for reaction path-1, results in a viable reaction pathway.

The actual reaction pathway will also depend on the availability of surface coverage for the required species for the various elementary reaction steps. The kinetics presents the rates and offers intrinsic information on how facile the elementary steps proceed. This study did not include a full micro-kinetic model and considered only the activation energy contribution to the kinetics for the elementary steps. Based on this limited analysis, it may be concluded that the activation energy of the elementary steps according to path-1 are lower than either path-2 or path-3. Hence, path-1 provides of set of facile reaction steps that may dominate in

forming H_2O_2. It is however noted that the latter remarks, can only be validated by a full micro-kinetic analysis contributing to the understanding of these surface reactions, since surface coverage of the species will be crucial to drive these reactions.

The oxygen reduction reaction via hydrogen assisted oxygen dissociation (O_2*+H*) has a lower activation barrier (see Figure 5.14), which can be taken as an indication that the formation of OOH under these conditions is facile. The dissociation of OOH into atomic O and OH, which is an essentially irreversible reaction, is more favoured than hydrogen peroxide formation (the dissociation of a surface OOH species is $3.27 \cdot 10^{3} \cdot \theta_* / \theta_H$ faster than its hydrogenation). Furthermore, the dissociation of OOH is highly exothermic implying that OOH-dissociation is essentially irreversible. The competition between oxygen reduction reaction via OOH* dissociation versus HOOH* formation may also explain why hydrogen peroxide species are formed in small concentrations in fuel cells conditions with the reported experimental concentration of 0-20%, depending on the potential (Stamenkovic et al., 2002; Nakanishi et al., 2000).

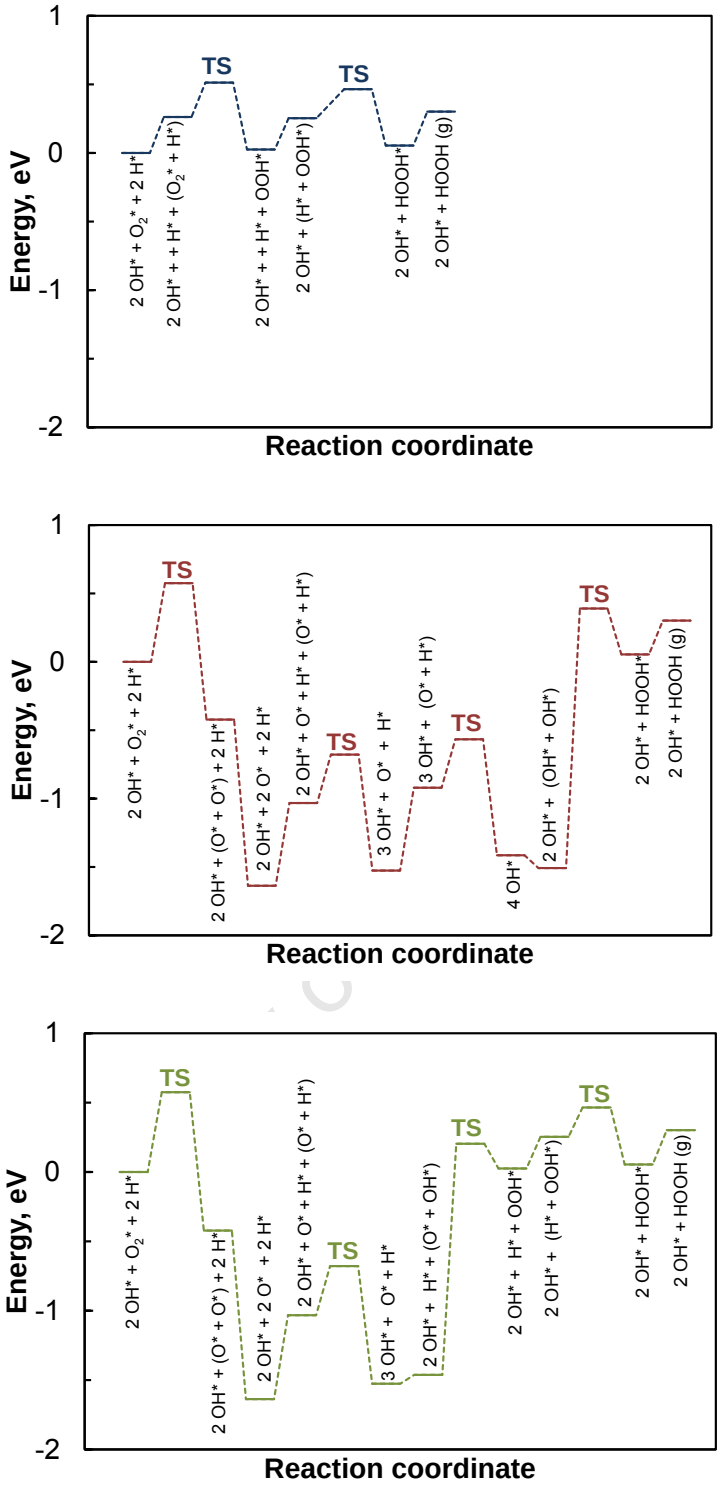

Figure 5.16: **1D potential energy surface (PES) for the formation of hydrogen peroxide during the oxygen reduction reaction in alkaline fuel cells involving only surface reactions on Pt(111) (TS: transition states; species in brackets are in close proximity) water**

Top: Path-1

Middle: Path-2

Bottom: Path-3

5.8 Conclusions

Self-consistent periodic DFT calculations have been performed to calculate the thermodynamics and kinetic contribution to the oxygen reduction reaction as well as the formation of hydrogen peroxide in fuel cells.

5.8.1 Hydrogen peroxide formation pathway

It is evident from this study that hydrogen peroxide may be formed via the addition of hydrogen to adsorbed molecular oxygen yielding OOH with an activation barrier of 0.51 eV (relative to separately adsorbed atomic hydrogen and molecular oxygen each at a coverage of 0.25 ML). A further addition of hydrogen to this species (H*+OOH*) has an overall activation barrier of 0.44 eV to form hydrogen peroxide (H_2O_2) (relative to separately adsorbed atomic hydrogen and OOH each at a coverage of 0.25 ML). This pathway may dominate in alkaline fuel cells, but may also play a role in proton exchange membrane (PEM) fuel cells with the only difference being the origin of H*. Figure 5.17 is the schematic representation of the pathway for the formation of H_2O_2 in an alkaline fuel cell.

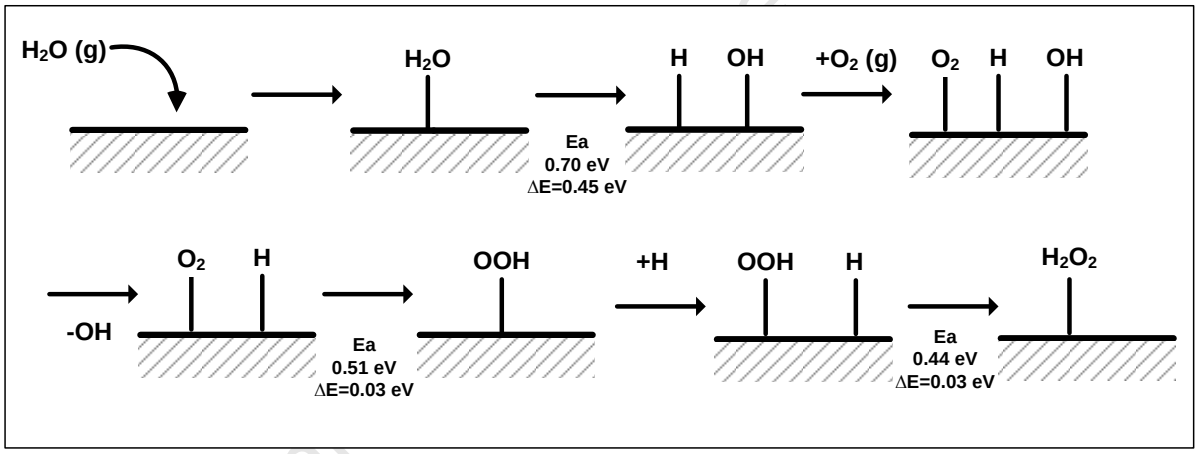

Figure 5.17: Pathway forming hydrogen peroxide in alkaline fuel cells (AFC), also indicating the activation energies for each intermediate reaction steps

5.8.2 Oxygen reduction reaction (ORR)

Oxygen reduction reaction is the main and desired reaction taking place at the cathode of a fuel cell, it is further reported that it accounts for the large fraction of the over-potential on commercial Pt-based catalyst (Wang et al., 2004), in addition to ohmic polarization and mass transfer limitations. The minimum energy pathway for oxygen reduction was calculated to be via the hydrogen assisted oxygen dissociation step on Pt(111). This was apparent since molecular oxygen dissociation was less facile with an activation barrier of 0.58 eV, whilst the activation step by hydrogen (H*) only had an activation barrier of 0.25 eV. However the latter is excluding the 0.26 eV energy cost to bring H* + O_2 at 0.5ML coverage. Hence, the two reaction are closely competitive, if the energy cost to bring

$H^*+O_2^*$ together is taken into consideration. The dominance of one reaction over the other is thus mainly determined by the ratio of the surface concentration with hydrogen and the surface concentration of vacancies. A comprehensive understanding of which of the two reactions will dominate can be addressed by a full micro-kinetic study. Figure 5.18 summarizes the main reaction pathway for the oxygen reduction reaction in an alkaline fuel cell. The key initiation steps for ORR, is governed by water dissociation or assisted by atomic oxygen and oxygen dissociation or hydrogen assisted oxygen dissociation. The activation barriers for these key steps are closely competitive and the relative facility of the reaction network's successive steps will indicate which reaction will dominate. Path A for ORR, will dominate due to facile intermediate steps. This means the ease to reduce the intermediate concentration of species through a series of facile steps will drive the reaction forward hence it will dominate, however this remarks exclude the surface concentration contributions to the rates of this reactions, therefore a full micro-kinetic analysis will give clear results.

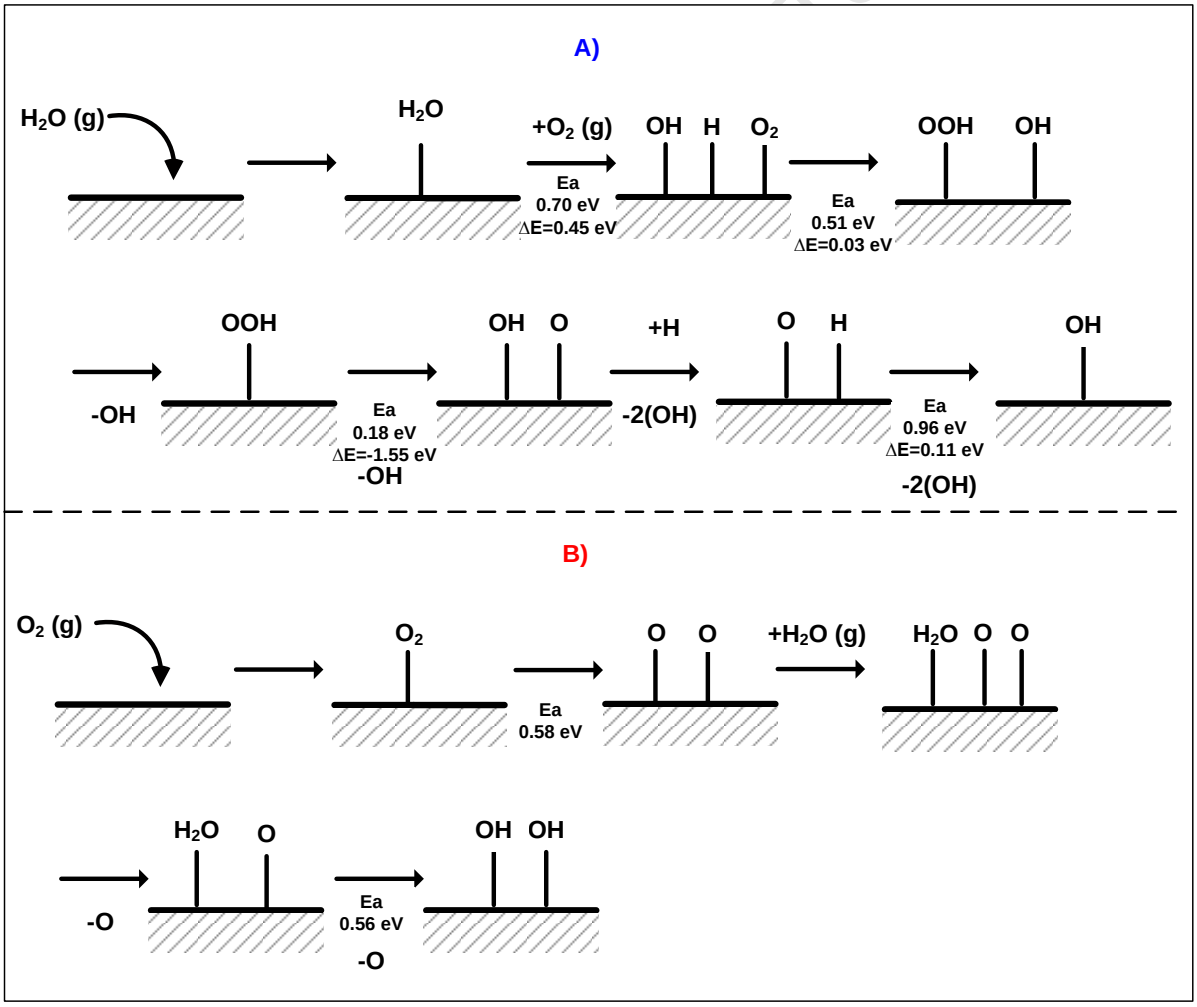

Figure 5.18: Oxygen reduction reaction pathway over Pt(111) in alkaline fuel cells

References

Barbir F., 'PEM Fuels Cells', Elsevier Academic Press (2005)

Bonnans J.F., Gilbert J.C., Lemararechal C., Sagastizabal C.A., Numerical optimization: Theoretical and practical aspects, University text, Springer-Verlag, Berlin (1997)

Damjanovic A., Brusic V., *Electrochimica Acta* **12** (1967), 615–628

Eichler A., Hafner, J., *Physical Review Letters* **79** (1997), 4481–4484

Eichler A., Mittendorfer F., Hafner J., *Physical Review B* **62** (2000), 4744–4755

Ford D.C., Nilekar A.U., Xu Y., Mavrikakis M., *Surface Science* **604** (2010), 1565–1575

Jónsson, H., group-site, <http://theory.cm.utexas.edu/vtsttools/neb/> UT Austin, viewed 16-07-2010 (2010)

Henkelman G., Uberuaga B.P., Jónsson H., *Journal of Chemical Physics* **113** (2000), 9901–9904

Hyman M.P., Medlin J.W., *The Journal Physical Chemistry B* **109** (2005), 6304–6314

Kresse G., Furthmuller J., *Physical Review B* **54** (1996), 11169–11186

Kresse G., Joubert J., *Physical Review B* **59** (1999), 1758–1775

Jónsson H., Mills G., Jacobsen K.W., World Scientific, Singapore (1998), 385–404

Michaelides A., HuP*., Journal of the American Chemical Society* **123** (2001), 4235–4242

Mills G., Jónsson H., *Physical Review Letter* **72** (1994), 1124–1127

Mills G., Jónsson H., Schenter G.K., *Surface Science* **324** (1995), 305–337

Nakanishi S., Mukouyama Y., Karasumi K., Imanishi A., Furuya N., Nakato Y., *The Journal of Physical Chemistry B* **104** (2000), 4181–4188

Nolan P.D., Lutz B.R., Tanaka P.L., Davis J.E., Mullins C.B., *Journal of Chemical Physics* **111** (1999), 3696–3704

Perdew J.P.,Burke K., Ernzerhof M., *Physical Review Letters* **77** (1996), 3865–3868

Phatak A.A., Delgass W.N., Ribeiro F.H., Schneider W.F., *The Journal of Physical Chemistry C* **113** (2009), 7269–7276

Sljivancanin Z., Hammer B., *Surface Science* **515** (2002), 235–244

Stair P.C., *Journal of the American Chemical Society* **104** (1982), 4044–4052

Stamenkovic V., Schmidt T.J., Ross P.N., Markovic N.M, *The Journal of Physical Chemistry B* **106** (2002), 11970–11979

Stipe B.C., Rezaei M.A., Ho W., Gao S., Persson M., Lundqvist B.I., *Physical Review Letter* **78** (1997), 4410–4413

Thiel P. A., Madey T.E., *Surface Science Reports* **7** (1987), 211–385

Van Santen, R.A., Niemantsverdriet, J.W., "Chemical Kinetics and Catalysis", Plenum Press, New York (1995)

Wang J.X., Markovic N.M., Adzic R.R., *The Journal of Physical Chemistry B* **108** (2004), 4127–4133

Yeager E., Razaq M., Gervasio D., Razak A., Tryk A.D., ‘Proceedings of workshop on structural effects in electrocatalysis and oxygen electrochemistry’ Electrochemical Society: Pennington, NJ, pp 440–473 (1992)

Chapter 6

6 GENERAL CONCLUSIONS

The objectives for this study were to investigate the stability of the species present during oxygen reduction (ORR) in an alkaline fuel cell when catalysed by platinum with the possibility to recombine and yield H_2O_2. The formation of H_2O_2 is undesired since it may affect the long-term stability of the cathode in the alkaline fuel cell. The study used density functional theory (DFT) to study potential pathways that could yield H_2O_2 during oxygen reduction reaction (ORR). The key initiation surface steps for oxygen reduction reaction (ORR) on Pt(111) were also investigated.

In alkaline fuel cells, H_2O and O_2 react to form OH^--ions. This reaction is said to be sluggish, hence contributing to the bulk of activation polarization in fuel cells. It was proposed that similar re-combination of the surface species may yield H_2O_2 through the following overall reaction:

$$2H_2O\,(g) + O_2(g) \rightarrow 2H_2O_2(g) \qquad (6.1)$$

The thermodynamics analysis for this reaction indicates that the reaction is non-spontaneous and has low equilibrium constant at 65°C.

The following species based on the literature review were proposed to be present during the oxygen reduction reaction (ORR): O_2, H_2O, H, O, OH and OOH. The combination between these species may yield H_2O_2. Based on earlier studies on pathways for the oxygen reduction reaction (ORR), it was proposed that H_2O_2 may potentially be formed through the following three unique paths.

Path-1: $$2\,H^* + O_2^* \rightarrow OOH^* + H^* \rightarrow H_2O_2^* \rightarrow H_2O_2\,(g) \qquad (6.2)$$

Path-2: $$H^* + O^* + OH^* \rightarrow OOH^* + H^* \rightarrow H_2O_2^* \rightarrow H_2O_2\,(g) \qquad (6.3)$$

Path-3: $$OH^*\,(aq) + OH^*(aq)\,H_2O_2^* \rightarrow H_2O_2\,(g) \qquad (6.4)$$

The strength of adsorption of the various species present during the oxygen reduction reaction (O_2, H_2O, H, O, OH, OOH and HOOH) were studied at a coverage of 0.25ML coverage on Pt(111) surface. It was noted that O, H, OH and OOH strongly bind to the surface. It has been proposed in earlier studies that some of these species, especially OH, have a poisoning effect on the surface.

The adsorption characteristics of this species allowed formulation of a potential energy surface (PES) illustrating the elementary steps towards forming H_2O_2. From the PES (see Figure 3.14) path-1 via O_2 activation with H showed to be the more favourable path, with the

lower activation barriers on the successive elementary steps estimated using BEP-relationship. The use of BEP-relationship to study activation barriers for the set of elementary steps must be applied with some caution since the parameters for this relationship are mainly derived from diatomic species.

The reaction between surface species requires the close proximity of the reacting species. Hence, the co-adsorption of various reaction intermediates was studied at an overall coverage of 0.5 ML. A unique phenomena was observed when increasing atomic oxygen coverage on Pt(111) to 0.5 ML, whereby the atomic oxygen species occupy neighbouring fcc and hcp 3-fold hollow sites. The surface showed to have been reconstructed where the platinum atoms on the top layer shifted out of the surface plane. This observation suggests further investigation on the atomic O saturation coverage on Pt(111) surface, since this phenomena could influence the catalytic properties of platinum during the oxygen reduction reaction (ORR). Furthermore, the co-adsorption of atomic oxygen at a high coverage resulted in a large energy requirement to bring these species together. This large repulsion between adsorbed atomic oxygen may moderate oxygen coverage on the surface during the oxygen reduction reaction (ORR).

The nudged elastic band (NEB) method was studied on the elementary steps during ORR towards forming H_2O_2. A good catalyst should completely reduce O_2 to water (PEM) or OH^- (AFC). However, a balance should be struck on its ability to catalyse O-O bond scission and O-H bond formation steps. Hydrogen peroxide was found to form via a side reaction of the hydrogen assisted oxygen dissociation step (O_2+H*), that has an activation barrier of 0.51 eV, a further addition of hydrogen only cost 0.44 eV towards forming hydrogen peroxide. With the favourable surface coverage of the required species, path-1 (see Figure 5.16) will dominate to yield hydrogen peroxide, due to the low activation barriers for the successive intermediate steps.

Various methods (BEP, Bader, NEB) were used to predict influences of the surface interaction on the activation barriers. Table 6.1 summarise all the results from various methods. It is apparent that the activation barriers for dissociation of oxygen and association of atomic oxygen and hydrogen (H*+O*) on Pt(111) can be estimated by BEP. The electrostatic forces acting on the charged species seems to be related to the activation energy (see Figure 6.1). The reactions, which require a co-adsorbed state, show a linear relationship between the obtained activation energy and the repulsive force between the species.

Table 6.1: Activation barriers estimated using BEP-relationship and calculated using NEB (with respect to separately adsorbed species at a coverage of 0.25 ML)

	BEP E_a(eV)	Electrostatic Force F(N)	NEB E_a(eV)
$H_2O^* \rightarrow OH^* + H^*$	1.29	3.78E-10	0.70
$O^*_2 \rightarrow O^* + O^*$	0.60	8.58E-09	0.58
$O^*_2 + H^* \rightarrow OOH^*$	1.07	4.26E-10	0.51
$O^* + H^* \rightarrow OH^*$	1.08	6.69E-10	0.96
$O^* + OH^* \rightarrow OOH^*$	3.73	8.85E-10	1.73
$H^* + OOH^* \rightarrow HOOH^*$	0.92	1.60E-10	0.44
$OH^* + OH^* \rightarrow HOOH^*$	4.58	1.04E-09	1.80

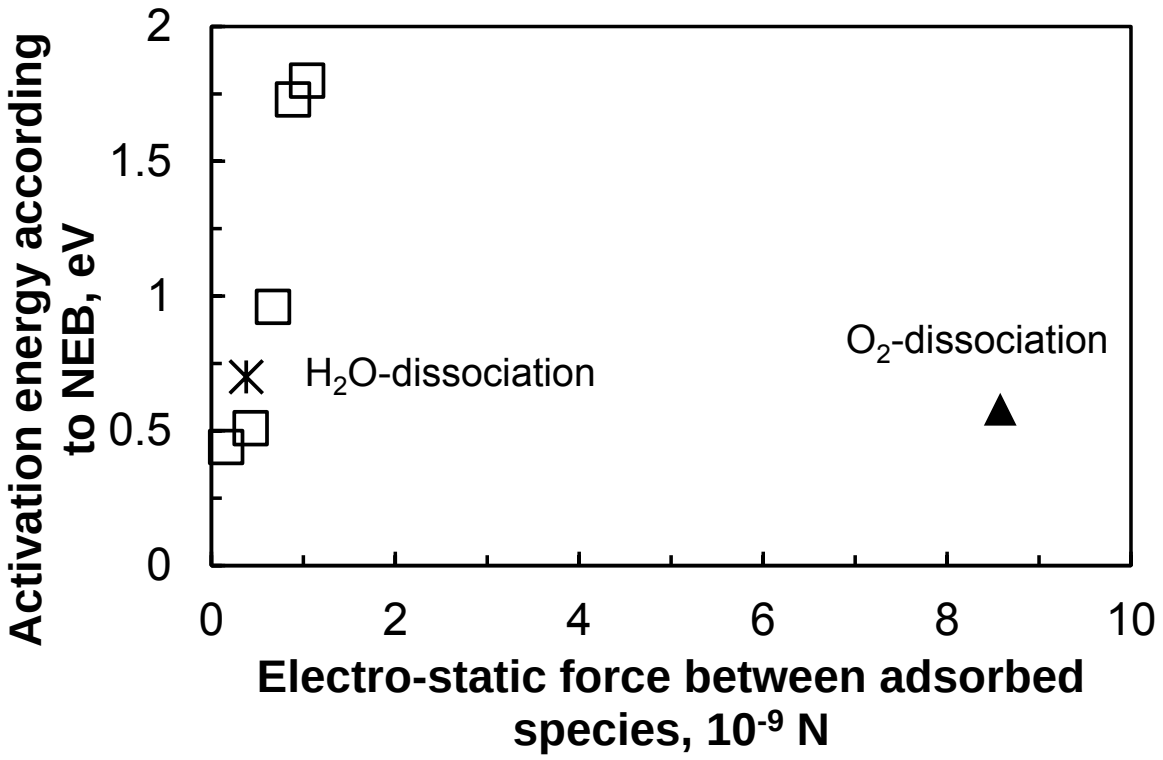

Figure 6.1: The activation energy as calculated using the NEB with respect to the separately adsorbed species at a coverage of 0.25 ML as a function of the electrostatic force between co-adsorbed species on a Pt(111) surface

Oxygen reduction reaction

It is desirable to completely reduce O_2 with ease, resulting in a lower activation polarization which will subsequently offer a high voltage from fuel cells. However from the intrinsic surface study and results for O_2 reduction on this work, it was shown that O_2 reduction on platinum to be a series of elementary steps which consequently may result in high energy losses in fuel cells. The origin of the slow kinetics for the oxygen reduction reactions (ORR) in alkaline fuel cell can be explained due to the high activation barriers for the reaction steps required to completely dissociate O_2 and to dissociate water as shown on Figure 5.15 and Figure 5.16. From this study, it is concluded that the oxygen reduction reaction (ORR) is governed by closely competing elementary steps. These conclusions are made with cautions since only a full micro-kinetic analysis can validate the current analysis.

6.1.1 Recommendations

The results discussed in this manuscript only focused on the activation energies contribution to the intrinsic reaction kinetics. However to get a more comprehensive analysis a full micro-kinetics study is recommended. The micro-kinetics study could be extended to the entropy effects as well as studying the concentration of the ORR species on the catalyst surface and also the availability of vacant sites on the catalyst surface. The micro-kinetic analysis will offer the rates of ORR v/s the rate of H_2O_2 formation and further gives information about the dominant/poisoning species available on the catalyst surface in fuel cells during ORR.

APPENDIX A

A.1 MODEL VALIDATION

K – POINTS AND CUT OFF ENERGY OPTIMISATION

All platinum bulk calculation were performed on a primitive unit cell

Table A. 1 : k-points optimisation (PAW-RPBE) at cut off energy (600 eV), where E_n is the energy of the last k-point mesh

K-Points	Irreducible k-points	Energy (eV)	$\Delta[E_i - E_n]$
11×11×11	56	-5.2490	1.47E-02
13×13×13	84	-5.2327	1.58E-03
10×10×10	110	-5.2346	3.85E-04
15×15×15	120	-5.2310	3.27E-03
12×12×12	182	-5.2347	4.88E-04
14×14×14	280	-5.2338	4.07E-04
16×16×16	408	-5.2342	

Table A. 2: cut-off energy optimisation (PAW-RPBE) at k-point setting of 12×12×12, where E_n is the energy of the last cut-off energy (600 eV)

Cut-off energy	Energy(eV)	$\Delta[E_i - E_n]$
300	-5.2299	4.8E-03
350	-5.2314	3.3E-03
400	-5.2332	1.5E-03
450	-5.2334	1.3E-03
500	-5.2337	1.0E-03
550	-5.2343	4.2E-04
600	-5.2347	

Table A. 3 : k- points optimisation (uspp-GGA-PW91) at cut off energy (600 eV), where E_n is the energy of the last k-point mesh

K-Points	Irreducible k-points	Energy (eV)	$\Delta[E_i - E_n]$
11×11×11	56	-5.9938	1.39E-02
13×13×13	84	-5.9768	3.13E-03
10×10×10	110	-5.9804	3.98E-04
15×15×15	120	-5.9768	3.17E-03
12×12×12	182	-5.9803	3.74E-04
14×14×14	280	-5.9796	3.19E-04
16×16×16	408	-5.9800	

Table A. 4 : cut-off energy optimisation (uspp-GGA-PW91) at k-point setting of 12×12×12,where E_n is the energy of the last cut-off energy (600 eV)

Cut-off energy	Energy(eV)	$\Delta[E_i - E_n]$
300	-5.9805	1.8E-04
350	-5.9810	6.5E-04
400	-5.9807	4.1E-04
450	-5.9803	7.0E-06
500	-5.9804	2.1E-05
550	-5.9804	5.4E-05
600	-5.9803	

Table A. 5 : k-points optimisation (PAW-PBE)at cut off energy (600 eV), where E_n is the energy of the last k-point mesh

K-Points	Irreducible k-points	Energy (eV)	$\Delta[E_i - E_n]$
11×11×11	56	-6.0514	1.51E-02
13×13×13	84	-6.0351	1.17E-03
10×10×10	110	-6.0367	3.87E-04
15×15×15	120	-6.0331	3.26E-03
12×12×12	182	-6.0368	5.37E-04
14×14×14	280	-6.0359	4.20E-04
16×16×16	408	-6.0363	

Table A. 6 : cut-off energy optimisation (PAW-PBE) at k-point setting of 12×12×12,where E_n is the energy of the last cut-off energy (600 eV)

Cut-off energy	Energy(eV)	$\Delta[E_i - E_n]$
300	-6.0355	1.3E-03
350	-6.0349	1.9E-03
400	-6.0361	7.9E-04
450	-6.0362	6.6E-04
500	-6.0363	5.3E-04
550	-6.0366	2.4E-04
600	-6.0368	

Table A. 7 : k-points optimisation (PAW-PW91) at cut off energy (600 eV),where E_n is the energy of the last k-point mesh

K-Points	Irreducible k-points	Energy (eV)	$\Delta[E_i - E_n]$
11×11×11	56	-6.0322	1.46E-02
13×13×13	84	-6.0157	1.90E-03
10×10×10	110	-6.0180	3.84E-04
15×15×15	120	-6.0143	3.28E-03
12×12×12	182	-6.0180	4.70E-04
14×14×14	280	-6.0172	3.92E-04
16×16×16	408	-6.0176	

Table A. 8: cut-off energy optimisation (PAW-PW91) at k-point setting of 12×12×12,where E_n is the energy of the last cut-off energy (600 eV)

Cut-off energy	Energy(eV)	$\Delta[E_i - E_n]$
300	-6.0180	1.3E-05
350	-6.0167	1.4E-03
400	-6.0175	5.8E-04
450	-6.0176	4.8E-04
500	-6.0176	4.1E-04
550	-6.0178	2.1E-04
600	-6.0180	

A.2 BULK PROPERTIES, CALCULATED RESULTS

	Bulk Modulus (B_0) Gpa	Pressure Derivative(B'_0)	Equilibrium Volume(V_0) Å^3	Lattice Constant
Experimental Values at 300K [a]Kittel,1996; [b]Ashcroft et al.,1988	**[a]278**	**5.610**	**15.095**	**[b]2.775**
PAW_RPBE	**216.2**	**5.549**	**16.022**	**2.838**
% Div from Experimental value	22.2	1.1	6.1	2.3
PAW_PBE	**231.8**	**5.473**	**15.830**	**2.783**
% Div from Experimental value	16.6	2.4	4.9	0.3
PAW_PW91	**228.7**	**5.457**	**15.939**	**2.776**
% Div from Experimental value	17.7	2.7	5.6	0.05
uspp_PW91	**220.5**	**5.388**	**16.009**	**2.844**
% Div from Experimental value	20.7	4.0	6.1	2.5

BIRCH-MURNAGHAN FIT ON THE DATA

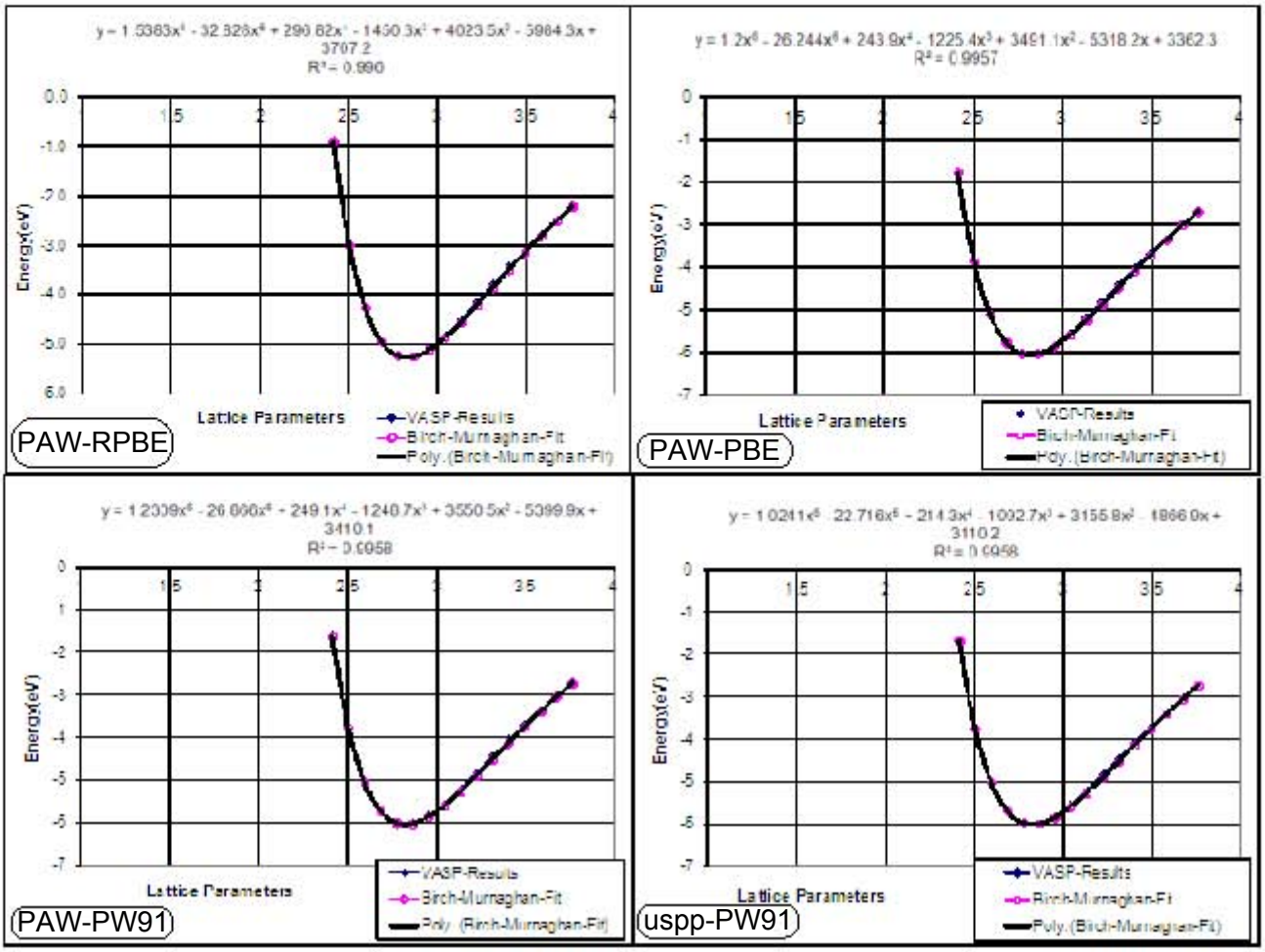

SURFACE CALCULATIONS

The platinum bulk structure with the corresponding lattice constant from the various functionals and supporting pseudo-potential was cleaved on a (111) plane

The Pt(111) surface energy slab were re-optimised with respect to k-points and cut-off energy:

Table A. 9 : k-points optimisation (PAW-RPBE) at cut off energy (600 eV), where E_n is the energy of the last k-point mesh

K-Points	Irreducible k-points	Energy (eV)	$\Delta[E_i - E_n]$
11×11×1	56	-51.5424	3.99E-03
13×13×1	84	-51.4586	1.28E-02
10×10×1	110	-51.4744	9.61E-03
15×15×1	120	-51.5037	3.75E-03
12×12×1	182	-51.5312	1.75E-03
14×14×1	280	-51.5225	

Table A. 10: cut-off energy optimisation (PAW-RPBE) at k-point setting of 12×12×1,where E_n is the energy of the last cut-off energy (600 eV)

Cut-off energy	Energy(eV)	$\Delta[E_i - E_n]$
300	-51.4926	7.72E-03
350	-51.5049	5.26E-03
400	-51.5194	2.35E-03
450	-51.5206	2.11E-03
500	-51.5237	1.50E-03
550	-51.5283	5.88E-04
600	-51.5312	

Table A. 11 : k-points optimisation (uspp-GGA-PW91) at cut off energy (600 eV), where E_n is the energy of the last k-point mesh dimension

K-Points	Irreducible k-points	Energy (eV)	$\Delta[E_i - E_n]$
11×11×1	56	-58.7878	4.35E-03
13×13×1	84	-58.7035	1.25E-02
10×10×1	110	-58.7260	8.02E-03
15×15×1	120	-58.7502	3.17E-03
12×12×1	182	-58.7754	1.86E-03
14×14×1	280	-58.7661	

Table A. 12: cut-off energy optimisation (uspp-GGA-PW91) at k-point setting of 12×12×1,where E_n is the energy of the last cut-off energy (600 eV)

Cut-off energy	Energy(eV)	$\Delta[E_i - E_n]$
300	-58.7761	1.35E-04
350	-58.7810	1.13E-03
400	-58.7786	6.37E-04
450	-58.7753	2.42E-05
500	-58.7755	3.38E-05
550	-58.7759	1.02E-04
600	-58.7754	

Table A. 13 : k-points optimisation (PAW-PBE) at cut off energy (600 eV), where E_n is the energy of the last k-point mesh dimension

K-Points	Irreducible k-points	Energy (eV)	$\Delta[E_i - E_n]$
11×11×1	56	-59.3029	3.68E-03
13×13×1	84	-59.2127	1.44E-02
10×10×1	110	-59.2199	1.29E-02
15×15×1	120	-59.2611	4.68E-03
12×12×1	182	-59.2829	3.15E-04
14×14×1	280	-59.2845	

Table A. 14: cut-off energy optimisation (PAW-PBE) at k-point setting of 12×12×1, where E_n is the energy of the last cut-off energy (600 eV)

Cut-off energy	Energy(eV)	$\Delta[E_i - E_n]$
300	-59.2727	2.05E-03
350	-59.2645	3.68E-03
400	-59.2758	1.43E-03
450	-59.2770	1.19E-03
500	-59.2781	9.62E-04
550	-59.2807	4.42E-04
600	-59.2829	

Table A. 15 : k-points optimisation (PAW-PW91) at cut off energy (600 eV), where E_n is the energy of the last k-point mesh dimension

K-Points	Irreducible k-points	Energy (eV)	$\Delta[E_i - E_n]$
11×11×1	56	-59.1013	3.28E-03
13×13×1	84	-59.0122	1.45E-02
10×10×1	110	-59.0221	1.26E-02
15×15×1	120	-59.0625	4.49E-03
12×12×1	182	-59.0857	1.64E-04
14×14×1	280	-59.0849	

Table A. 16: cut-off energy optimisation (PAW-PW91) at k-point setting of 12×12×1,where E_n is the energy of the last cut-off energy (600 eV)

Cut-off energy	Energy(eV)	$\Delta[E_i - E_n]$
300	-59.0880	4.65E-04
350	-59.0732	2.51E-03
400	-59.0811	9.20E-04
450	-59.0821	7.25E-04
500	-59.0827	6.08E-04
550	-59.0845	2.34E-04
600	-59.0857	

VACUUM SPACING OPTIMISATION

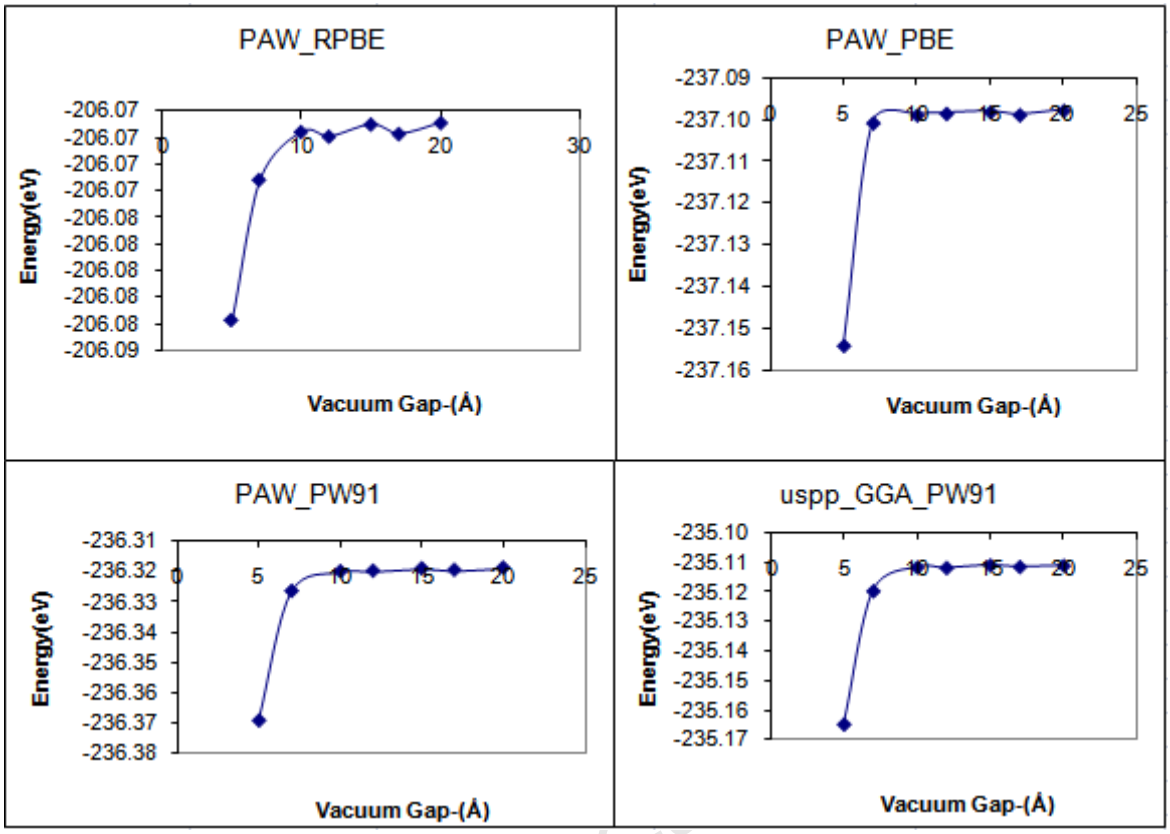

Figure A.1: Vacuum spacing optimisation for all the functionals and their supporting pseudo potential studied, showing convergence at a vacuum gap of 10 (Å), with the k-point mesh at 6×6×1 (unit cell size p(2×2)) and the cut-off energy at 400 eV

The data used to produce Figure A. 1 is also outlined in the followingtables (unit cell size p(2×2)):

Table A. 17: Data for vacuum optimisation at k-point settings of 6×6×1 and cut off of 400 (eV)

PAW_RPBE		
Vacuum gap(Å)	Energy(eV)	$\Delta[E_n - E_{n-1}]$
5	-206.0838	
7	-206.0732	1.06E-02
10	-206.0696	3.60E-03
12	-206.0699	3.47E-04
15	-206.0690	9.15E-04
17	-206.0697	7.20E-04
20	-206.0689	8.31E-04

Table A. 18: Data for vacuum optimisation at k-point settings of 6×6×1 and cut off of 400 (eV)

PAW_PBE		
Vacuum gap(Å)	Energy (eV)	$\Delta[E_n - E_{n-1}]$
5	-237.1541	
7	-237.1007	5.34E-02
10	-237.0988	1.87E-03
12	-237.0984	3.62E-04
15	-237.0981	3.78E-04
17	-237.0988	7.06E-04
20	-237.0977	1.03E-03

Table A. 19: Data for vacuum optimisation at k-point settings of 6×6×1 and cut off of 400 (eV)

PAW_PW91		
Vacuum gap(Å)	Energy (eV)	$\Delta[E_n - E_{n-1}]$
5	-236.3693	
7	-236.3266	8.55E-03
10	-236.3201	1.29E-03
12	-236.3199	3.52E-05
15	-236.3191	1.59E-04
17	-236.3196	1.03E-04
20	-236.3189	1.43E-04

Table A. 20: Data for vacuum optimisation at k-point settings of 6×6×1 and cut off of 400 (eV)

uspp_GGA_PW91		
Vacuum gap(Å)	Energy (eV)	$\Delta[E_n - E_{n-1}]$
5	-235.1649	
7	-235.1196	4.53E-02
10	-235.1115	8.06E-03
12	-235.1117	1.68E-04
15	-235.1109	8.41E-04
17	-235.1114	5.10E-04
20	-235.1110	4.23E-04

VACUUM OPTIMISATION ON A P(1×1) UNIT CELL

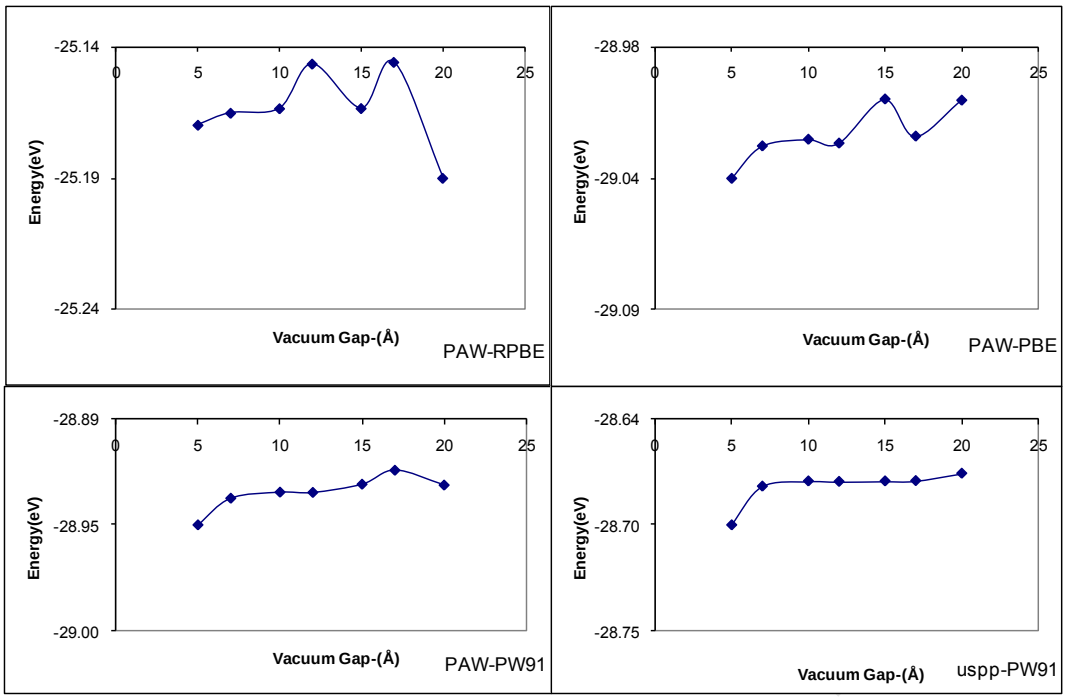

SURFACE ENERGY CALCULATIONS ON P(1×1) UNIT CELL

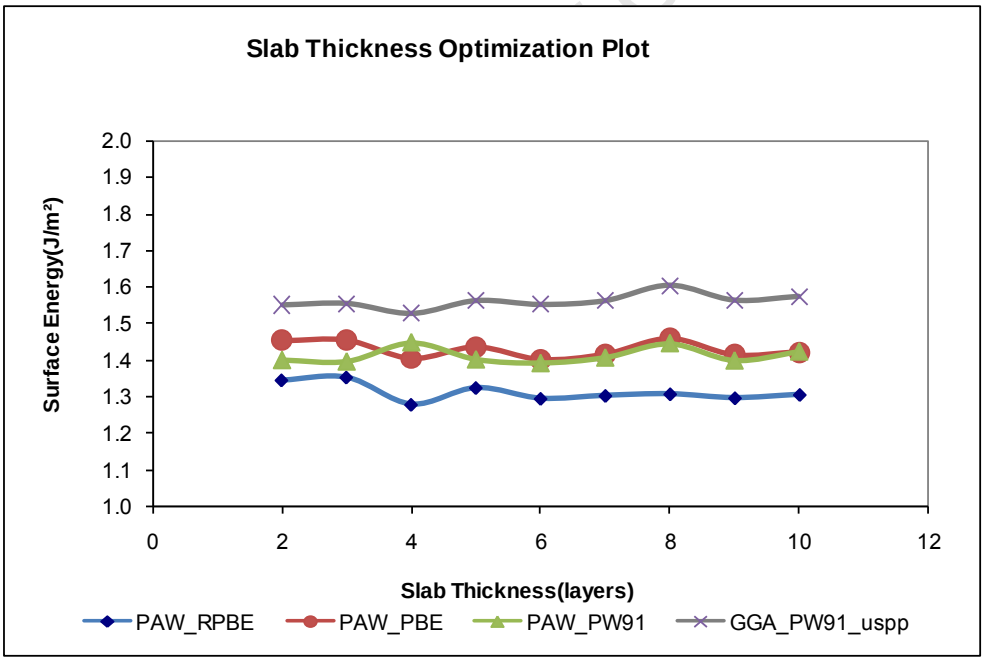

SLAB THICKNESS OPTIMISATION

The slab thickness optimisation was performed on a p(2×2) unit cell with PAW-PBE. The surface was probed by atomic oxygen, which allowed for slab thickness optimisation with respect to adsorption energy ($E_{ads} = E_{slab+species} - E_{slab} - E_{O\text{-}gas}$). The study tested for energy convergence for the top three and two layers free to relax.

Table A. 21: Slab thickness optimisation, allowing the top three layers to relax (k-points: 6×6×1 (unit cell size: Cut-off: 400 eV)

Slab Thickness	Adsorption Energy (eV)	$\Delta[E_n - E_{n-1}]$
3	-3.7883	
4	-3.6584	1.30E-01
5	-3.7368	7.84E-02
6	-3.7169	2.00E-02
7	-3.7236	6.75E-03
8	-3.7212	2.43E-03

The convergence was kept at ~1 meV/O-atom. The data for the top three relaxed layers, the data did not show a smooth convergence.

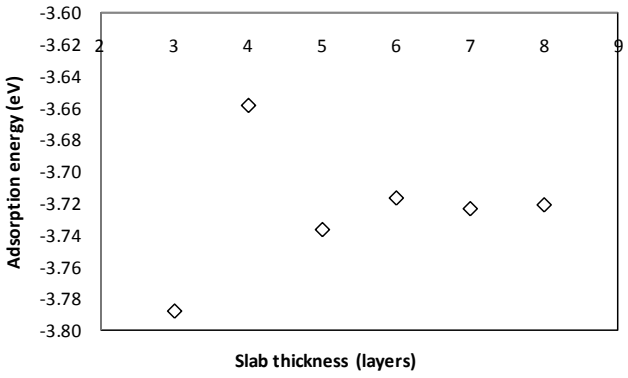

Figure A.2: Slab thickness optimization with the first top three layers free to relax: (k-points: 6×6×1, Cut-off:400 eV)

The following data represents the slab thickness test when only allowing the top two layers to relax.

Table A. 22: Slab thickness test with the top two layers allowed to relax: k-points:6×6×1, cu-off: 400 eV

Slab Thickness	Adsorption Energy (eV)	$\Delta[E_n - E_{n-1}]$
4	-3.6404	
5	-3.7239	8.34E-02
6	-3.7101	1.37E-02
7	-3.7113	1.17E-03
8	-3.7115	1.68E-04

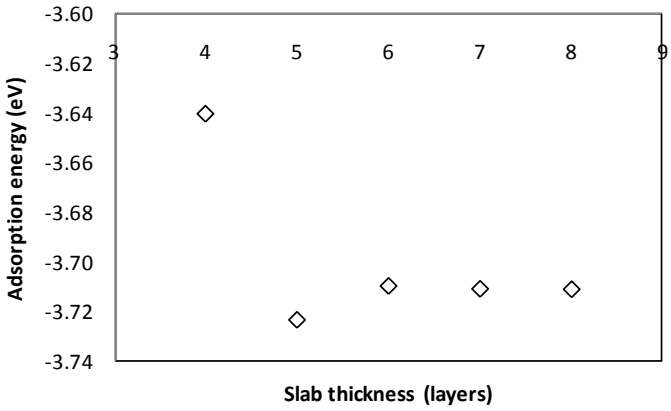

Figure A. 3: Slab thickness optimization with the first top two layers free to relax: (k-points: 6×6×1, Cut-off:400 eV)

THERMODYNAMIC CALCULATIONS:

The formulas are based on work done by Hirano (1993), ref: Hirano T., in MOPAC Manual, 7th edition, Sterwart J.J.P., Ed 1993

No all the thermodynamic equations were used in the manuscript:

Enthalpy:

$H(T) = E_{VIB}(T) + E_{ROT}(T) + E_{TRANS}(T)$

Subscripts stand for vibrational, rotational and translational contributions respectively

$$E_{\text{trans}} = \frac{3}{2} \cdot R \cdot T$$

$$E_{\text{rot}}(linear) = R \cdot T$$

$$E_{\text{rot}}(non-linear) = \frac{3}{2} \cdot R \cdot T$$

$$E_{\text{vib}} = \frac{\text{R}}{\kappa} \cdot \frac{1}{2} \cdot \sum_i \hbar \cdot \nu_i + \frac{R}{\kappa} \cdot \sum_i \frac{\hbar \nu_i \exp(-\hbar \nu_i / \kappa T)}{[1 - \exp(-\hbar \nu_i / \kappa T)]}$$

k is the Boltzmann's constant, *h*is the Plank's constant, V_i are the individual vibrational frequencies

Entropy

The entropy contributions, S, are given by the following expressions:

$$S_{\text{trans}} = \frac{5}{2} \cdot R \ln T + \frac{3}{2} \cdot R \ln w - R \ln p - 2.31482$$

$$S_{\text{rot}}(linear) = R \ln \left[\frac{8\pi^2 IKT}{\sigma \cdot \hbar^2} \right] + R$$

$$S_{\text{rot}}(non-linear) = \frac{R}{2} \ln \left[\frac{\pi}{\sqrt{\sigma}} \cdot \frac{8\pi^2 c I_A}{\hbar} \cdot \frac{8\pi^2 c I_B}{\hbar} \cdot \frac{8\pi^2 c I_C}{\hbar} \cdot \left(\frac{\kappa T}{\hbar c} \right)^3 \right] + \frac{3}{2} R$$

$$S_{\text{vib}} = R\sum_i \frac{\hbar\nu_i/\kappa T \cdot \exp(-\hbar\nu_i/\kappa T)}{1-\exp(-\hbar\nu_i/\kappa T)} - R\sum_i \ln[1-\exp(-\hbar\nu_i/\kappa T)]$$

w molecular weight, *p* pressure, *I* moment of inertia, σ symmetrical number

APPENDIX B

CHAPTER 3

ADSORPTION MODELS

Different configurations for all the species presented on this manuscript were studied to find the most stable (minimum in energy) configuration and preferred site.

Molecular oxygen adsorption configurations:

HCP site

Configuration one

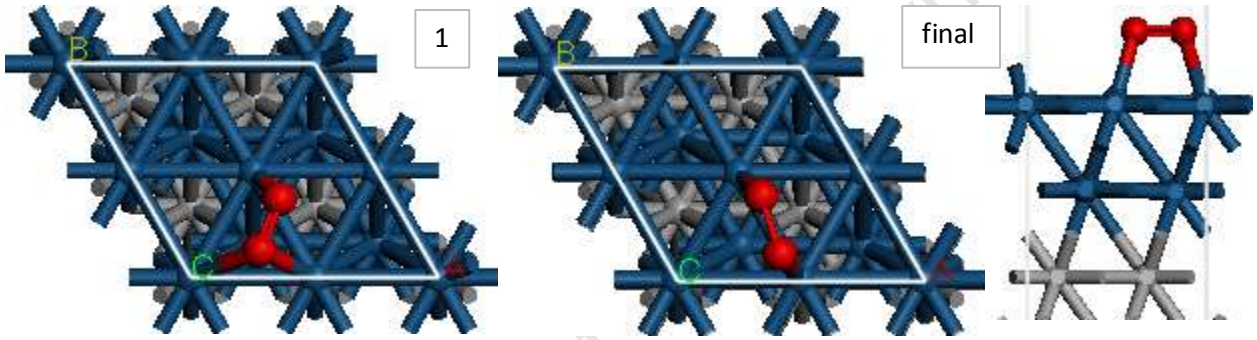

Energy = -150.915 eV

Configuration two

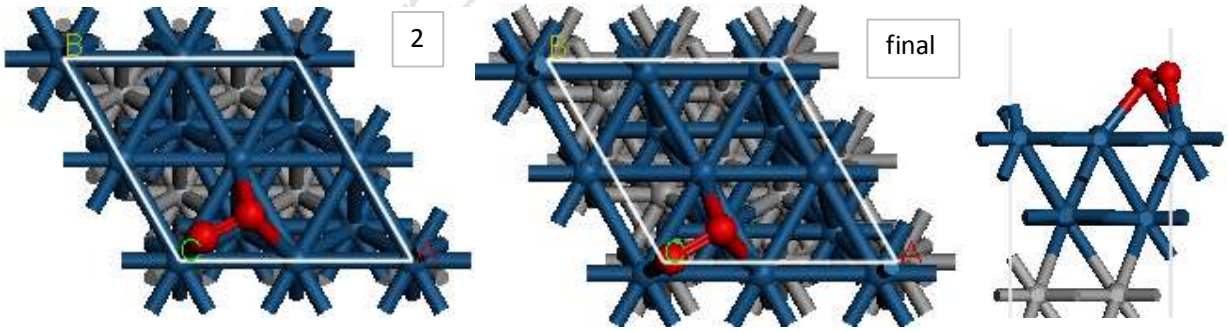

Energy = -150.853 eV

Configuration three

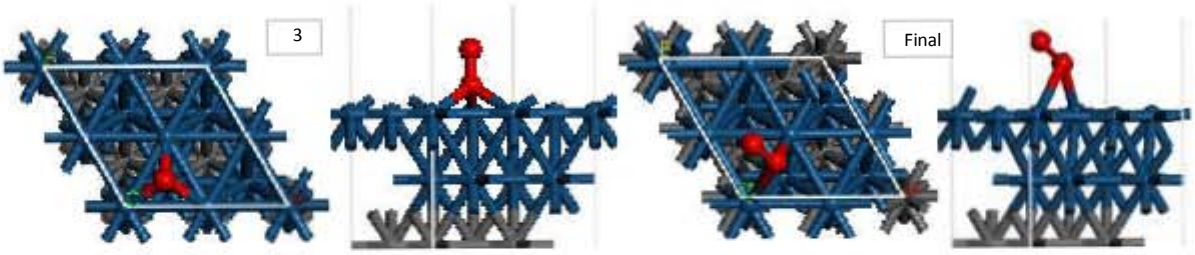

Energy = -150.270 eV

FCC site

Configuration one

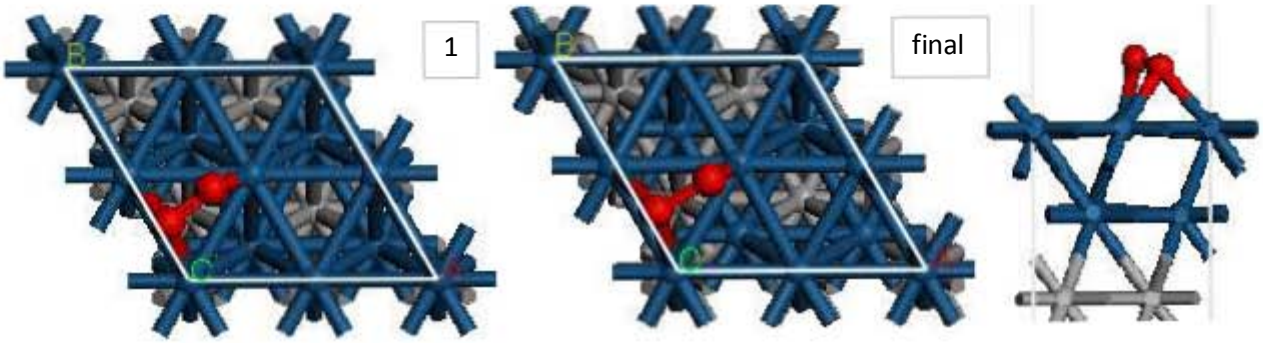

Energy = - 150.959 eV

Configuration two

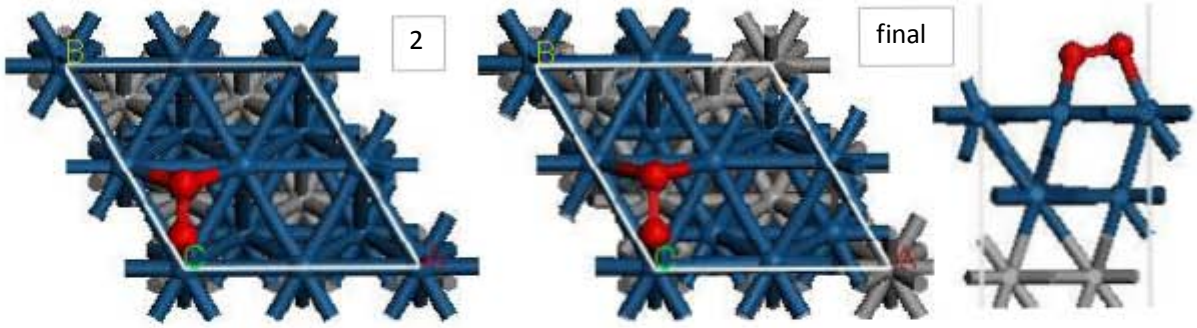

Energy = - 150.960 eV

Configuration three

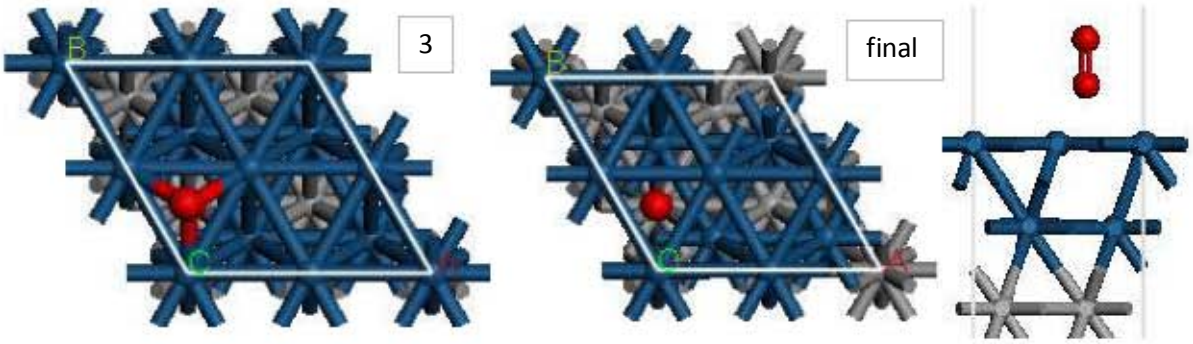

Energy = - 150.095 eV

Bridge site

Configuration one

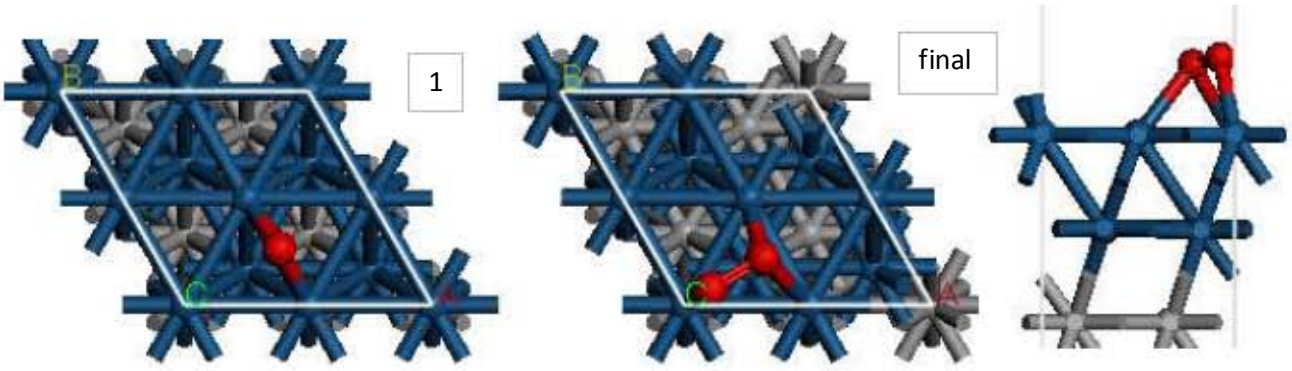

Energy = - 150.422 eV

Configuration two

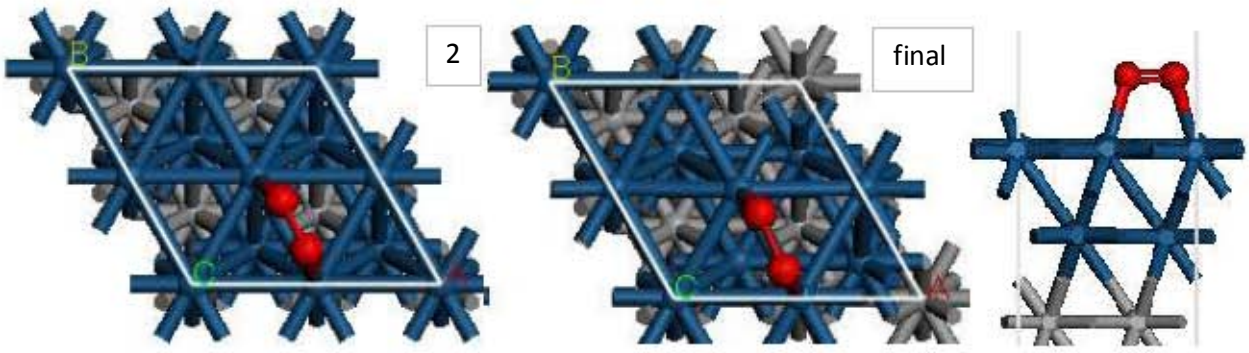

Energy = - 150.916 eV

On-Top site

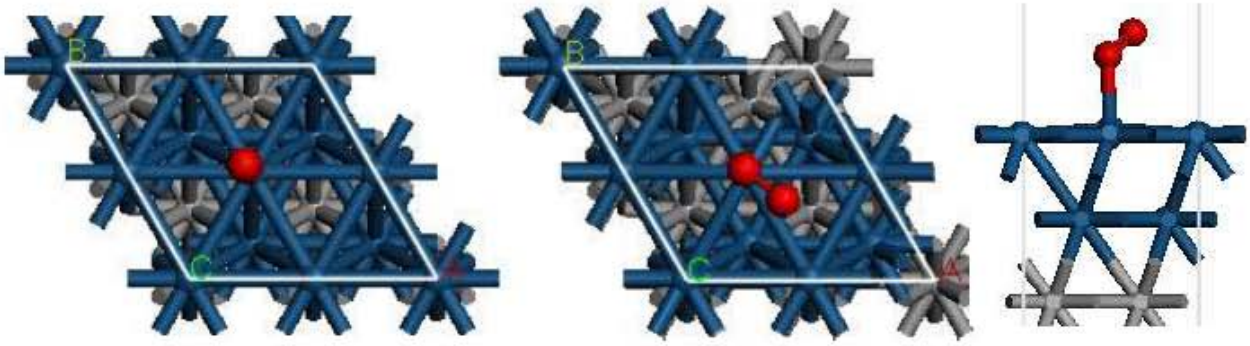

Energy = -150.422 eV

Oxygen on the bridge to bridge sites:

Initial

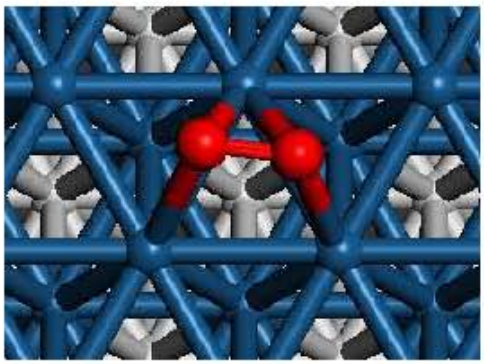

Final

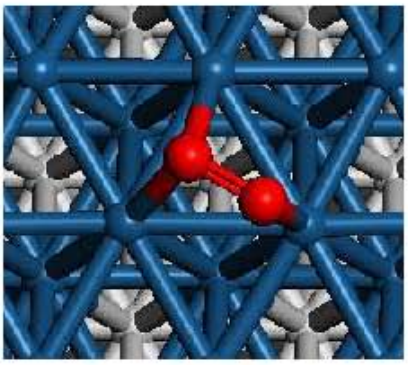

Energy: -151.87 eV

Initial

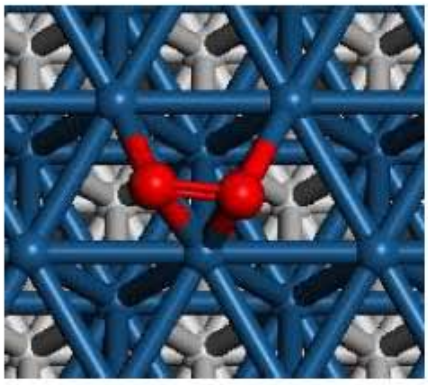

Final

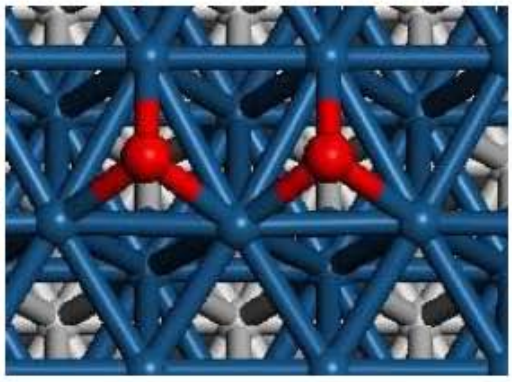

Energy: -150.96 eV

Water adsorption configurations:

HCP site

Configuration one

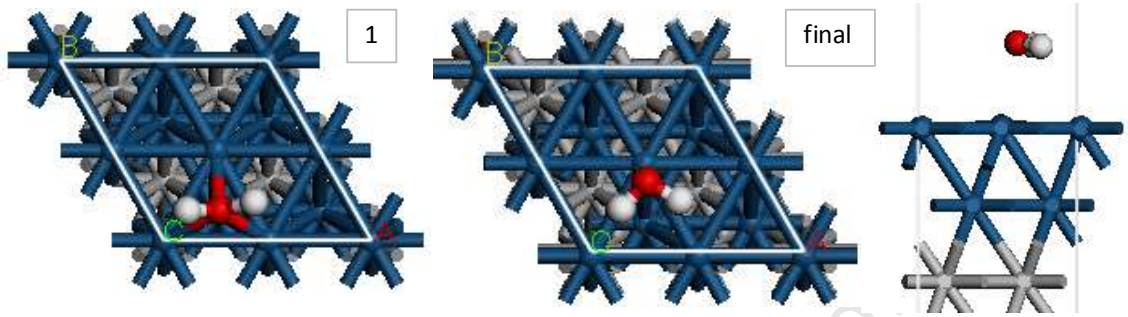

Energy = -154.934 eV

Configuration two

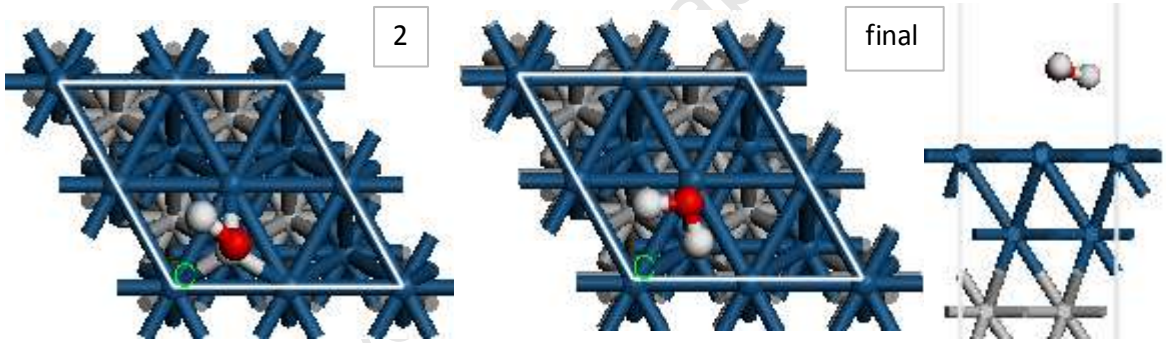

Energy = -154.930 eV

Configuration three

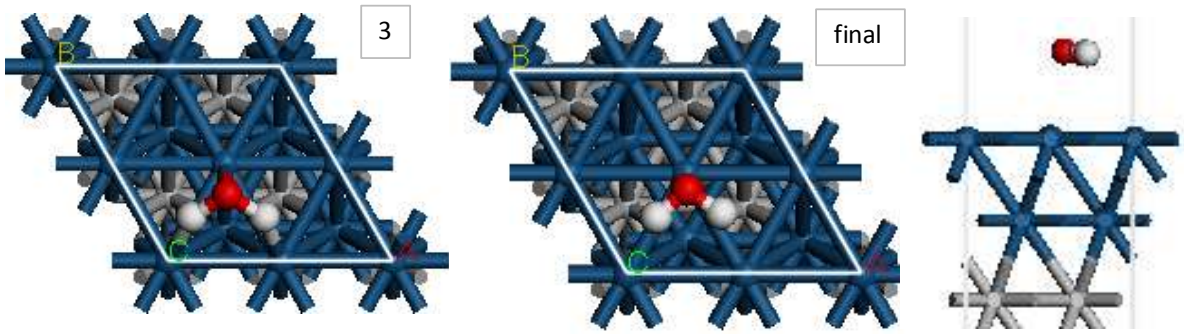

Energy = - 154.945 eV

Configuration 4

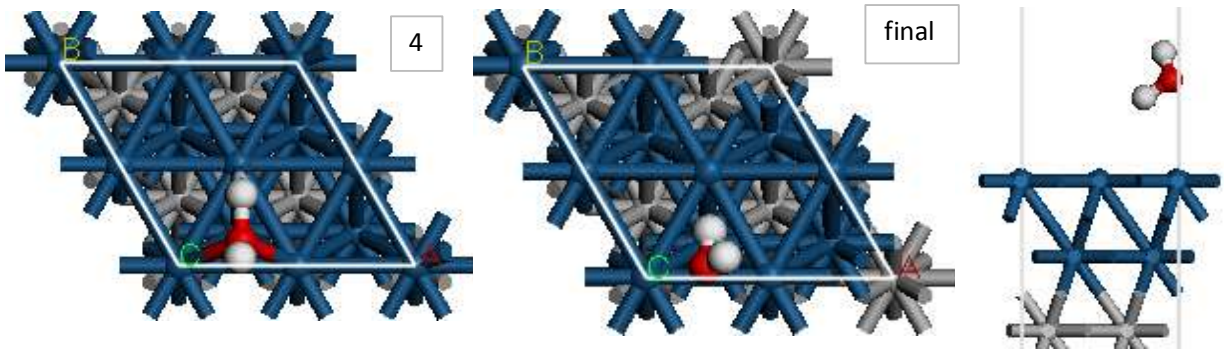

Energy = - 154.816 eV

Configuration 5

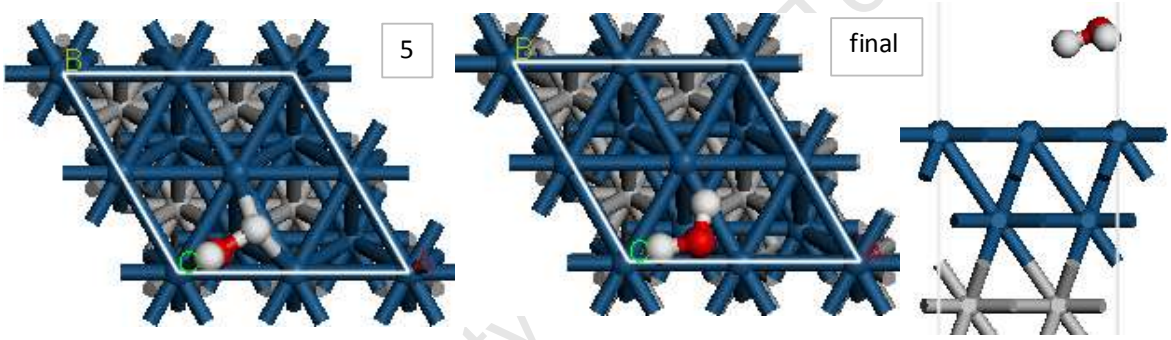

Energy = - 154.852 eV

FCC site

Configuration one

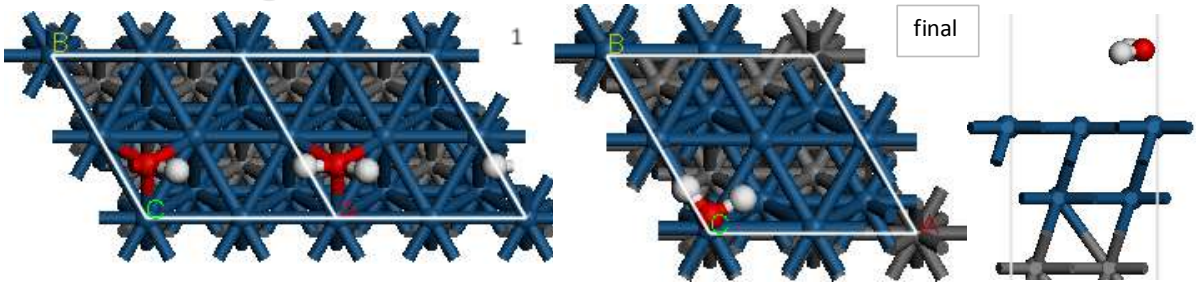

Energy = -154.939 eV

Configuration two

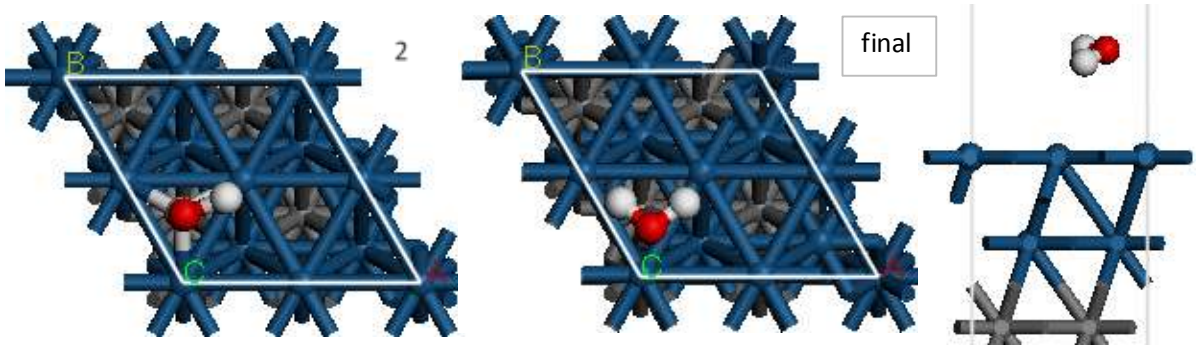

Energy = - 154.865 eV

Configuration three

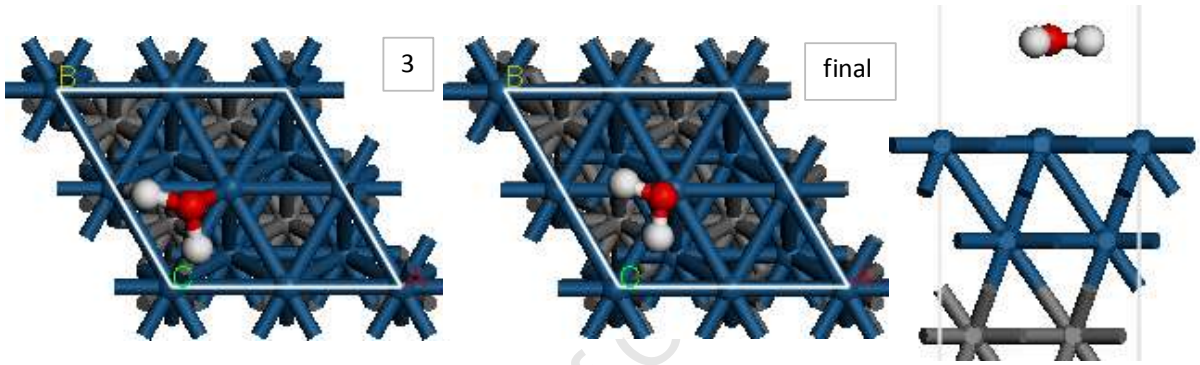

Energy = - 154.942 eV

Configuration four

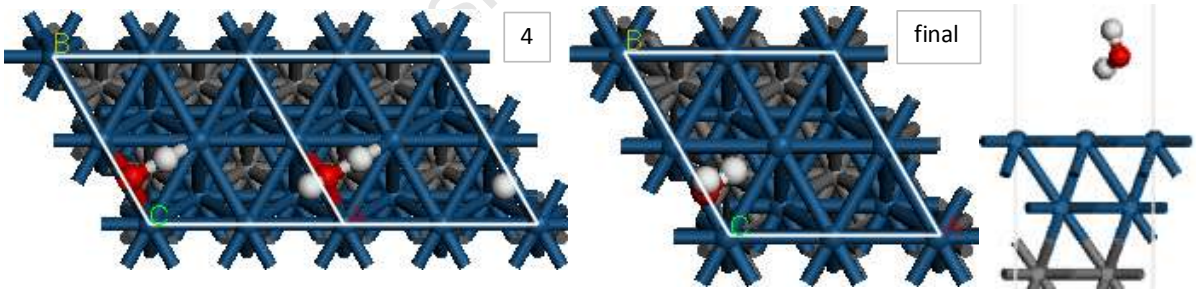

Energy = - 154.780 eV

Configuration five

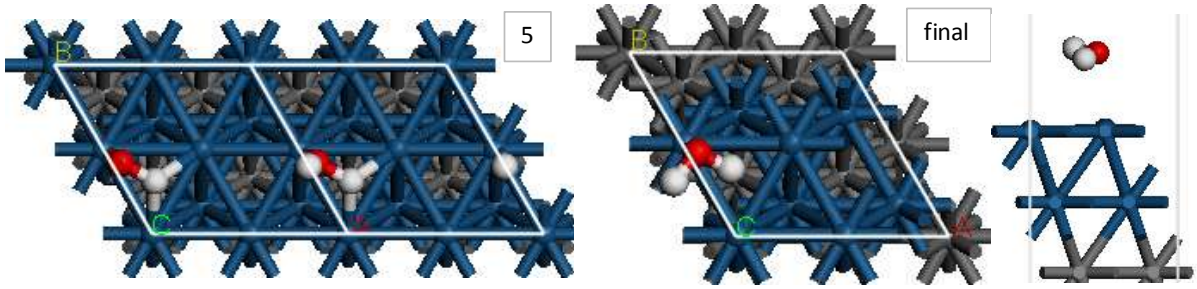

Energy = - 154.933 eV

On-Top site

Configuration one

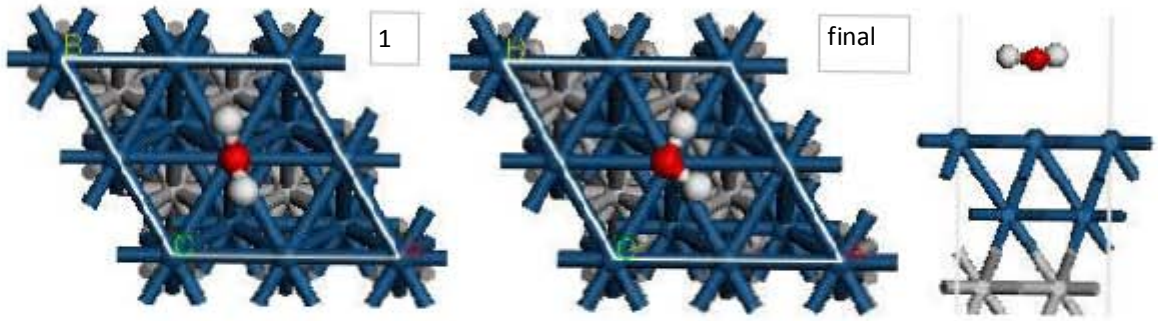

Energy = - 154.904 eV

Configuration two

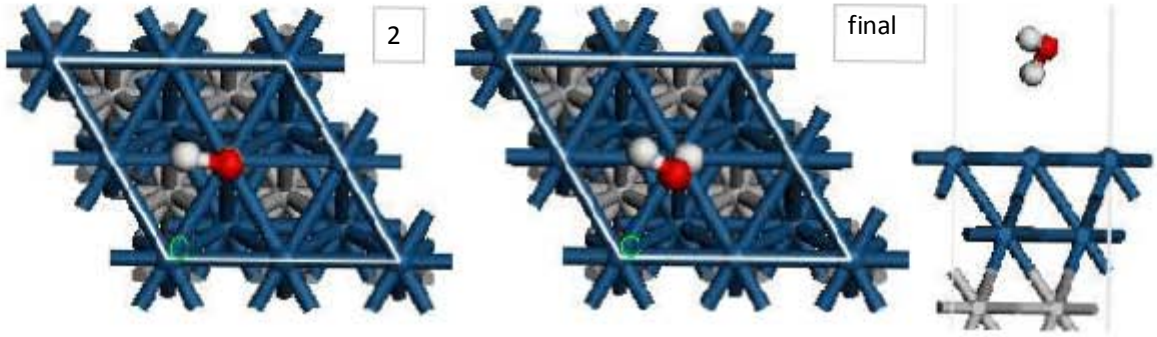

Energy = - 154.814 eV

Bridge site

Configuration one

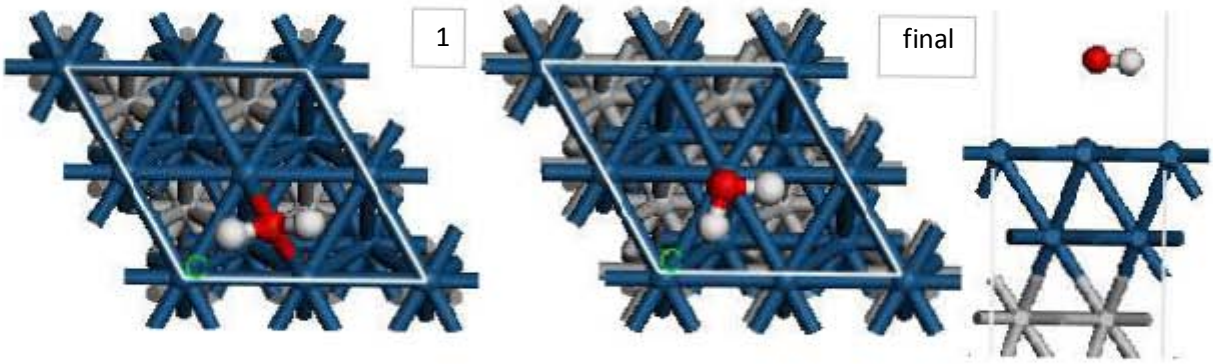

Energy = - 154.923 eV

Configuration two

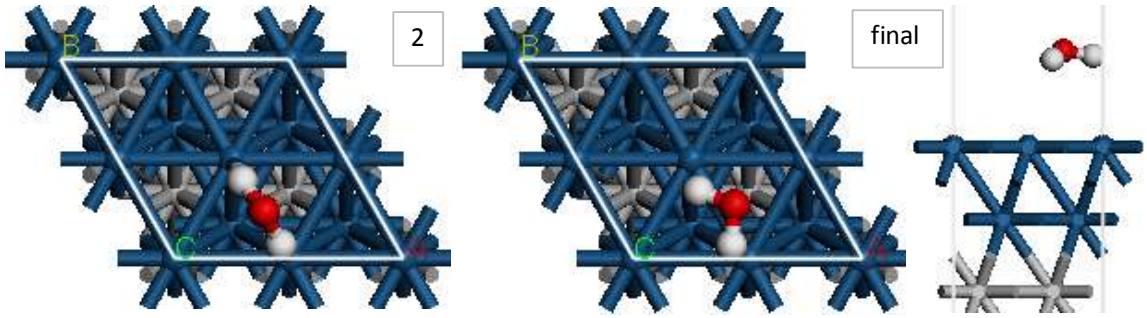

Energy = - 154.833 eV

Configuration three

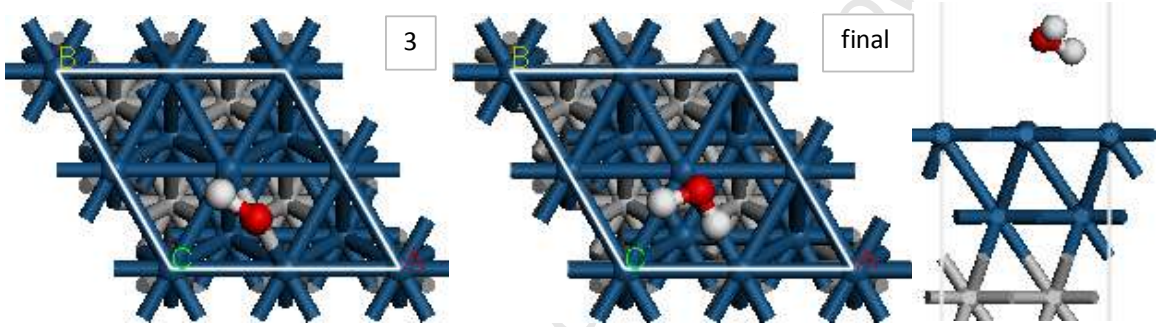

Energy = - 154.911 eV

Configuration four

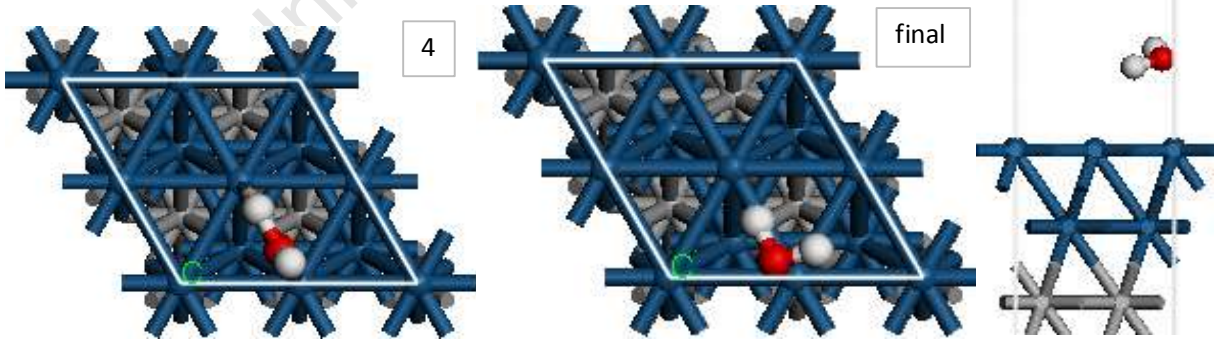

Energy = - 154.905 eV

OH adsorption configuration:

Configuration one

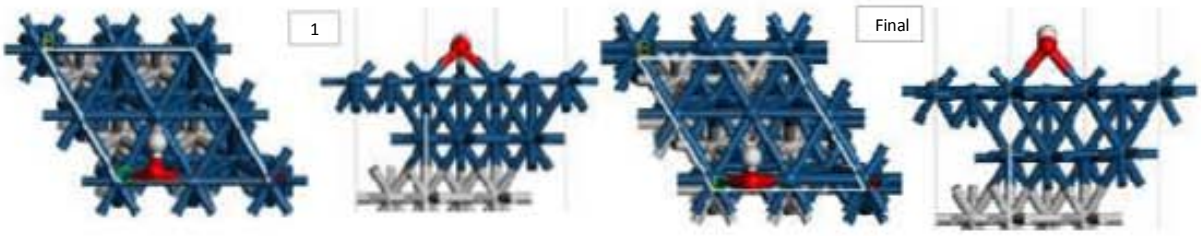

Energy = - 150.471 eV

Configuration two

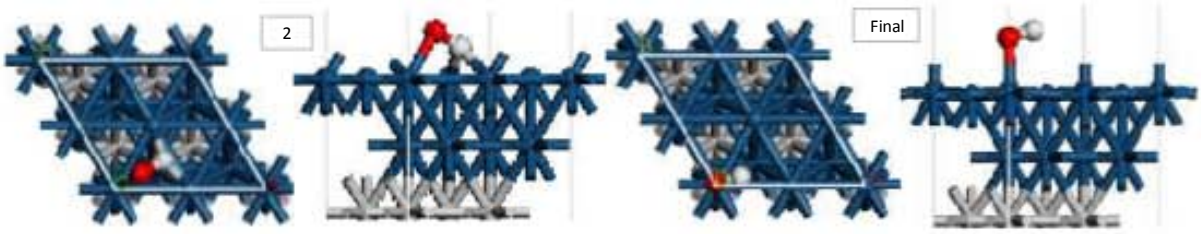

Energy = -150.422 eV

Configuration three

Energy = - 150.471 eV

Configuration four

Energy = - 150.471 eV

OOH adsorption configuration:

HCP site

Configuration one

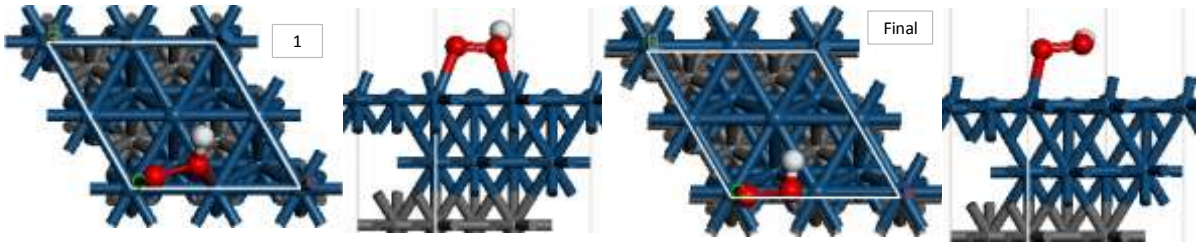

Energy = - 154.885 eV

Configuration two

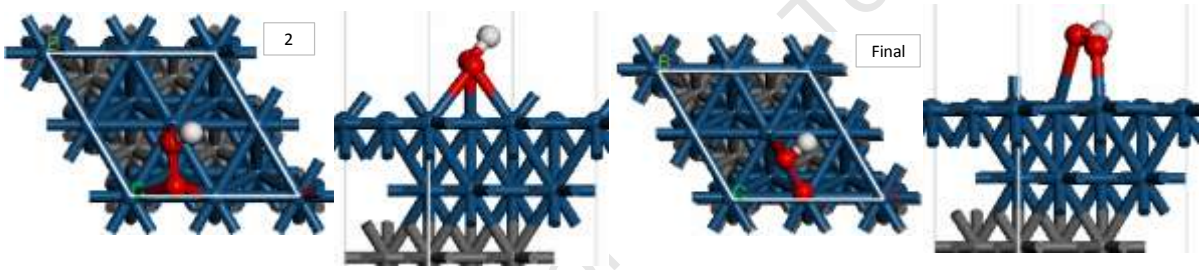

Energy = - 154.886 eV

Configuration three

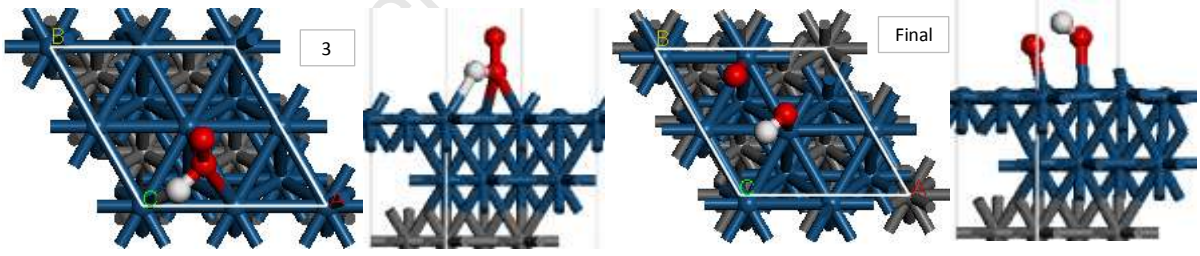

Energy = - 154.623 eV

Configuration four

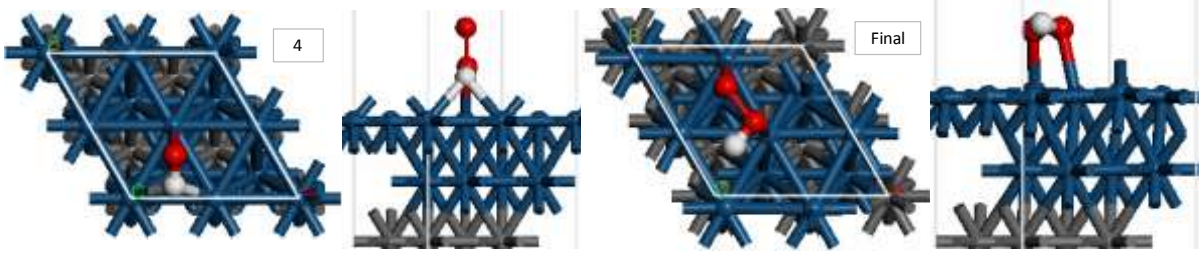

Energy = - 154.529 eV

Configuration five

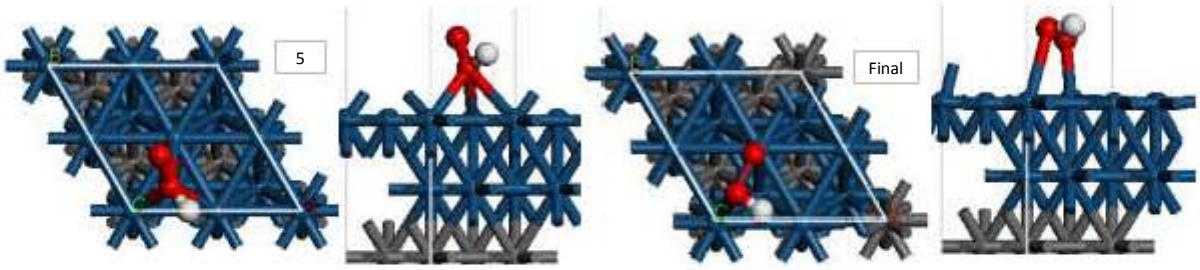

Energy = - 154.891 eV

Configuration six

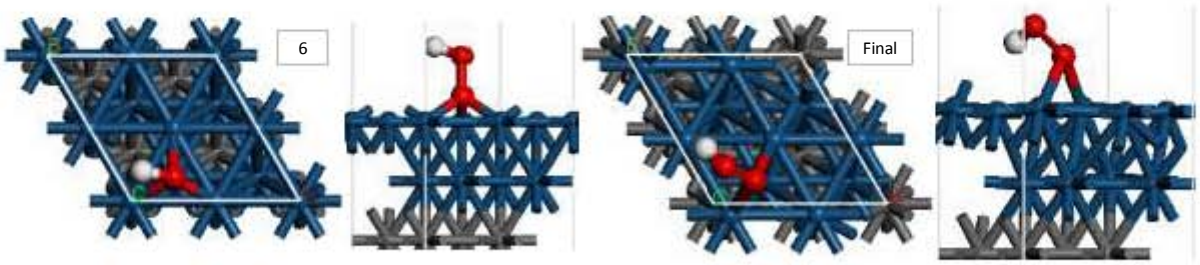

Energy = - 154.689 eV

Configuration seven

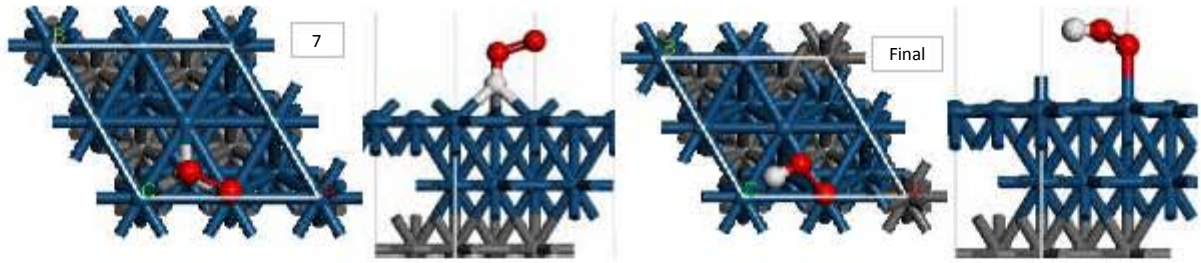

Energy = - 154.897 eV

FCC

Configuration one

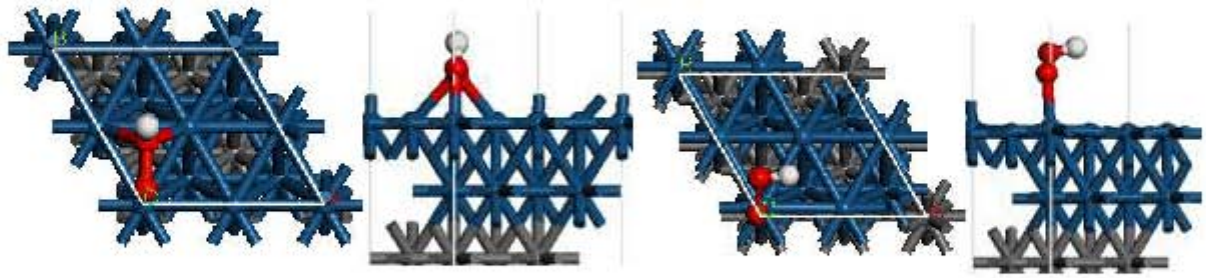

-154.854 eV

Configuration two

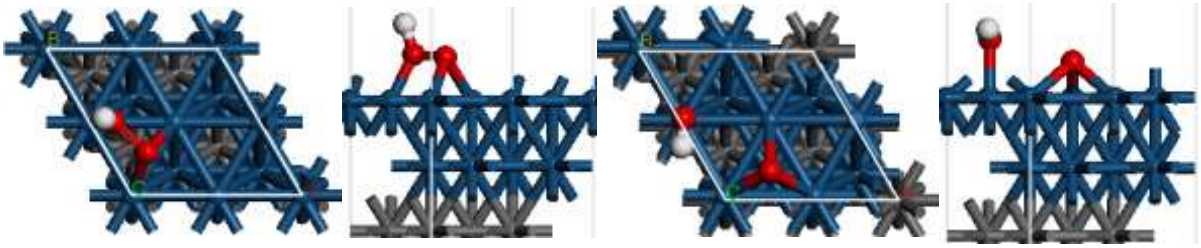

-156.013 eV

Configuration three

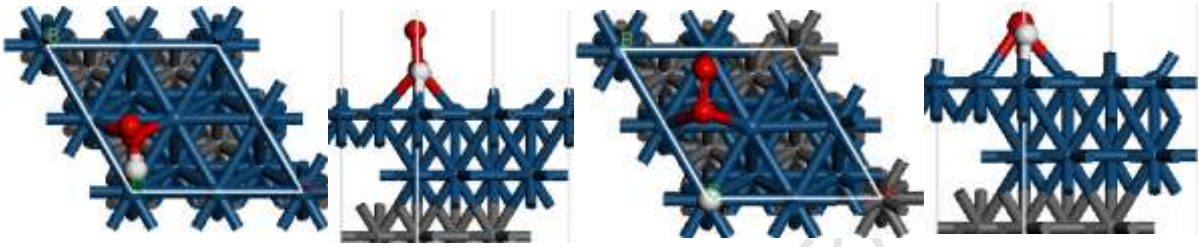

-154.472 eV

Configuration four

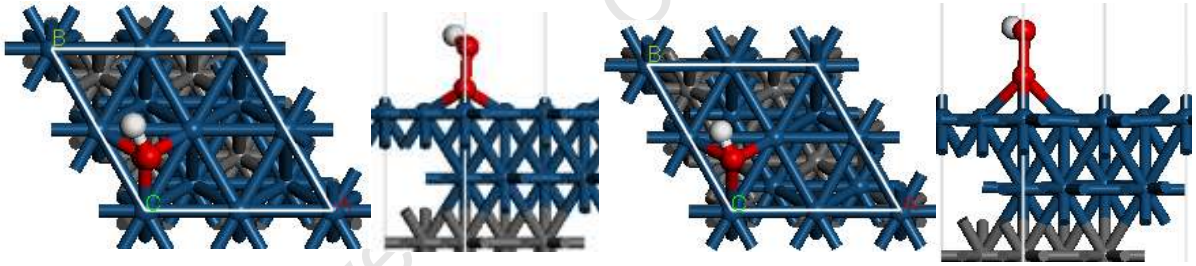

-154.407 eV

Configuration five

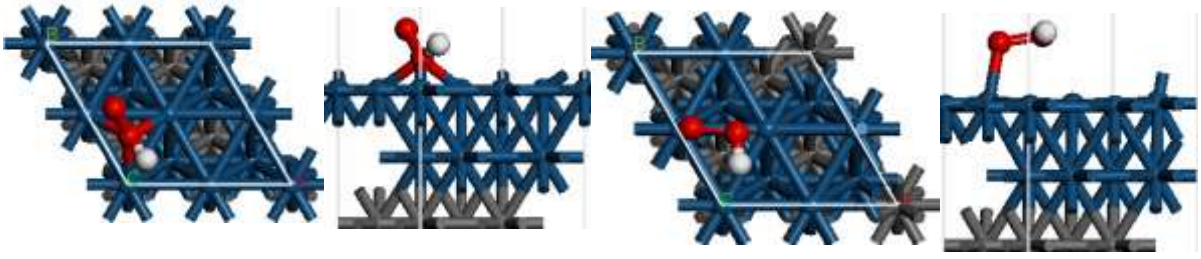

-154.457 eV

Configuration six

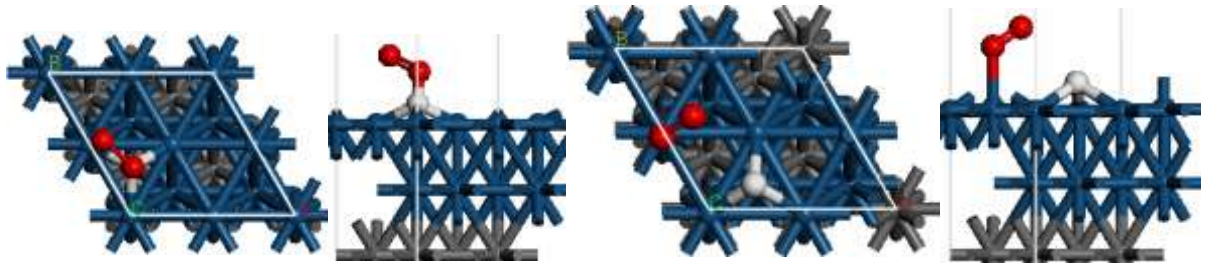

-154.886 eV

Bridge:

Configuration two

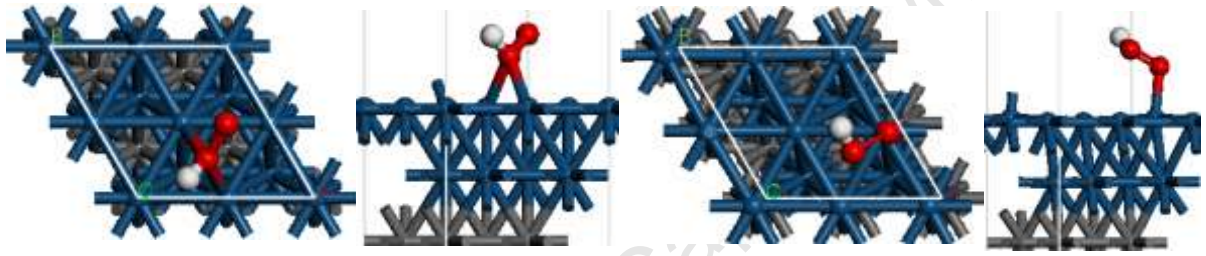

-154.777 eV

on-Top

Configuration one:

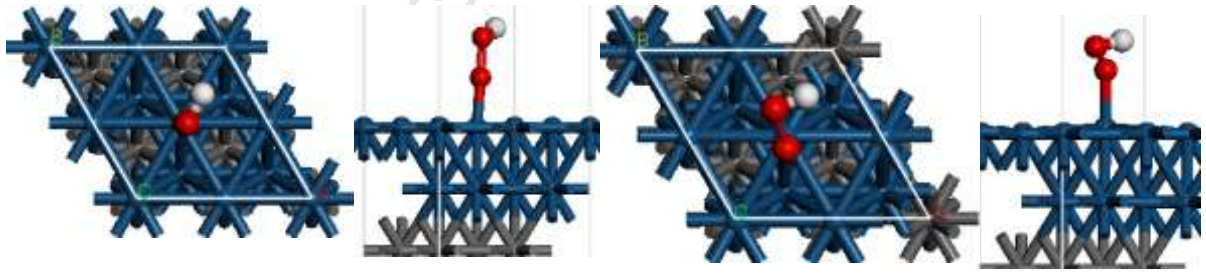

-154.699 eV

Configuration two

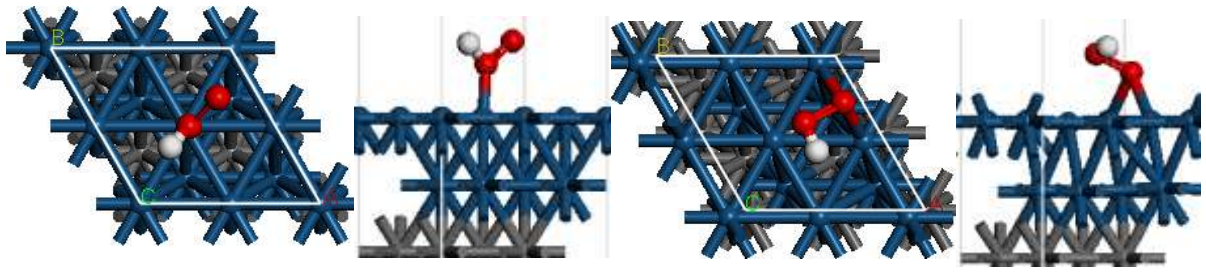

-154.854 eV

Configuration three

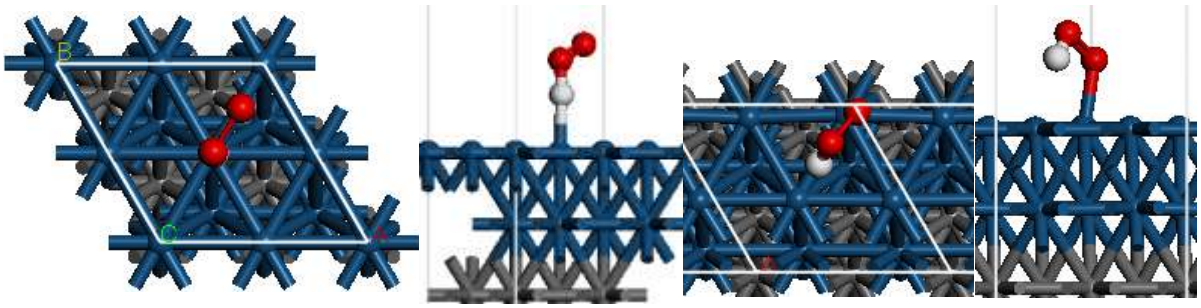

-154.541 eV

HOOH adsorption configuration:

HCP site

Configuration one

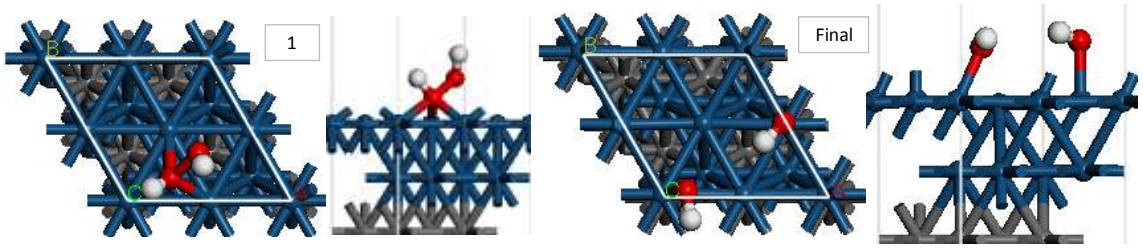

Energy = - 160.668 eV

Configuration two

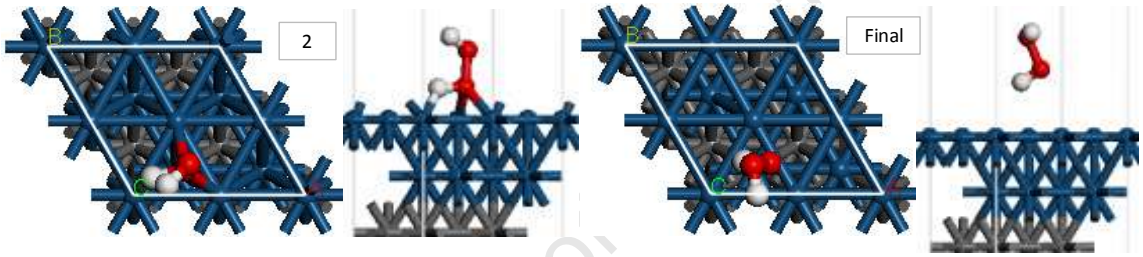

Energy = - 160.503 eV

Configuration three

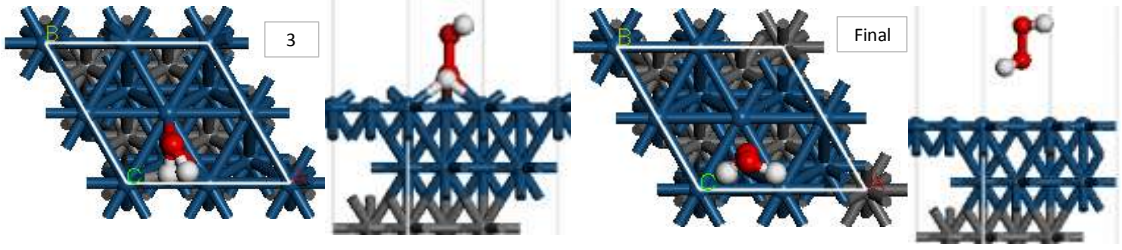

Energy = - 158.794 eV

Configuration four

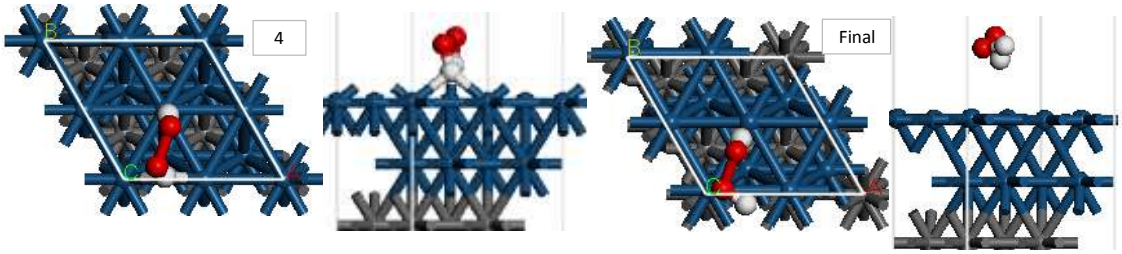

Energy = - 158.801 eV

Configuration five

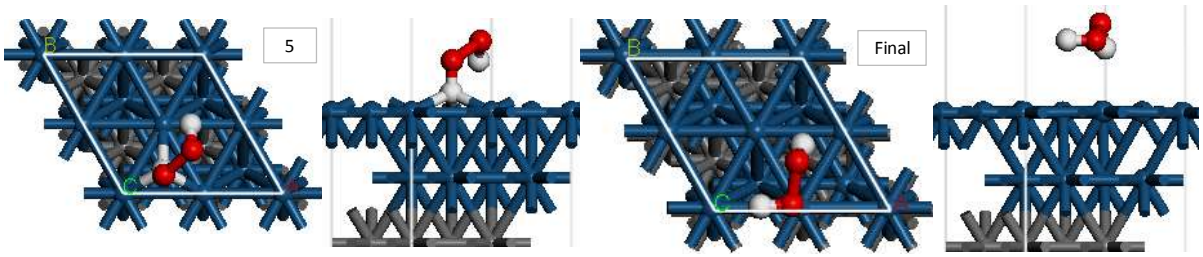

Energy = - 158.878 eV

FCC

Configuration one

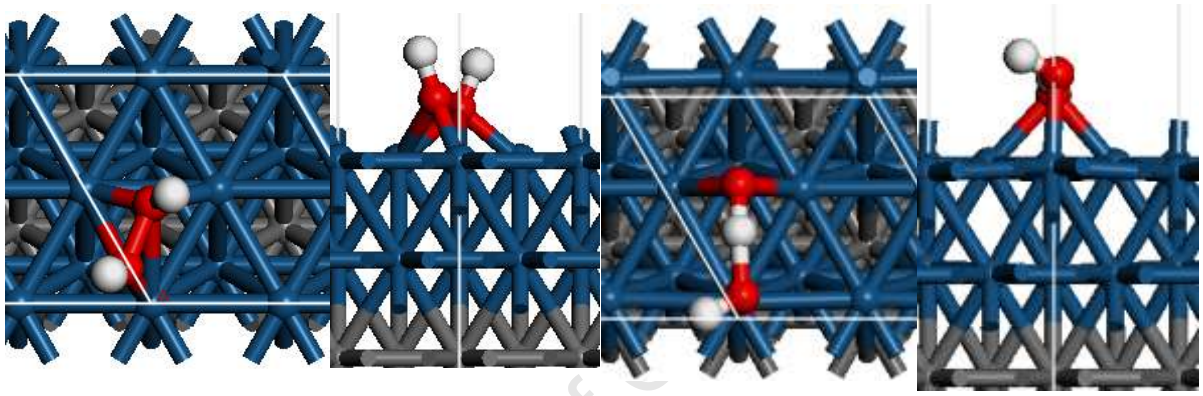

-160.765 eV

Configuration two

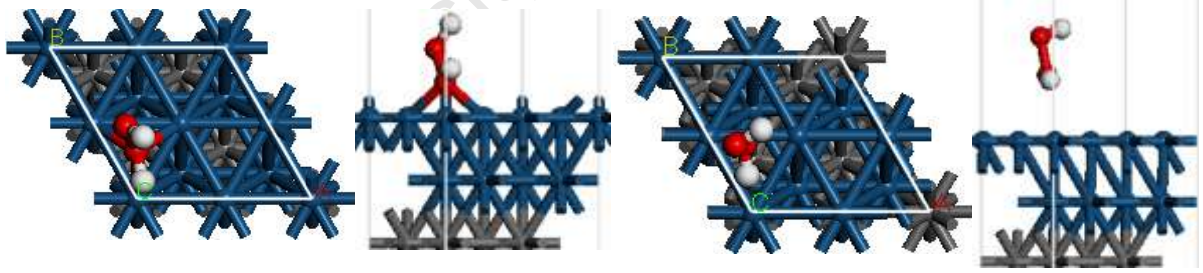

-158.791 eV

Configuration three

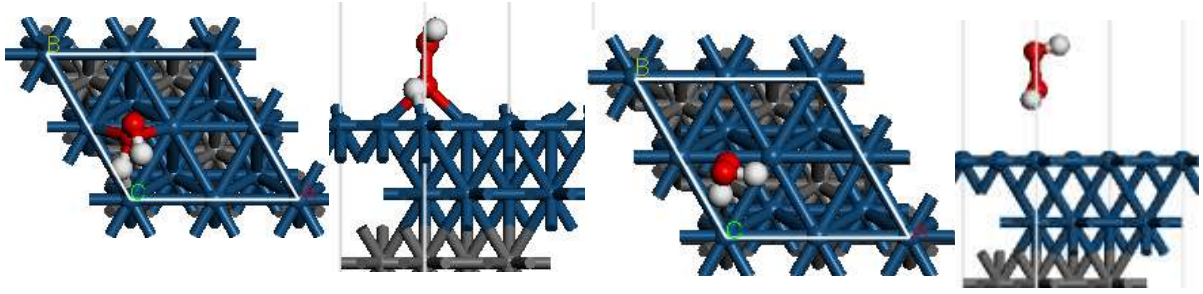

-158.801 eV

Configuration four

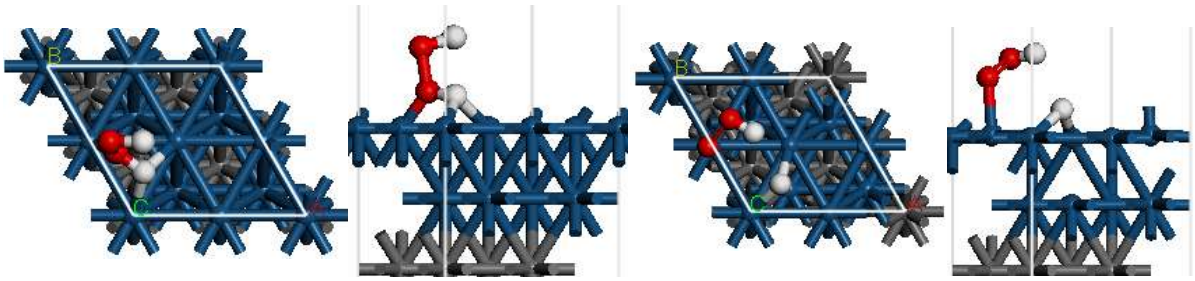

-158.618 eV

Configuration five

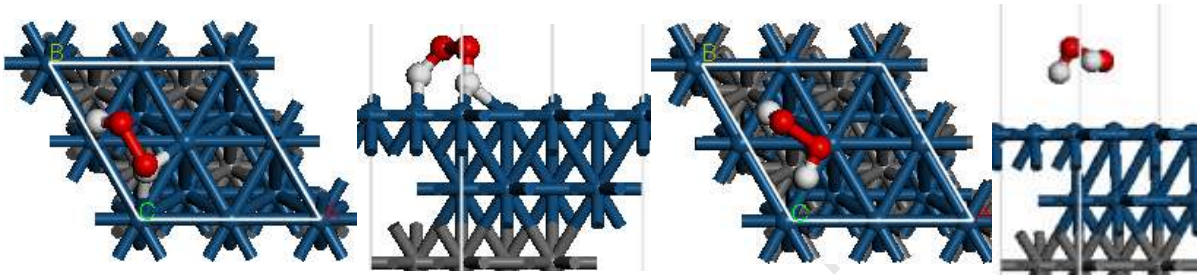

-158.883 eV

Configuration six

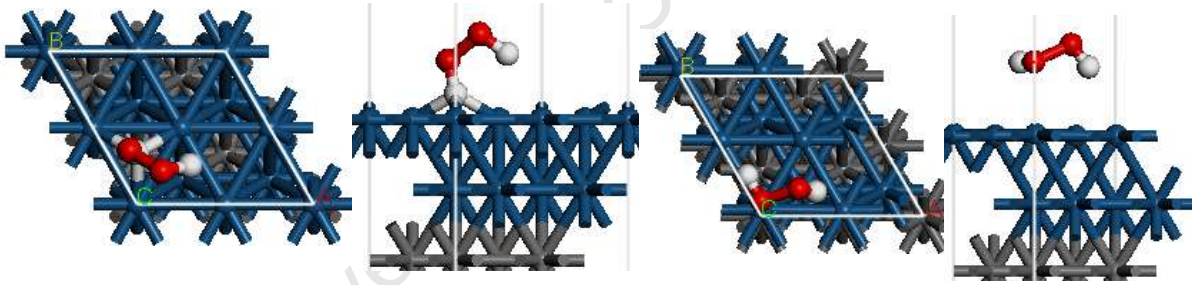

-158.888 eV

Bridge:

Configuration one

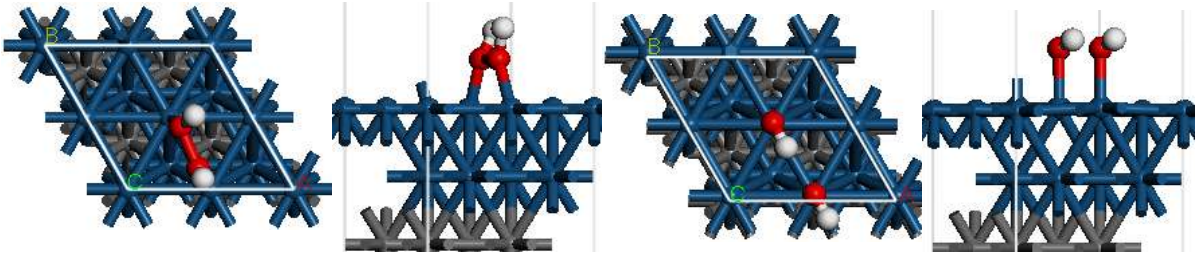

-160.739 eV

Configuration two

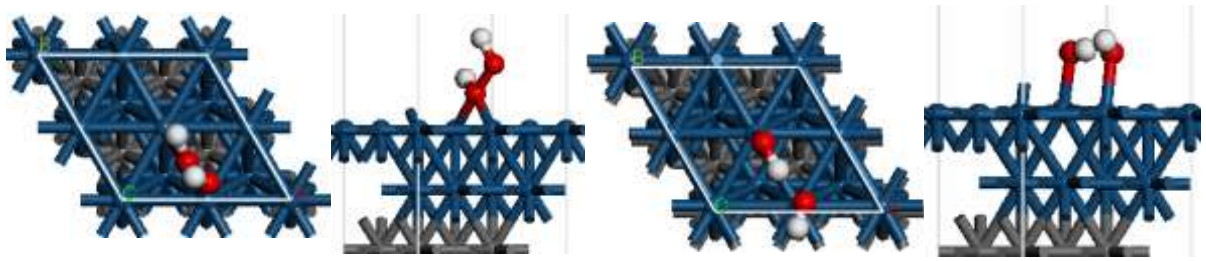

-160.355 eV

Configuration three

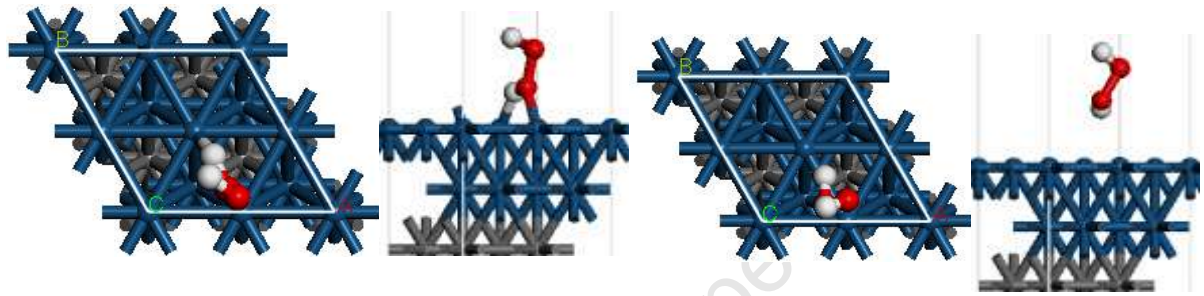

-158.786 eV

Configuration four

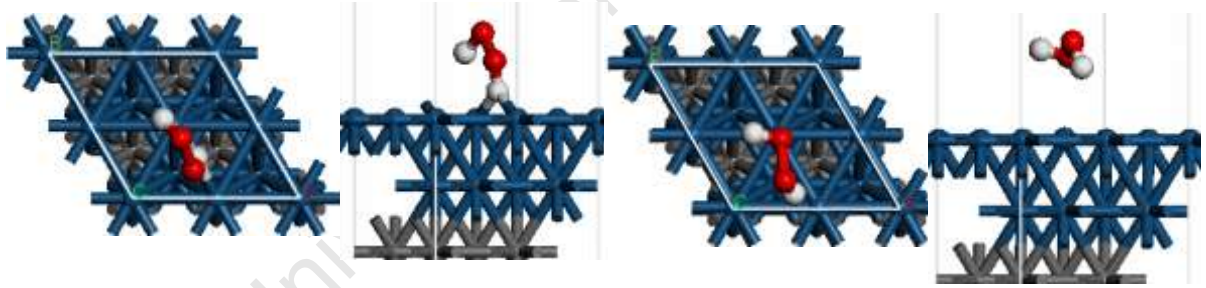

-158.879 eV

On-Top:

Configuration one:

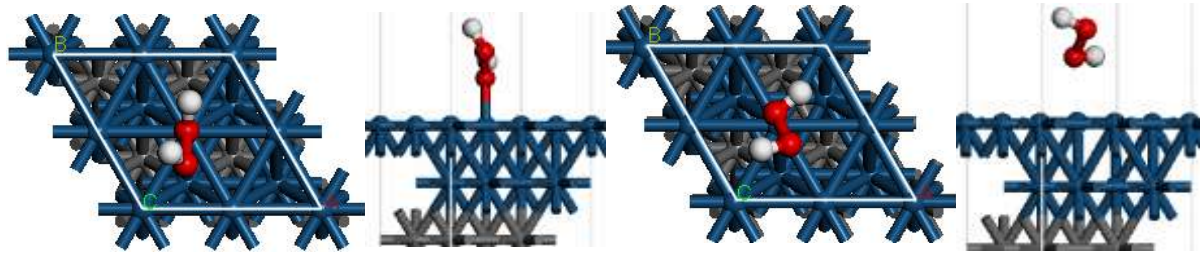

-158.756 eV

Configuration two:

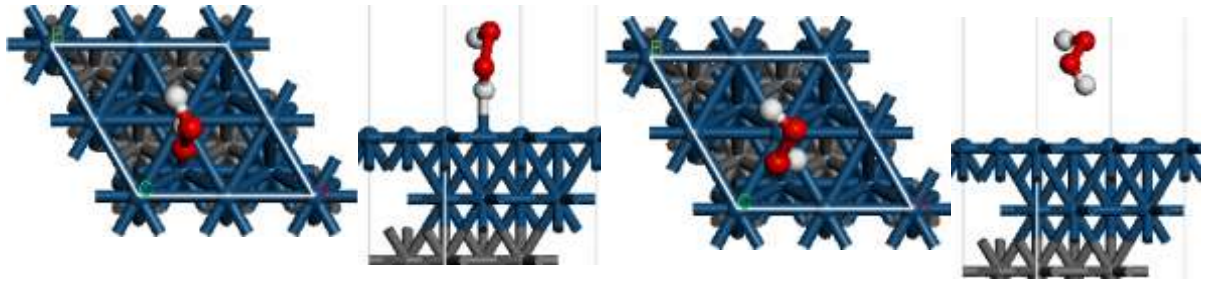

-158.776 eV

Additional Information: atomic O adsorption on a p(3×3) unit cell:

These configurations were studied to investigate the surface roughening effect observed at higher coverage's in chapter-4. It is noted that as the coverage increases, the surface does show a little sign of reconstruction. This contributes towards finding the saturation coverage for oxygen. Furthermore the roughening effect could be explained by the strong interaction of the atomic oxygen with the Pt(111) surface, with the adsorption energy of -4.07 eV.

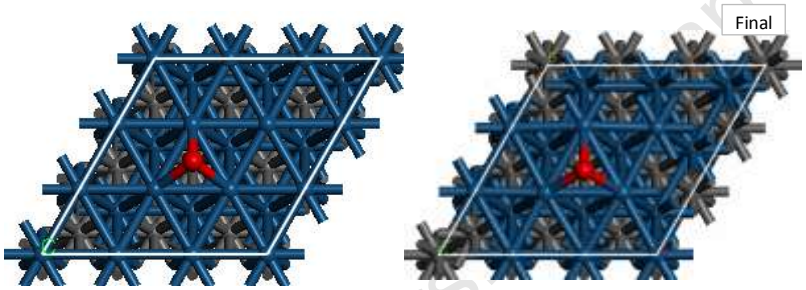

Energy = - 322.249 eV

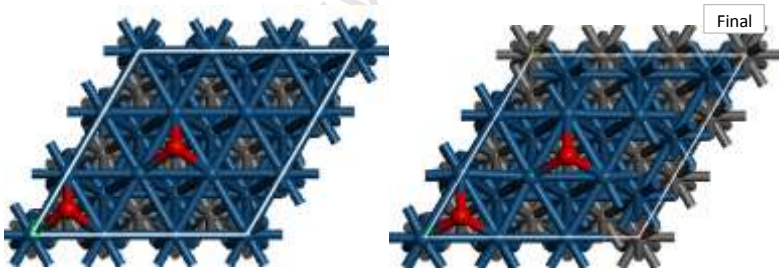

Energy = - 328.112 eV

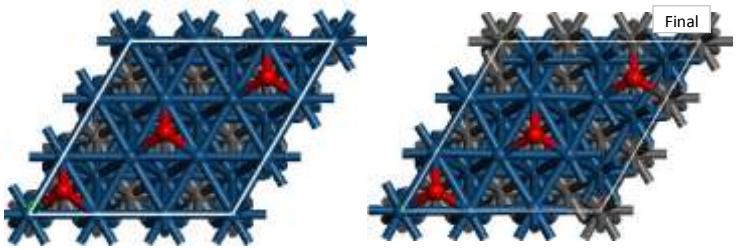

Energy = - 333.737 eV

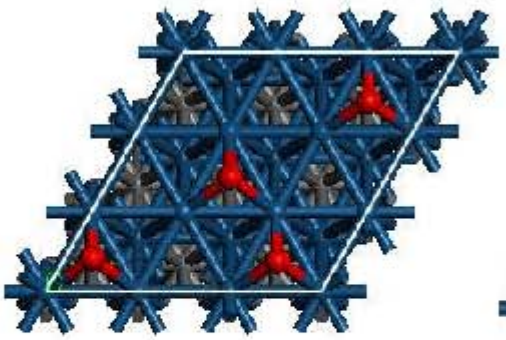

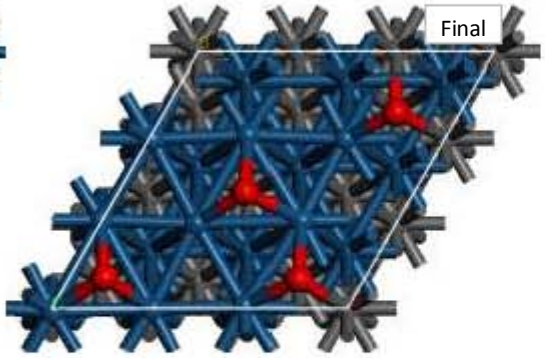

Energy = - 339.009 eV

Vibrational Frequency (cm^{-1})			
1 - O	2 - O	3 -O	4 - O
438.756	446.105	439.305	483.411
373.494	431.217	434.770	460.324
366.609	392.476	434.113	459.865
		377.857	443.944
		377.483	435.798
		377.091	435.088
		376.065	394.048
		365.169	385.028
		364.482	384.488
			364.638
			362.137
			361.404

Potential energy data

Path-1	Path-2	Path-3	
$2H_2O(g)+O_2(g)$	$2H_2O(g)+O_2(g)$	$2H_2O(g)+O_2(g)$	1
$2H_2O^*+O_2(g)$	$2H_2O^*+O_2(g)$	$2H_2O^*+O_2(g)$	2
$2(OH^*+H^*)+O_2(g)$	$2(OH^*+H^*)+O_2(g)$	$2(OH^*+H^*)+O_2(g)$	3
$2(OH^*+H^*)+O^*_2$	$2(OH^*+H^*)+(O^*_2)$	$2(OH^*+H^*)+(O^*_2)$	4
$2(OH^*)+H^*+((H^*+O^*_2)\rightarrow OOH^*)$	$2(OH^*)+2(H^*)+((O^*_2)\rightarrow O^*+O^*)$	$2(OH^*)+2(H^*)+((O^*_2)\rightarrow O^*+O^*)$	5
$2(OH^*)+((H^*+OOH^*)\rightarrow HOOH^*)$	$2(OH^*)+2((H^*+O^*)\rightarrow 2OH^*)$	$2(H^*)+2(OH^*+O^*)\rightarrow 2OOH$	6
$((HOOH^*)+(OH^*+OH^*))\rightarrow 2HOOH^*$	$2(OH^*+OH^*)\rightarrow 2HOOH^*$	$2(OOH^*+H^*)\rightarrow HOOH^*$	7
$2HOOH(g)$	$2HOOH(g)$	$2HOOH(g)$	8

	Path - 1	Path - 2	Path - 3
Elementary steps	Energy difference(eV)	Energy difference(eV)	Energy difference(eV)
1	0	0	0
2	-0.25	-0.25	-0.25
3	0.66	0.66	0.66
4	0.14	0.14	0.14
5	0.23	-1.50	-1.50
6	0.19	-1.29	1.74
7	1.67	1.67	1.67
8	2.16	2.16	2.16

APPENDIX C

Chapter 5

NUDGED ELASTIC BAND METHOD RESULTS

Water dissociation:

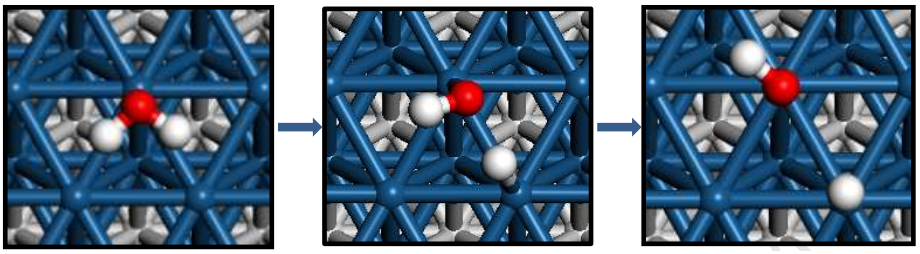

$(H_2O)_{ads}$ TS $(OH+H)_{co\text{-}ads}$

Images	Energy(eV)	Largest Single Absolute Force (eV/Å)	O-H Bond Å
0	-154.95		0.98
1	-154.94	0.20	0.98
2	-154.89	0.13	1.00
3	-154.58	1.24	1.11
4	-154.42	1.17	1.20
5	-154.16	0.43	1.45
6	-154.11	0.03	1.71
7	-154.14	0.10	1.98
8	-154.12	0.16	1.95
9	-154.17	0.17	2.21
10	-154.20	0.13	2.39
11	-154.22	0.08	2.51
12	-154.24		2.64

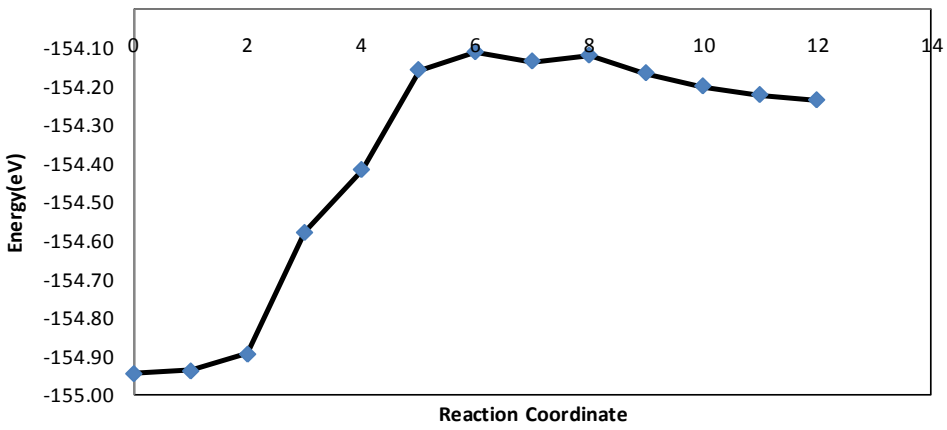

Oxygen assisted water dissociation

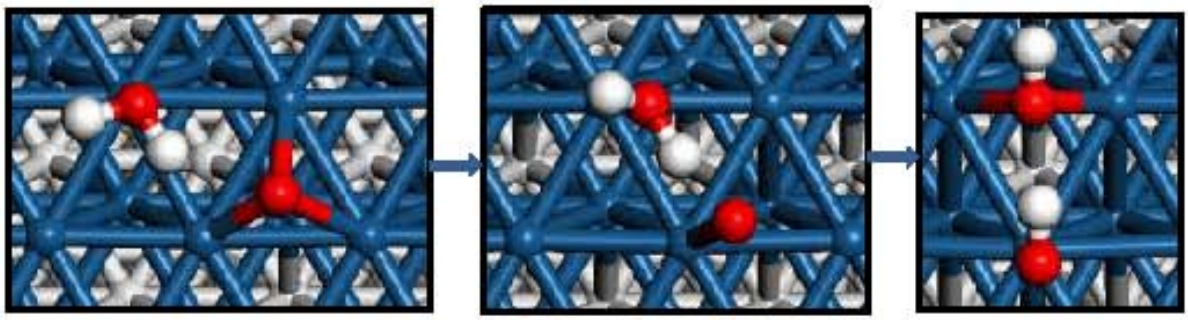

H2O+O→2OH

Images	Energy	Largest Single Absolute Force (eV/Å)	O-H Bond Å
0	-160.60		2.50
1	-160.57	0.12	2.33
2	-160.49	0.24	2.23
3	-160.32	0.53	2.12
4	-160.12	0.16	1.91
5	-160.01	0.33	1.72
6	-159.99	0.14	1.53
7	-160.17	0.55	1.16
8	-160.39	0.30	1.04
9	-160.49	0.34	1.03
10	-160.55	0.17	1.00
11	-160.50	0.12	0.99
12	-160.52		0.99

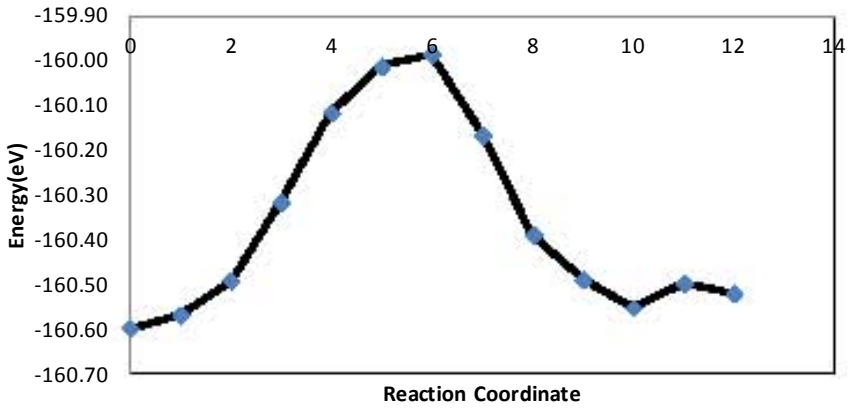

Oxygen dissociation:

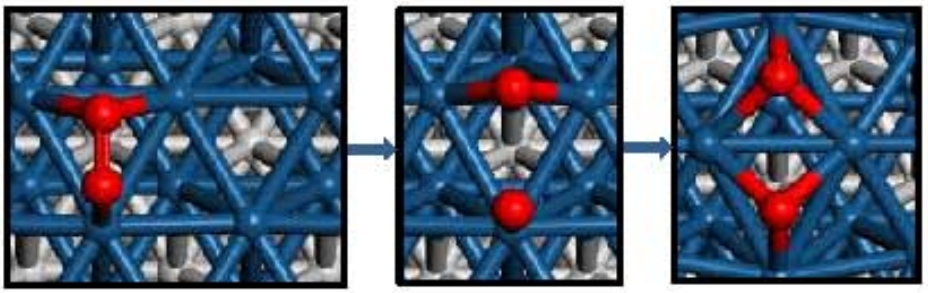

$(O_2)_{ads}$ TS $(O+O)_{co\text{-}ads}$

O_2 Dissociation			
Images	Energy(eV)	Largest Single Absolute Force (eV/Å)	O-O Bond Å
0	-150.96		1.40
1	-150.81	1.29	1.54
2	-150.43	0.45	1.94
3	-150.38	0.17	2.12
4	-150.35	0.02	2.31
5	-150.36	0.18	2.51
6	-150.42	0.43	2.68
7	-150.50	0.52	2.83
8	-150.50	0.22	2.77
9	-150.50	0.38	2.62
10	-151.00	0.76	2.54
11	-151.36	0.23	2.58
12	-151.38		2.63

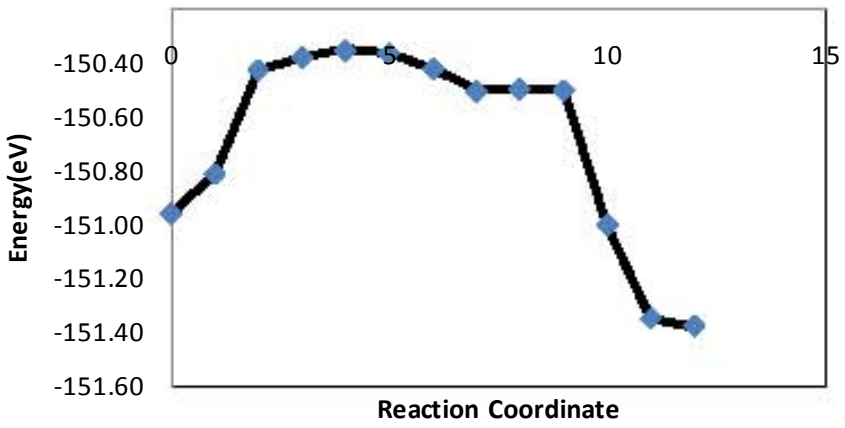

Oxygen hydrogenation:

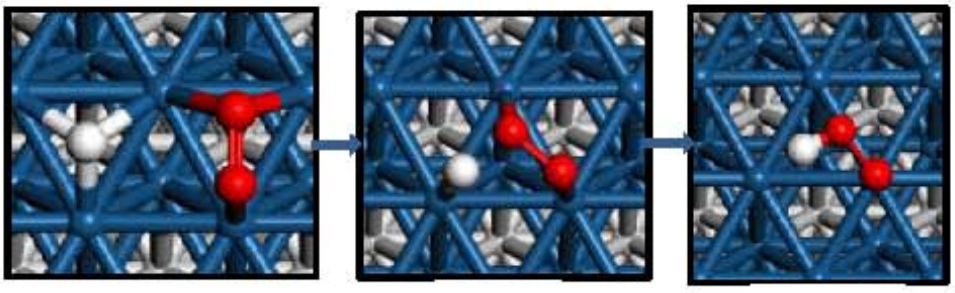

$(O_2+H)_{co\text{-}ads}$ TS $(OOH)_{ads}$

Oxygen Hydrogenation			
Images	Energy(eV)	Largest Single Absolute Force(eV/Å)	O-H Bond Å
0	-154.59		2.98
1	-154.54	0.13	2.81
2	-154.44	0.13	2.62
3	-154.40	0.21	2.44
4	-154.36	0.30	2.09
5	-154.57	0.21	2.26
6	-154.32	0.01	1.49
7	-154.48	0.74	1.20
8	-154.70	0.42	1.05
9	-154.79	0.23	1.01
10	-154.85	0.14	1.00
11	-154.86	0.26	1.01
12	-154.89	0.21	1.00
13	-154.90		0.99

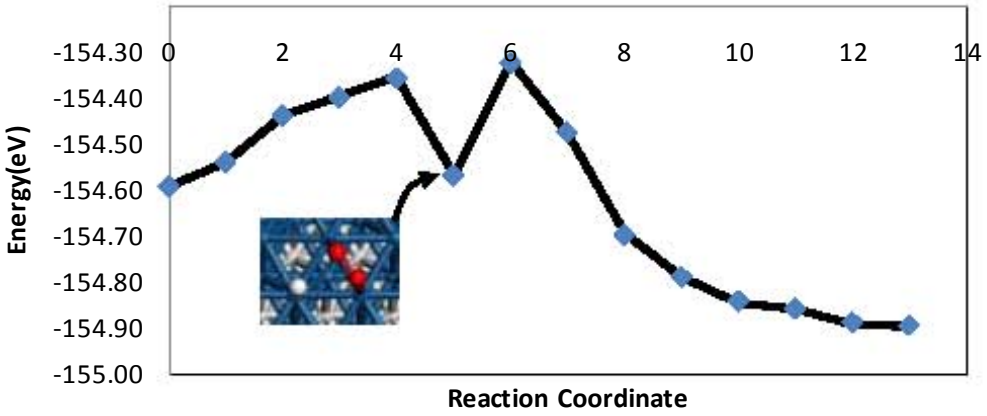

Peroxide intermediate hydrogenation:

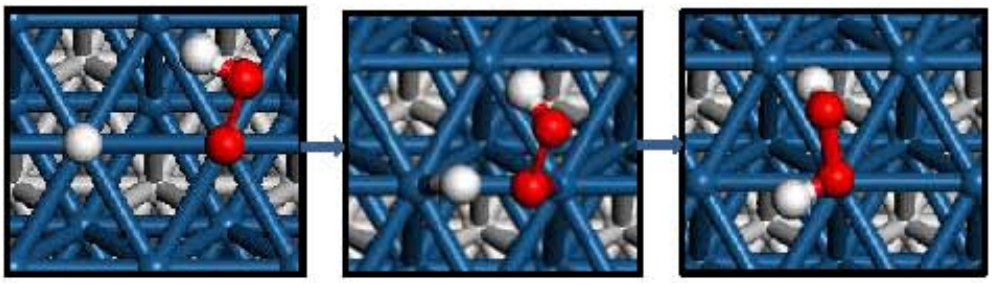

$(H+OOH)_{co\text{-}ads}$ TS $(HOOH)_{ads}$

OOH Hydrogenation			
Images	Energy(eV)	Largest Single Absolute Force (eV/Å)	O-H Bond Å
0	-158.67		2.83
1	-158.65	0.11	2.60
2	-158.60	0.21	2.36
3	-158.52	0.27	2.08
4	-158.43	0.28	1.79
5	-158.41	0.21	1.68
6	-158.39	0.03	1.50
7	-158.47	0.65	1.27
8	-158.68	0.62	1.09
9	-158.76	0.57	1.06
10	-158.90	0.09	1.00
11	-158.94	0.07	0.99
12	-158.96		0.99

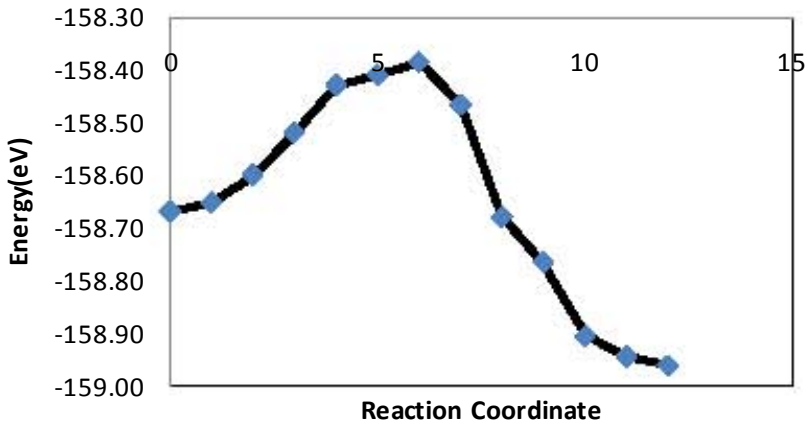

Atomic oxygen hydrogenation:

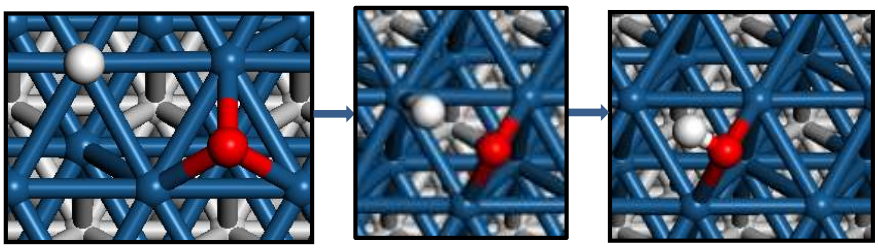

$(H+O)_{co\text{-}ads}$ TS $(OH)_{ads}$

O+H→OH

Images	Energy(eV)	Largest Single Absolute Force (eV/Å)	O-H Bond Å
0	-149.89		3.20
1	-149.88	0.04	3.13
2	-149.85	0.09	2.98
3	-149.71	0.31	2.59
4	-149.58	0.21	2.19
5	-149.49	0.01	1.72
6	-149.88	1.65	1.24
7	-150.40	0.31	1.01
8	-150.47	0.07	0.99
9	-150.48		0.98

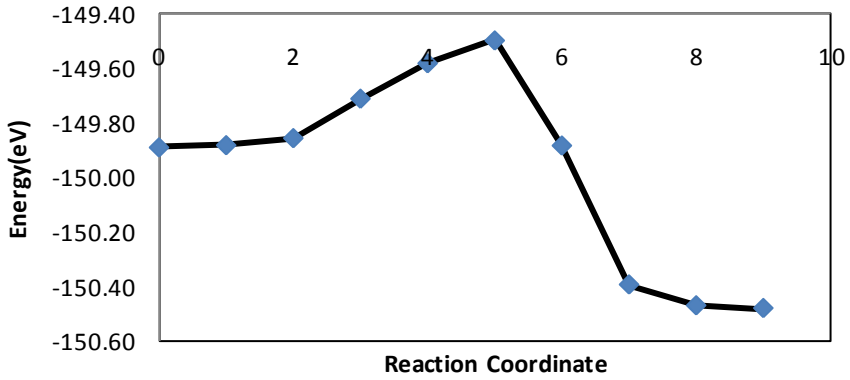

Oxygen addition to hydroxyl species:

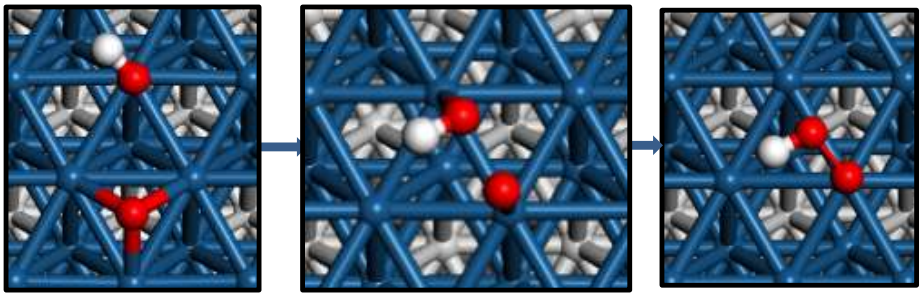

$(O+OH)_{co\text{-}ads}$ TS $(OOH)_{ads}$

O+OH→OOH			
Images	Energy(eV)	Largest Single Absolute Force (eV/Å)	O-O Bond Å
0	-156.43		3.54
1	-156.37	0.20	3.38
2	-156.36	0.09	3.22
3	-156.24	0.61	3.00
4	-155.32	1.06	2.67
5	-154.87	0.45	2.38
6	-154.93	0.27	2.44
7	-154.84	0.40	2.36
8	-154.91	0.29	2.31
9	-154.84	0.34	2.02
10	-154.78	0.07	1.75
11	-154.84	0.26	1.54
12	-154.86	0.10	1.49
13	-154.85	0.13	1.46
14	-154.89	0.07	1.44
15	-154.90		1.43

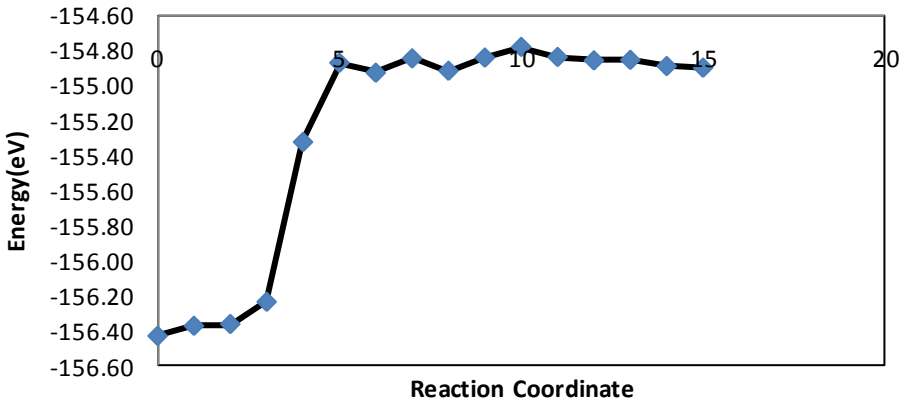

Hydroxyls species recombination:

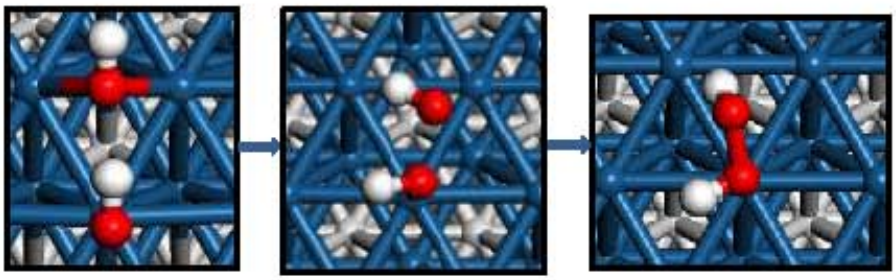

$(OH+OH)_{co\text{-}ads}$ TS $(HOOH)_{ads}$

OH+OH→HOOH (1)			
Images	Energy	Largest Single Absolute Force (eV/Å)	O-O Bond Å
0	-160.52		2.70
1	-160.49	0.09	2.72
2	-160.35	0.39	2.73
3	-160.04	0.36	2.72
4	-160.03	0.26	2.79
5	-159.38	1.39	2.24
6	-159.02	1.18	2.11
7	-158.68	0.67	1.95
8	-158.61	0.45	1.86
9	-158.57	0.05	1.75
10	-158.61	0.58	1.62
11	-158.72	0.41	1.51
12	-158.77	0.37	1.50
13	-158.88	0.18	1.48
14	-158.94	0.06	1.47
15	-158.96		1.47

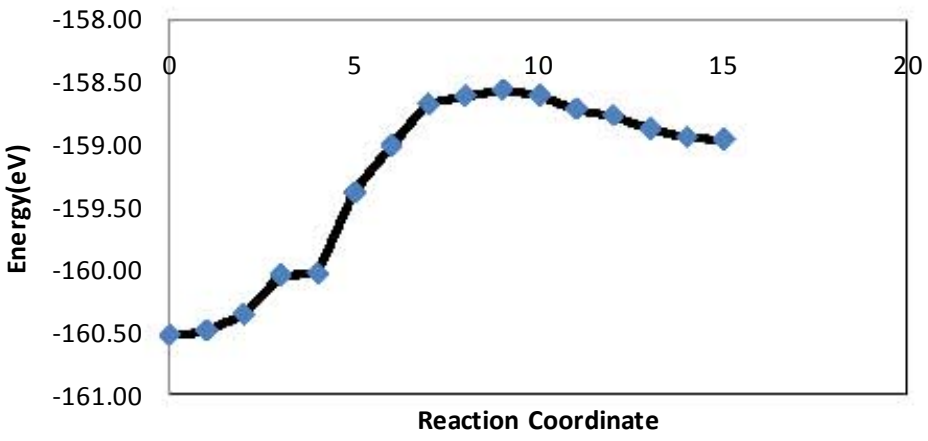

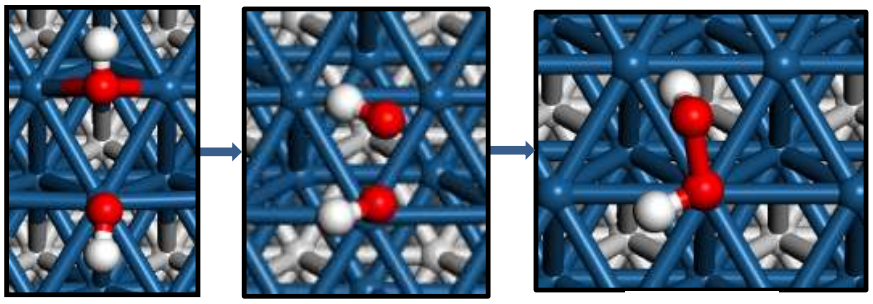

$(OH+OH)_{co\text{-}ads}$ TS $(HOOH)_{ads}$

OH+OH→HOOH (2)

Images	Energy	Largest Single Absolute Force (eV/Å)	O-O Bond Å
0	-160.34		2.70
1	-160.30	0.07	2.67
2	-160.20	0.28	2.67
3	-159.87	0.35	2.58
4	-159.47	1.56	2.37
5	-159.41	1.37	2.27
6	-158.76	0.77	2.06
7	-158.78	0.81	2.05
8	-158.61	0.43	1.92
9	-158.56	0.06	1.78
10	-158.64	0.69	1.60
11	-158.76	0.40	1.54
12	-158.61	0.72	1.47
13	-158.89	0.21	1.47
14	-158.95	0.06	1.47
15	-158.96		1.47

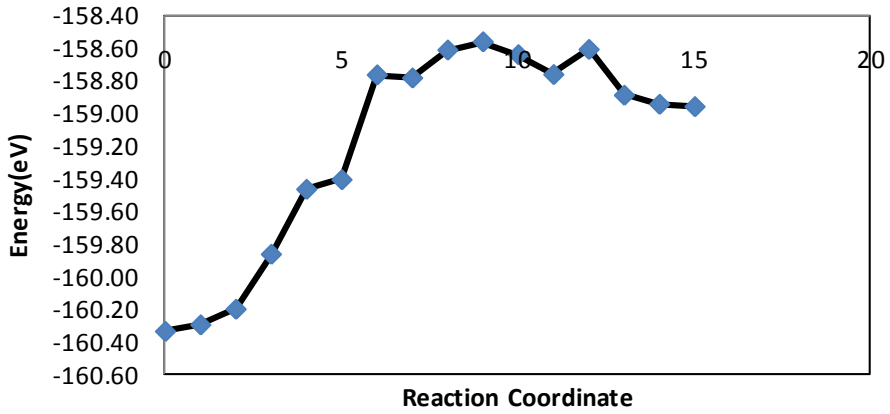

APPENDIX D

MICRO-KINETICS MODEL INFORMATION:

Species	Gas phase energy(eV)	Energy(eV) on Pt(111)	Vibrational frequency (cm^{-1}) on Pt(111)	Vibrational frequency (cm^{-1}) gas
H_2O	-14.22	-154.95	3684.44 3581.09 1575.60 513.06 452.11 169.29 122.34 106.71 86.34	3858.60 3742.41 1593.00 29.62 26.08 5.94 -1.25 -34.68 -50.30
O_2	-9.85	-150.96	823.45 509.72 364.49 321.84 236.86 136.91	1564.43 6.10 0.25 -0.37 -19.70 -45.32
OH	-7.73	-150.48	3614.55 722.58 686.14 387.87 214.53 203.08	3618.58 63.60 2.32 -0.15 -5.46 -89.83
H	-1.11	-144.42	1117.34 635.03 599.83	
O	-1.89	-146.57	468.64 385.19 383.47	
OOH	-13.26	-154.90	1721.80 1305.56	

			1073.91 539.41 455.49 319.88 304.37 159.60 114.60	
HOOH	-18.15	-158.96	3576.01 3185.16 1383.72 1279.30 855.96 510.49 299.22 222.02 132.62 107.86 95.16 30.41	3684.79 3675.66 1385.13 1286.04 920.73 371.76 33.90 21.42 -0.34 -10.47 -24.04 -116.24
6-layer-slab		-140.54		

Reaction	Vibrational frequency (cm^{-1}) reactants	Vibrational frequency (cm^{-1}) Transition State	Vibrational frequency (cm^{-1}) products	E_a ZPE corrected (eV)
	Energy(eV) -154.95	Energy(eV) -154.11	Co-adsorbed Energy(eV) -154.24	
$H_2O^* \rightarrow OH^* + H^*$	3684.44 3581.09 1575.60 513.06 452.11 169.29 122.34 106.71 86.34	3665.35 1707.87 872.99 657.85 469.38 357.38 300.22 150.79 -319.05	3668.70 2291.77 942.70 518.33 476.48 365.12 147.10 112.91 89.97	0.70
	Energy(eV) -150.96	Energy(eV) -150.35	Co-adsorbed Energy(eV) -151.38	
$O^*_2 \rightarrow O^* + O^*$	823.45	671.66	489.45	0.58

	509.72	522.40	450.18	
	364.49	367.50	413.86	
	321.84	181.18	389.16	
	236.86	92.89	380.96	
	136.91	-134.62	288.76	
	Co-adsorbed Energy(eV) -154.59	Energy(eV) -154.32	Energy(eV) -154.90	
$O^*_2 + H^* \rightarrow OOH^*$	1169.04	1369.61	1721.80	0.25
	849.63	897.32	1305.56	
	706.76	819.36	1073.91	
	675.45	505.04	539.41	
	503.48	354.98	455.49	
	348.31	298.21	319.88	
	331.65	191.33	304.37	
	214.34	155.06	159.60	
	120.90	-739.13	114.60	
	Co-adsorbed Energy(eV) -149.89	Energy(eV) -149.50	Energy(eV) -150.48	
$O^* + H^* \rightarrow OH^*$	2279.92	1889.18	3614.55	0.35
	448.50	591.97	722.58	
	436.94	513.04	686.14	
	432.98	351.26	387.87	
	314.22	244.97	214.53	
	313.13	-569.71	203.08	
	Co-adsorbed Energy(eV) -156.43	Energy(eV) -154.76	Energy(eV) -154.90	
$O^* + OH^* \rightarrow OOH^*$	3675.48	3600.83	1721.80	1.67
	948.57	901.79	1305.56	
	520.53	715.36	1073.91	
	471.47	561.17	539.41	
	385.81	400.16	455.49	
	376.21	239.01	319.88	
	150.23	167.35	304.37	
	129.93	114.53	159.60	
	83.40	-279.97	114.60	
	Co-adsorbed Energy(eV) -158.67	Energy(eV) -158.39	Energy(eV) -158.96	
$H^* + OOH^* \rightarrow HOOH^*$	3509.96	3357.63	3576.01	0.21

	2300.61	1350.68	3185.16	
	1325.02	1329.88	1383.72	
	864.55	863.44	1279.30	
	475.89	740.07	855.96	
	429.69	409.71	510.49	
	392.78	364.19	299.22	
	364.45	291.98	222.02	
	243.36	208.08	132.62	
	138.52	117.69	107.86	
	92.41	86.76	95.16	
	75.30	-540.78	30.41	
	Co-adsorbed Energy(eV) -160.52	Energy(eV) -158.57	Energy(eV) -158.96	
OH* + OH* → HOOH* (1)	3621.62	3580.73	3576.01	1.90
	3534.12	3377.90	3185.16	
	947.14	1030.12	1383.72	
	799.37	970.88	1279.30	
	782.32	593.83	855.96	
	504.73	459.27	510.49	
	396.09	367.68	299.22	
	327.31	169.34	222.02	
	266.54	135.58	132.62	
	210.34	108.32	107.86	
	179.97	84.84	95.16	
	83.30	-400.52	30.41	
	Co-adsorbed Energy(eV) -160.34	Energy(eV) -158.58	Energy(eV) -158.96	
OH* + OH* → HOOH* (2)	3624.78	3582.57	3576.01	1.70
	3517.81	3400.69	3185.16	
	1038.94	1030.23	1383.72	
	772.31	966.69	1279.30	
	678.01	593.26	855.96	
	529.95	458.72	510.49	
	513.03	371.64	299.22	
	379.08	164.93	222.02	
	304.01	139.24	132.62	
	181.82	106.64	107.86	
	164.59	93.84	95.16	
	77.66	-374.72	30.41	
	Energy(eV) -154.90	Energy(eV) -154.76	Co-adsorbed Energy(eV) -156.43	
OOH* → OH* + O*	1721.80	3600.83	3675.48	0.11

	1305.56	901.79	948.57
	1073.91	715.36	520.53
	539.41	561.17	471.47
	455.49	400.16	385.81
	319.88	239.01	376.21
	304.37	167.35	150.23
	159.60	114.53	129.93
	114.60	-279.97	83.40

	Co-adsorbed Energy(eV) -160.60	Energy(eV)	Energy(eV) -160.52
$H_2O^*+O^* \rightarrow OH^*$	3729.43	3690.77	3509.96
	3620.12	2407.56	2300.61
	1574.77	1360.10	1325.02
	539.70	1038.70	864.55
	534.63	691.38	475.89
	417.63	551.43	429.69
	282.44	401.63	392.78
	277.45	291.83	364.45
	190.34	174.56	243.36
	156.54	136.20	138.52
	124.25	19.98	92.41
	98.24	-172.29	75.30